Unbalanced Voltage Compensation using Interfacing Converters in Hybrid AC/DC Microgrids

by

Farzam Nejabatkhah

A thesis submitted in partial fulfillment of the requirements for the degree of

Doctor of Philosophy

in

Energy Systems

Department of Electrical and Computer Engineering
University of Alberta

Abstract

Today, conventional power systems are evolving into modern smart grids, where interconnected microgrids may dominate the distribution system with high penetration of renewable energies and storage elements (SEs). The hybrid AC/DC systems with DC and AC sources/loads are considered to be the most likely future distribution or even transmission structures. For such hybrid AC/DC microgrids, control strategies are one of the most critical operation aspects. Also, unbalanced voltage caused by ever-increasing unbalanced distribution of single-phase/unbalanced loads, single-phase/unbalanced distributed generations (DGs), and remote grid faults has raised serious concern about such hybrid microgrids due to the adverse effects on the power system and equipment. In hybrid AC/DC microgrids, the high penetration level of power electronics interfacing converters creates great ancillary services potential such as unbalanced voltage compensation. These interfacing converters (IFCs) are the interfacing converters of DGs/SEs, and AC and DC-subsystems IFCs (they can also be called solid-state transformers). These IFCs can be single three-phase IFCs, parallel three-phase IFCs (when larger power and current capacity are needed), or single-phase IFCs.

However, the operating interfacing converters under unbalanced voltage will introduce some adverse effects such as output power oscillations, DC link voltage oscillations (especially when the DC link capacitance is designed to be small for a three-phase converter), and the output peak current enhancement. Therefore, designing suitable control strategies for these IFCs for operation under

unbalanced AC voltage or even to compensate for the voltage unbalance with consideration of the above adverse effects is very important. Moreover, since the compensation is realized through the available rating of IFCs, it is equally important to consider the effectiveness of the control strategy for unbalanced voltage compensation.

The purpose of this research work is to develop control strategies for the interfacing converters for unbalanced voltage operation or compensation in hybrid AC/DC microgrids. Three interfacing converters configurations, single three-phase IFCs, parallel three-phase IFCs, and single-phase IFCs, are considered. Specifically, for single three-phase IFC control, the focus is on the minimization of adverse effects such as DC link voltage ripple and the effectiveness of the unbalanced compensation, while providing an adjustable level of unbalanced compensation ability. For parallel three-phase IFCs, which usually have the same DC link (the DC link of the DG, SE or the DC subsystem), since adverse effects can be multiplied by the number of IFCs, the control focus is to optimally utilize the parallel IFCs to minimize their adverse effects on each other. For this purpose, either one IFC can focus on the adverse effects minimization, or all IFCs can share it. For single-phase IFCs, the focus is to coordinate multiple IFCs to compensate the unbalanced condition while providing an adjustable level.

Acknowledgements

First and foremost I want to thank my Ph.D. supervisor, Professor Yunwei (Ryan) Li. It has been an honor to be his Ph.D. student, and his advice on both research as well as on my career have been inevitable. I appreciate all his contributions of ideas and time to make my Ph.D. experience productive. His profound knowledge in the area of power engineering and also his enthusiasm to research was contagious and motivational for me, and I will forever be thankful to him.

I would like to express my appreciation to Prof. Bin Wu and Dr. Kai Sun for their contributions in my Ph.D. research. I would also like to thank Dr. Jinwei He, Dr. Alexandre Nassif, Dr. Ye (Eric) Zhang, and Dr. Arash Khabbazibasmenj for their help and support during my Ph.D.

I would also like to thank Alberta Innovates Graduate Student Scholarships program for their financial support during my Ph.D.

Table of Contents

List of Tables

List of Figures

List of Acronyms

DG	Distributed generation
RE	Renewable energy
AE	Alternative energy
SE	Storage element
IFC	Interfacing converter
UPQC	Unified power quality conditioner
STATCOM	Static synchronous compensators
PEVs	Plug-in electric vehicles
PF	Power factor
PCC	Point of common coupling
FLL	Frequency-locked loop
PR	Proportional-resonant
rms	Root mean square
KKT	Karush–Kuhn–Tucker

List of Symbols

v_{PCC}	PCC three-phase voltage vector
v_{PCC_a}	Phase-a voltage phasor of PCC
v_{PCC_b}	Phase-b voltage phasor of PCC
v_{PCC_c}	Phase-c voltage phasor of PCC
i_{PCC}	PCC three-phase current vector
i_{PCC_a}	Phase-a current phasor of PCC
i_{PCC_b}	Phase-b current phasor of PCC
i_{PCC_c}	Phase-c current phasor of PCC
$v_{PCC_\perp}$	Orthogonal vector to v_{PCC}
v_{PCC}^{+}	Positive sequence of PCC three-phase voltage vector
v_{PCC}^{-}	Negative sequence of PCC three-phase voltage vector
v_{PCC}^{0}	Zero sequence of PCC three-phase voltage vector
i_{PCC}^{+}	Positive sequence of PCC three-phase current vector
$i_{PCC_p}^{+}$	Positive sequence of PCC three-phase active current vector
$i_{PCC_q}^{+}$	Positive sequence of PCC three-phase reactive current vector
i_{PCC}^{-}	Negative sequence of PCC three-phase current vector
$i_{PCC_p}^{-}$	Negative sequence of PCC three-phase active current vector
$i_{PCC_q}^{-}$	Negative sequence of PCC three-phase reactive current vector
i_{PCC}^{0}	Zero sequence of PCC three-phase current vector
$i_{PCC_p}^{0}$	Zero sequence of PCC three-phase active current vector
$i_{PCC_q}^{0}$	Zero sequence of PCC three-phase reactive current vector
$v_{PCC_\perp}^{+}$	Positive sequence of PCC three-phase voltage orthogonal vector
$v_{PCC_\perp}^{-}$	Negative sequence of PCC three-phase voltage orthogonal vector
$v_{PCC_\perp}^{0}$	Zero sequence of PCC three-phase voltage orthogonal vector
p_{PCC}	Instantaneous active power at the PCC

q_{PCC}	Instantaneous reactive power at the PCC
P_{PCC}	Average term of instantaneous active power at the PCC
ΔP_{PCC}	Oscillatory term of instantaneous active power at the PCC
P_{PCC_0}	Zero sequence average term of instantaneous active power at the PCC
ΔP_{PCC_0}	Zero sequence oscillatory term of instantaneous active power at the PCC
Q_{PCC}	Average term of instantaneous reactive power at the PCC
ΔQ_{PCC}	Oscillatory term of instantaneous reactive power at the PCC
P_{PCC}^{+}	Positive sequences of average active power at the PCC
P_{PCC}^{-}	Negative sequences of average active power at the PCC
Q_{PCC}^{+}	Positive sequences of average reactive power at the PCC
Q_{PCC}^{-}	Negative sequences of average reactive power at the PCC
a^{+}	Positive sequence instantaneous conductance
a^{-}	Negative sequence instantaneous conductance
b^{+}	Positive sequence instantaneous susceptance
b^{-}	Negative sequence instantaneous susceptance
k_1	Weighting factor of positive sequence average active power over average active power
k_2	Weighting factor of positive sequence average reactive power over average reactive power
k_p	Weighting factor for active or reactive power oscillation cancellation under unity power factor
k_q	Weighting factor for active or reactive power oscillation cancellation under zero power factor
i_{PCC_p}	PCC three-phase active current vector
i_{PCC_q}	PCC three-phase reactive current vector
A_{a_p}	Phase-a instantaneous conductance
B_{a_q}	Phase-a instantaneous susceptance
A_{b_p}	Phase-b instantaneous conductance
B_{b_q}	Phase-b instantaneous susceptance
A_{c_p}	Phase-c instantaneous conductance
B_{c_q}	Phase-c instantaneous susceptance

$i_{PCC_{ap}}$	PCC active current in phase-a
$i_{PCC_{bp}}$	PCC active current in phase-b
$i_{PCC_{cp}}$	PCC active current in phase-c
$i_{PCC_{aq}}$	PCC reactive current in phase-a
$i_{PCC_{bq}}$	PCC reactive current in phase-b
$i_{PCC_{cq}}$	PCC reactive current in phase-c
$P_{PCC,a}$	Phase-a average active power at the PCC
$P_{PCC,b}$	Phase-b average active power at the PCC
$P_{PCC,c}$	Phase-c average active power at the PCC
$Q_{PCC,a}$	Phase-a reactive power at the PCC
$Q_{PCC,b}$	Phase-b reactive power at the PCC
$Q_{PCC,c}$	Phase-c reactive power at the PCC
$i^{-}_{PCC_p}$	Negative sequence of PCC three-phase active current
$i^{-}_{PCC_q}$	Negative sequence of PCC three-phase reactive current
$i^{0}_{PCC_p}$	Zero sequence of PCC three-phase active current
$i^{0}_{PCC_q}$	Zero sequence of PCC three-phase reactive current
v	IFC output three-phase voltage vector
i	IFC output three-phase current vector
v_g or v_{Grid}	Grid three-phase voltage vector
Z_{Grid}	Grid coupling impedance
P	IFC output average active power
Q	IFC output average reactive power
v^{+}	Positive sequence of IFC output three-phase voltage vector
v^{-}	Positive sequence of IFC output three-phase voltage vector
i^{+}	Positive sequence of IFC output three-phase current vector
i^{-}	Positive sequence of IFC output three-phase current vector
i^{-}_{Grid}	Negative sequence of grid three-phase current vector
Z^{+}	IFC positive sequence virtual impedance
Z^{-}	IFC negative sequence virtual impedance
Z^{+}_{Grid}	Positive sequence of grid coupling impedance

Z_{Grid}^{-}	Negative sequence of grid coupling impedance
Z_{L1}, Z_{L2}, Z_{L3}	Unbalance load impedance connected to PCC
Z_{PCC}^{+}	Positive sequence impedance seen from the PCC
Z_{PCC}^{-}	Negative sequence impedance seen from the PCC
i_{load}^{-}	Equivalent current source representing the positive sequence equivalent network together with unbalance load
ΔP	IFC output active power oscillation
i_i	i^{th}-IFC output three-phase current vector
p_i	i^{th}-IFC output instantaneous active power
P_i	i^{th}-IFC output average active power
q_i	i^{th}-IFC output instantaneous reactive power
Q_i	i^{th}-IFC output average reactive power
i_{IFCs}	Parallel IFCs collective current vector
i_{pi}	i^{th}-IFC output three-phase active current vector
i_{qi}	i^{th}-IFC output three-phase reactive current vector
ΔP_{pi}	Active component of i^{th}-IFC output active power oscillation
ΔP_{qi}	Reactive component of i^{th}-IFC output active power oscillation
ΔQ_{pi}	Active component of i^{th}-IFC output reactive power oscillation
ΔQ_{qi}	Reactive component of i^{th}-IFC output reactive power oscillation
$i_{IFCs}^{*}\vert_{\Delta P=0}$	Parallel IFCs collective current vector
i_{xi}'	Projection of current ellipse of i^{th}-IFC on the x-axis
I_{xi}^{max}	Maximum current at phase-x of i^{th}-IFC
I_i^{max}	Peak current of individual i^{th}-IFC
$\delta\vert_{I_i^{max}}$	Phase angle of i^{th}-IFC's peak current
i_{x-IFCs}'	Projection of n-parallel IFCs' collective current ellipse on phase-x
$I_{x-IFCs}^{max}\vert_{\Delta P=0}$	Maximum collective current of n-parallel IFCs at phase-x under zero active power oscillation
$I_{IFCs}^{max}\vert_{\Delta P=0}$	Peak collective current of n-parallel IFCs under zero active power oscillation
$\delta\vert_{I_{IFCs}^{max}\vert_{\Delta P=0}}$	Phase angle of peak collective current of n-parallel IFCs under zero active power oscillation
i_{xpi}'	Projection of current ellipse of i^{th}-IFC on the x-axis under unity PF operation

I_{xpi}^{max}	Maximum current at phase-x of i^{th}-IFC under unity PF operation
I_{pi}^{max}	Peak current of individual i^{th}-IFC under unity PF operation
$\delta\|_{I_{pi}^{max}}$	Phase angle of i^{th}-IFC's peak current under unity PF operation
$i'_{xp-IFCs}$	Projection of n-parallel IFCs' collective current ellipse on phase-x under unity PF operation
$I_{xp-IFCs}^{max}\|_{\Delta P=0}$	Maximum collective current of n-parallel IFCs at phase-x under zero active power oscillation and unity PF operation
$I_{p-IFCs}^{max}\|_{\Delta P=0}$	Peak collective current of n-parallel IFCs under zero active power oscillation and unity PF operation
$\delta\|_{I_{p-IFCs}^{max}\|_{\Delta P=0}}$	Phase angle of peak collective current of n-parallel IFCs under zero active power oscillation and unity PF operation
$Q_{PCC,x_{V-reg}}^{max}$	Upper limit of phase-*x* reactive power for voltage regulation
$Q_{PCC,x_{V-reg}}^{min}$	Lower limit of phase-*x* reactive power for voltage regulation
$Q_{PCC,x_{IFCs}}^{max}$	Upper limit of phase-*x* reactive power due to maximum available reactive power of single-phase IFCs
$Q_{PCC,x_{IFCs}}^{min}$	Lower limit of phase-*x* reactive power due to maximum available reactive power of single-phase IFCs
Q_{IFCs_x}	Total reference reactive powers of single-phase IFCs in phase-*x*
$Q_{IFC_{i_x}}$	Reference reactive power of single-phase i^{th}-IFC in phase-*x*
$Q_{IFC_{i_x}}^{max}$	Maximum available reactive power of single-phase i^{th}-IFC in phase-*x*

Chapter 1

Hybrid AC/DC Microgrids and their Power Quality Issues

1.1 Introduction to Hybrid AC/DC Microgrids

Smartgrids are being developed as the next generation of power systems. These smartgrids encompass interconnected microgrids, especially at the distribution level where distributed generations (DGs) are increasingly being used. The DG technologies can be classified into power generation from renewable energy (RE) resources such as wind, photovoltaic, micro hydro, biomass, geothermal, ocean wave and tides; the clean alternative energy (AE) generation technologies such as fuel cells and microturbines; and the traditional rotational machine-based technologies such as diesel generators. Due to the benefits of these sources, such as cleanness and simple technologies, as well as the increasing demands for electrical energy, and the exhaustible nature of fossil fuels, the RE and AE-based DGs play an important role in microgrids.

The microgrids can work in grid-connected or stand-alone operation modes. In particular, the stand-alone operation can provide improved reliability to the smart grids, but maybe for a very limited period. Some other systems, such as electric vehicles and electric ships, can be considered as always operating in the stand-alone mode. Due to the intermittent nature of renewable energy resources, other energy sources (such as diesel) and storage elements (SEs) are critical for enabling the stand-alone operation of microgrids or smoothing the microgrid power during the grid-connected operation. SEs can be classified into two

categories: capacity-oriented energy storage and access-oriented energy storage [1]-[3]. Capacity-oriented energy storage does not have a fast response time and is used for long-term energy balancing to buffer out the low-frequency power oscillation of DGs' output power and to compensate for the intermittency of the renewable energy sources in microgrids [4]. Batteries, pumped hydroelectric systems, compressed air energy storage (CAES), and hydrogen storage are types of capacity-oriented energy storage. Access-oriented storage devices have a fast response time and are responsible for short time disturbances in microgrids by providing the high-frequency component of the power. These devices can either supply or absorb the high-power transients with high power density [4]. Flywheels, supercapacitors, and superconducting magnetic energy storage (SMES) are considered as access-oriented storage devices.

In microgrids, due to the presence of DC power sources such as PVs, fuel cells, energy storages, and modern DC loads, and also given the existing century-old AC power systems, interest in hybrid AC/DC microgrids are growing rapidly. These hybrid AC/DC microgrids contain AC/DC loads and power sources, have the advantages of both AC and DC power systems, and are considered to be the most likely future distribution and transmission systems. One critical aspect of the operation of such hybrid AC/DC microgrids is the control and power management strategy, which is essential for providing sound operation in both the grid-connected and stand-alone operation modes. The objective of the short-term power management strategy is to affect the instantaneous operational conditions of certain desired parameters such as the voltage, current, power and frequency. The short-term power management is more relevant to the interface and control of power converters in the hybrid microgrid and could also address the power quality issues.

1.2 Structures, Control Strategies and Power Management Schemes of Hybrid AC/DC Microgrids[1]

The term "Hybrid AC/DC Microgrid" refers to a microgrid which contains both AC/DC power sources and AC/DC loads. Depending on how the sources and loads are connected to the system and how the AC and DC buses are configured, the structure of hybrid AC/DC microgrids can be classified into AC-coupled, DC-coupled and AC-DC-coupled hybrid microgrids.

In an AC-coupled hybrid microgrid, as shown in Figure 1.1, various DGs and SEs are connected to the common AC subsystem/bus through their interfacing converters (IFCs). In general, the DGs/SEs can be single-phase or three-phase. In this structure, AC and DC loads are also connected to the AC bus with or without power electronic converters. This structure is commonly used when dominant generation sources in the microgrid produce grid level AC voltages directly (such as from diesel generator) or indirectly through interfacing power converters.

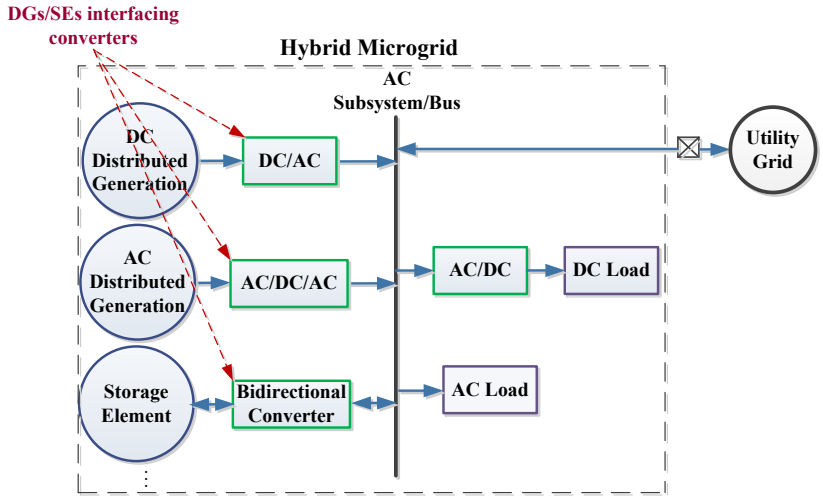

Figure 1.1 AC-coupled hybrid microgrid.

[1] For full review of hybrid AC/DC microgrid structures, control strategies, and power management schemes, we have publications listed below:

- F. Nejabatkhah, and Y. W. Li, "Overview of Power Management Strategies of Hybrid AC/DC Microgrid", *IEEE Transactions on Power Electronics, vol. 30, no. 12, pp. 7072–7089, Dec. 2015*.
- Y. W. Li, and F. Nejabatkhah, "Overview of Control, Integration and Energy Management of Microgrids", *Journal of Modern Power Systems and Clean Energy*, *Aug. 2014.*

Nowadays, the AC-coupled hybrid microgrid is the dominant structure due to its simple structure and simple control and power management scheme. Around the world, most implemented hybrid AC/DC microgrids are AC-coupled such as Hachinohe microgrid in Japan, Bronsbergen Holiday Park in Netherland, Kythnos Greece and Aichi microgrid in central Japan airport city [5]-[8].

The control strategy and power management scheme of AC-coupled hybrid microgrid mainly focus on power generation/consumption balance and the AC subsystem voltage/frequency control, especially in the stand-alone operation mode. Moreover, in the grid-connected operation mode, DGs/SEs IFCs can be used for the AC grid support (power quality issues such as grid voltage and frequency regulations).

The DC-coupled hybrid microgrid is shown in Figure 1.2, where all DGs and SEs are connected to the common DC subsystem/bus through their interfacing converters, and the AC and DC subsystems are linked by DC/AC interfacing converters. The AC and DC-subsystems IFCs can also be referred as solid state transformers, and in general, they can be three-phase or single-phase. This structure can be used when DC power sources are major power generation units in the microgrid. In this DC-coupled microgrid, variable frequency AC load such as adjustable speed motors can be connected to DC bus with a DC/AC converter (to

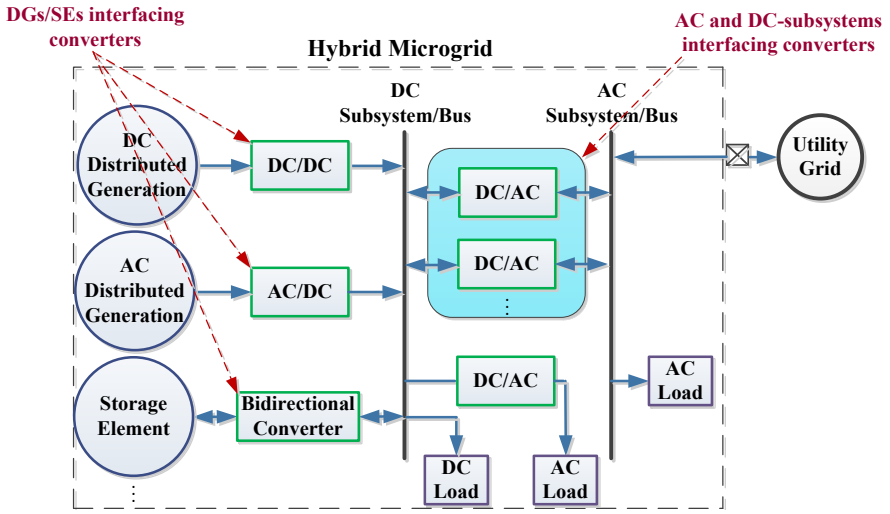

Figure 1.2 DC-coupled hybrid microgrid.

avoid the extra AC/DC conversion for AC bus connection). In this system, the DC and AC-subsystems IFCs provide bi-directional power flow capability. Depending on the power exchange requirement between DC and AC buses, parallel IFCs are typically used with increased rating and reliability. Around the world, various projects have been implemented in the DC-coupled hybrid microgrids like Italy CESI RICERCA DER microgrid, and Kahua Ranch Hawaii Hydrogen Power Park in USA [9], [10].

The DC-coupled microgrid features simple structure and does not need any synchronization when integrating different DGs/SEs. However, the control and power management of parallel IFCs, and their output voltage synchronization (with each other or with the grid) can present some challenges. In this hybrid microgrid, the DC subsystem voltage control, power balancing between generation and demand, and AC subsystem voltage and frequency control (especially in stand-alone mode) are the objectives of control and power management schemes. Moreover, the grid support functions can be realized in the grid-connected operation. Unlike in AC-coupled microgrid where the function can be realized by the DGs/SEs interfacing converters, the grid support is realized by the DC and AC-subsystems IFCs here in the DC-coupled microgrid.

In Figure 1.3, the AC-DC-coupled hybrid microgrid is shown in which both DC and AC subsystems have DGs and SEs, and these buses are linked by

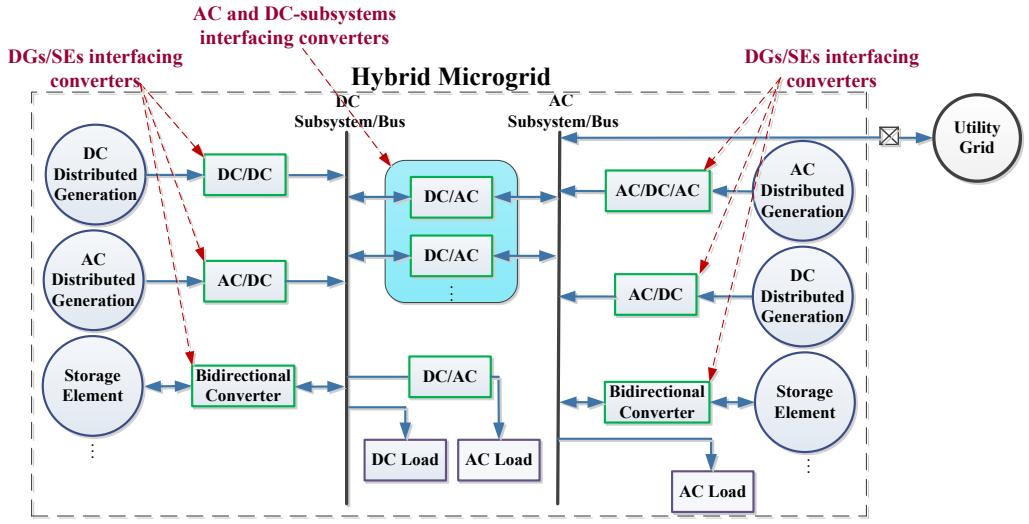

Figure 1.3 AC-DC-coupled hybrid microgrid.

interfacing converters. Similar to the DC-coupled hybrid microgrid, the AC and DC-subsystems IFCs can be called solid state transformers, which can be single-phase or three-phase in general. Different from the DC-coupled system, this hybrid microgrid has single-phase/three-phase DGs and SEs on the AC bus too, and requires more coordination for the voltage and power control between the DC and AC subsystems.

In the AC-DC-coupled microgrid, the DC and AC-subsystems IFC can work on the bi-directional power control mode, the DC link voltage control mode, or the AC link voltage control mode. In the power control mode, the converter output current or voltage is controlled to regulate the IFC output power on its reference value. In the DC link voltage control mode, the IFC controls DC link voltage and therefore balancing the power generation and consumption on DC bus. This operation mode is used when the control of output power of grid-connected IFC is not required. The AC link voltage control mode is mainly for the stand-alone microgrid operation, where the IFC controls the AC subsystem voltage and frequency. These control strategies can be applied to the AC and DC-subsystems IFCs in the DC-coupled hybrid microgrids.

Similar to the DC-coupled microgrid, parallel IFCs can be desired to link AC and DC buses with increased capacity and reliability. In presence of the parallel IFCs, in both DC-coupled and AC-DC-coupled hybrid microgrids, control strategies such as master-slave [11], and instantaneous current sharing methods such as average current control [12] and circular-chain control [13] can be used. In addition to aforementioned communication-based method, communication-less control strategy (such as droop control) [14]-[16] can also be used for controlling the parallel converters, which may be important when the parallel IFCs are not physically close as there might be multiple links between the DC and AC subsystem at various locations with higher reliability.

In general, AC-DC-coupled structure is appropriate if major power sources include both DC and AC powers, and it improves overall efficiency and reduces the system cost with reduced number of power converters by connecting sources and loads to the AC and DC buses with minimized power conversion

requirements. Considering these benefits together with increasing of modern DC loads and the necessity of connecting more renewable energy sources and SEs into the grid, AC-DC-coupled hybrid microgrids will be the most promising microgrid structures in the near future. Europe is leading research efforts in this direction through the European supergrid [17], [18], where power of various DC and AC power sources such as offshore wind turbines and desert-based solar are transmitted using AC and DC grids.

Although idea of the AC-DC-coupled hybrid microgrid is promising, it necessitates thorough studies and investigations, particularly for control strategies and power management aspects. In the AC-DC-coupled hybrid microgrids, control strategies need to consider both DC and AC bus voltages (and frequency) control, as well as the power balance within the DC and AC subsystems. Furthermore, in the grid-connected operation modes, similar to the other structures of hybrid microgrids, DGs/SEs interfacing converters on the AC bus together with AC and DC-subsystems IFCs can be controlled to realize the grid support functions.

1.3 Hybrid AC/DC Microgrids under AC voltage Unbalance

In future hybrid AC/DC microgrids with more interfacing power electronics from the DGs, SEs and the loads, together with the increasing nonlinear/unbalanced loads, power quality will be an important topic. Currently, harmonics, unbalances, and voltage sag/swell have already caused concern in today's power system, and it may get worse in the near future. Among the various power quality issues, unbalanced voltage has raised serious concern in hybrid microgrids, which is caused by ever-increasing unbalanced distribution of single-phase/unbalanced loads, such as household power demands and plug-in electric vehicles (PEVs), single-phase/unbalanced distributed generations, such as roof-top PV systems, and remote grid faults. In such systems, single-phase/unbalanced loads cause unequal power consumption in the three phases, which causes

unbalanced voltage and current [19]-[20]. Moreover, due to PEVs random charging behaviors as well as single-phase connections for slow charging, the increasing PEVs penetrations further contribute to the unbalanced voltage and current production [21]-[24]. In addition, single-phase DGs, such as single-phase PV systems, produce unequal power in the three phases, which further leads to unbalanced condition [25]-[27].

The unbalanced voltage has adverse effects on the power system and equipment such as electrical machine overheating, transformer overloading, capacity limitation of power electronics devices, more losses and less stability of power system, negative impacts on induction motors and adjustable speed drives [27]-[29]. In addition, unbalanced voltage causes double-frequency power oscillations at the output of three-phase power electronic converters, which are reflected as ripple in the DC link voltage. This is particularly true considering that the DC link capacitors in three-phase power systems are typically small. These oscillations in some cases lead to instability or system protection if the DC bus voltage exceeds the maximum limit. Moreover, unbalanced voltage will increase the peak current of the power converter in the same active and reactive powers production, which may result in over currents protection. In Figure 1.4, the performance of the three-phase power electronic interfacing converter under unbalanced voltage is shown. As seen from the figure, when unbalance condition is applied, the IFC's output peak current increases. Also, the output power starts to oscillate at two times of grid frequency, which is reflected as ripple in the DC

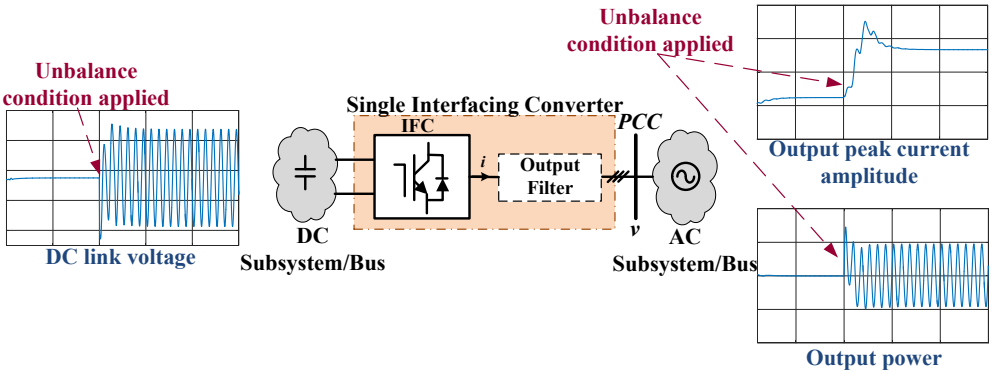

Figure 1.4 Typical three-phase interfacing converter performance under unbalanced condition.

link voltage.

Therefore, the unbalanced voltage concerns will lead the next generation of grid codes to consider the voltage support control in the steady-state and transient operation [30], and appropriate methods should be applied in the hybrid AC/DC microgrids in order to compensate unbalanced condition.

In general, the unbalanced voltage can be compensated using power electronics-based equipment such as series active power filter by injecting negative sequence voltage [31], [32], shunt active power filter by injecting negative sequence current [33], [34], series-parallel compensators such as unified power quality conditioner (UPQC) by injecting negative sequence voltage with series converter and negative sequence current with parallel converter [35], and static synchronous compensators (STATCOM) by injecting positive and negative sequence reactive powers [28], [36], [37]. Moreover, passive devices such as shunt capacitor can also be used for unbalanced voltage compensation [38], [39]. In addition, equalizing power generation and load consumption in the three phases reduce the unbalance condition [19], [20].

In aforementioned strategies, additional equipment is used for unbalanced compensation purposes. However, installing this additional equipment increases the total investment cost in hybrid AC/DC microgrids. With the increasing penetration of interfacing converters in hybrid AC/DC microgrids, they can be properly controlled to help address the power quality issues and support the grid in addition to their power management targets. This is a promising idea since most interfacing converters are not operating at full rating all the time due to the intermittent nature of renewable energy sources. Therefore, the available converters rating in hybrid AC/DC microgrids can be used in a smart way to help improve the unbalanced condition.

For interfacing converters in hybrid AC/DC microgrids, three types of configurations can be considered:

1) Single three-phase interfacing converter. The single three-phase IFC can be DG/SE interfacing converter in AC-coupled or AC-DC-coupled hybrid microgrids. It can also be the AC and DC-subsystems interfacing

converter (solid-state transformer) in DC-coupled or AC-DC-coupled hybrid microgrids.

2) Parallel three-phase interfacing converters. The parallel three-phase IFCs are usually used when larger power and current capacity are needed. These parallel converters can be the interfacing converter between the AC and DC subsystems (parallel solid-state transformers) in DC-coupled or AC-DC-coupled hybrid microgrids. Moreover, DGs/SEs with large capacity can also be connected to the AC subsystem through parallel interfacing converters in AC-coupled or AC-DC coupled hybrid microgrids.
3) Single-phase interfacing converters: The single-phase IFCs can be single-phase DGs/SEs interfacing converters connected to the AC subsystem in AC-coupled or AC-DC coupled hybrid microgrids. Also, the DC subsystem can be connected by single-phase IFC to one of the phases of the three-phase AC subsystem in DC-coupled or AC-DC-coupled hybrid microgrids.

Furthermore, considering the adverse effects of unbalanced voltage on interfacing converters' operation and also IFCs' capabilities for unbalanced voltage compensation, two situations can be considered:

1) Operation of IFCs under the unbalanced voltage situation with a control effort to reduce/minimize the adverse effects on IFCs. Note that the unbalanced compensation is not the primary focus here and the compensation is done without an adjustable level.
2) Use the IFCs to compensate unbalanced AC voltage directly (with an adjustable compensation level) and improving the AC subsystem power quality.

The control strategies of single and parallel three-phase IFCs and multiple singe-phase IFCs under unbalanced voltage will be addressed in detail as follows:

1.3.1 Single three-phase interfacing converter performance under unbalanced voltage

The control strategies of single three-phase power electronic interfacing converter under unbalanced voltage can be studied in two groups. In the first group, control strategies focus on operation of IFCs under unbalance condition, and they only protect IFC from adverse effects of unbalanced voltage by cancelling out output power oscillations and DC link ripple [40]-[44]. In these control strategies, since the positive and negative sequence active and reactive powers are not controlled directly, the level of unbalanced voltage compensation cannot be adjusted (although it is improved). In these strategies, the peak current of IFC can be controlled using IFC average active and reactive powers control [43], [44].

In the second group, control strategies focus on adjustable unbalanced voltage compensation [43], [45]-[51]. These control strategies, which are based on symmetric sequences, control interfacing converter output positive and negative sequence active powers [46], positive and negative sequence reactive powers [47], [48] or positive and negative sequence active and reactive powers [43], [49], [50] for unbalanced voltage compensation. Although these control strategies sacrifice the IFC local power quality problems (output power oscillations, DC link ripples, and peak current enhancement), some of these problems have been considered. For example, directly unbalanced voltage compensation has been considered together with IFC peak current control in [43], [46], [49], while IFC output active power oscillation control has been considered in [43], [51]. However, these control strategies do not address all unbalanced voltage adverse effects on IFC together with adjustable compensation at the same time.

From the literature review, it is obvious that previous works either focused on operating IFCs under unbalanced voltage (without an adjustable level of compensation) while considering the adverse effects of the IFC itself (such as power oscillation and DC voltage ripple, etc.), or controlling IFCs for unbalance compensation without sufficient care of its adverse effects on IFCs operation. Therefore, study of control strategy that can address both adverse effects of

unbalanced voltage on the IFC's operation and adjustable unbalanced voltage compensation at the same time is necessary. Additionally, as the unbalanced voltage compensation is based on the IFC's available power rating, it is also important to design control strategies that can compensate unbalanced AC voltage effectively.

1.3.2 Parallel three-phase interfacing converters performance under unbalanced voltage

Researches on the control of parallel three-phase IFCs under unbalanced voltage conditions are quite limited, and they are commonly focusing on parallel DGs/SEs interfacing converters without common DC link [29], [52]-[57]. Mainly, these control strategies are compensating unbalanced voltage without considering its adverse effects on IFCs operation such as output power oscillations and peak current enhancement [29], [52]-[56]. In the parallel IFCs with AC link voltage control (such as droop controllers), complementary controllers are added to conventional voltage controllers for unbalanced voltage compensation purposes. These complementary controllers are mainly based on unbalanced voltage level factor control [56], [57], IFCs negative sequence impedance/current control [53]-[55], or negative sequence reactive power control [29], [52].

There are not enough literatures addressing operation of parallel IFCs under unbalanced voltage, especially IFCs with common DC link. In the literature, the control strategies of parallel IFCs with common DC link are mainly focusing on power sharing among IFCs and controlling circulating current. However, in hybrid AC/DC microgrids, when parallel IFCs with common DC link are used under unbalanced voltage, the adverse effects (such as output power oscillations, DC link ripples, and output current enhancement) could be amplified by the number of parallel converters. Therefore, addressing operation of parallel IFCs with common DC link under unbalanced voltage is very important. But, if IFCs are controlled properly, the adverse effects from each IFC could be cancelled out, resulting in enhanced power quality in both the AC and DC subsystems.

Therefore, comprehensive study about control strategies of parallel IFCs under unbalanced voltage is necessary.

1.3.3 Multiple single-phase interfacing converters performance under unbalanced voltage

In addition to three-phase interfacing converters, high penetration levels of single-phase IFCs provide great potential for unbalance compensation. So far, there are not enough literatures addressing unbalance compensation using single-phase IFCs. In [58], reactive powers of single-phase PEVs' interfacing converters are controlled for negative sequence current compensation. However, just one PEV is considered in each phase, which is not useful for distributed compensation. Moreover, zero sequence current compensation and phase voltages regulation are not considered. In [59]-[61], single-phase DGs' IFCs for unbalanced compensation are considered. However, in the control strategies, the PCC current is measured to calculate the reference negative and zero sequences current for DGs directly. As there is not any optimization involved, these methods cannot easily include practical constraints such as IFCs available ratings and the need of phase voltages regulation during the compensation. Additionally, the task sharing among multiple IFCs are not considered either.

It is obvious from the literature review that unbalanced condition compensation using single-phase IFCs coordination has not been addressed enough. Therefore, comprehensive study of control strategies for multiple single-phase IFCs for unbalanced condition compensation in hybrid AC/DC microgrids is necessary.

1.4 Thesis Objectives and Motivation

The overall objective of this thesis is to deal with the unbalanced voltage in hybrid AC/DC microgrids. Given the adverse effects of unbalanced voltage on power electronics interfacing converters' operation and also the IFCs' capabilities for unbalanced voltage compensation, two scenarios are addressed in this thesis; first, the reduction of adverse effects during the operation of IFCs under

unbalanced voltage, and second, the utilization of IFCs to improve the power quality. According to previously discussed different categories of IFCs, single three-phase IFC, parallel three-phase IFCs, and single-phase IFCs are considered in this thesis.

For the single three-phase IFC, researches have been focusing either on adverse effects reduction of the unbalanced voltage in the IFC's operation, in which the level of unbalanced voltage compensation cannot be controlled directly, or on adjustable unbalanced voltage compensation, but the unbalanced voltage adverse effects on IFC operation (output power oscillations, DC link ripples, and peak current enhancement) have not been considered sufficiently. Further investigation and study of single three-phase IFC control strategies under unbalanced voltage, addressing both the adjustable compensation level and the adverse effects of compensation on the IFC's operation at the same time, are necessary. On the other hand, the effectiveness of the control strategy for unbalanced voltage compensation is equally important since the compensation is done based on the IFC available power rating. This issue should be considered in future studies.

On the other hand, when parallel three-phase IFCs with a common DC link are operating under unbalanced voltage, new challenges and opportunities are produced. Since the adverse effects of unbalanced voltage on parallel IFCs operation can be amplified due to interactions, the focus of the control strategies should be on minimizing/reducing such adverse effects. Such control strategies could provide the unbalanced voltage compensation, but without an adjustable compensation level. In general, the two possibilities for controlling parallel IFCs' operation under unbalanced voltage are (1) the use of one IFC focused on adverse effects minimization, and (2) the use of all IFCs to share the adverse effects minimization. No literature is available in this regard, and a thorough study on this topic is essential.

Furthermore, ever-increasing penetration level of single-phase IFCs has created a great opportunity for unbalanced voltage compensation. Due to the lack of research in this area, a thorough study of multiple single-phase IFCs control for

unbalanced voltage compensation is necessary. In such single-phase IFCs operating at given real powers production, only reactive powers can be controlled for the purpose of compensation with an adjustable level. Moreover, practical considerations such as three-phase voltage regulation, IFCs maximum available ratings for compensation purposes, and compensation sharing among IFCs are also important, and should be addressed in future studies.

Motivated by the above considerations, the following research tasks are carried out in this work:

Task 1 Develop control strategy for single three-phase interfacing converter to compensate for the unbalanced voltage and consider its adverse effects at the same time.

Task 2 Design control strategy for parallel three-phase interfacing converters to operate under unbalanced voltage: one dedicated IFC utilization for adverse effects minimization.

Task 3 Design control strategy for parallel three-phase interfacing converters to share unbalanced voltage adverse effects minimization.

Task 4 Develop control strategy for multiple single-phase interfacing converters for unbalanced voltage compensation.

1.5 Thesis Outline

In Chapter 2, an instantaneous power analysis from a three-phase system perspective is provided. Then, an instantaneous power analysis from a single-phase system perspective is developed, and the results are compared with those from the three-phase system perspective. The provided instantaneous power analyses are used to generate different reference currents for interfacing converters to achieve specific performances. These reference currents are used in the rest of this thesis in the proposed control strategies for IFCs.

Two new control strategies for a single three-phase IFC under unbalanced voltage in hybrid AC/DC microgrids are proposed in Chapter 3 to address Task 1. The first strategy aims at compensating for the unbalanced voltage with an

adjustable level and by considering the active power oscillation minimization of the IFC. The second strategy focuses on the effectiveness of the unbalanced voltage compensation. These two proposed control strategies provide a great opportunity for the three-phase IFCs of hybrid AC/DC microgrids to compensate for the unbalanced voltage and address the adverse effects on the IFCs' operation at the same time. The performances of the two proposed control strategies under different IFC's operations and grid conditions are studied, and their validity is verified by using both simulations and experiments.

In Chapter 4, a novel control strategy for parallel three-phase IFCs' operation under unbalanced voltage in hybrid AC/DC microgrids is proposed. This chapter, which concentrates on Task 2, aims at minimizing the adverse effects of unbalanced voltage on IFCs' operation by using one dedicated IFC named as redundant. This control strategy provides the opportunity for unbalanced voltage compensation, but the compensation level cannot be adjusted. In this chapter, a thorough study of the peak current of individual and parallel IFCs under unbalanced voltage is carried out to provide a reduced peak current for the redundant IFC. The performance of the proposed control strategy is evaluated by using both simulation and experimental results under different operating conditions.

In the proposed strategy in Chapter 4, since only a redundant IFC is used to minimize the adverse effects of the unbalanced voltage on parallel IFCs' operation, this IFC's power rating should be large enough. Moreover, since the collective peak current of parallel IFCs is not shared among IFCs based on their power ratings, some IFCs work at their rating limits while the others operate far from their limits. Considering these current-sharing concerns, two control strategies for parallel three-phase IFCs are proposed in Chapter 5 where minimization of the unbalanced voltage adverse effects on parallel IFCs operation is shared among the IFCs. (Task 3 is addressed in this chapter.) Similarly, these control strategies provide the opportunity for unbalanced voltage compensation in hybrid AC/DC microgrids, but without an adjustable level. The proposed control strategies also maximize the power/current transferring capability of parallel IFCs

and provide the same available rooms for IFCs' operation. In this chapter, simulation and experimental results are provided for evaluating the performance of the proposed control strategies.

Chapter 6, which addresses Task 4, focuses on the development of a new control strategy for multiple single-phase IFCs to compensate for the unbalanced condition of hybrid microgrids. In the proposed control strategy, the power factors of IFCs are controlled without modifying the active powers production. The proposed control strategy compensates for the AC subsystem unbalanced voltage in terms of the negative and zero sequences, and leads to DC subsystem power quality improvement as well. In the proposed control strategy, practical constraints such as three-phase voltage regulation and the available power ratings of single-phase IFCs for compensation are also considered. The proposed control strategy is verified by using the IEEE 13-node system.

It should be mentioned that the proposed control strategies for three-phase and single-phase IFCs of hybrid AC/DC microgrids in Chapter 3 to Chapter 6 can also be used for conventional AC power systems to compensate the unbalanced condition by using power electronic converters of DGs/SEs.

Finally, in Chapter 7, the main conclusions and contributions of this thesis are presented. Also, suggestions for future works are provided.

Chapter 2

Instantaneous Power Theory

In this chapter, an instantaneous power analysis of the three-phase power system from the three-phase and single-phase perspectives is provided. Then, the analysis is used to determine the different reference currents to be tracked by the interfacing power converters to achieve specific performances. The reference currents are used in the proposed control strategies in the following chapters. Finally, in this chapter, discussions and comparisons of the instantaneous power analysis from the three-phase and single-phase systems perspectives are provided.

2.1 Principles of Instantaneous Power Theory

From Figure 2.1 and according to instantaneous power theory [45], [62], the instantaneous active and reactive powers injected to the grid at the point of common coupling (PCC) could be described as in (2.1) and (2.2).

$$p_{PCC} = v_{PCC}.i_{PCC} = v_{PCC_a} i_{PCC_a} + v_{PCC_b} i_{PCC_b} + v_{PCC_c} i_{PCC_c} \tag{2.1}$$

$$q_{PCC} = v_{PCC_\perp}.i_{PCC} = v_{PCC_{a_\perp}} i_{PCC_a} + v_{PCC_{b_\perp}} i_{PCC_b} + v_{PCC_{c_\perp}} i_{PCC_c} \tag{2.2}$$

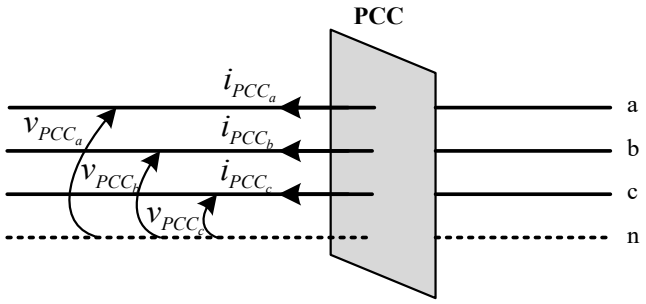

Figure 2.1 Three-phase power system at the PCC.

where $v_{PCC} = [\, v_{PCC_a}, v_{PCC_b}, v_{PCC_c}]$ and $i = [i_{PCC_a}, i_{PCC_b}, i_{PCC_c}]$ are three-phase PCC voltage vector and the current vector, and $v_{PCC_\perp}$ lags v_{PCC} by 90°. Considering symmetric-sequence component of the PCC voltage vector and the current vector, (2.1) and (2.2) can be described as:

$$\begin{aligned} p_{PCC} &= \left(v^+_{PCC} + v^-_{PCC} + v^0_{PCC}\right).\left(i^+_{PCC} + i^-_{PCC} + i^0_{PCC}\right) = \left(v^+_{PCC}.i^+_{PCC} + v^-_{PCC}.i^-_{PCC}\right) + \\ &\left(v^+_{PCC}.i^-_{PCC} + v^-_{PCC}.i^+_{PCC}\right) + \left(v^0_{PCC}.i^0_{PCC}\right) = P_{PCC} + \Delta P_{PCC} + \left(P_{PCC_0} + \Delta P_{PCC_0}\right) \end{aligned} \tag{2.3}$$

$$\begin{aligned} q_{PCC} &= \left(v^+_{PCC_\perp} + v^-_{PCC_\perp} + v^0_{PCC_\perp}\right).\left(i^+_{PCC} + i^-_{PCC} + i^0_{PCC}\right) = \\ &\left(v^+_{PCC_\perp}.i^+_{PCC} + v^-_{PCC_\perp}.i^-_{PCC}\right) + \left(v^+_{PCC_\perp}.i^-_{PCC} + v^-_{PCC_\perp}.i^+_{PCC}\right) \\ &= Q_{PCC} + \Delta Q_{PCC} \end{aligned} \tag{2.4}$$

where $v^+_{PCC}, v^-_{PCC}, v^0_{PCC}, i^+_{DG}, i^-_{DG}, i^0_{DG}$ are positive, negative, and zero sequence vectors of three-phase PCC voltage vector and current vector, P_{PCC} and ΔP_{PCC} are average and oscillatory terms of instantaneous active power, P_{PCC_0} and ΔP_{PCC_0} are zero sequence average and oscillatory terms of instantaneous active power, and Q_{PCC} and ΔQ_{PCC} are average and oscillatory terms of instantaneous reactive power. It should be mentioned that in (2.3) and (2.4), $v^+_{PCC}.i^0_{PCC} = v^-_{PCC}.i^0_{PCC} = 0$. Moreover, orthogonal vectors for positive, negative and zero sequence vectors could be achieved using transformation matrix in (2.5), if positive direction of phasors rotation is assumed clockwise. From (2.5), it is clear that $v^+_{PCC_\perp}.i^0_{PCC} = v^-_{PCC_\perp}.i^0_{PCC} = 0$ in (2.4), and also $v^0_{PCC_\perp} = 0$.

$$v^{+,-,0}_{PCC_\perp} = \frac{1}{\sqrt{3}}\begin{bmatrix} 0 & 1 & -1 \\ -1 & 0 & 1 \\ 1 & -1 & 0 \end{bmatrix} v^{+,-,0}_{PCC} \tag{2.5}$$

In (2.3) and (2.4), the average active and reactive powers (P_{PCC} and Q_{PCC}) can be decompose into their positive and negative sequence components as follows:

$$P_{PCC} = P^+_{PCC} + P^-_{PCC} = \left(v^+_{PCC}.i^+_{PCC}\right) + \left(v^-_{PCC}.i^-_{PCC}\right) \tag{2.6}$$

$$Q_{PCC} = Q^{+}_{PCC} + Q^{-}_{PCC} = \left(v^{+}_{PCC_{\perp}} . i^{+}_{PCC}\right) + \left(v^{-}_{PCC_{\perp}} . i^{-}_{PCC}\right) \tag{2.7}$$

where P^{+}_{PCC} and P^{-}_{PCC} are the positive and negative sequences of average active power, and Q^{+}_{PCC} and Q^{-}_{PCC} are the positive and negative sequences of average reactive power.

2.2 Power Control using Instantaneous Power Theory from Three-Phase System Perspective

Here, proper reference currents calculations to be applied to the three-phase interfacing converters to achieve specific performances are provided. Thus, the instantaneous power analysis from the three-phase system perspective is used in the calculations. In this study, it is assumed that the three-phase IFC is connected to the grid at the PCC, thus IFC's output voltage and current are the same as PCC voltage and current (v_{PCC}, i_{PCC}). Moreover, the power system has three wires, so there is no active power contribution from zero sequence current. Therefore, zero sequence voltage will be neglected. In Figure 2.2, a typical grid-connected three-phase IFC with its control block diagram is shown. As mentioned, here the focus is on reference current generation for IFC.

Two different reference currents calculations are provided. In the first one, injection of both positive and negative sequences current into the grid at the

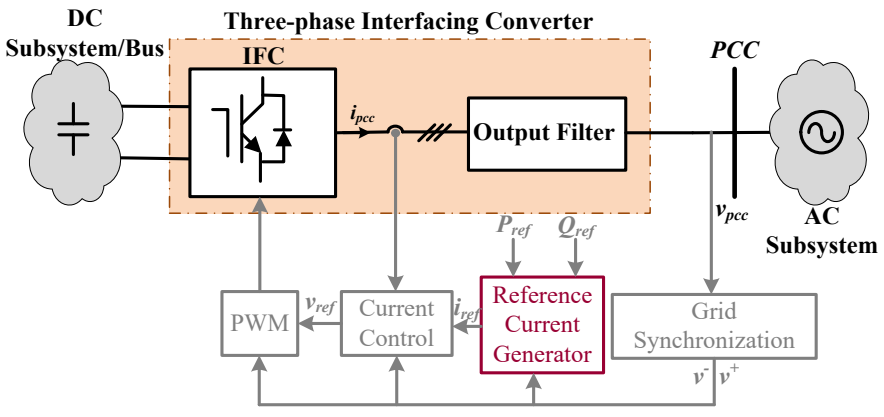

Figure 2.2 Typical grid-connected three-phase interfacing converter with its control strategy.

fundamental frequency is desired, which is suitable for an adjustable unbalanced compensation [45], [63]. The second reference current is derived to provide an easy way to reduce the adverse effects of unbalanced voltage on IFC operation in terms of output powers oscillation cancellation [64]-[66].

2.2.1 Reference current focusing on unbalanced condition compensation

In this strategy, the reference current of three-phase IFC is calculated to flexibly inject both positive and negative sequences active and reactive currents into the grid to compensate unbalanced condition. In other words, this method is useful if the adjustable unbalanced compensation is a preferential issue.

According to (2.3) and (2.4), the current vector that is aligned with voltage vector will generate active power while the current vector that is aligned with orthogonal voltage vector will generate reactive power. Therefore, total IFC's reference current vector to inject positive and negative sequences current could be expressed as:

$$i_{PCC}^{*} = a^{+}v_{PCC}^{+} + a^{-}v_{PCC}^{-} + b^{+}v_{PCC_{\perp}}^{+} + b^{-}v_{PCC_{\perp}}^{-} \tag{2.8}$$

where $a^{+}, a^{-}, b^{+}, b^{-}$ are positive and negative sequences instantaneous conductances and susceptances. If just either positive or negative sequence current had to be injected to the exchange of a certain amount of power with the grid (P_{PCC} and Q_{PCC}), the values of conductances and susceptances will be as follows:

$$a^{+} = \frac{P_{PCC}}{\left|v_{PCC}^{+}\right|^{2}} \;;\; a^{-} = \frac{P_{PCC}}{\left|v_{PCC}^{-}\right|^{2}} \;;\; b^{+} = \frac{Q_{PCC}}{\left|v_{PCC}^{+}\right|^{2}} \;;\; b^{-} = \frac{Q_{PCC}}{\left|v_{PCC}^{-}\right|^{2}} \tag{2.9}$$

In the condition that injection of both positive and negative sequences active and reactive powers into the grid is desired, both sequences should be regulated to keep reference active and reactive powers constant. As a result, weighting factors k_1 and k_2 are defined as $k_1 = \frac{P_{PCC}^{+}}{P_{PCC}}$ and $k_2 = \frac{Q_{PCC}^{+}}{Q_{PCC}}$ to regulate the proportions of each sequence power delivered into the grid as follows [45], [63]:

$$i_{PCC}^{*}=\frac{P_{PCC}\,k_1}{\left|v_{PCC}^{+}\right|^2}v_{PCC}^{+}+\frac{P_{PCC}\left(1-k_1\right)}{\left|v_{PCC}^{-}\right|^2}v_{PCC}^{-}+\frac{Q_{PCC}\,k_2}{\left|v_{PCC}^{+}\right|^2}v_{PCC_\perp}^{+}+\frac{Q_{PCC}\left(1-k_2\right)}{\left|v_{PCC}^{-}\right|^2}v_{PCC_\perp}^{-} \quad (2.10)$$

As seen from (2.10), k_1 and k_2 can be controlled to adjust positive and negative sequences active and reactive currents to compensate the unbalanced condition. From (2.3), (2.4), and (2.10), the active and reactive powers oscillations at the IFC output connected to the PCC can be achieved as:

$$\Delta P_{PCC}=\left(\frac{P_{PCC}\,k_1}{\left|v_{PCC}^{+}\right|^2}+\frac{P_{PCC}\left(1-k_1\right)}{\left|v_{PCC}^{-}\right|^2}\right)v_{PCC}^{+}.v_{PCC}^{-}+\left(\frac{Q_{PCC}\,k_2}{\left|v_{PCC}^{+}\right|^2}-\frac{Q_{PCC}\left(1-k_2\right)}{\left|v_{PCC}^{-}\right|^2}\right)v_{PCC_\perp}^{+}.v_{PCC}^{-} \quad (2.11)$$

$$\Delta Q_{PCC}=\left(\frac{P_{PCC}\,k_1}{\left|v_{PCC}^{+}\right|^2}-\frac{P_{PCC}\left(1-k_1\right)}{\left|v_{PCC}^{-}\right|^2}\right)v_{PCC}^{+}.v_{PCC_\perp}^{-}+\left(\frac{Q_{PCC}\,k_2}{\left|v_{PCC}^{+}\right|^2}+\frac{Q_{PCC}\left(1-k_2\right)}{\left|v_{PCC}^{-}\right|^2}\right)v_{PCC_\perp}^{+}.v_{PCC_\perp}^{-} \quad (2.12)$$

Considering (2.11) and (2.12), the active and reactive powers oscillations can be cancelled out considering following values of k_1 and k_2:

$$\Delta P_{PCC}=0\Rightarrow k_1=\frac{\left|v_{PCC}^{+}\right|^2}{\left|v_{PCC}^{+}\right|^2-\left|v_{PCC}^{-}\right|^2}\ \ \&\ \ k_2=\frac{\left|v_{PCC}^{+}\right|^2}{\left|v_{PCC}^{+}\right|^2+\left|v_{PCC}^{-}\right|^2} \quad (2.13)$$

$$\Delta Q_{PCC}=0\Rightarrow k_1=\frac{\left|v_{PCC}^{+}\right|^2}{\left|v_{PCC}^{+}\right|^2+\left|v_{PCC}^{-}\right|^2}\ \ \&\ \ k_2=\frac{\left|v_{PCC}^{+}\right|^2}{\left|v_{PCC}^{+}\right|^2-\left|v_{PCC}^{-}\right|^2} \quad (2.14)$$

2.2.2 Reference current focusing on active and reactive powers cancellation

In this strategy, the reference current is calculated to easily control/cancel out the three-phase IFC's output active and reactive powers oscillations due to unbalance condition. Although the power oscillations can be cancelled out considering (2.13) and (2.14) in the reference current (2.10), this control strategy provides much more easier way for power oscillation cancellation, especially when parallel IFCs are used.

Considering (2.3) and (2.4), in unity PF where $Q_{PCC}=0$, since $v_{PCC}^{+}\cdot i_{PCC}^{-}$ and $v_{PCC}^{-}\cdot i_{PCC}^{+}$, and also $v_{PCC_\perp}^{+}\cdot i_{PCC}^{-}$ and $v_{PCC_\perp}^{-}\cdot i_{PCC}^{+}$ are in-phase quantities, the

active or reactive power oscillation of IFC can be compensated using scalar coefficient k_p as follows [64]-[66]:

$$\Delta P_{PCC} = 0 \Rightarrow v^{+}_{PCC}.i^{-}_{PCC_p} = -k_p\, v^{-}_{PCC}.i^{+}_{PCC_p} \qquad k_{pi} \geq 0 \tag{2.15}$$

$$\Delta Q_{PCC} = 0 \Rightarrow v^{+}_{PCC_\perp}.i^{-}_{PCC_p} = -k_p\, v^{-}_{PCC_\perp}.i^{+}_{PCC_p} \qquad k_{pi} \geq 0 \tag{2.16}$$

where subscript "p" is related to unity PF operation. From (2.3), (2.4), (2.15) and (2.16), the IFC's reference current vector under unity PF can be obtained:

$$i^{*}_{PCC_p} = \frac{P_{PCC}}{\left|v^{+}_{PCC}\right|^2 + k_p \left|v^{-}_{PCC}\right|^2} v^{+}_{PCC} + \frac{P_{PCC}\, k_p}{\left|v^{+}_{PCC}\right|^2 + k_p \left|v^{-}_{PCC}\right|^2} v^{-}_{PCC} \tag{2.17}$$

Similarly, under zero PF operation mode ($P_{PCC} = 0$), the active or reactive power oscillation can be compensated using scalar coefficient k_q as follows [64]-[66]:

$$\Delta P_{PCC} = 0 \Rightarrow v^{+}_{PCC}.i^{-}_{PCC_q} = -k_q\, v^{-}_{PCC}.i^{+}_{PCC_q} \qquad k_{qi} \geq 0 \tag{2.18}$$

$$\Delta Q_{PCC} = 0 \Rightarrow v^{+}_{PCC_\perp}.i^{-}_{PCC_q} = -k_q\, v^{-}_{PCC_\perp}.i^{+}_{PCC_q} \qquad k_{qi} \geq 0 \tag{2.19}$$

where subscript "q" is related to reactive power control. From (2.3), (2.4), (2.18), and (2.19), the IFC's reference current vector under zero PF can be derived as:

$$i^{*}_{PCC_q} = \frac{Q_{PCC}}{\left|v^{+}_{PCC}\right|^2 + k_q \left|v^{-}_{PCC}\right|^2} v^{+}_{PCC_\perp} + \frac{Q_{PCC}\, k_q}{\left|v^{+}_{PCC}\right|^2 + k_q \left|v^{-}_{PCC}\right|^2} v^{-}_{PCC_\perp} \tag{2.20}$$

Combining (2.17) and (2.20), the IFC's reference current vector is obtained:

$$\begin{aligned} i^{*}_{PCC} = i^{*}_{PCC_p} + i^{*}_{PCC_q} = &\left(\frac{P_{PCC}}{\left|v^{+}_{PCC}\right|^2 + k_p \left|v^{-}_{PCC}\right|^2} v^{+}_{PCC} + \frac{P_{PCC}\, k_p}{\left|v^{+}_{PCC}\right|^2 + k_p \left|v^{-}_{PCC}\right|^2} v^{-}_{PCC} \right) + \\ &\left(\frac{Q_{PCC}}{\left|v^{+}_{PCC}\right|^2 + k_q \left|v^{-}_{PCC}\right|^2} v^{+}_{PCC_\perp} + \frac{Q_{PCC}\, k_q}{\left|v^{+}_{PCC}\right|^2 + k_q \left|v^{-}_{PCC}\right|^2} v^{-}_{PCC_\perp} \right) \end{aligned} \tag{2.21}$$

From (2.3), (2.4), and (2.21), the IFC's output active and reactive powers oscillations at the PCC can be derived as:

$$\Delta P_{PCC} = \frac{P_{PCC}\left(1+k_p\right)\left(v^{+}_{PCC}.v^{-}_{PCC}\right)}{\left|v^{+}_{PCC}\right|^2 + k_p\left|v^{-}_{PCC}\right|^2} + \frac{Q_{PCC}\left(1-k_q\right)\left(v^{+}_{PCC_\perp}.v^{-}_{PCC}\right)}{\left|v^{+}_{PCC}\right|^2 + k_q\left|v^{-}_{PCC}\right|^2} \tag{2.22}$$

$$\Delta Q_{PCC} = \frac{P_{PCC}\left(1-k_p\right)\left(v^{+}_{PCC}.v^{-}_{PCC_\perp}\right)}{\left|v^{+}_{PCC}\right|^2 + k_p\left|v^{-}_{PCC}\right|^2} + \frac{Q_{PCC}\left(1+k_q\right)\left(v^{+}_{PCC_\perp}.v^{-}_{PCC_\perp}\right)}{\left|v^{+}_{PCC}\right|^2 + k_q\left|v^{-}_{PCC}\right|^2} \tag{2.23}$$

Considering (2.22)-(2.23), $k_p = -1$ & $k_q = 1$ and $k_p = 1$ & $k_q = -1$ result in IFC's active and reactive powers oscillation cancellation, respectively (more discussion will be provided in Figure 4.2). As clear, this reference current provides much easier way for IFC's output power oscillations cancellation (see (2.13) and (2.14)).

2.3 Power Control using Instantaneous Power Theory from Single-Phase System Perspective

In this section, appropriate reference current calculation to be applied into single-phase IFCs to achieve specific performance is provided. Due to control of single-phase IFCs, the instantaneous power theory from the single-phase system perspective is developed. In this method, it is assumed that one single-phase IFC is connected to each phase of the three-phase grid at the PCC, therefore IFCs output voltages and currents are similar to the PCC voltages and currents in that phase (similar to Figure 2.2 but one single-phase IFC is connected to each phase). In addition, the power system has four wires, which results in presence of zero sequence current and voltage.

In this strategy, reference currents for single-phase IFCs are calculated to inject desired active and reactive powers into the unbalanced grid and compensate the unbalanced condition. In other words, this method is useful if the unbalanced compensation of power system by single-phase IFCs is a preferential issue.

As mentioned, the current vector that is aligned with voltage vector will generate active power while the current vector that is aligned with orthogonal voltage vector will generate reactive power (see (2.1) and (2.2)). Thus, from

single-phase perspective, total reference currents for single-phase IFCs in phase-*a,* -*b,* and -*c* could be defined as:

$$i^*_{PCC_a} = \underbrace{A_{a_p} v_{PCC_a}}_{i^*_{PCC_{ap}}} + \underbrace{B_{a_q} v_{PCC_{a_\perp}}}_{i^*_{PCC_{aq}}} \tag{2.24}$$

$$i^*_{PCC_b} = \underbrace{A_{b_p} v_{PCC_b}}_{i^*_{PCC_{bp}}} + \underbrace{B_{b_q} v_{PCC_{b_\perp}}}_{i^*_{PCC_{bq}}} \tag{2.25}$$

$$i^*_{PCC_c} = \underbrace{A_{c_p} v_{PCC_c}}_{i^*_{PCC_{cp}}} + \underbrace{B_{c_q} v_{PCC_{c_\perp}}}_{i^*_{PCC_{cq}}} \tag{2.26}$$

where $i^*_{PCC_a}$, $i^*_{PCC_b}$, and $i^*_{PCC_c}$ are the total reference currents for single-phase IFCs connected to the phase-*a*, -*b,* and -*c*, $\left(A_{a_p}, B_{a_q}\right)$, $\left(A_{b_p}, B_{b_q}\right)$, and $\left(A_{c_p}, B_{c_q}\right)$ are instantaneous conductances and susceptances in each phase, $i_{PCC_{ap}}$, $i_{PCC_{bp}}$, and $i_{PCC_{cp}}$ are active currents of IFCs in phase-*a*, -*b,* and -*c*, and $i_{PCC_{aq}}$, $i_{PCC_{bq}}$, and $i_{PCC_{cq}}$ are reactive currents of IFCs in phase-*a*, -*b,* and -*c*. The active and reactive currents generate the active and reactive powers in three phases, respectively. In (2.24) to (2.26), the values of conductances and susceptances that give rise to the exchange of certain amount of powers with the grid in each phase, $\left(P_{PCC,a}, Q_{PCC,a}\right)$, $\left(P_{PCC,b}, Q_{PCC,b}\right)$, and $\left(P_{PCC,c}, Q_{PCC,c}\right)$, under given voltage conditions can be obtained as:

$$\begin{aligned} A_{a_p} &= \frac{P_{PCC,a}}{\left|v_{PCC_a}\right|^2} \;;\; B_{a_q} = \frac{Q_{PCC,a}}{\left|v_{PCC_a}\right|^2} \;;\; A_{b_p} = \frac{P_{PCC,b}}{\left|v_{PCC_b}\right|^2} \;;\; B_{b_q} = \frac{Q_{PCC,b}}{\left|v_{PCC_b}\right|^2} \\ A_{c_p} &= \frac{P_{PCC,c}}{\left|v_{PCC_c}\right|^2} \;;\; B_{a_q} = \frac{Q_{PCC,c}}{\left|v_{PCC_c}\right|^2} \end{aligned} \tag{2.27}$$

Therefore, the total reference currents for single-phase IFCs in each phase will be:

$$\begin{cases} i^*_{PCC_a} = i^*_{PCC_{ap}} + i^*_{PCC_{aq}} = \dfrac{P_{PCC,a}}{\left|v_{PCC_a}\right|^2} v_{PCC_a} + \dfrac{Q_{PCC,a}}{\left|v_{PCC_a}\right|^2} v_{PCC_{a\perp}} \\ i^*_{PCC_b} = i^*_{PCC_{bp}} + i^*_{PCC_{bq}} = \dfrac{P_{PCC,b}}{\left|v_{PCC_b}\right|^2} v_{PCC_b} + \dfrac{Q_{PCC,b}}{\left|v_{PCC_b}\right|^2} v_{PCC_{b\perp}} \\ i^*_{PCC_c} = i^*_{PCC_{cp}} + i^*_{PCC_{cq}} = \dfrac{P_{PCC,c}}{\left|v_{PCC_c}\right|^2} v_{PCC_c} + \dfrac{Q_{PCC,c}}{\left|v_{PCC_c}\right|^2} v_{PCC_{c\perp}} \end{cases} \tag{2.28}$$

Finally, sequential analysis of three-phase active and reactive currents in (2.28) results in following positive, negative and zero sequences current:

$$\begin{aligned} & i^{+^*}_{PCC} = i^{+^*}_{PCC_p} + i^{+^*}_{PCC_q} = \\ & \frac{1}{3}\left(\frac{P_{PCC,a}}{\left|v_{PCC_a}\right|^2} v_{PCC_a} + \frac{P_{PCC,b}}{\left|v_{PCC_b}\right|^2} e^{j\frac{2\pi}{3}} v_{PCC_b} + \frac{P_{PCC,c}}{\left|v_{PCC_c}\right|^2} e^{j\frac{4\pi}{3}} v_{PCC_c} \right) + \\ & \frac{1}{3}\left(\frac{Q_{PCC,a}}{\left|v_{PCC_a}\right|^2} v_{PCC_{a\perp}} + \frac{Q_{PCC,b}}{\left|v_{PCC_b}\right|^2} e^{j\frac{2\pi}{3}} v_{PCC_{b\perp}} + \frac{Q_{PCC,c}}{\left|v_{PCC_c}\right|^2} e^{j\frac{4\pi}{3}} v_{PCC_{c\perp}} \right) \end{aligned} \tag{2.29}$$

$$\begin{aligned} & i^{-^*}_{PCC} = i^{-^*}_{PCC_p} + i^{-^*}_{PCC_q} = \\ & \frac{1}{3}\left(\frac{P_{PCC,a}}{\left|v_{PCC_a}\right|^2} v_{PCC_a} + \frac{P_{PCC,b}}{\left|v_{PCC_b}\right|^2} e^{j\frac{4\pi}{3}} v_{PCC_b} + \frac{P_{PCC,c}}{\left|v_{PCC_c}\right|^2} e^{j\frac{2\pi}{3}} v_{PCC_c} \right) + \\ & \frac{1}{3}\left(\frac{Q_{PCC,a}}{\left|v_{PCC_a}\right|^2} v_{PCC_{a\perp}} + \frac{Q_{PCC,b}}{\left|v_{PCC_b}\right|^2} e^{j\frac{4\pi}{3}} v_{PCC_{b\perp}} + \frac{Q_{PCC,c}}{\left|v_{PCC_c}\right|^2} e^{j\frac{2\pi}{3}} v_{PCC_{c\perp}} \right) \end{aligned} \tag{2.30}$$

$$\begin{aligned} & i^{0^*}_{PCC} = i^{0^*}_{PCC_p} + i^{0^*}_{PCC_q} = \\ & \frac{1}{3}\left(\frac{P_{PCC,a}}{\left|v_{PCC_a}\right|^2} v_{PCC_a} + \frac{P_{PCC,b}}{\left|v_{PCC_b}\right|^2} v_{PCC_b} + \frac{P_{PCC,c}}{\left|v_{PCC_c}\right|^2} v_{PCC_c} \right) + \\ & \frac{1}{3}\left(\frac{Q_{PCC,a}}{\left|v_{PCC_a}\right|^2} v_{PCC_{a\perp}} + \frac{Q_{PCC,b}}{\left|v_{PCC_b}\right|^2} v_{PCC_{b\perp}} + \frac{Q_{PCC,c}}{\left|v_{PCC_c}\right|^2} v_{PCC_{c\perp}} \right) \end{aligned} \tag{2.31}$$

Considering (2.29)-(2.31), it is clear that three-phase active and reactive powers can be controlled to adjust the positive, negative, and zero sequences current, which leads to adjustable unbalanced compensation.

2.4 Discussion

In Sections 2.2 and 2.3, the instantaneous power analysis from the three-phase and single-phase system perspectives are used to generate reference currents for the three-phase and single-phase IFCs to adjustably compensate the unbalance condition. Since in both strategies, certain amount of powers are exchanged with the grid (P_{PCC} and Q_{PCC}), the generated reference currents need to be equal under similar operating conditions. Here, two simple examples are provided to compare the generated reference currents from the two perspectives.

2.4.1 Example-1: only positive sequence active current injection

In Section 2.2.1, the instantaneous power theory from the three-phase system perspective is used to generate reference current to flexibly inject both positive and negative sequences current into the unbalanced grid. From (2.10), if just positive sequence current has to be injected to the exchange of a certain amount of active power with the grid (P_{PCC}), (2.10) can be written as follows:

$$i_{PCC}^{+*} = \frac{P_{PCC}}{\left|v_{PCC}^{+}\right|^2} v_{PCC}^{+} \tag{2.32}$$

Replacing v_{PCC}^{+} with phase voltages, the following relation will be achieved:

$$i_{PCC}^{+*} = \frac{P_{PCC}}{3\left|v_{PCC}^{+}\right|^2} \left(v_{PCC_a} + e^{j\frac{2\pi}{3}} v_{PCC_b} + e^{j\frac{4\pi}{3}} v_{PCC_c} \right) \tag{2.33}$$

On the other hand, in Section 2.3, the instantaneous power theory from the single-phase system perspective is used to generate reference currents for single-phase IFCs (connected to PCC in each phase) to inject desired active and reactive

currents into the unbalanced grid. From (2.29), the positive sequence of PCC current under just active powers injection can be obtained as follows:

$$i_{PCC}^{+*} = \frac{P_{PCC}}{3}\left(\frac{u_1}{\left|v_{PCC_a}\right|^2}v_{PCC_a} + \frac{u_2}{\left|v_{PCC_b}\right|^2}e^{j\frac{2\pi}{3}}v_{PCC_b} + \frac{u_3}{\left|v_{PCC_c}\right|^2}e^{j\frac{4\pi}{3}}v_{PCC_c}\right) \tag{2.34}$$

where $u_1 + u_2 + u_3 = 1$. It is worth mentioning that the average of three-phase instantaneous active power is equal to summation of average active powers of three phases ($P_{PCC} = P_{PCC,a} + P_{PCC,b} + P_{PCC,c}$).

Comparing (2.33) with (2.34) clarifies that these two positive sequence reference currents looks similar, however they are not equal due to different operating conditions. In other words, in (2.33), just positive sequence current is injected while (2.34) is the positive sequence component of the reference current in (2.28), which also contains negative and zero sequences current. To compare these two positive sequence currents ((2.33) and (2.34)), the negative and zero sequences current of (2.28), which are presented in (2.30) and (2.31), should be set to zero as follows:

$$i_{PCC}^{-*} = \frac{P_{PCC}}{3}\left(\frac{u_1}{\left|v_{PCC_a}\right|^2}v_{PCC_a} + \frac{u_2}{\left|v_{PCC_b}\right|^2}e^{j\frac{4\pi}{3}}v_{PCC_b} + \frac{u_3}{\left|v_{PCC_c}\right|^2}e^{j\frac{2\pi}{3}}v_{PCC_c}\right) = 0 \tag{2.35}$$

$$i_{PCC}^{0*} = \frac{P_{PCC}}{3}\left(\frac{u_1}{\left|v_{PCC_a}\right|^2}v_{PCC_a} + \frac{u_2}{\left|v_{PCC_b}\right|^2}v_{PCC_b} + \frac{u_3}{\left|v_{PCC_c}\right|^2}v_{PCC_c}\right) = 0 \tag{2.36}$$

Solving (2.35) and (2.36), following relations are achieved:

$$\begin{cases} \dfrac{u_1}{\left|v_{PCC_a}\right|} = \dfrac{u_2}{\left|v_{PCC_b}\right|} = \dfrac{u_3}{\left|v_{PCC_c}\right|} \\ \angle\theta_{v_{PCC_a}} = \angle\theta_{v_{PCC_b}} + \dfrac{2\pi}{3} = \angle\theta_{v_{PCC_c}} + \dfrac{4\pi}{3} \end{cases} \tag{2.37}$$

Applying the conditions in (2.37) into (2.33) and (2.34) and assuming that average active powers in three phases are equal ($u_1 = u_2 = u_3 = 1/3$), following relations will be resulted:

$$i_{PCC}^{+*} = \frac{P_{PCC}}{3\left|v_{PCC}^{+}\right|^2}\left(v_{PCC_a} + e^{j\frac{2\pi}{3}} v_{PCC_b} + e^{j\frac{4\pi}{3}} v_{PCC_c} \right) = \frac{P_{PCC}}{3\left|v_{PCC}^{+}\right|^2} v_{PCC_a} \tag{2.38}$$

$$i_{PCC}^{+*} = \frac{P_{PCC}}{3}\left(\frac{u_1}{\left|v_{PCC_a}\right|^2} v_{PCC_a} + \frac{u_2}{\left|v_{PCC_b}\right|^2} e^{j\frac{2\pi}{3}} v_{PCC_b} + \frac{u_3}{\left|v_{PCC_c}\right|^2} e^{j\frac{4\pi}{3}} v_{PCC_c} \right) = \frac{P_{PCC}}{3\left|v_{PCC}^{+}\right|^2} v_{PCC_a} \tag{2.39}$$

Thus, from (2.38) and (2.39), it is seen that the reference currents from the three-phase perspective and the single-phase perspective are equal under similar operating condition.

2.4.2 Example-2: only negative sequence active current injection

As another example, negative sequence active current injection to the grid is considered, and reference currents generated in Sections 2.2.1 and 2.3 are compared. From the three-phase system perspective, (2.10) can be written as follows:

$$i_{PCC}^{-*} = \frac{P_{PCC}}{3\left|v_{PCC}^{-}\right|^2}\left(v_{PCC_a} + e^{j\frac{4\pi}{3}} v_{PCC_b} + e^{j\frac{2\pi}{3}} v_{PCC_c} \right) \tag{2.40}$$

From (2.30), the negative sequence current under active power injection from the single-phase system perspective will be as follows:

$$i_{PCC}^{-*} = \frac{P_{PCC}}{3}\left(\frac{u_1}{\left|v_{PCC_a}\right|^2} v_{PCC_a} + \frac{u_2}{\left|v_{PCC_b}\right|^2} e^{j\frac{4\pi}{3}} v_{PCC_b} + \frac{u_3}{\left|v_{PCC_c}\right|^2} e^{j\frac{2\pi}{3}} v_{PCC_c} \right) \tag{2.41}$$

However, for only negative sequence current injection from the single-phase system perspective, the positive and zero sequences current of (2.29) and (2.31) should be set to zero as follows:

$$i_{PCC}^{+*} = \frac{P_{PCC}}{3}\left(\frac{u_1}{\left|v_{PCC_a}\right|^2} v_{PCC_a} + \frac{u_2}{\left|v_{PCC_b}\right|^2} e^{j\frac{2\pi}{3}} v_{PCC_b} + \frac{u_3}{\left|v_{PCC_c}\right|^2} e^{j\frac{4\pi}{3}} v_{PCC_c} \right) = 0 \tag{2.42}$$

$$i_{PCC}^{0^*} = \frac{P_{PCC}}{3}\left(\frac{u_1}{\left|v_{PCC_a}\right|^2}v_{PCC_a} + \frac{u_2}{\left|v_{PCC_b}\right|^2}v_{PCC_b} + \frac{u_3}{\left|v_{PCC_c}\right|^2}v_{PCC_c}\right) = 0 \tag{2.43}$$

Solving (2.42) and (2.43), the single-phase system parameters should have the following relations:

$$\begin{cases} \dfrac{u_1}{\left|v_{PCC_a}\right|} = \dfrac{u_2}{\left|v_{PCC_b}\right|} = \dfrac{u_3}{\left|v_{PCC_c}\right|} \\ \angle\theta_{v_{PCC_a}} = \angle\theta_{v_{PCC_b}} + \dfrac{4\pi}{3} = \angle\theta_{v_{PCC_c}} + \dfrac{2\pi}{3} \end{cases} \tag{2.44}$$

Applying the relations in (2.44) into (2.40) and (2.41) to unify the operating conditions and assuming equal average active powers in three phases, following results will be achieved:

$$i_{PCC}^{-^*} = \frac{P_{PCC}}{3\left|v_{PCC}^{-}\right|^2}\left(v_{PCC_a} + e^{j\frac{4\pi}{3}}v_{PCC_b} + e^{j\frac{2\pi}{3}}v_{PCC_c}\right) = \frac{P_{PCC}}{3\left|v_{PCC}^{-}\right|^2}v_{PCC_a} \tag{2.45}$$

$$i_{PCC}^{-^*} = \frac{P_{PCC}}{3}\left(\frac{u_1}{\left|v_{PCC_a}\right|^2}v_{PCC_a} + \frac{u_2}{\left|v_{PCC_b}\right|^2}e^{j\frac{4\pi}{3}}v_{PCC_b} + \frac{u_3}{\left|v_{PCC_c}\right|^2}e^{j\frac{2\pi}{3}}v_{PCC_c}\right) = \frac{P_{PCC}}{3\left|v_{PCC}^{-}\right|^2}v_{PCC_a} \tag{2.46}$$

From (2.45) and (2.46), it is clear that under similar operating conditions, the reference currents from the single-phase system perspective and the three-phase system perspective are equal.

2.5 Conclusion

This chapter reviewed and derived an instantaneous power analysis from three-phase and single-phase system perspectives to calculate the reference currents for interfacing converters to achieve specific goals. Three methods to generate the reference currents were provided, which are used in the rest of the thesis in the proposed control strategies. In the first reference current, which was derived for a three-phase IFC to adjustably compensate for the unbalanced condition, the positive and negative sequences' active and reactive currents are directly controlled by the two coefficients k_1 and k_2. This reference current will

be used in the proposed control strategies for IFCs in Chapter 3. The second reference current was derived to easily reduce/minimize the adverse effects of unbalanced voltage on three-phase IFCs' operation. This reference current will be used in Chapter 4 and Chapter 5 to cancel out parallel three-phase IFCs' active power oscillation and DC link voltage ripple by controlling the two coefficients k_p and k_q. It should be mentioned that adverse effects reduction such as power oscillation cancellation can be done by the first generated reference current (using k_1 and k_2), but the second one provides an easy way to achieve this goal, especially when parallel IFCs are used. The third reference current was developed for single-phase IFCs to adjustably compensate for the unbalanced condition. In this reference current, which is used in Chapter 6, three-phase active and reactive powers are controlled to adjust the positive, negative and zero sequences current.

Chapter 3

Single Three-Phase Interfacing Converter Control for Unbalanced Voltage Compensation in Hybrid AC/DC Microgrids[1]

In hybrid AC/DC microgrids, three-phase power electronics interfacing converters (IFCs) have great potential to be used for unbalanced voltage compensation. These IFCs can be DG/SE IFC connected to the AC subsystem or the AC and DC-subsystems' interfacing converter. The unbalanced voltage has adverse effects on the IFCs' operation such as output active power oscillation and DC link voltage variations. Also, since the compensation is realized through the available rating of IFCs, it is equally important to consider the effectiveness of the control strategy for unbalanced voltage compensation. Considering these challenging issues, two unbalanced voltage compensation strategies for single three-phase power electronics IFC are proposed. In both proposed control strategies, the instantaneous power analysis from a three-phase system perspective, presented in Section 2.2.1 of Chapter 2, is used. Both proposed methods are based on the IFC's equivalent negative sequence virtual impedance amplitude and phase angle control. In the first strategy, the IFC's output active power oscillation is minimized to reduce the adverse effects of unbalanced voltage on IFC operation in addition to providing unbalanced voltage compensation. This method is named active power oscillation minimization in this chapter. In the second strategy, an effective method for reducing the negative

[1] Publication out of this Chapter:

- F. Nejabatkhah, Y. W. Li, and B. Wu, "Control Strategies of Three-Phase Distributed Generation Inverters for Grid Unbalanced Voltage Compensation", *IEEE Transactions on Power Electronics, vol. 31, no. 7, pp. 5228–5241, Jul. 2016*.

sequence voltage is proposed in which the IFC's injected negative sequence current is controlled to be in the same phase as the grid negative sequence current. This method is named in-phase current compensation in this chapter. The performances of the two proposed control strategies under different grid conditions and IFC operating conditions are studied. Recommendations for appropriate strategy utilization under various conditions are provided. In addition, the validity of proposed strategies is verified by simulations and experiments.

3.1 Three-Phase IFC Instantaneous Power Analysis and Sequence Network Model

Figure 3.1 shows a three-phase interfacing converter (IFC) connected to the AC subsystem (sometimes refer as an AC grid in this chapter) at the point of common coupling (PCC) with LCL filter, and an unbalance load is connected to PCC as a source of unbalanced voltage. The IFC can be the AC and DC-subsystems' IFC in DC-coupled or AC-DC-coupled hybrid microgrids or the IFC of DG/SE connected to the AC subsystem in AC-coupled or AC-DC-coupled hybrid microgrids.

In this Chapter, since unbalanced voltage compensation with adjustable level is desired, the reference current calculated in Section 2.2.1 of Chapter 2 is used to directly control both positive and negative sequences current. Different from Section 2.2.1, here the IFC's output voltage and current vectors are represented by v and i, instead of v_{PCC} and i_{PCC}, which is shown in Figure 3.1. Moreover, the IFC's output average active and reactive powers are represented by P and Q.

From Section 2.2.1, the reference current of three-phase IFC to flexibly

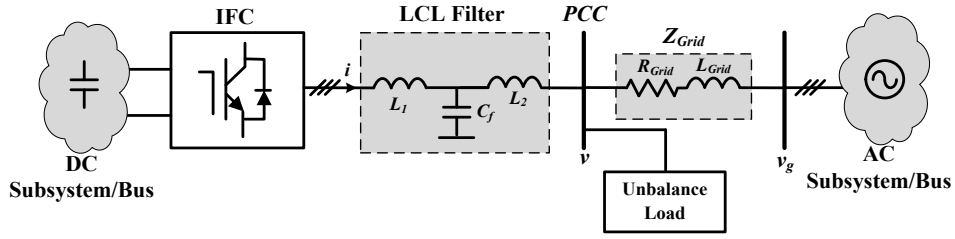

Figure 3.1 Single three-phase interfacing converter.

control both positive and negative sequences current injection to the grid is provided in following:

$$i^{*} = i_p^{+} + i_p^{-} + i_q^{+} + i_q^{-} = \frac{P k_1}{\left|v^{+}\right|^2} v^{+} + \frac{P(1-k_1)}{\left|v^{-}\right|^2} v^{-} + \frac{Q k_2}{\left|v^{+}\right|^2} v_{\perp}^{+} + \frac{Q(1-k_2)}{\left|v^{-}\right|^2} v_{\perp}^{-} \tag{3.1}$$

As clear from (3.1), portions of positive and negative sequences active and reactive currents can be adjusted by k_1 and k_2 to achieve different control objectives. For example, $k_1 = 1$ leads negative sequence active current to zero, and $k_2 = 1$ sets negative sequence reactive current to zero. Moreover, when $k_1 = k_2 = 1$, balance three-phase current is injected to the grid. Using (3.1), the positive and negative sequence components of IFC's reference current vectors can be expressed as:

$$i^{+^{*}} = Y^{+} v^{+} = \left(\frac{P k_1}{\left|v^{+}\right|^2} - \frac{Q k_2}{\left|v^{+}\right|^2} e^{j\frac{\pi}{2}} \right) v^{+} \tag{3.2}$$

$$i^{-^{*}} = Y^{-} v^{-} = \left(\frac{P(1-k_1)}{\left|v^{-}\right|^2} + \frac{Q(1-k_2)}{\left|v^{-}\right|^2} e^{j\frac{\pi}{2}} \right) v^{-} \tag{3.3}$$

From (3.2) and (3.3), sequence network model of single three-phase IFC can be achieved. Figure 3.2 shows the equivalent negative sequence model of single grid-connected three-phase IFC (no zero sequence in the system). In this figure, the positive sequence equivalent network together with unbalance load are represented by an equivalent current source i_{load}^{-} (which value depends on the unbalance load configuration as well as the positive sequence network parameters as will be discussed later). Moreover, in Figure 3.2, IFC is represented as a virtual impedance Z^{-} in order to emulate its behaviour in the negative sequence circuit (see (3.3)), the grid negative sequence impedance (Z_{Grid}^{-}) is shown in parallel configuration, and the currents directions are assumed as shown in figure for better explanation.

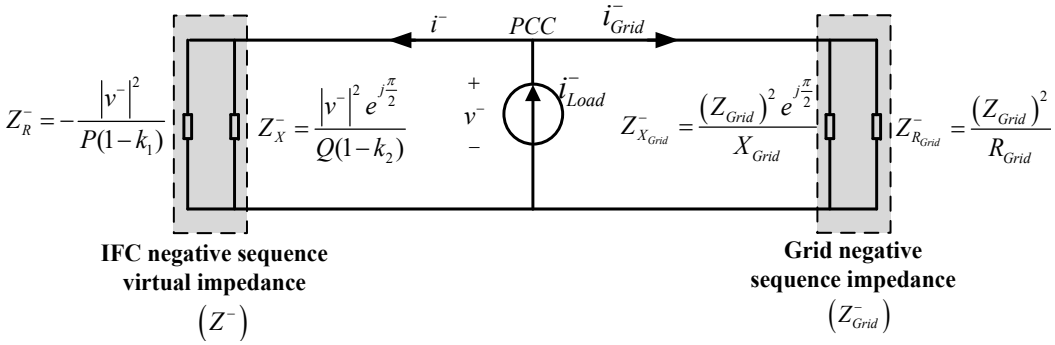

Figure 3.2 Sequence network model of single grid-connected three-phase IFC.

If the three-phase unbalance load is connected to the PCC in star connection (Z_{L1}, Z_{L2}, Z_{L3}), i^-_{load} can be represented as (3.4). (Note that using three-phase network symmetrical component analysis, i^-_{load} can be extended to other load types, e.g. single-phase load [67]).

$$i^-_{load} = \frac{E(a^2 Z_{L1} + aZ_{L2} + Z_{L3})}{Z_{L1}Z_{L3} + Z_{L2}Z_{L3} + Z_{L1}Z_{L2} + Z^-_{PCC}Z_L + Z^+_{PCC}Z_L + 3Z^+_{PCC}Z^-_{PCC}} \tag{3.4}$$

where Z_L is the summation of load impedances ($Z_L = Z_{L1}+Z_{L2} + Z_{L3}$), and a is the rotation operator $\left(a = e^{j\frac{2\pi}{3}}\right)$. Moreover, E represents the voltage of the PCC under balance condition (without presence of unbalance load), and Z^+_{PCC} and Z^-_{PCC} are positive and negative sequences impedance seen from the PCC. Considering Figure 3.1 and Figure 3.2, these parameters can be achieved as follows:

$$E = \frac{Z^+_{PCC}}{Z^+_{PCC} + Z^+_{Grid}} \times v_g \tag{3.5}$$

$$Z^+_{PCC} = Z^+ || \, Z^+_{Grid} \tag{3.6}$$

$$Z^-_{PCC} = Z^- || \, Z^-_{Grid} \tag{3.7}$$

where Z^+_{Grid} is the grid positive sequence impedance, v_g is the grid (AC subsystem) voltage, and Z^+ is the IFC's positive sequence virtual impedance that can be expressed as (3.8) by using (3.2).

$$Z^+ = Z^+_R || \, Z^+_X = \left(-\frac{|v^+|^2}{Pk_1}\right) || \left(\frac{|v^+|^2}{Qk_2} e^{-j\frac{\pi}{2}}\right) \tag{3.8}$$

In the two proposed control strategies to be discussed later, for better explanation and comparison, i_{load}^{-} will be considered as a constant value based on fixed values of $|i^{-}|$ and IFC's active-reactive powers. Considering (3.4) to (3.8), this assumption is valid since Z_{PCC}^{+} and E are approximately constant values in the aforementioned conditions. Moreover, the variations of Z_{PCC}^{-} in the two proposed control strategies will not influence the denominator of (3.4) due to its small amplitude (in the both proposed control strategies, Z^{-} is controlled to be much smaller than the grid impedance). However, it is worth mentioning again that this assumption is just for better explanations and comparison, and the proposed strategies are still valid without this assumption.

Considering the sequence network equivalent circuit in Figure 3.2, two scenarios are discussed:

3.1.1 IFC produces balance current without unbalanced voltage compensation

In the case that weighting factors k_1 and k_2 are equal to one ($k_1 = 1$ and $k_2 = 1$), just positive sequence active and reactive powers are injected to the grid. From Figure 3.2, both Z_R^{-} and Z_X^{-} are open circuit, and the negative sequence voltage of PCC can be expressed as (3.9).

$$|v^{-}| = |i_{load}^{-}| \times |Z_{Grid}^{-}| \tag{3.9}$$

3.1.2 IFC produces unbalance current for unbalanced voltage compensation

In the case that weighting factors k_1 and k_2 are not equal to one ($k_1 \neq 1$ and $k_2 \neq 1$), positive and negative sequence active and reactive powers are injected to the grid. From Figure 3.2, the negative sequence voltage of PCC can be achieved:

$$|v^{-}| = |i_{load}^{-}| \times |Z_{Grid}^{-} \,//\, Z^{-}| \tag{3.10}$$

From (3.9), (3.10) and Figure 3.2, it can be seen that injecting the negative sequence active and reactive powers to the grid by single three-phase IFC could compensate the PCC unbalanced voltage. In other words, the negative sequence

virtual impedance of IFC (Z^-) can be controlled to be much smaller than the grid impedance, directing i_{load}^- to flow to the IFC side and leading to an improved PCC voltage. However, how the control of IFC negative sequence virtual impedance or negative sequence current can minimize the IFC's output active power oscillation and effectively reduce the negative sequence voltage of IFC will be discussed in the following section.

3.2 Two Proposed Control Strategies for Single Three-Phase IFC for Unbalanced Voltage Compensation in Hybrid AC/DC Microgrids

3.2.1 Unbalanced voltage compensation with active power oscillation minimization

As shown in (2.11), to compensate the PCC voltage unbalance, the IFC negative sequence currents produce active power oscillation at the DG output, which leads to DC link voltage oscillation. The DC link ripples have adverse effects on the DC subsystem and may produce harmonics at IFCs AC output. The active power oscillation in (2.11) is presented in following again:

$$\Delta P = \left(\frac{Pk_1}{|v^+|^2} + \frac{P(1-k_1)}{|v^-|^2}\right) v^+ \cdot v^- + \left(\frac{Qk_2}{|v^+|^2} - \frac{Q(1-k_2)}{|v^-|^2}\right) v_\perp^+ \cdot v^- \qquad (3.11)$$

In active power oscillation cancellation strategy [40], the level of unbalanced voltage compensation cannot be controlled directly. Therefore, in order to control and compensate the AC subsystem steady-state unbalanced voltage and to reduce the adverse effects of this unbalance compensation, this proposed control strategy aims at minimizing the active power oscillation while with adjustable unbalance compensation levels. This strategy is named active power oscillation minimization or ΔP-minimization strategy.

In this control strategy, the amplitude and phase angle of IFC's negative sequence current is controlled (i.e. IFC's negative sequence virtual impedance can be controlled which are the same approach) to minimize the active power

oscillation and compensate unbalanced voltage. From (3.3), the amplitude of IFC's desired negative sequence current is defined as:

$$\left|i^{-^*}\right| = \frac{|v^-|}{|Z^-|} = \sqrt{\left(\frac{P(1-k_1)}{|v^-|}\right)^2 + \left(\frac{Q(1-k_2)}{|v^-|}\right)^2} \tag{3.12}$$

Considering (3.10), the active power oscillation in stationary $\alpha\beta$ reference frame can be achieved as (3.13).

$$\begin{aligned}\Delta P = &\frac{3}{2}\left(\frac{Pk_1}{|v^+|^2} + \frac{P(1-k_1)}{|v^-|^2}\right)\left(v_\alpha^+ v_\alpha^- + v_\beta^+ v_\beta^-\right) \\ &+ \frac{3}{2}\left(\frac{Qk_2}{|v^+|^2} - \frac{Q(1-k_2)}{|v^-|^2}\right)\left(v_\beta^+ v_\alpha^- - v_\alpha^+ v_\beta^-\right)\end{aligned} \tag{3.13}$$

Using Clarke transformation, the PCC positive and negative sequences voltage in stationary $\alpha\beta$ reference frame can be expressed as follows:

$$v_\alpha^+ = |v^+|\cos(\omega t + \theta^+) \tag{3.14}$$

$$v_\beta^+ = |v^+|\cos\left(\omega t - \frac{\pi}{2} + \theta^+\right) \tag{3.15}$$

$$v_\alpha^- = |v^-|\cos(\omega t - \theta^-) \tag{3.16}$$

$$v_\beta^- = |v^-|\cos\left(\omega t + \frac{\pi}{2} - \theta^-\right) \tag{3.17}$$

where θ^+ and θ^- are the phase angle jumps. From (3.13) to (3.17), the active power oscillation can be expressed as follows:

$$\begin{aligned}\Delta P = &\frac{3}{2}\left(\frac{Pk_1}{|v^+|^2} + \frac{P(1-k_1)}{|v^-|^2}\right)|v^+||v^-|\cos(2\omega t + \theta) \\ &+ \frac{3}{2}\left(\frac{Qk_2}{|v^+|^2} - \frac{Q(1-k_2)}{|v^-|^2}\right)|v^+||v^-|\sin(2\omega t + \theta)\end{aligned} \tag{3.18}$$

where $\theta^+ - \theta^- = \theta$ is the phase angle between positive and negative sequences. In order to minimize sinusoidal active power oscillation in (3.18), following objective function is defined:

$$\left[\left(\frac{Pk_1}{|v^+|^2}+\frac{P(1-k_1)}{|v^-|^2}\right)|v^+||v^-|\right]^2+\left[\left(\frac{Qk_2}{|v^+|^2}-\frac{Q(1-k_2)}{|v^-|^2}\right)|v^+||v^-|\right]^2 \quad (3.19)$$

This objective function should be minimized subjected to the constraint in (3.12) which provides controllable unbalanced voltage compensation. With the assumption of $k_1-1=l_1$ and $k_2-1=l_2$, the objective function in (3.19) and the constraint in (3.12) could be expressed as (3.20) and (3.21), respectively.

$$J(l_1,l_2)=A^2l_1^2+B^2l_2^2+Cl_1+El_2+F \quad (3.20)$$

$$P^2l_1^2+Q^2l_2^2=D^2 \quad (3.21)$$

where $A, B, C, D, E,$ and F are defined as $A=\frac{P\left(|v^+|^2-|v^-|^2\right)}{|v^+||v^-|}$, $B=\frac{Q\left(|v^+|^2+|v^-|^2\right)}{|v^+||v^-|}$, $C=\frac{2P^2|v^-|^2\left(|v^+|^2-|v^-|^2\right)}{|v^+|^2|v^-|^2}$, $D=|v^-|\left|i_{ref}^-\right|$, $E=\frac{-2Q^2|v^-|^2\left(|v^+|^2+|v^-|^2\right)}{|v^+|^2|v^-|^2}$, $F=\frac{|v^-|^2(P^2+Q^2)}{|v^+|^2|v^-|^2}$.

Considering (3.20) and (3.21), the objective function and constraint are quadratic functions that can be represented in the general form of $(1/2)x^TPx+q^Tx+r$. Since P in both functions are positive semidefinite, the close form analytical solution can be found using Lagrangian method [68]. Utilizing this deterministic method, l_1 and l_2 can be determined analytically as a function of system operating point. Due to the limited computation and deterministic solution in comparison to heuristic optimization methods, these parameters can be easily updated online in a digital controller. From (3.20) and (3.21), the Lagrangian function is defined as follows:

$$L(l_1,l_2,\lambda)=A^2l_1^2+B^2l_2^2+Cl_1+El_2+F+\lambda(P^2l_1^2+Ql_2^2-D^2) \quad (3.22)$$

where λ is Lagrangian multiplier. Setting each of the partial derivatives of this function equal to zero $\left(\frac{\partial L}{\partial l_1}=0,\frac{\partial L}{\partial l_2}=0,\frac{\partial L}{\partial \lambda}=0\right)$, the optimal values of l_1 and l_2 are calculated analytically, leading to k_1 and k_2 determination. In control system, in each time step, l_1 and l_2 are updated based on system parameters.

3.2.2 Unbalanced voltage compensation to minimize the PCC negative sequence voltage

In order to effectively compensate the grid unbalanced voltage, or in other words to minimize the PCC negative sequence voltage under a given IFC's negative sequence current level, the phase angles of IFC and the grid negative sequence currents should be the same. In this case, by assuming constant negative sequence load current (i_{load}^{-}) in the fixed $|i^{-}|$, minimum negative sequence current will be directed to the grid, resulting in minimum negative sequence voltage at the PCC ($|v^{-}| = |i_{Grid}^{-}| \times |Z_{Grid}^{-}|$). In this control strategy, the active power oscillation at IFC output is not controlled directly. In this chapter, this strategy is named in-phase current compensation strategy.

In this control strategy, the amplitude and phase angle of IFC's negative sequence current (or IFC's negative sequence virtual impedance) is controlled to minimize the negative sequence voltage of the PCC without active power oscillation consideration. In this method, the phase angles of IFC and the grid negative sequence impedances (see Figure 3.2) are controlled to be the same as in (3.23).

$$\measuredangle Z^{-} = \measuredangle Z_{Grid}^{-} \tag{3.23}$$

Considering (3.12) and (3.23), k_1 and k_2 can be achieved as follows:

$$k_1 = 1 \pm \frac{|v^{-}||i^{-^*}|}{P \times \sqrt{1 + \left(\frac{Z_{X\,Grid}^{-}}{Z_{R\,Grid}^{-}}\right)^2}} \tag{3.24}$$

$$k_2 = 1 \pm \frac{Z_{X\,Grid}^{-}}{Z_{R\,Grid}^{-}} \times \frac{|v^{-}||i^{-^*}|}{Q \times \sqrt{1 + \left(\frac{Z_{X\,Grid}^{-}}{Z_{R\,Grid}^{-}}\right)^2}} \tag{3.25}$$

Considering (3.12), (3.24), and (3.25), it can be concluded that if $k_1 > 1$ and $k_2 < 1$, IFC's negative sequence current will be in-phase with the grid negative sequence current. However, $k_1 < 1$ and $k_2 > 1$ will cause them to be 180° out of

phase. Considering (3.24), and (3.25), in this strategy just the ratio of the grid reactance to resistance in fundamental frequency is needed, which can be easily obtained using different methods [69]-[71]. In this chapter, this ratio is considered as a known value in the control system.

Finally, the overall control block diagram is shown in Figure 3.3. This control system contains outer loop which is responsible for IFC's reference current generation, and inner current control loop which is responsible for tracking the reference current quickly and accurately (see Figure 2.2). The control is implemented in the stationary $\alpha\beta$ reference frame to avoid multiple frame transformations for different sequence components control. In the outer loop, among different sequence extractors [72]-[74], frequency-locked loop (FLL) based sequence extractor in [74] is used to separate the PCC voltage into positive and negative sequences. Moreover, weighting factors k_1 and k_2 are determined by either the active power oscillation minimization or in-phase current compensation strategy. In Figure 3.3, $|i^{-*}|$ can be set directly through the desired IFC's negative sequence virtual impedance using (3.12). Either way, the IFC's available rating for unbalance compensation need to be a constraint. In the inner control loop, IFC is controlled in current control operation mode using proportional-resonant controller [75].

3.3 Comparisons of the Proposed Control Strategies

In this section, detailed study of each proposed control strategy and their differences are concluded, and the influences of IFC's operating conditions in

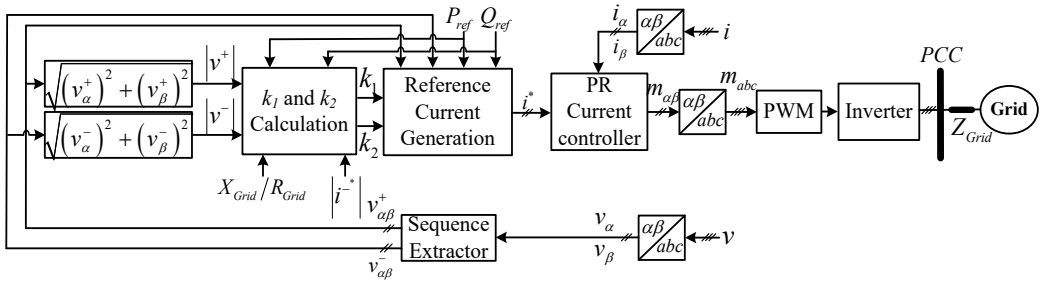

Figure 3.3 Proposed control strategies for single three-phase IFC for the unbalanced voltage compensation.

TABLE 3.1 Case study results for both proposed control strategies with $|\dot{\imath}|$=10A under different IFC's output P/Q ratios (S=20.61kVA) and the grid conditions ($|Z_{Grid}|$=0.75398 Ω).

Grid impedance conditions		$X_{Grid} \gg R_{Grid}$ $R = 1\times10^{-3}\Omega;\ X = 0.753\Omega$		$X_{Grid} \ll R_{Grid}$ $R = 0.753\Omega;\ X = 1\times10^{-3}\Omega$	
IFC's output active-reactive powers		$20kW$ $5kVar$	$5kW$ $20kVar$	$20kW$ $5kVar$	$5kW$ $20kVar$
$\lvert v^{-}\rvert$ (V)	No compensation	13.66	15.70	12.88	10.74
	ΔP-minimization	9.10	8.26	6.25	6.88
	In-phase current	6.23	8.26	6.15	4.00
	$\frac{\Delta P-\text{minimization}}{\text{In-phase current}}$ ratio	1.46	1	1.01	1.72
ΔP (W)	No compensation	1368	1368	1228	1228
	ΔP-minimization	2177	2835	2643	1921
	In-phase current	3005	2862	2673	2626
	$\frac{\Delta P-\text{minimization}}{\text{In-phase current}}$ ratio	0.72	0.99	0.98	0.73
ΔQ (VAr)	No compensation	1368	1368	1228	1228
	ΔP-minimization	4007	4267	3840	3487
	In-phase current	3297	4248	3820	2850
	$\frac{\Delta P-\text{minimization}}{\text{In-phase current}}$ ratio	1.21	1.004	1.005	1.22

terms of output P/Q ratios and the grid conditions in terms of different X_{Grid}/R_{Grid} ratios are investigated. These discussions are supported by a case study in TABLE 3.1, Figure 3.4, and Figure 3.5, where a three-phase grid-connected IFC is simulated. In this case study for better explanation and comparison, the performance of the two proposed control strategies in normal grid with inductive impedance (large X_{Grid}/R_{Grid} ratio) and weak grid with resistive impedance (small X_{Grid}/R_{Grid} ratio) under different IFC's output P/Q ratio are presented. The IFC's apparent power (S) and the amplitude of the grid impedance ($|Z_{Grid}|$) are considered to be constant. Complete simulation results and the parameters and specifications of the simulated system will be provided in simulation section.

First of all, with IFC's compensation and the equivalent small negative sequence virtual impedance, the negative sequence load current is directed to the IFC side, resulting in less negative sequence current in the grid (i_{Grid}^{-}) and therefore the negative sequence voltage at PCC are reduced in all conditions in the both proposed methods. However, considering (2.3) and (2.4), the presence of i^{-} increase the active and reactive powers oscillations in comparison to balance current injection. These results can be confirmed by TABLE 3.1.

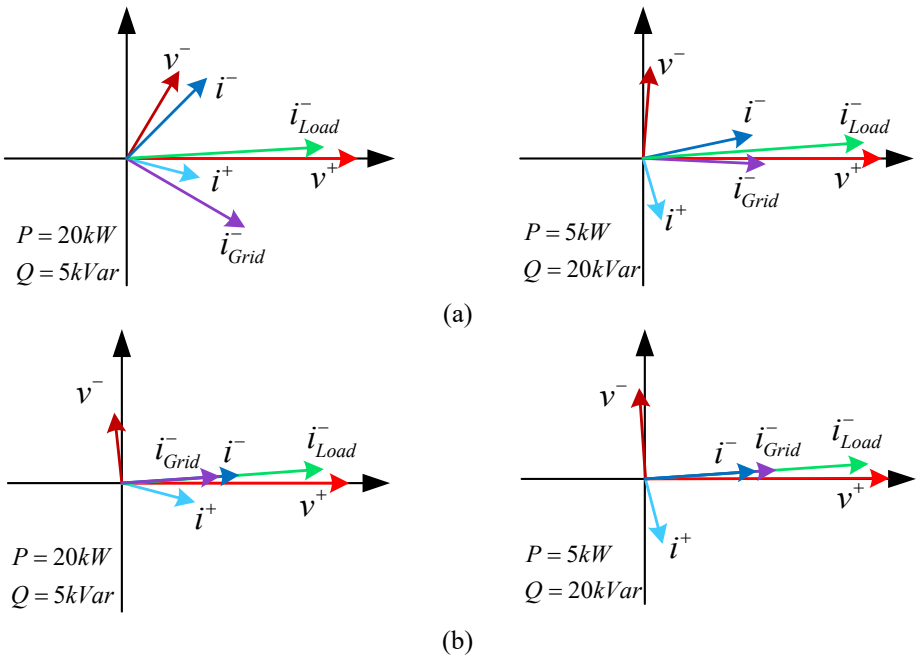

Figure 3.4 Phasor diagrams of the case study in phase-a with $|\dot{i}|$=*10A* under $X_{Grid} \gg R_{Grid}$ and different *P/Q* ratios (v^+ and i^+ with the scale of 0.1); (a) ΔP-minimization strategy, (b) in-phase current compensation strategy.

In the active power oscillation minimization strategy, IFC's negative sequence current (or IFC's negative sequence virtual impedance) is controlled in order to minimize the active power oscillation at IFC output. Therefore, the active power oscillation in this strategy is smaller than the in-phase current compensation method in all operating conditions ($\Delta P_{\Delta P-minimization} < \Delta P_{in-phase}$). As shown in TABLE 3.1, the ratios of active power oscillation in ΔP-minimization strategy over in-phase current compensation strategy are always less than one under the same operating conditions. At the same time, it can also be observed that the reactive power oscillations in the active power oscillation minimization will be larger than in-phase current compensation ($\Delta P_{\Delta P-minimization} > \Delta P_{in-phase}$). This is because, considering (3.11) and (3.19), for active power oscillation minimization $|P(1-k_1)/|v^-|^2|$ and $|Q(1-k_2)/|v^-|^2|$ should reach $-|Pk_1/|v^+|^2|$ and $|Qk_2/|v^+|^2|$, respectively. In this case, the reactive power oscillations will increase according to (2.12).

For the in-phase current compensation strategy, the phase angles of i^-_{load}, i^- and i^-_{Grid} are the same. Obviously, with the same $|i^-_{load}|$ and $|i^-|$, $|i^-_{Grid}|$ in the in-phase current compensation strategy will be smaller than ΔP-minimization

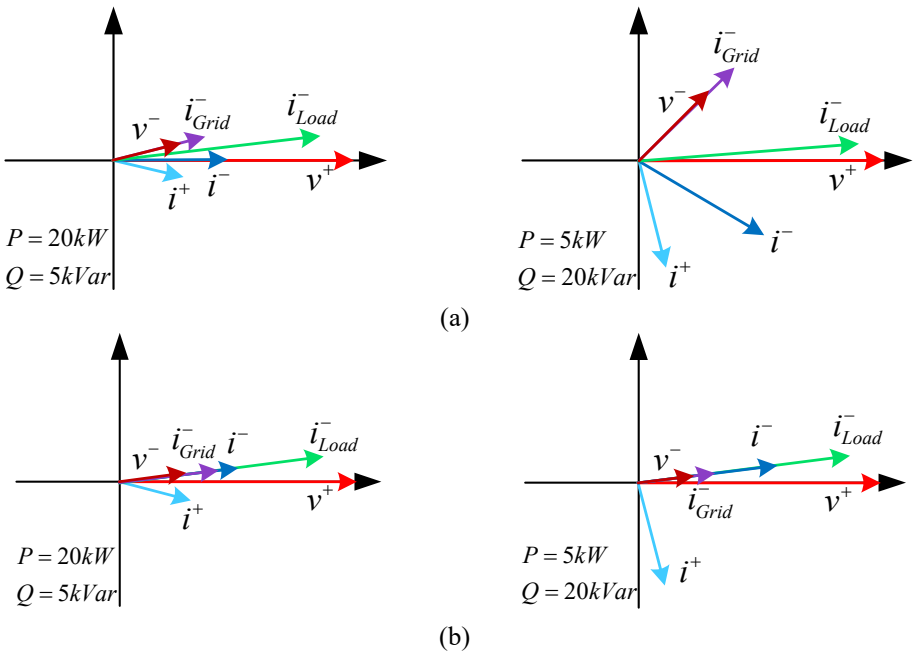

Figure 3.5 Phasor diagrams of the case study in phase-a with $|\dot{i}|$=*10A* under $X_{Grid} \ll R_{Grid}$ and different *P/Q* ratios (v^+ and i^+ with the scale of 0.1); (a) Δ*P*-minimization strategy, (b) in-phase current compensation strategy.

strategy $\left(|i^-_{Grid}|_{\Delta P-minimization} > |i^-_{Grid}|_{in-phase}\right)$. The relationship is more clearly shown in the phasor plot in Figure 3.4 and Figure 3.5. Therefore, the negative sequence voltage at the PCC in the in-phase current compensation will be smaller than the active power oscillation minimization strategy $\left(|v^-|_{\Delta P-minimization} > |v^-|_{in-phase}\right)$. As shown in TABLE 3.1, the ratios of negative sequence voltage in p̃-minimization strategy over in-phase current compensation are always greater than one under the same operating conditions.

In the both methods, increasing $|i^-|$ will reduce $|i^-_{Grid}|$, which leads to more reduction of negative sequence voltage at PCC. However, considering (2.3) and (2.4), the active and reactive powers oscillation will increase with higher unbalance compensation level. In small IFCs, due to lower $|i^-|$, performance difference of the two proposed control strategies in terms of the negative sequence voltage reduction will not be very obvious. Therefore, the active power oscillation will be a dominant factor when comparing the two methods. On the other hand, in large DGs, due to possibility of high $|i^-|$, the difference negative sequence voltage reduction between the two methods will be more obvious and become a dominant factor when comparing the two methods. The influence of $|i^-|$ in two

proposed methods will be shown in the simulation section. Additional comparisons of the two proposed strategies are provided in the following subsections.

3.3.1 Inductive grid under various IFC's output P/Q ratios

The performance of the two proposed methods in normal grid with inductive impedance where X_{Grid} is much large than R_{Grid} ($X_{Grid} \gg R_{Grid}$) is studied. In the inductive grid impedance, the negative sequence current of the grid and the negative sequence voltage of PCC are approximately orthogonal.

In the ΔP-minimization strategy, with small values of P/Q ratio ($P \ll Q$) at the IFC output when IFC mainly produces reactive power support, the phase angle between v^- and i^- will be close to 90° according to (3.3). As a result, the IFC and the grid negative sequence currents will be approximately in-phase (small phase angle between i^- and i^-_{Grid}). This can also be seen in phasor plots in Figure 3.4 and Figure 3.5. Therefore, with inductive grid impedance, the results of active power oscillation minimization and in-phase current compensation strategies are approximately the same in small P/Q ratios at the IFC output. As shown in TABLE 3.1, the ratios of negative sequence voltage, and active and reactive power oscillations in ΔP-minimization strategy over in-phase current compensation are 1, 0.99, and 1.004, respectively. On the other hand, if IFC operates with unity or high power factor, the performance difference of the two methods will be very obvious in terms of active power oscillation and effectiveness of negative sequence voltage reduction (see TABLE 3.1 in which the negative sequence voltage of ΔP-minimization strategy is 1.46 times larger than in-phase current compensation while its active power oscillation is 0.72 of in-phase current compensation).

Moreover, in the both methods the ratio of P/Q at the IFC output will influence the effectiveness of $|v^-|$ reduction. For the active power oscillation minimization, this is straightforward to understand as lower P/Q ratio makes this method performance closer to the in-phase current compensation (see Figure 3.4

and Figure 3.5), leading to more effective $|v^-|$ reduction as explained earlier (shown in TABLE 3.1 $|v^-|$ is $9.10V$ with $P/Q = 4$ and $8.26V$ with $P/Q = 1/4$).

For the in-phase current compensation, increasing P/Q ratio will cause more reduction of $|v^-|$ ($8.26V$ with $P/Q = 1/4$ to $6.23V$ with $P/Q = 4$ as shown in TABLE 3.1). The reason is that since i^- is in-phase with i^-_{Grid} (i^-_{Grid} and v^- are approximately orthogonal in the normal inductive grid), considering (3.3) the reactive power component of i^- will be much larger than the active power component $\left(\left|\frac{Q(1-k_2)}{|v^-|^2}\right| \gg \left|\frac{P(1-k_1)}{|v^-|^2}\right|\right)$ (see Figure 3.4 and Figure 3.5). In other words, k_1 is very close to 1. As a result, considering equivalent circuit in Figure 3.2, Z^-_R can be considered as an open circuit. Therefore, $|i^-|$ can be achieved as $|i^-| = \frac{|v^-|}{Z^-_X} = \frac{Q(1-k_2)}{|v^-|}$. Considering $|i^-|$ as a fixed value, increasing the value of Q will lead to $|v^-|$ enhancement.

3.3.2 Weak grid under various IFC's output P/Q ratios

In the weak grid, the ratio of X_{Grid}/R_{Grid} is small, and the grid has higher resistance. Here, in order to better explain the difference of the two proposed methods, the grid impedance with small X_{Grid}/R_{Grid} ratios ($X_{Grid} \ll R_{Grid}$) is studied. The conclusions can be extended to the weak grids with comparable X_{Grid} and R_{Grid}, which will be discussed in simulation section.

In the weak grid with small X_{Grid}/R_{Grid} ratio, the phase angle between negative sequence grid current and the negative sequence PCC voltage is small. In the ΔP-minimization strategy in large values of P/Q ratio ($P \gg Q$) at the IFC output with high power factor, the phase angle between v^- and i^- will be small according to (3.8). As a result, i^- and i^-_{Grid} will be approximately in-phase (small phase angle between i^- and i^-_{Grid}). This can be seen in phasor plots in Figure 3.4 and Figure 3.5. Therefore, the results of active power oscillation minimization strategy and in-phase current compensation are approximately the same in large P/Q ratios at IFC output. As shown in TABLE 3.1, the ratios of negative sequence voltage, and active and reactive powers oscillations in ΔP-minimization strategy over in-phase current compensation are 1.01, 0.98, and 1.005,

respectively. So if high power factor control of the IFC is required, the two methods will perform similarly under weak grid condition with small X_{Grid}/R_{Grid} ratios.

Similarly, the value of P/Q ratio at IFC output will affect the effectiveness of $|v^-|$ reduction in both methods under a weak grid. As explained earlier, increasing P/Q ratio will make the ΔP-minimization strategy performance closer to the in-phase current compensation in a weak grid condition (see Figure 3.4 and Figure 3.5), and therefore high P/Q ratio will be more effective for $|v^-|$ reduction under the active power oscillation minimization method. As shown in TABLE 3.1, $|v^-|$ is changed from $6.88V$ with $P/Q = 1/4$ to $6.25V$ with $P/Q = 4$.

For the in-phase current compensation, decreasing P/Q ratio at IFC output will cause more reduction of $|v^-|$ ($6.15V$ with $P/Q = 4$ to $4V$ with $P/Q = 1/4$ as shown in TABLE 3.1). The reason is that since i^- is in-phase with i^-_{Grid}, considering (3.3) the active power component of i^- will be much larger than the reactive power component $\left(\left|\frac{Q(1-k_2)}{|v^-|^2}\right| \ll \left|\frac{P(1-k_1)}{|v^-|^2}\right|\right)$ (see Figure 3.4 and Figure 3.5). In other words, k_2 is very close to 1. As a result, considering equivalent circuit in Figure 3.2, Z_X^- can be considered as an open circuit. Therefore, $|i^-|$ can be achieved as $|i^-| = \frac{|v^-|}{Z_R^-} = \frac{P(1-k_1)}{|v^-|}$. Considering $|i^-|$ as a fixed value, increasing the value of P will lead to $|v^-|$ enhancement.

3.4 Simulations and Experiments

In order to verify the effectiveness and performance of the two proposed control strategies, simulation and experimental results are provided.

3.4.1 Simulation verification

A three-phase grid-connected IFC has been simulated utilizing the two proposed control strategies in MATLAB/Simulink. The simulated system parameters are shown in TABLE 3.2.

TABLE 3.2 System parameters for simulations.

	Symbol	Value
DC link voltage	v_{dc}	$800V$
IFC's reference active power	P_{ref}	$20kW \rightarrow 5kW$
IFC's reference reactive power	Q_{ref}	$5kVAR \rightarrow 20kVAR$
Three phase unbalance load	R_{Load}	Three phase: $18\Omega, 5\Omega, 3\Omega$
Grid phase voltage (rms)	v_g	$240V$
Grid frequency	f_g	$60Hz$
Grid coupling impedance	Z_{Grid}	$X_{Grid}: 0.753\Omega \rightarrow 1m\Omega$ $R_{Grid}: 1m\Omega \rightarrow 0.753\Omega$

In these simulations, in order to investigate the performance of the two proposed methods under different grid conditions and IFC operating conditions, and to study the influence of IFC's size on the compensation strategies, the results for $\left|i^{-^*}\right| = 5A$ and $\left|i^{-^*}\right| = 10A$ under different IFC's output P/Q ratios and the grid X_{Grid}/R_{Grid} ratios are shown in TABLE 3.3 and TABLE 3.4. In all the

TABLE 3.3 Simulation results for two proposed control strategies with $|\bar{i}|$=5A under different IFC's output *P/Q* ratios and the grid conditions.

Grid impedance conditions		$X_{Grid} \gg R_{Grid}$ $R = 1 \times 10^{-3}\Omega;\ X = 0.753\Omega$			$X_{Grid} = R_{Grid}$ $R = 0.533\Omega;\ X = 0.533\Omega$			$X_{Grid} \ll R_{Grid}$ $R = 0.753\Omega;\ X = 1 \times 10^{-3}\Omega$		
IFC's output active-reactive powers		$20kW$ $5kVar$	$14.5kW$ $14.5kVar$	$5kW$ $20kVar$	$20kW$ $5kVar$	$14.5kW$ $14.5kVar$	$5kW$ $20kVar$	$20kW$ $5kVar$	$14.5kW$ $14.5kVar$	$5kW$ $20kVar$
$\lvert\bar{i}_{Grid}\rvert$	No compensation	18.12	20.00	20.82	17.70	18.10	17.40	17.08	16.13	14.24
	ΔP-minimization	15.75	15.87	15.90	13.50	13.51	13.46	12.74	12.66	12.48
	In-phase current	13.20	15.10	15.90	13.14	13.51	12.85	12.60	11.70	9.80
$\lvert\bar{i}_{Load}\rvert$	No compensation	18.12	20.00	20.82	17.74	18.15	17.45	17.08	16.13	14.24
	ΔP-minimization	17.68	19.78	20.85	17.79	18.51	17.94	17.60	16.60	14.50
	In-phase current	18.20	20.10	20.90	18.14	18.51	17.85	17.60	16.70	14.80
$\lvert v^- \rvert$	No compensation	13.66	15.08	15.70	13.35	13.64	13.13	12.88	12.16	10.74
	ΔP-minimization	11.88	11.97	11.99	10.18	10.19	10.15	9.59	9.54	9.41
	In-phase current	10.00	11.36	11.97	9.90	10.18	9.68	9.50	8.70	7.40
ΔP	No compensation	1368	1368	1368	1264	1264	1264	1228	1228	1228
	ΔP-minimization	351	619	734	668	723	630	705	568	280
	In-phase current	1624	1220	805	960	723	937	770	1100	1405
ΔQ	No compensation	1368	1368	1368	1264	1264	1264	1228	1228	1228
	ΔP-minimization	2738	2790	2815	2600	2613	2580	2540	2495	2425
	In-phase current	2028	2536	2795	2485	2613	2452	2516	2252	1762

TABLE 3.4 Simulation results for two proposed control strategies with $|\dot{i}^-|$=*10A* under different IFC's output *P/Q* ratios and the grid conditions.

Grid impedance conditions		$X_{Grid} \gg R_{Grid}$ $R = 1\times10^{-3}\Omega;\ X = 0.753\Omega$			$X_{Grid} = R_{Grid}$ $R = 0.533\Omega;\ X = 0.533\Omega$			$X_{Grid} \ll R_{Grid}$ $R = 0.753\Omega;\ X = 1\times10^{-3}\Omega$		
IFC's output active-reactive powers		$20kW$ $5kVar$	$14.5kW$ $14.5kVar$	$5kW$ $20kVar$	$20kW$ $5kVar$	$14.5kW$ $14.5kVar$	$5kW$ $20kVar$	$20kW$ $5kVar$	$14.5kW$ $14.5kVar$	$5kW$ $20kVar$
$\lvert i^-_{Grid}\rvert$	No compensation	18.12	20.00	20.82	17.70	18.10	17.40	17.08	16.13	14.24
	ΔP-minimization	12.07	11.28	10.96	9.04	8.93	9.09	8.30	8.50	9.10
	In-phase current	8.26	10.13	10.96	8.56	8.93	8.26	8.20	7.20	5.30
$\lvert i^-_{Load}\rvert$	No compensation	18.12	20.00	20.82	17.74	18.15	17.45	17.08	16.13	14.24
	ΔP-minimization	17.42	19.63	20.80	18.35	18.93	18.41	18.17	17.14	15.12
	In-phase current	18.26	20.13	20.95	18.56	18.93	18.26	18.20	17.20	15.30
$\lvert v^-\rvert$	No compensation	13.66	15.08	15.70	13.35	13.64	13.13	12.88	12.16	10.74
	ΔP-minimization	9.10	8.50	8.26	6.82	6.73	6.85	6.25	6.41	6.88
	In-phase current	6.23	7.64	8.26	6.45	6.73	6.22	6.15	5.44	4.00
ΔP	No compensation	1368	1368	1368	1264	1264	1264	1228	1228	1228
	ΔP-minimization	2177	2640	2835	2620	2707	2550	2643	2413	1921
	In-phase current	3005	2965	2862	2760	2710	2715	2673	2697	2626
ΔQ	No compensation	1368	1368	1368	1264	1264	1264	1228	1228	1228
	ΔP-minimization	4007	4183	4267	3917	3956	3866	3840	3710	3487
	In-phase current	3297	3927	4248	3803	3959	3738	3820	3473	2850

simulations, IFC's apparent power and the amplitude of grid impedance are considered to be constant $S = 20.61kVA$ and $|Z_{Grid}| = 0.75398\Omega$. For better comparison, the results of balance current injection from IFC without compensation ($k_1 = k_2 = 1$) are presented, too.

Considering the results in TABLE 3.3 and TABLE 3.4, the following conclusions can be achieved that verify the previous discussions in Sections 3.2 and 3.3:

- The i^-_{load} is approximately constant in the fixed $\left|i^{-^*}\right|$ and IFC's active-reactive powers. Negative sequence voltage at the PCC is reduced utilizing the two proposed control strategies in all IFC's operating conditions and the grid X_{Grid}/R_{Grid} ratios.
- The PCC negative sequence voltage in the in-phase current compensation is smaller than active power oscillation minimization strategy.

- The active power oscillation minimization provides the minimum active power oscillation in each operation point. However, reactive power oscillation in this method is larger than in-phase current compensation strategy.
- In the inductive grid if IFC works as a reactive power compensator ($P \ll Q$) or in the weak grid if IFC works with high power factor ($P \gg Q$), performance of two proposed control strategies are similar and the results of these strategies are close to each other.
- In the inductive grid if IFC works with high power factor ($P \gg Q$) or in the weak grid if IFC works as a reactive power compensator ($P \ll Q$), performance difference of the two methods will be very obvious in terms of

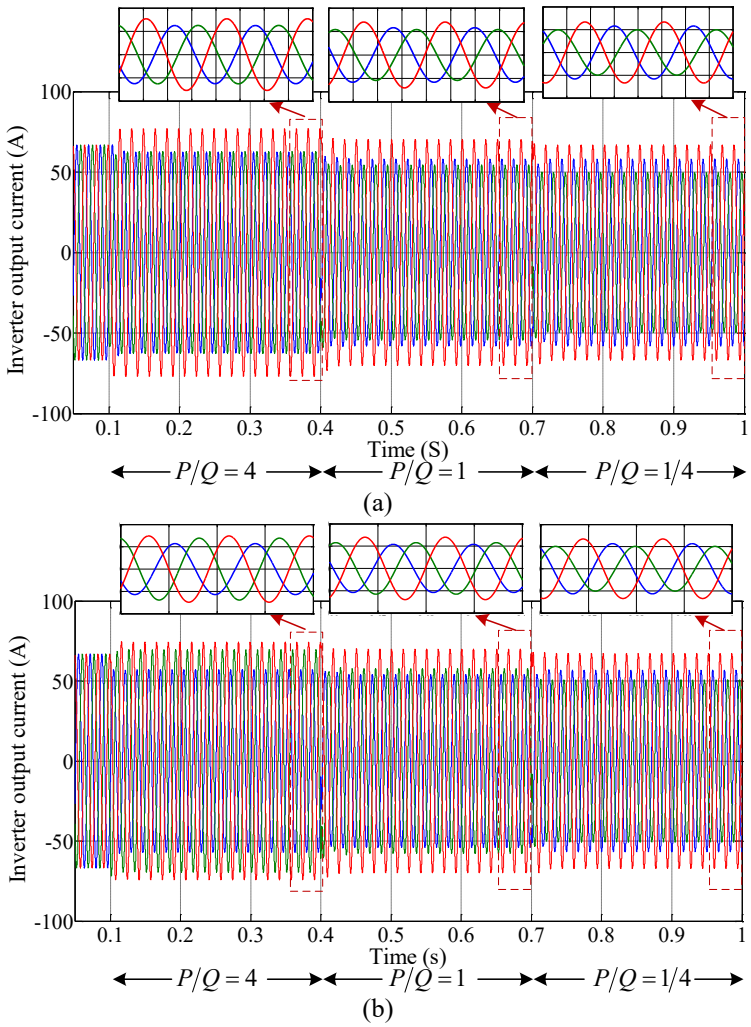

Figure 3.6 IFC output current in the inductive grid; (a) ΔP-minimization strategy, (b) in-phase current compensation strategy.

active power oscillation and the effectiveness of negative sequence voltage reduction.

- In the both proposed control strategies, increasing $|i^{-^*}|$ causes more reduction of $|i_{Grid}^{-}|$, resulting in more reduction of $|v^{-}|$**.** However, the active and reactive powers oscillations increase in both methods.
- With higher $|i^{-^*}|$, difference of two proposed strategies in terms of unbalanced voltage compensation is more obvious.

The waveforms of simulation results in the two proposed control strategies with $|i^{-^*}| = 10A$ (see TABLE 3.4) for inductive grid (with $X_{Grid} \gg R_{Grid}$) and weak grid (with $X_{Grid} \ll R_{Grid}$) are shown in Figure 3.6 to Figure 3.8 and Figure 3.9 to Figure 3.11, respectively. In these simulations during $t < 0.1$, the IFC

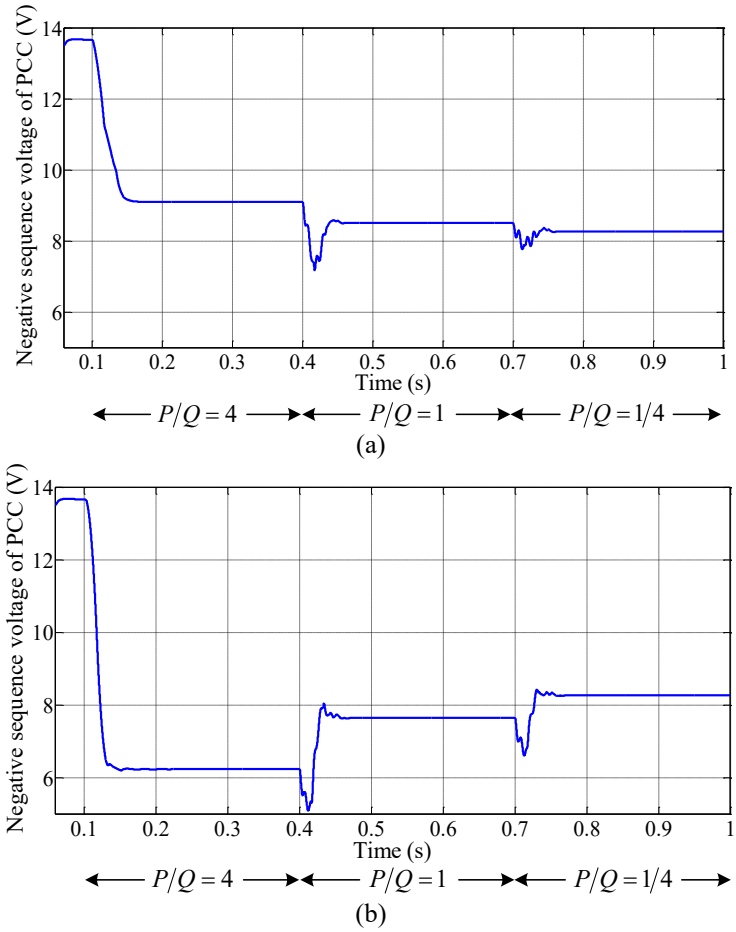

Figure 3.7 Negative sequence voltage of PCC in the inductive grid; (a) Δ*P*-minimization strategy, (b) in-phase current compensation strategy.

produces balance current ($k_1 = k_2 = 1$). At $t = 0.1$, the proposed control strategies are applied to the grid-connected IFC system. During $0.1 < t < 0.4$, the IFC's output active and reactive powers are $P_{ref} = 20kW, Q_{ref} = 5kVAR$ while during $0.4 < t < 0.7$ and $0.7 < t < 1$ these powers are set to $P_{ref} = 14.5kW, Q_{ref} = 14.5kVAR$ and $P_{ref} = 5kW, Q_{ref} = 20kVAR$, respectively.

Figure 3.6 shows the output current of IFC in the inductive grid. The phasor diagrams of the IFC output current are shown in Figure 3.4. Figure 3.7 shows the negative sequence voltage of PCC in the inductive grid. From this figure, it can be observed that the PCC negative sequence voltage is reduced in all IFC's operating conditions, and the reduction level in the in-phase current compensation strategy is more than active power oscillation minimization strategy. Active power oscillations at the IFC output is shown in Figure 3.8, which proves that the active

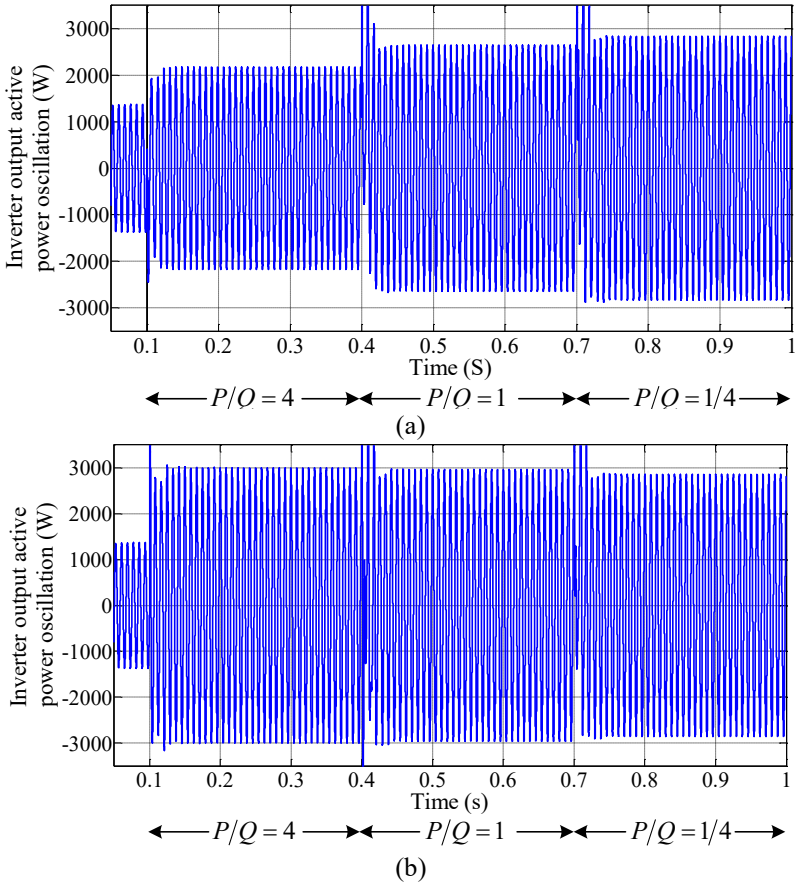

Figure 3.8 Active power oscillations at the IFC output in the inductive grid; (a) Δ*P*-minimization strategy, (b) in-phase current compensation strategy.

power oscillation minimization strategy leads to smaller active power oscillation in all operating conditions. However, the reduction is more obvious at high power factor operation conditions.

In Figure 3.9, IFC's output current in the resistive grid is shown, and its phasor diagrams are shown in Figure 3.5. From negative sequence voltage of PCC shown in Figure 3.10, it can be observed that although both control strategies reduce the negative sequence voltage, the reduction level of in-phase current compensation strategy is more than active power oscillation minimization strategy, which is more obvious at reactive power compensation operating condition. Similar to inductive grid, the active power oscillation minimization

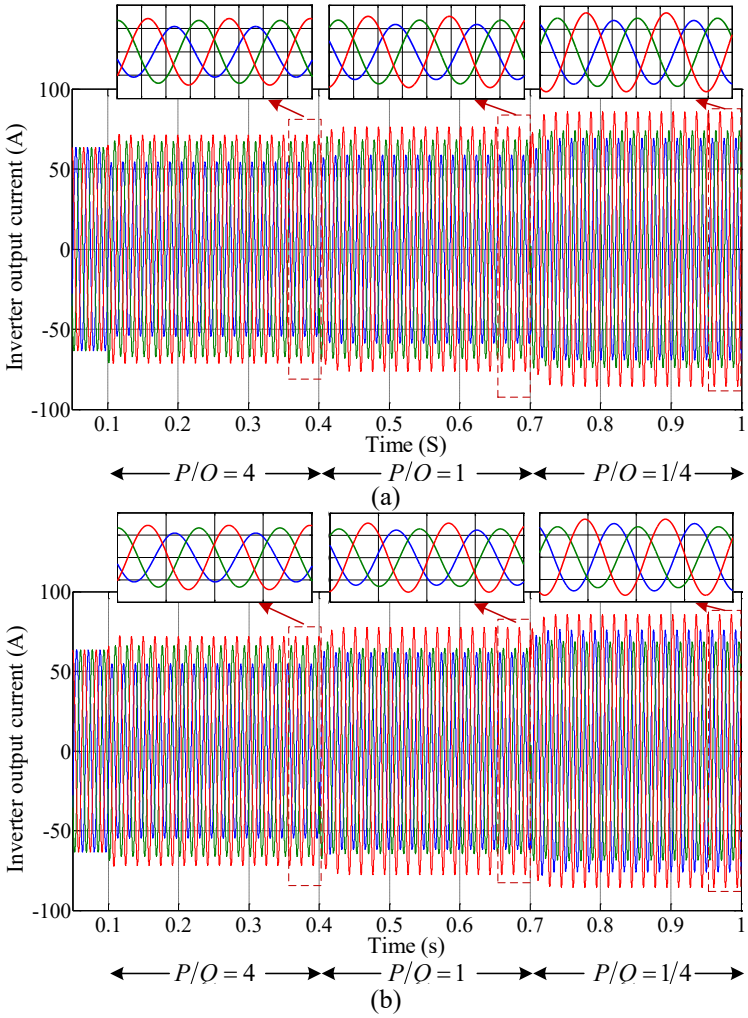

Figure 3.9 IFC output current in the weak resistive grid; (a) Δ*P*-minimization strategy, (b) in-phase current compensation strategy.

strategy minimizes the IFC output power oscillation in all operating conditions, shown in Figure 3.11.

3.4.2 Experimental verification

To verify the effectiveness of the two proposed control strategies, experiments are also conducted on a three-phase grid-connected IFC prototype. The experimental set-up parameters are shown in TABLE 3.5 and the system is controlled by dSPACE 1103. The two proposed control strategies are tested under two grid conditions: (1) inductive grid ($X_{Grid} = 1.88\Omega$ and $R_{Grid} = 0.2\Omega$) with $|i^{-^*}| = 2.5A$, and (2) weak resistive grid ($X_{Grid} = 0.94\Omega$ and $R_{Grid} = 1.9\Omega$) with $|i^{-^*}| = 1.5A$. In each test, IFC works with high power factor (large P/Q ratio; $P_{ref} = 280W, Q_{ref} = 70VAR$) and as a reactive power compensator (small P/Q

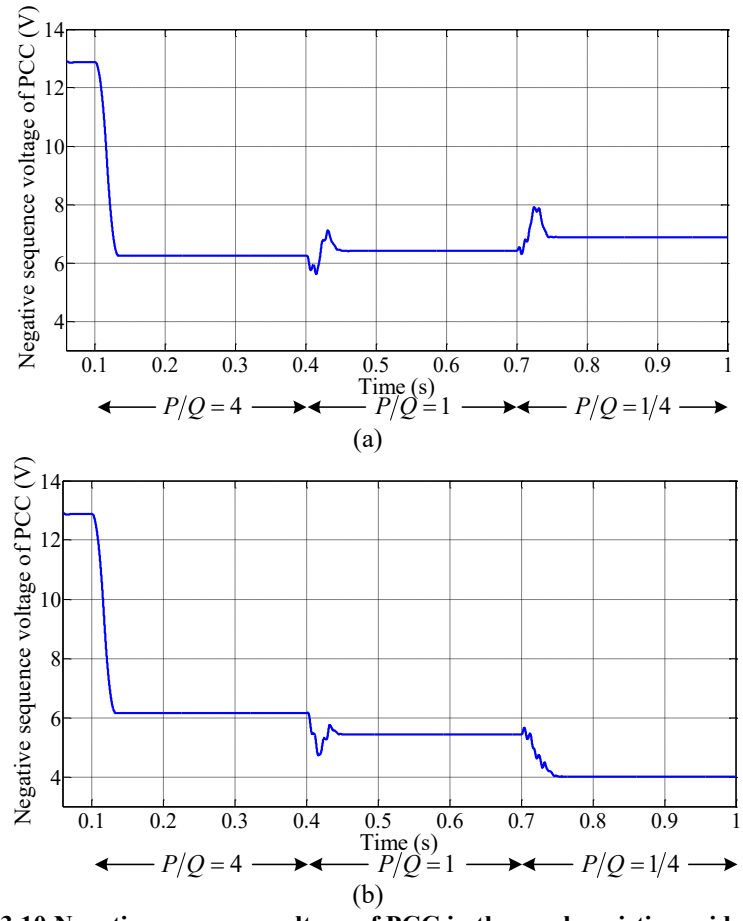

Figure 3.10 Negative sequence voltage of PCC in the weak resistive grid; (a) ΔP-minimization strategy, (b) in-phase current compensation strategy.

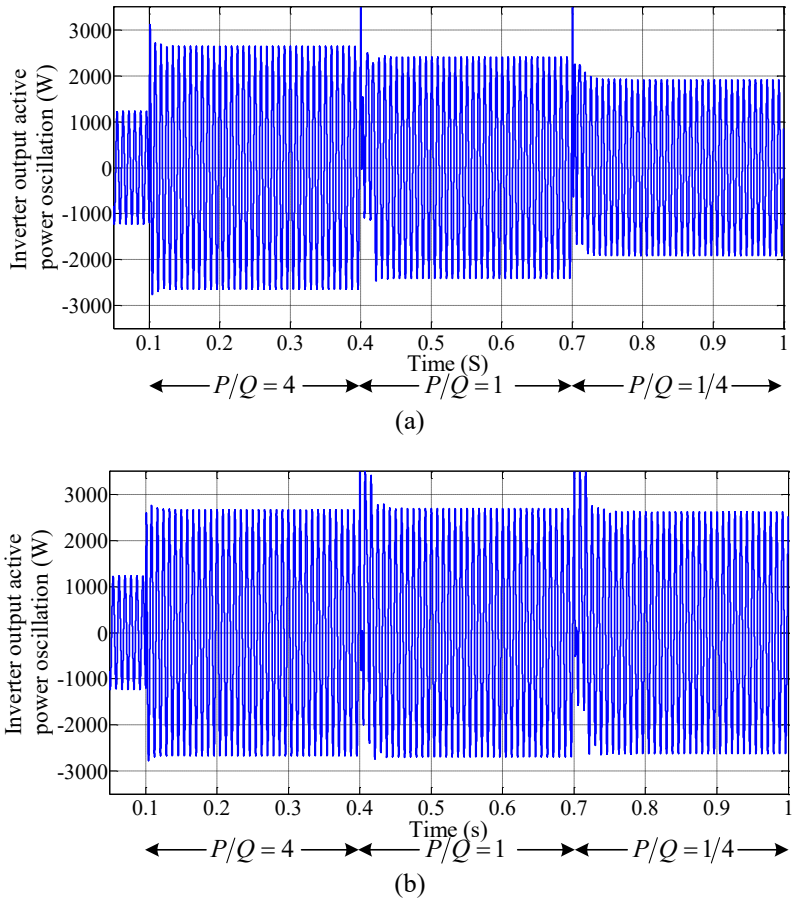

Figure 3.11 Active power oscillations at the IFC output in the weak resistive grid; (a) ΔP-minimization strategy, (b) in-phase current compensation strategy.

ratio; $P_{ref} = 70W, Q_{ref} = 280VAR$). To start the tests, k_1 and k_2 are set to 1, where IFC produces balance three-phase current without compensation. Then, the proposed control strategy is applied. The results are shown in Figure 3.12 to Figure 3.15.

In Figure 3.12 and Figure 3.13, the negative sequence voltage of PCC and IFC's output active power oscillations in the inductive grid are shown, respectively. The experimental results for negative sequence voltage of PCC and the active power oscillations of IFC in the resistive grid are shown in Figure 3.14 and Figure 3.15, respectively. Similar to inductive grid, in this test the control strategy is switched from balance IFC current injection without compensation strategy to the proposed control strategies. The experimental tests results are summarized in TABLE 3.6

TABLE 3.5 System parameters for experiments.

	Symbol	Value
DC link voltage	v_{dc}	$150V$
Reference active power	P_{ref}	$280W \rightarrow 70W$
Reference reactive power	Q_{ref}	$70VAR \rightarrow 280VAR$
Three phase unbalance load	R_{Load}	Three phase: $9\Omega, 5\Omega, 3\Omega$
Grid phase voltage (rms) and frequency	$v_g - f_g$	$50V$-$60Hz$
Grid impedance	Z_{Grid}	X_{Grid}: $1.88\Omega \rightarrow 0.94\Omega$ R_{Grid}: $0.2\Omega \rightarrow 1.9\Omega$

Considering the experimental results and TABLE 3.6, it can be observed that utilizing the two proposed methods results in the grid unbalanced voltage compensation in which the compensation level of the in-phase current compensation strategy is higher than active power oscillation minimization strategy. Moreover, the active power oscillation minimization strategy minimizes the IFC's output active power oscillation in each operation point. Similar to simulation results, the two proposed control strategies have the similar

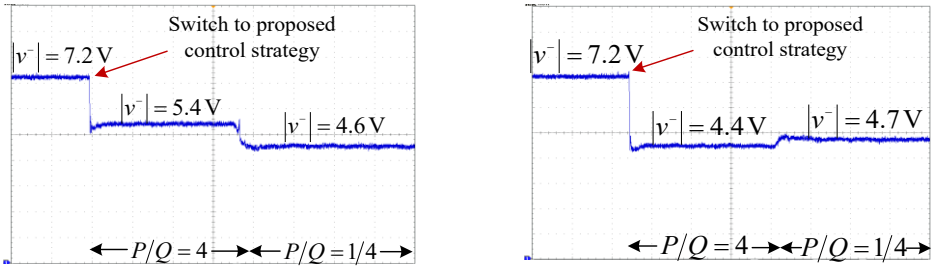

Figure 3.12 Negative sequence voltage of PCC in the inductive grid; (a) ΔP-minimization strategy, (b) in-phase current compensation strategy (time: 1 s/div, voltage: 1 V/div).

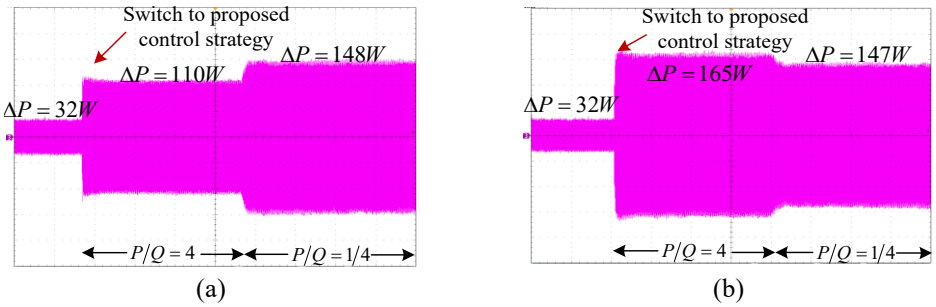

Figure 3.13 Active power oscillations in the inductive grid; (a) ΔP-minimization strategy, (b) in-phase current compensation strategy (time: 1 s/div, power: 50 W/div).

TABLE 3.6 Summary of experimental results for the two proposed control strategies.

Grid impedance conditions		Inductive grid $R = 0.2\Omega;\ X = 1.88\Omega$		Resistive grid $R = 1.9\Omega;\ X = 0.94\Omega$	
IFC's output active-reactive powers		$280W$ $70Var$	$70W$ $280Var$	$280W$ $70Var$	$70W$ $280Var$
$\lvert v^- \rvert$	ΔP-minimization	5.4	4.6	4	4.4
	In-phase current	4.4	4.7	4	3.4
	$\frac{\Delta P-\text{minimization}}{\text{In-phase current}}$ ratio	1.22	0.98	1	1.29
ΔP	ΔP-minimization	110	148	75	62
	In-phase current	165	147	76	100
	$\frac{\Delta P-\text{minimization}}{\text{In-phase current}}$ ratio	0.66	1.00	0.99	0.62

performance under inductive grid and IFC works as a reactive power compensator ($P \ll Q$), or weak grid and IFC works with high power factor ($P \gg Q$).

Considering aforementioned explanation, experimental results under different grid conditions and IFC's output active-reactive powers verify the simulation results and discussions about control strategies and their performance.

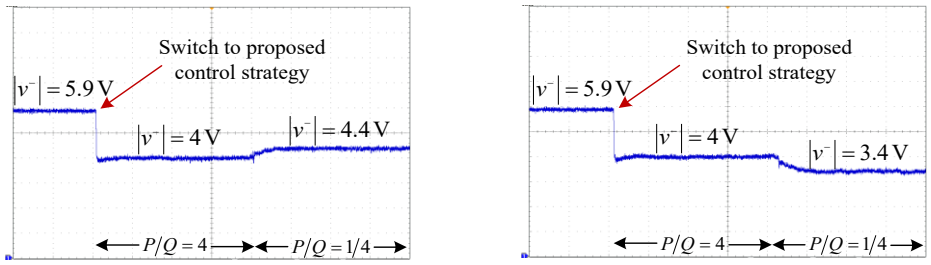

Figure 3.14 Negative sequence voltage of PCC in the weak resistive grid; (a) ΔP-minimization strategy, (b) in-phase current compensation strategy (time: 1 s/div, voltage: 1 V/div).

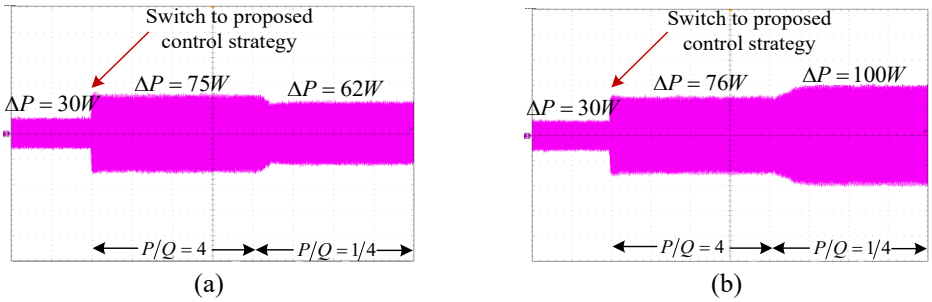

Figure 3.15 Active power oscillations in the weak resistive grid; (a) ΔP-minimization strategy, (b) in-phase current compensation strategy (time: 1 s/div, power: 50 W/div).

TABLE 3.7 Control strategy recommendation under different grid conditions and IFC operating conditions.

Grid impedance conditions		Large X_{Grid}/R_{Grid} ratios		$X_{Grid}/R_{Grid} \approx 1$		Small X_{Grid}/R_{Grid} ratios	
IFC's output powers		$P \gg Q$	$P \ll Q$	$P \gg Q$	$P \ll Q$	$P \gg Q$	$P \ll Q$
ΔP		$\Delta P_{\Delta P-min} < \Delta P_{in-phase}$	$\Delta P_{\Delta P-min} \approx \Delta P_{in-phase}$	$\Delta P_{\Delta P-min} \approx \Delta P_{in-phase}$	$\Delta P_{\Delta P-min} \approx \Delta P_{in-phase}$	$\Delta P_{\Delta P-min} \approx \Delta P_{in-phase}$	$\Delta P_{\Delta P-min} < \Delta P_{in-phase}$
ΔQ		$\Delta Q_{\Delta P-min} > \Delta Q_{in-phase}$	$\Delta Q_{\Delta P-min} \approx \Delta Q_{in-phase}$	$\Delta Q_{\Delta P-min} \approx \Delta Q_{in-phase}$	$\Delta Q_{\Delta P-min} \approx \Delta Q_{in-phase}$	$\Delta Q_{\Delta P-min} \approx \Delta Q_{in-phase}$	$\Delta Q_{\Delta P-min} > \Delta Q_{in-phase}$
$\lvert v^- \rvert$		$\lvert v^- \rvert_{\Delta P-min} > \lvert v^- \rvert_{in-phase}$	$\lvert v^- \rvert_{\Delta P-min} \approx \lvert v^- \rvert_{in-phase}$	$\lvert v^- \rvert_{\Delta P-min} \approx \lvert v^- \rvert_{in-phase}$	$\lvert v^- \rvert_{\Delta P-min} \approx \lvert v^- \rvert_{in-phase}$	$\lvert v^- \rvert_{\Delta P-min} \approx \lvert v^- \rvert_{in-phase}$	$\lvert v^- \rvert_{\Delta P-min} > \lvert v^- \rvert_{in-phase}$
$\lvert \bar{i_{Grid}} \rvert$		$\lvert \bar{i_{Grid}} \rvert_{\Delta P-min} > \lvert \bar{i_{Grid}} \rvert_{in-phase}$	$\lvert \bar{i_{Grid}} \rvert_{\Delta P-min} \approx \lvert \bar{i_{Grid}} \rvert_{in-phase}$	$\lvert \bar{i_{Grid}} \rvert_{\Delta P-min} \approx \lvert \bar{i_{Grid}} \rvert_{in-phase}$	$\lvert \bar{i_{Grid}} \rvert_{\Delta P-min} \approx \lvert \bar{i_{Grid}} \rvert_{in-phase}$	$\lvert \bar{i_{Grid}} \rvert_{\Delta P-min} \approx \lvert \bar{i_{Grid}} \rvert_{in-phase}$	$\lvert \bar{i_{Grid}} \rvert_{\Delta P-min} > \lvert \bar{i_{Grid}} \rvert_{in-phase}$
Control Strategy Recom.	ΔP is small	ΔP-minimization	Both methods	Both methods	Both methods	Both methods	ΔP-minimization
	ΔQ is small	In-phase current	Both methods	Both methods	Both methods	Both methods	In-phase current
	$\lvert v^- \rvert$ is small	In-phase current	Both methods	Both methods	Both methods	Both methods	In-phase current

3.5 Summary and Recommendations

In TABLE 3.7, the previous discussions and comparisons are summarized, and appropriate control strategy under different grid conditions in terms of X_{Grid}/R_{Grid} ratio and different IFC's operating conditions in terms of P/Q ratio is recommended.

Considering TABLE 3.7, performance of the two proposed control strategies are similar to each other under three conditions: (1) in the normal inductive grid with large X_{Grid}/R_{Grid} ratios and IFC works as a reactive power compensator, (2) in the weak grid with $X_{Grid}/R_{Grid} \approx 1$ and IFC works in different output active-reactive power ratios, or (3) in the weak grid with small X_{Grid}/R_{Grid} ratios and IFC works with high power factor. On the other hands, performance of the two methods are very different under the conditions of (1) normal inductive grid with large X_{Grid}/R_{Grid} ratios and IFC works with high power factor, or (2) weak grid with small X_{Grid}/R_{Grid} ratios and IFC works as a reactive power compensator. In this case, active power oscillation minimization or in-phase current compensation method can be selected according to the objectives on power oscillation or PCC negative sequence voltage reduction.

Considering the size and capacity difference of IFCs, different methods can be recommended also. In small IFCs, due to low IFC negative sequence current

$|i^-|$, the difference of two proposed control strategies in terms of $|v^-|$ reduction will not be very obvious. However, the active power oscillation minimization strategy provides minimum active power oscillation in each operation points. As a result in small IFC, if $|v^-|$ reduction is not the desired control parameter, active power oscillation minimization strategy is recommended.

In large IFCs, due to possibility of high IFC negative sequence current $|i^-|$, $|v^-|$ can be obviously changed, and difference of the two proposed method in terms of $|v^-|$ reduction will be more obvious. However, these two methods difference in terms of ΔP reduction may not be more obvious in comparison to small IFC (as high $|i^-|$ tends to increase ΔP but low $|v^-|$ tends to decrease ΔP). As a result in large IFC, in-phase current compensation strategy is recommended.

Finally, when multiple IFCs participate in the unbalanced voltage compensation, active power oscillation minimization strategy may result in different IFCs acting as virtual negative sequence impedances with different phase angles according to their active and reactive powers output. This will lead to negative sequence current circulation in the active power oscillation minimization strategy. However, the in-phase current compensation method will guarantee that all IFCs behave as negative sequence impedances with the same phase angle as the grid, resulting in zero negative sequence circulation current among IFCs. Therefore, the in-phase current compensation would be a good choice.

3.6 Conclusion

In this chapter, two control strategies for single three-phase interfacing convector were proposed in order to compensate for the steady-state unbalanced voltage in hybrid AC-DC microgrids. In the first method, in order to reduce the adverse effects of compensation on the IFCs' operation, the IFC's active power oscillation was minimized in the compensation strategy. In the second method, in order to effectively reduce the negative sequence voltage of the grid, the IFC's negative sequence current was set to be in-phase with the grid negative sequence current. Both methods are based on the IFC's equivalent negative sequence virtual

impedance amplitude and phase angle control. The analysis in the chapter showed that the two methods had a similar performance under (1) a normal inductive grid with large X_{Grid}/R_{Grid} ratios and the IFC operating as a reactive power compensator ($P \ll Q$), (2) a weak grid with $X_{Grid}/R_{Grid} \approx 1$ and the IFC operating in different output active-reactive power ratios, or (3) a weak grid with small X_{Grid}/R_{Grid} ratios and the IFC operating with a high power factor ($P \gg Q$). However, the performance of the two methods in terms of power oscillations and the PCC negative sequence voltage reduction obviously differed under (1) the normal inductive grid with large X_{Grid}/R_{Grid} ratios and the IFC controlled with a high power factor, or (2) the weak grid with small X_{Grid}/R_{Grid} ratios and the IFC worked as a reactive power compensator. Recommendations for selecting different methods under various conditions were presented in the chapter. The validity and effectiveness of the two proposed control strategies was verified by simulations and experimental tests.

Chapter 4

Parallel Three-Phase Interfacing Converters Control under Unbalanced Voltage in Hybrid AC/DC Microgrids: Active Power Oscillation Cancellation using Redundant Interfacing Converter[1]

In hybrid AC/DC microgrids, parallel three-phase interfacing converters (IFCs) with the same DC link are commonly used to handle higher power and currents. These converters are used to connect an AC and DC subsystems or to connect DGs/SEs to AC subsystem. Since the unbalanced voltage adverse effects on parallel IFCs' operation can be amplified by the number of IFCs due to the interactions, a coordinate control strategy to prevent those adverse effects is essential. In this chapter, a novel control strategy for parallel IFCs' operation under unbalanced voltage in hybrid AC/DC microgrids is proposed. In the proposed strategy, one IFC identified as redundant is controlled to cancel out the collective active power oscillations of the other IFCs, and results in DC link/subsystem voltage ripple cancellation. This method could improve the power quality in both AC and DC subsystems. Also, the control strategy provides unbalanced voltage compensation, but without an adjustable level of

[1] Publications out of this Chapter:

- F. Nejabatkhah, Y. W. Li, and K. Sun, "Parallel Three-Phase Interfacing Converters Operation under Unbalanced Voltage in Hybrid AC/DC Microgrid", *IEEE Transactions on Smart Grid, in press, 2017*.
- K. Sun, X. Wang, Y. W. Li, F. Nejabatkhah, Y. Mei, and X. Lu, "Parallel Operation of Bi-directional Interfacing Converters in a Hybrid AC/DC Microgrid under Unbalanced Grid Voltage Conditions", *IEEE Transactions on Power Electronics, vol. 32, no. 3, pp. 1872-1884, Mar. 2017*.

compensation. In this control strategy, the reason for using the redundant IFC is that all IFCs want to operate under zero active power oscillations, but they may exceed their rating currents due to unbalanced voltage. The redundant converter cancels out the oscillations resulting from the peak current control of the other IFCs. In the proposed control strategy, an instantaneous power analysis from a three-phase system perspective, which is presented in Section 2.2.2 of Chapter 2, is used. In Chapter 4, a thorough study of the peak current of individual and parallel IFCs is conducted, and their relationship with active power oscillation mitigation is analyzed. The analysis shows that under zero active power oscillation, the collective peak current of parallel IFCs is a constant under fixed average active and reactive powers. The proposed control strategy keeps the individual IFCs' peak currents in the same phase as that of the collective peak current of the parallel IFCs, and thus ensures a reduced peak current for the redundant IFC.

4.1 Parallel Three-Phase IFCs Instantaneous Power Analysis

4.1.1 Parallel interfacing converters

Figure 4.1 shows n-parallel three-phase IFCs with common DC and AC links. The IFCs are connected to the point of common coupling (PCC) with output

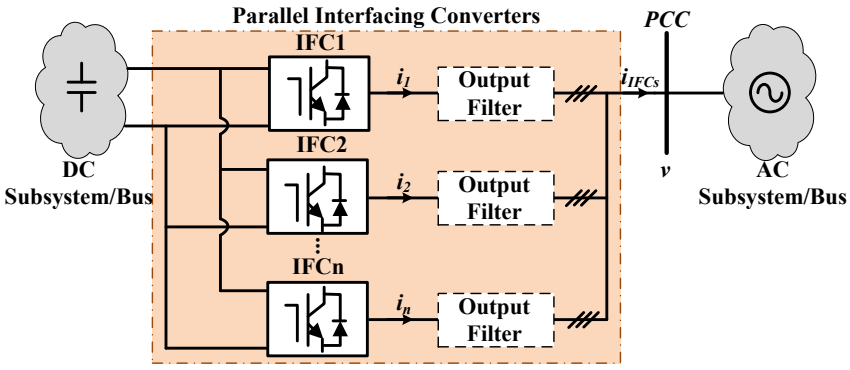

Figure 4.1 Parallel interfacing converters with common DC and AC links.

filters. These parallel IFCs can be interlinking path between AC and DC-subsystems in DC-coupled or AC-DC-coupled hybrid microgrids, or interfacing converters of DGs/SEs connected to the AC subsystem in AC-coupled or AC-DC-coupled hybrid microgrids.

In this Chapter, since control of adverse effects of unbalanced voltage on parallel IFCs operation is desired, the calculated reference current in Section 2.2.2 of Chapter 2 is used to easily control/cancel out the three-phase IFCs powers oscillation under unbalanced condition. The calculated reference current for individual three-phase IFC, which has been presented in (2.21), is provided in following again:

$$\begin{aligned} i_i^* = i_{pi}^* + i_{qi}^* = &\left(\frac{P_i}{|v^+|^2 + k_{pi}|v^-|^2} v^+ + \frac{P_i k_{pi}}{|v^+|^2 + k_{pi}|v^-|^2}\, v^-\right) \\ &+ \left(\frac{Q_i}{|v^+|^2 + k_{qi}|v^-|^2} v_\perp^+ + \frac{Q_i k_{qi}}{|v^+|^2 + k_{qi}|v^-|^2}\, v_\perp^-\right) \end{aligned} \tag{4.1}$$

In this Chapter, different from Section 2.2.2, the IFCs output voltage is represented by v, the i^{th}-IFC's output current and the average active and reactive powers are represented by i_i, P_i, and Q_i. Moreover, parallel IFCs collective current vector is represented by i_{IFCs}. These parameters are shown in Figure 4.1. From (4.1), and considering (2.3) and (2.4), the i^{th}-IFC's instantaneous output active and reactive powers can be achieved as:

$$p_i = P_i + \underbrace{\frac{P_i(1+k_{pi})(v^+.v^-)}{|v^+|^2 + k_{pi}|v^-|^2}}_{\Delta P_{pi}} + \underbrace{\frac{Q_i(1-k_{qi})(v_\perp^+.v^-)}{|v^+|^2 + k_{qi}|v^-|^2}}_{\Delta P_{qi}} \tag{4.2}$$

$$q_i = Q_i + \underbrace{\frac{P_i(1-k_{pi})(v^+.v_\perp^-)}{|v^+|^2 + k_{pi}|v^-|^2}}_{\Delta Q_{pi}} + \underbrace{\frac{Q_i(1+k_{qi})(v_\perp^+.v_\perp^-)}{|v^+|^2 + k_{qi}|v^-|^2}}_{\Delta Q_{qi}} \tag{4.3}$$

From (4.1)-(4.3), it can be concluded that under unbalanced voltage, i^{th}-IFC's current will increase and the output active and reactive powers will oscillate. The IFC's output current will be balanced under $k_p = k_q = 0$. Moreover, the two components of active power oscillations (ΔP_{pi} and ΔP_{qi}) are orthogonal, and

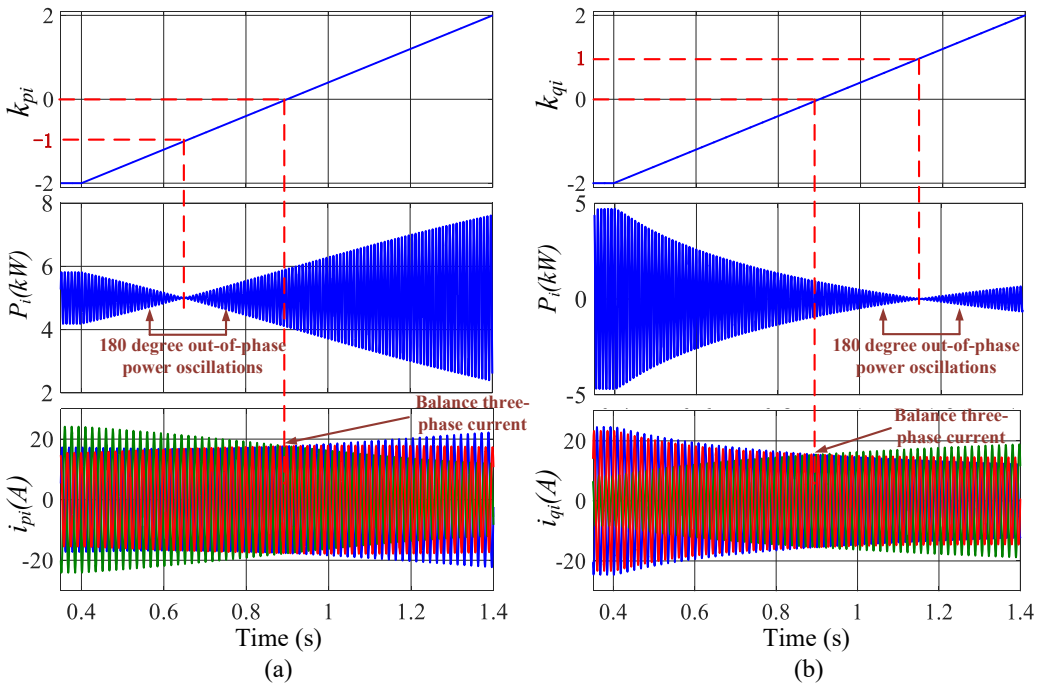

Figure 4.2 Individual IFC's output active power and three-phase currents under unbalanced voltage condition a) different k_{pi} in unity PF operation mode and b) different k_{qi} in zero PF operation mode.

$k_{pi} = -1$ and $k_{qi} = 1$ result in zero active power oscillations. It is worth mentioning that aforementioned operating points are independent from average active and reactive powers flow directions. As an example, in Figure 4.2, a typical individual IFC's output active power and three-phase currents under different k_{pi} and k_{qi} in unity PF and zero PF operations are shown, which verify the aforementioned discussions.

Using individual IFC's relations in (4.1)-(4.3), the reference current vector and instantaneous active and reactive powers of n-parallel IFCs in Figure 4.1 can be achieved as follows:

$$i_{IFCs}^{*} = \sum_{i=1}^{n} i_i^{*} = \sum_{i=1}^{n} \frac{P_i}{|v^+|^2 + k_{p_i}|v^-|^2} v^+ + \sum_{i=1}^{n} \frac{P_i k_{p_i}}{|v^+|^2 + k_{p_i}|v^-|^2} v^- + \sum_{i=1}^{n} \frac{Q_i}{|v^+|^2 + k_{q_i}|v^-|^2} v_{\perp}^{+} + \sum_{i=1}^{n} \frac{Q_i k_{q_i}}{|v^+|^2 + k_{q_i}|v^-|^2} v_{\perp}^{-} \quad (4.4)$$

$$p = \sum_{i=1}^{n} P_i + \underbrace{\sum_{i=1}^{n} \frac{P_i\left(1+k_{p_i}\right)(v^+.v^-)}{|v^+|^2+k_{p_i}|v^-|^2}}_{\Delta P_p} + \underbrace{\sum_{i=1}^{n} \frac{Q_i\left(1-k_{q_i}\right)(v_\perp^+.v^-)}{|v^+|^2+k_{q_i}|v^-|^2}}_{\Delta P_q} \tag{4.5}$$

$$q = \sum_{i=1}^{n} Q_i + \underbrace{\sum_{i=1}^{n} \frac{P_i\left(1-k_{p_i}\right)(v^+.v_\perp^-)}{|v^+|^2+k_{p_i}|v^-|^2}}_{\Delta Q_p} + \underbrace{\sum_{i=1}^{n} \frac{Q_i\left(1+k_{q_i}\right)(v_\perp^+.v_\perp^-)}{|v^+|^2+k_{q_i}|v^-|^2}}_{\Delta Q_q} \tag{4.6}$$

4.1.2 Active power oscillation cancellation constraints in parallel IFCs

From (4.5) in order to cancel out the collective active power oscillations of n-parallel IFCs in proposed control strategy, the following constraint should be satisfied:

$$\begin{aligned} &\sum_{i=1}^{n} \Delta P_{p_i} = \sum_{i=1}^{n} \frac{P_i\left(1+k_{p_i}\right)(v^+.v^-)}{|v^+|^2+k_{p_i}|v^-|^2} = 0 \\ &\Rightarrow \sum_{i=1}^{n} \frac{P_i}{|v^+|^2+k_{p_i}|v^-|^2} = \frac{\sum_{i=1}^{n} P_i}{|v^+|^2-|v^-|^2} \end{aligned} \tag{4.7}$$

$$\begin{aligned} &\sum_{i=1}^{n} \Delta P_{q_i} = \sum_{i=1}^{n} \frac{Q_i\left(1-k_{q_i}\right)(v_\perp^+.v^-)}{|v^+|^2+k_{q_i}|v^-|^2} = 0 \\ &\Rightarrow \sum_{i=1}^{n} \frac{Q_i}{|v^+|^2+k_{q_i}|v^-|^2} = \frac{\sum_{i=1}^{n} Q_i}{|v^+|^2+|v^-|^2} \end{aligned} \tag{4.8}$$

Considering (4.4)-(4.6) and (4.7)-(4.8), the reference current vector, and instantaneous active-reactive powers of n-parallel IFCs under zero active power oscillations are obtained as:

$$\begin{aligned} i_{IFCs}^*|_{\Delta P=0} = &\frac{\sum_{i=1}^{n} P_i}{|v^+|^2-|v^-|^2} v^+ + \frac{-\sum_{i=1}^{n} P_i}{|v^+|^2-|v^-|^2} v^- + \frac{\sum_{i=1}^{n} Q_i}{|v^+|^2+|v^-|^2} v_\perp^+ \\ &+ \frac{\sum_{i=1}^{n} Q_i}{|v^+|^2+|v^-|^2} v_\perp^- \end{aligned} \tag{4.9}$$

$$p = \sum_{i=1}^{n} P_i \tag{4.10}$$

$$q = \sum_{i=1}^{n} Q_i + \frac{2(v^+ . v_\perp^-)}{|v^+|^2 - |v^-|^2} \sum_{i=1}^{n} P_i + \frac{2(v_\perp^+ . v_\perp^-)}{|v^+|^2 + |v^-|^2} \sum_{i=1}^{n} Q_i \tag{4.11}$$

From (4.9), it is observed that under zero active power oscillations, the current is independent from k_{pi} and k_{qi}, and is affected by $\sum_{i=1}^{n} P_i$ and $\sum_{i=1}^{n} Q_i$ variations. Moreover, from (4.11) it can be concluded that the reactive power oscillations are independent from k_{pi} and k_{qi} under $\Delta P = 0$.

4.2 Three-Phase IFCs' Peak Currents under Unbalanced Voltage

Under unbalanced voltage, individual IFCs' peak currents should be controlled not to exceed their rating limits. Moreover, relation between parallel IFCs' active power oscillation and the IFCs' peak currents should be studied to analyze the influence of active power oscillation cancellation on IFCs' peak currents. As will be shown in parallel IFCs under zero active power oscillations, the collective peak current is constant in the fixed average active-reactive powers.

4.2.1 Individual interfacing converter

From (4.1), i^{th}-IFC's active and reactive reference current vectors can be rewritten as follows:

$$i_{pi}^* = i_{pi}^+ + i_{pi}^- = \frac{P_i}{|v^+|^2 + k_{pi}|v^-|^2} v^+ + \frac{P_i k_{pi}}{|v^+|^2 + k_{pi}|v^-|^2} v^- \tag{4.12}$$

$$i_{qi}^* = i_{qi}^+ + i_{qi}^- = \frac{Q_i}{|v^+|^2 + k_{qi}|v^-|^2} v_\perp^+ + \frac{Q_i k_{qi}}{|v^+|^2 + k_{qi}|v^-|^2} v_\perp^- \tag{4.13}$$

where $v^+ = |v^+| e^{j(\omega t + \theta^+)}$ and $v^- = |v^-| e^{j(-\omega t - \theta^-)}$. Considering (4.12) and (4.13), the loci of i^{th}-IFC's active and reactive reference current vectors are ellipses in which their semi major and semi minor axis' lengths can be achieved as:

$$I_{pLi} = \frac{P_i |v^+|}{|v^+|^2 + k_{pi}|v^-|^2} + \frac{P_i k_{pi} |v^-|}{|v^+|^2 + k_{pi}|v^-|^2} \tag{4.14}$$

$$I_{pSi} = \frac{P_i|v^+|}{|v^+|^2 + k_{pi}|v^-|^2} - \frac{P_i k_{pi}|v^-|}{|v^+|^2 + k_{pi}|v^-|^2} \tag{4.15}$$

$$I_{qLi} = \frac{Q_i|v^+|}{|v^+|^2 + k_{qi}|v^-|^2} + \frac{Q_i k_{qi}|v^-|}{|v^+|^2 + k_{qi}|v^-|^2} \tag{4.16}$$

$$I_{qSi} = \frac{Q_i|v^+|}{|v^+|^2 + k_{qi}|v^-|^2} - \frac{Q_i k_{qi}|v^-|}{|v^+|^2 + k_{qi}|v^-|^2} \tag{4.17}$$

The maximum current at each phase of i^{th}-IFC is the maximum projection of the current ellipse on the abc axis [45]. From (4.12)-(4.17), the projection of current ellipse on the abc axis can be derived as:

$$\begin{aligned} i_{xi}^{*\prime} = &\left(I_{pLi}\cos\gamma - I_{qLi}\sin\gamma\right)\cos(\omega t) + \left(-I_{qSi}\cos\gamma \right. \\ &\left. - I_{pSi}\sin\gamma\right)\sin(\omega t) \quad x = a,b,c \end{aligned} \tag{4.18}$$

where γ is rotation angle which is equal to ρ, $\rho + \pi/3$ and $\rho - \pi/3$ for *abc* axis, respectively where ρ is defined as $\rho = (\theta^+ - \theta^-)/2$. Using (4.14)-(4.18), the maximum current at each phase of i^{th}-IFC can be expressed as:

$$I_{xi}^{max} = \sqrt{\begin{aligned} &\frac{{P_i}^2}{\left(|v^+|^2 + k_{pi}|v^-|^2\right)^2}\left(|v^+|^2 + |v^-|^2 k_{pi}^2 + 2|v^+||v^-|k_{pi}\cos(2\gamma)\right) + \\ &\frac{{Q_i}^2}{\left(|v^+|^2 + k_{qi}|v^-|^2\right)^2}\left(|v^+|^2 + |v^-|^2 k_{qi}^2 - 2|v^+||v^-|k_{qi}\cos(2\gamma)\right) - \\ &\frac{2P_iQ_i|v^+||v^-|}{\left(|v^+|^2 + k_{pi}|v^-|^2\right)\left(|v^+|^2 + k_{qi}|v^-|^2\right)}\left(k_{pi} + k_{qi}\right)\sin(2\gamma) \end{aligned}} \tag{4.19}$$

x=a,b,c

From (4.19), peak current of individual i^{th}-IFC can be achieved as follows:

$$I_i^{max} = max(I_{ai}^{max}, I_{bi}^{max}, I_{ci}^{max}) \tag{4.20}$$

Moreover, considering (4.14)-(4.18), the phase angle of i^{th}-IFC's peak current can be derived as:

$$\delta|_{I_i^{max}} = \tan^{-1}\left(\frac{\left(\frac{P_i(|v^+| + k_{Pi}|v^-|)}{|v^+|^2 + k_{Pi}|v^-|^2}\right)\cos\gamma + \left(\frac{-Q_i(|v^+| + k_{qi}|v^-|)}{|v^+|^2 + k_{qi}|v^-|^2}\right)\sin\gamma}{\left(\frac{-Q_i(|v^+| - k_{qi}|v^-|)}{|v^+|^2 + k_{qi}|v^-|^2}\right)\cos\gamma + \left(\frac{-P_i(|v^+| - k_{Pi}|v^-|)}{|v^+|^2 + k_{Pi}|v^-|^2}\right)\sin\gamma}\right) \tag{4.21}$$

Considering (4.19)-(4.21), it can be understood that the amplitude and phase angle of individual IFC's peak current depend on IFC output average active and reactive powers, PCC positive and negative sequence voltages, and k_{Pi} and k_{qi}.

4.2.2 Parallel interfacing converters

Considering (4.14)-(4.18), the projection of n-parallel IFCs' collective current ellipse on each phase can be expressed as:

$$\begin{aligned} i_{x-IFCs}^{*\prime} &= \sum_{i=1}^{n} i_x^{*\prime} \\ &= \left(\sum_{i=1}^{n}\frac{P_i|v^+|}{|v^+|^2 + k_{p_i}|v^-|^2} + \sum_{i=1}^{n}\frac{P_i k_{p_i}|v^-|}{|v^+|^2 + k_{p_i}|v^-|^2}\right)\cos\gamma\cos\omega t \\ &- \left(\sum_{i=1}^{n}\frac{Q_i|v^+|}{|v^+|^2 + k_{q_i}|v^-|^2} + \sum_{i=1}^{n}\frac{Q_i k_{q_i}|v^-|}{|v^+|^2 + k_{q_i}|v^-|^2}\right)\sin\gamma\cos\omega t \\ &- \left(\sum_{i=1}^{n}\frac{Q_i|v^+|}{|v^+|^2 + k_{q_i}|v^-|^2} - \sum_{i=1}^{n}\frac{Q_i k_{q_i}|v^-|}{|v^+|^2 + k_{q_i}|v^-|^2}\right)\cos\gamma\sin\omega t \\ &- \left(\sum_{i=1}^{n}\frac{P_i|v^+|}{|v^+|^2 + k_{p_i}|v^-|^2}\right. \\ &\left. - \sum_{i=1}^{n}\frac{P_i k_{p_i}|v^-|}{|v^+|^2 + k_{p_i}|v^-|^2}\right)\sin\gamma\sin\omega t \qquad x = a, b, c \end{aligned} \tag{4.22}$$

From (4.22), it is clear that the amplitude and phase angle of the collective current projection on each phase depend on average active and reactive powers, positive and negative sequence of PCC voltage, and k_{Pi} and k_{qi}. In (4.22), applying the active power oscillation cancellation constraints in (4.7) and (4.8), the maximum collective current amplitude at each phase, the peak current, and the peak current phase angle are:

$$I_{x-IFCs}^{max}|_{\Delta P=0} = \sqrt{\left(\left(\frac{\sum_{i=1}^{n} P_i}{|v^+|^2-|v^-|^2}\right)^2+\left(\frac{\sum_{i=1}^{n} Q_i}{|v^+|^2+|v^-|^2}\right)^2\right)\times \atop (|v^+|^2+|v^-|^2-2|v^+||v^-|\cos(2\gamma))} \quad x=a,b,c \tag{4.23}$$

$$I_{IFCs}^{max}|_{\Delta P=0} = max(I_{a-IFCs}^{max}|_{\Delta P=0}, I_{b-IFCs}^{max}|_{\Delta P=0}, I_{c-IFCs}^{max}|_{\Delta P=0}) \tag{4.24}$$

$$\delta|_{I_{IFCs}^{max}|_{\Delta P=0}} = \tan^{-1}\left(\frac{\left(\frac{(|v^+|-|v^-|)\sum_{i=1}^{n} P_i}{|v^+|^2-|v^-|^2}\right)\cos\gamma+\left(-\frac{(|v^+|+|v^-|)\sum_{i=1}^{n} Q_i}{|v^+|^2+|v^-|^2}\right)\sin\gamma}{\left(-\frac{(|v^+|-|v^-|)\sum_{i=1}^{n} Q_i}{|v^+|^2+|v^-|^2}\right)\cos\gamma-\left(\frac{(|v^+|+|v^-|)\sum_{i=1}^{n} P_i}{|v^+|^2-|v^-|^2}\right)\sin\gamma}\right) \tag{4.25}$$

From (4.23)-(4.25), it can be seen that under zero active power oscillations of parallel IFCs, the collective peak current amplitude and phase angle of parallel IFCs are independent from k_{Pi} and k_{qi}, and are constant values under fixed average active and reactive powers output.

4.2.3 Discussions

Under zero active power oscillation, the collective peak current of parallel IFCs is independent from k_{pi} and k_{qi}, and it is a constant value under fixed values of active and reactive powers (see (4.23) and (4.24)). If all IFCs' peak currents are in the same phase as the collective peak current of parallel IFCs, the summation of their peak currents' amplitudes will be reduced.

However, considering (4.19) and (4.23), under $\Delta P = 0$ the peak currents of individual IFCs can be in the same phase with collective peak current of parallel IFCs or in different phases, depending on k_{pi} and k_{qi} values with given P_i and Q_i. For example in two-parallel IFCs with $P_1 = 4kW$, $Q_1 = 7kVar$, $P_2 = 5kW$ and $Q_2 = 0.5kVar$, under $k_{p1} = -0.74$, $k_{q1} = 0.74$, $k_{p2} = -1.20$, and $k_{q2} = 6.27$, the system has $\Delta P = 0$, and the peak currents of two IFCs and the collective peak current of parallel IFCs are in phase b. In this operating point, the collective peak current is $I_{IFCs}^{max}|_{\Delta P=0} = 49.02A$ which is shared between the two IFCs as $I_1^{max} = 30A$ and $I_2^{max} = 23.79A$ (the difference between $I_1^{max} + I_2^{max}$ and $I_{IFCs}^{max}|_{\Delta P=0}$ is due to phase angle difference between $\delta|_{I_1^{max}}$ and $\delta|_{I_2^{max}}$). Under $k_{p1} = -1.81$,

$k_{q1} = -1.39$, $k_{p2} = -0.24$, and $k_{q2} = -15.85$ operating point, the collective active power oscillations is zero again. However, the peak current of first, second and collective peak current are in phase c, a, and b, respectively. In this operating point, the collective peak current is similar to previous operating point and equal to $I_{IFCs}^{max}|_{\Delta P=0} = 49.02A$ (independent from k_{Pi} and k_{qi} under $\Delta P = 0$) while the first and second IFCs' peak currents are $I_1^{max} = 42.05A$ and $I_2^{max} = 33.36A$. As clear from the example, under $\Delta P = 0$, when all IFCs' peak currents are in the same phase with collective peak current of parallel IFCs, the summation of their peak currents' amplitudes are reduced. It will be explained that since all IFCs, except redundant one, are controlled based on their current ratings, keeping all IFCs peak currents in the same phase with collective peak current will reduce redundant IFC's peak current (which is controlled by constraints in (4.7) and (4.8)).

Considering aforementioned discussions, k_{pi} and k_{qi} of individual IFCs can be controlled to lead their peak currents in the same phase with collective peak current of parallel IFCs.

4.3 Boundary Conditions for Parallel Three-Phase IFCs' Peak Currents Control

In this section, different conditions in which the peak currents of individual IFCs and collective peak current of parallel IFCs are in the same phase are studied. Considering these conditions, appropriate boundaries are proposed for coefficient factors to keep the peak currents of individual IFCs and collective peak current in the same phase, which leads to smaller peak currents' amplitudes summation of parallel IFCs.

Considering (4.23), among three phases, the collective peak current of parallel IFCs is in the phase where $\cos(2\gamma)$ has its minimum value.

For individual i^{th}-IFC, the maximum current expression at each phase in (4.19) can be rewritten as follows:

$$I_{xi}^{max} = \sqrt{F_{1i} - \sqrt{(F_{2i})^2 + (F_{3i})^2}\, cos(2\gamma + \beta_i)} \qquad x = a, b, c \tag{4.26}$$

where

$$F_{1i} = \frac{P_i^2}{\left(|v^+|^2 + k_{pi}|v^-|^2\right)^2}\left(|v^+|^2 + |v^-|^2 k_{pi}^2\right) + \frac{Q_i^2}{\left(|v^+|^2 + k_{qi}|v^-|^2\right)^2}\left(|v^+|^2 + |v^-|^2 k_{qi}^2\right) \tag{4.27}$$

$$F_{2i} = \frac{2|v^+||v^-| \times \left(P_i^2 k_{pi}\left(|v^+|^2 + k_{qi}|v^-|^2\right)^2 - Q_i^2 k_{qi}\left(|v^+|^2 + k_{pi}|v^-|^2\right)^2\right)}{\left(|v^+|^2 + k_{pi}|v^-|^2\right)^2\left(|v^+|^2 + k_{qi}|v^-|^2\right)^2} \tag{4.28}$$

$$F_{3i} = -\frac{2P_i Q_i |v^+||v^-|\left(k_{pi} + k_{qi}\right)}{\left(|v^+|^2 + k_{pi}|v^-|^2\right)\left(|v^+|^2 + k_{qi}|v^-|^2\right)} \tag{4.29}$$

$$\beta_i = tan^{-1}\left(\frac{P_i^2 k_{pi}\left(|v^+|^2 + k_{qi}|v^-|^2\right)^2 - Q_i^2 k_{qi}\left(|v^+|^2 + k_{pi}|v^-|^2\right)^2}{-P_i Q_i\left(k_{pi} + k_{qi}\right)\left(|v^+|^2 + k_{pi}|v^-|^2\right)\left(|v^+|^2 + k_{qi}|v^-|^2\right)}\right) + \frac{\pi}{2} \tag{4.30}$$

Considering (4.26)-(4.30), for individual IFC, the phase with minimum value of $\cos(2\gamma + \beta_i)$ will have maximum current. Therefore, the phase of i^{th}-IFC's peak current depends on γ (or in other words, ρ) and β_i values. Since under zero active power oscillations, $|v^+|$, $|v^-|$ and ρ are constant values under fixed average active and reactive powers (see (4.9)), β_i (or in other words, k_{pi} and k_{qi})

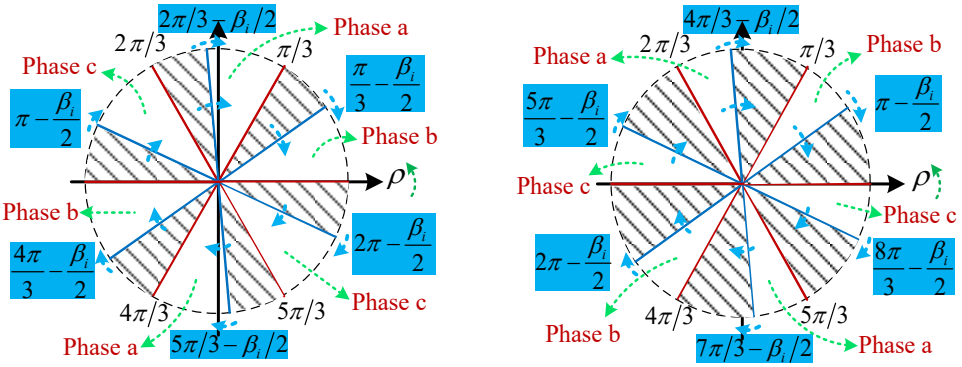

Figure 4.3 Relation between the phase of individual i^{th}-IFC peak current and parallel IFCs' collective peak current (peak currents are in the same phase in unshaded areas and in different phases in shaded areas); (a) $0 < \beta_i < 2\pi/3$**, (b)** $4\pi/3 < \beta_i < 2\pi$**.**

can determine the phase of IFC's peak current. In Figure 4.3, conditions in which the peak current of individual i^{th}-IFC and collective peak current of parallel IFCs under $\Delta P = 0$ are in different phases are shown with shaded area while in the unshaded area these peak currents are in the same phase. From Figure 4.3, if β_i of i^{th}-IFC is in the boundary of $0 < \beta_i < 2\pi/3$ or $4\pi/3 < \beta_i < 2\pi$ and ρ is in the unshaded areas, the peak current of that i^{th}-IFC will be in the same phase with collective peak current of parallel IFCs. On the other hand, in the condition that β_i of individual IFC is in the boundary of $2\pi/3 < \beta_i < 4\pi/3$, the peak current of that individual IFC and the collective peak current of parallel IFCs will always be in different phases, which is not shown in Figure 4.3. It is worth mentioning that in Figure 4.3, shaded and unshaded areas are controlled by β_i values (or in other words, by k_{pi} and k_{qi} values). Since ρ is a constant value under fixed values of average active and reactive powers, β_i can be controlled to lead individual IFC's peak current to the same phase with collective peak current of parallel IFCs.

4.3.1 IFCs under unity power factor operation mode

Considering (4.30), under unity PF operation mode ($Q_i = 0$), if $k_{Pi} < 0$, $\beta_i = 0$, and if $k_{Pi} > 0$, $\beta_i = \pi$. Therefore, $k_{Pi} < 0$, the peak current of individual i^{th}-IFC will be in the same phase with collective peak current of parallel IFC, regardless the value of ρ and active power flow direction (under $\beta_i = 0$, the dashed areas are not exist in Figure 4.3).

Considering aforementioned discussions, in the proposed control strategy under unity PF operation mode, k_{pi} will be controlled to be less than zero to keep all individual IFCs' peak currents and collective peak current of parallel IFCs in the same phase, leading to reduced peak currents' summation of parallel IFCs.

4.3.2 IFCs under non-unity power factor operation mode

Under non-unity PF operation mode considering (4.30), determination of boundaries in which the individual IFCs' peak currents are in the same phase with collective peak current of parallel IFCs is challenging, and they should be updated under average active-reactive powers' variations. However, (4.30) can be

simplified and boundaries can be determined under specific relation between k_{pi} and k_{qi} as:

$$k_{pi} + k_{qi} = 0 \qquad i = 1, \dots, n-1 \tag{4.31}$$

In this Chapter, since redundant IFC is utilized for active power oscillation cancellation using (4.7) and (4.8), (4.31) may not be applicable for redundant IFC. The relation between k_{pn} and k_{qn} of redundant IFC will be discussed later.

Applying (4.31) for all IFCs except redundant one, if $k_{pi} < 0; i = 1, \dots, n-1$ (or $k_{qi} > 0; i = 1, \dots, n-1$), the peak current of individual i^{th}-IFC and collective peak current of parallel IFCs will be in the same phase since $\beta_i = 0$, regardless of value of ρ and average active and reactive powers flow directions. Moreover, $k_{pi} > 0; i = 1, \dots, n-1$ (or $k_{qi} < 0; i = 1, \dots, n-1$) will lead peak currents to different phases since $\beta_i = \pi$.

Considering individual IFC's power oscillation and its peak current in (4.2) and (4.19), (4.31) could also satisfy the active power oscillation-free operation of individual IFCs under $k_{pi} = -1$ and $k_{qi} = 1$, and provide minimum peak current of individual IFC under $k_{pi} = k_{qi} = 0$. Therefore, in the proposed control strategy under non-unity PF operation mode, (4.31) will be applied to all individual IFCs except redundant one, and their k_{pi} will be controlled to be less than zero to keep their peak currents in the same phase with collective peak current of parallel IFCs.

As mentioned, the redundant IFC cancels out active power oscillations using (4.7) and (4.8). As a result, the relation between k_{pn} and k_{qn} of redundant IFC can be achieved as following:

$$G_n = \frac{k_{qn}}{k_{pn}} = \frac{\left[Q_n - |v^+|^2\left(\frac{\sum_{i=1}^{n} Q_i}{|v^+|^2+|v^-|^2} - \sum_{i=1}^{n-1}\frac{Q_i}{|v^+|^2-k_{p_i}|v^-|^2}\right)\right]}{\left[P_n - |v^+|^2\left(\frac{\sum_{i=1}^{n} P_i}{|v^+|^2-|v^-|^2} - \sum_{i=1}^{n-1}\frac{P_i}{|v^+|^2+k_{p_i}|v^-|^2}\right)\right]} \times \frac{\left[\frac{\sum_{i=1}^{n} P_i}{|v^+|^2-|v^-|^2} - \sum_{i=1}^{n-1}\frac{P_i}{|v^+|^2+k_{p_i}|v^-|^2}\right]}{\left[\frac{\sum_{i=1}^{n} Q_i}{|v^+|^2+|v^-|^2} - \sum_{i=1}^{n-1}\frac{Q_i}{|v^+|^2-k_{p_i}|v^-|^2}\right]} \tag{4.32}$$

In the proposed strategy, all IFCs will work under the same power factor. Thus, following relation can be considered:

$$\frac{P_i}{Q_i} = \frac{\sum_{i=1}^{n} P_i}{\sum_{i=1}^{n} Q_i} = \frac{1}{U} \qquad i = 1, \dots, n \tag{4.33}$$

where U is a number. Assuming $|v^-| = M \times |v^+|$ in which M is the unbalanced ratio and $0 \le M \le 1$, (4.32) can be rewritten as following:

$$G_n = \frac{\left[P_n - \left(\frac{\sum_{i=1}^{n} P_i}{1+M^2} - \sum_{i=1}^{n-1}\frac{P_i}{1-k_{p_i}M^2}\right)\right] \times \left[\frac{\sum_{i=1}^{n} P_i}{1-M^2} - \sum_{i=1}^{n-1}\frac{P_i}{1+k_{p_i}M^2}\right]}{\left[P_n - \left(\frac{\sum_{i=1}^{n} P_i}{1-M^2} - \sum_{i=1}^{n-1}\frac{P_i}{1+k_{p_i}M^2}\right)\right] \times \left[\frac{\sum_{i=1}^{n} P_i}{1+M^2} - \sum_{i=1}^{n-1}\frac{P_i}{1-k_{p_i}M^2}\right]} \tag{4.34}$$

In practical power system, M is a small value (based on IEEE Standard, typical value of M in a three-phase power system under steady state operation is less than 3% [76]). Assuming that $|v^+|$ and $|v^-|$ are constant values and since $-1 \le k_{pi} \le 0; i = 1, \dots, n-1$, $k_{pi}M^2$ will be small enough to be neglected in (4.34). Therefore, (4.34) can be simplified as following:

$$G_n = \frac{k_{qn}}{k_{pn}} = \frac{M^2\left(P_n + M^2\sum_{i=1}^{n-1} P_i\right)\sum_{i=1}^{n} P_i}{-M^2\left(P_n - M^2\sum_{i=1}^{n-1} P_i\right)\sum_{i=1}^{n} P_i} = -\frac{P_n + M^2\sum_{i=1}^{n-1} P_i}{P_n - M^2\sum_{i=1}^{n-1} P_i} \tag{4.35}$$

Considering (4.35), G_n will be close to -1 depend on the number of parallel IFCs, the power rating of redundant IFC in comparison to other IFCs, and the value of M. As a result, considering (4.35), β_n will be very small value close to zero degree, which results in small shaded area in Figure 4.3. In this case, even though we fall in this small area (this area is the transition that the peak current is switched from one phase to another phase), the peak current basically does not

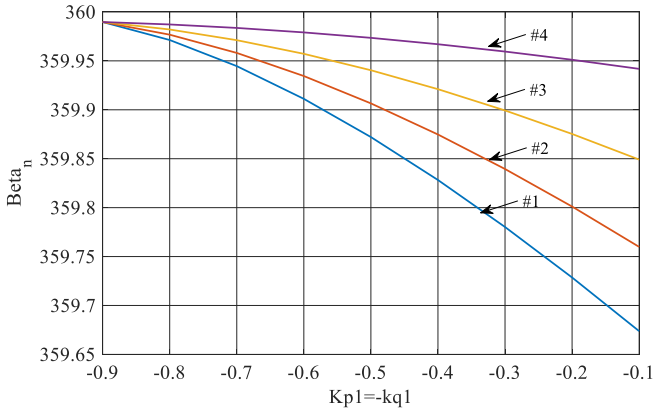

Figure 4.4 The variations of B_3 (for redundant IFC) under k_{p2}=-k_{q2}=-0.9, S_3=0.5S_T, U=1/15, M=0.3, and different IFCs apparent powers: Case#1: P_1=7kW, Q_1=466.6Var, P_2=2.979kW, Q_2=198.52Var; Case#2: P_1=5kW, Q_1=333.3Var, P_2=4.977kW, Q_2=331.85Var; Case#3: P_1=3kW, Q_1=200Var, P_2=2.979kW, Q_2=198.52Var; Case#4: P_1=1kW, Q_1=66.6Var, P_2=8.977kW, Q_2=598.52Var.

change that much. In other words, the peak currents of two phases are almost the same. Therefore, it does not matter in which phase the peak current is.

As a numerical example, three-parallel IFCs have been simulated under the same PF ($U = 1/15$) and different apparent powers and coefficient factors. In this example, $M = 0.3$, $S_3 = 0.5S_T$ (S_T is total apparent power), $k_{p1} = -k_{q1}: -0.9 \longrightarrow -0.1$, $k_{p2} = -k_{q2} = -0.9$, and the third IFC (redundant one) cancels out active power oscillations. The variations of β_3 under different operating conditions are shown in Figure 4.4. From the figure, β_3 is change within 0.4 degree under different operating conditions, leading to small shaded areas.

Considering aforementioned discussions, $k_{pi};\ i = 1, \dots, n$ will be controlled to be less than zero to provide reduced peak currents' summation of parallel IFCs (in other words, to reduce the redundant IFC's peak current).

4.4 Proposed Control Strategy for Parallel Three-Phase IFCs' Operation under Unbalanced Voltage: Active Power Oscillations Cancellation using Redundant IFC

A novel control strategy is proposed for parallel IFCs with various PFs under unbalanced voltage, which reduces the adverse effects of unbalanced voltage on IFCs' operation, and could also improve the unbalanced condition of AC

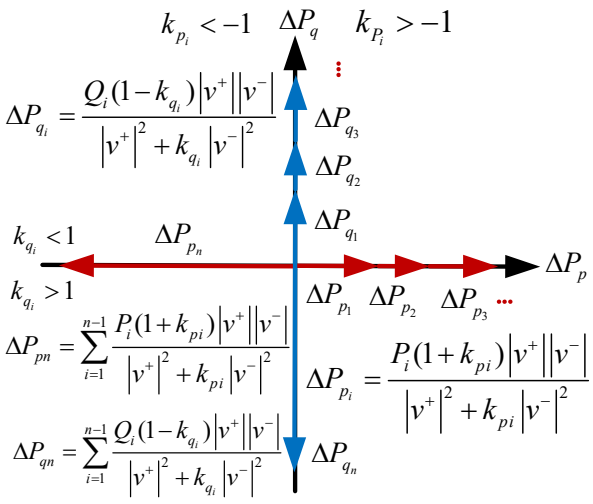

Figure 4.5 Vector representation of ΔP cancellation using redundant IFC.

subsystem/grid. In the proposed control strategy, one interfacing converter which has the largest power rating among parallel IFCs, named redundant IFC, cancels out active power oscillations produced by other parallel IFCs, which results in DC subsystem/link voltage oscillation cancellation. In Figure 4.5, vector representation of active power oscillations cancellation using redundant IFC is shown. In this figure, it is assumed that $P_i > 0$ and $Q_i > 0$ $i = 1, \dots, n$, $\theta = \theta^+ - \theta^- = 0$, and $k_{pi} \geq -1$ and $k_{qi} \leq 1$ $i = 1, \dots, n-1$ (except redundant IFC). As a result, redundant IFC works under $k_{pn} \leq -1$ and $k_{qn} \geq 1$ to produce 180-degree out-of-phase power oscillation to cancel out active power oscillations.

4.4.1 IFCs under unity power factor operation mode

In this control strategy, the redundant IFC is controlled based on active power oscillation cancellation constraints in (4.7) to cancel out ΔP_{Pi} part of active power oscillations of parallel IFCs, and the other IFCs are controlled based on their peak currents rating limits. The block diagram of the proposed control strategy is shown in Figure 4.6. In this control strategy, I_{Pi}^{max} can be measured or calculated using (4.19)-(4.20), and the system is started under $k_{pi} = -1;\ i = 1,2, \dots, n$ where $\Delta P_{p_i} = 0$. If the peak current of each $n-1$ IFC exceeds its rating current limit (I_i^{rate}), its k_{pi} will move toward zero to limit its peak current on the rating value. As a result, the peak currents of IFCs except the redundant one are constant

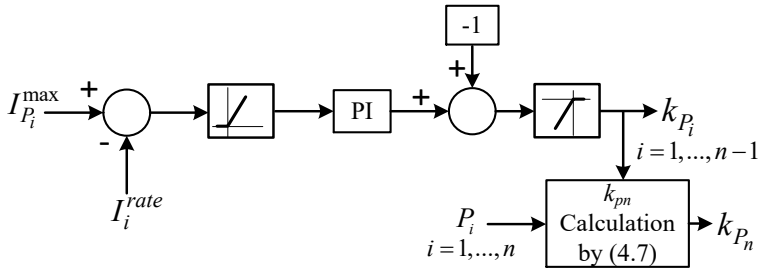

Figure 4.6 The proposed control strategy under unity PF operation mode.

values under fixed average active powers in different operation conditions (under $k_{pi} = -1$ or under their rating values). All information of $n-1$ IFCs (P_i and k_{pi}) is sent to redundant IFC's controller. Based on information, k_{pn} of the redundant converter is determined using (4.7) to cancel active power oscillations.

In this control strategy, IFCs operate under $k_{Pi} \leq 0$, so IFCs' peak currents will be in the same phase with collective peak current of parallel IFCs as discussed in Section 4.3.1, which leads to reduced peak currents' summation of IFCs (see Section 4.2.3). Since all IFCs' peak currents except the redundant one are constant values under fixed average active powers in different operation conditions (see Figure 4.6), the redundant IFC's peak current will be reduced when peak currents are in the same phase. This capability of control strategy is important since the redundant IFC cancels out other IFCs active power oscillations and then its peak current will be much higher. The variation of IFCs' average powers flow direction and values will not affect the proposed control strategy performance although the operating point will be changed.

4.4.2 IFCs under non-unity power factor operation mode

The proposed control strategy block diagram under non-unity PF mode is shown in Figure 4.7. Considering the block diagram, the performance of control scheme under non-unity PF mode is similar to unity PF operation mode in which all $n-1$ IFCs are controlled based on their current rating limits, and redundant IFC is controlled based on information communicated from other IFCs (P_i, k_{Pi}, Q_i, k_{qi}) and using (4.7)-(4.8) to cancel out ΔP_{Pi} and ΔP_{qi} parts of active power

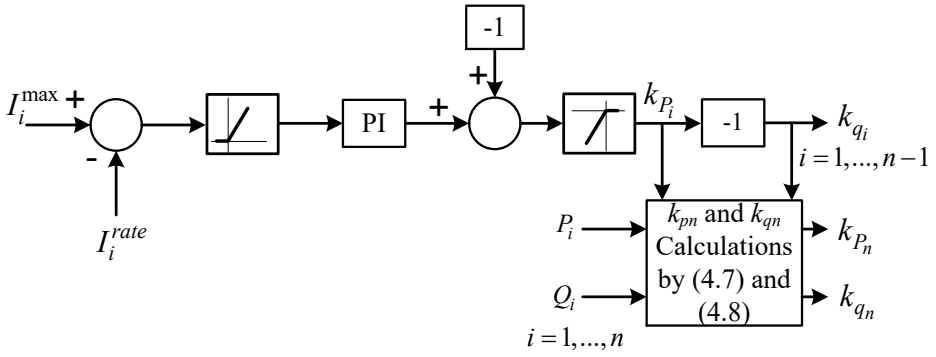

Figure 4.7 The proposed control strategy under non-unity PF operation mode.

oscillations of parallel IFCs. From Figure 4.7, the system is started under $k_{pi} = -1;\ i = 1,2,\ldots,n$ (result in $k_{qi} = 1$ considering (4.31)) which provides zero active power oscillation of individual IFCs. This operating point will be changed if each IFC peak current exceeds its rating limit (I_i^{rate}). Thus, k_{pi} of those IFCs that hit the current limits will move toward zero (k_{qi} will move toward zero, too), and the redundant IFC will cancel out active power oscillation produced by peak currents control. Here, I_i^{max} can be measured or calculated using (4.19).

In the proposed control strategy, $k_{pi} \leq 0; i = 1,\ldots,n-1$, and relations between coefficient factors of k_{pi} and k_{qi} for all IFCs except redundant one are controlled using (4.31), which lead those IFCs peak currents to the same phase with collective peak current of parallel IFCs. For redundant IFC as mentioned in Section 4.3.2, since relation between coefficient factors of k_{pn} and k_{qn} is very close to -1, $k_{pn} \leq 0$ may lead the redundant IFC's peak current to the same phase with collective peak current. In case that they are not in the same phase, the peak current basically does not change that much due to small value of β_n. As a result, $k_{pi} \leq 0; i = 1,\ldots,n$ provides reduced peak current for redundant IFC.

Similarly, average active and reactive power flow direction will not affected the performance of the proposed control strategy.

4.4.3 Control scheme

In the proposed control strategy, distributed control structure can be used for parallel IFCs' control. The k_{pi} and k_{qi} of IFCs are generated in the outer control

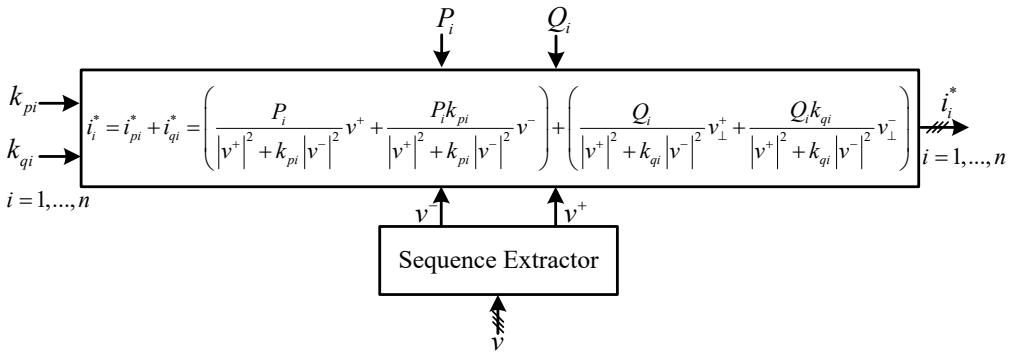

Figure 4.8 Individual IFCs' reference current production scheme.

layer of IFCs' local controllers by the proposed control strategy (see Figure 4.6 and Figure 4.7). These parameters are used in the inner control loops for individual IFCs' reference currents production, which is shown in Figure 4.8 (see Figure 2.2). In the control system, it is assumed that IFCs average active-reactive powers have been determined in high-level control layer, and their flow can be bi-directional in each IFC. In this Chapter, all parallel IFCs operate on power/current control mode in which the output currents of individual IFCs are controlled to regulate output average powers on their reference values (similar to Figure 3.3). Among different current control methods, closed-loop current control with practical proportional-resonant (PR) controller in the stationary $\alpha\beta$ reference frame is adopted. Frequency-locked loop (FLL) based sequence extractor in [74] is used to separate the PCC voltage into positive and negative sequences among different sequence extractors [72]-[74].

4.5 Simulation Verification

Three parallel IFCs have been simulated by the proposed control strategy in MATLAB/Simulink. The simulated system parameters are shown in TABLE 4.1. In the simulations, the third IFC with largest power/current rating is considered as the redundant converter. Two-phase unbalance fault with the fault resistance of 2Ω is applied to the system at $t = 0.15s$ as a source of unbalanced voltage. In the simulations during $0 < t < 0.3$, k_{pi} and k_{qi} of all IFCs are set to zero, and three-phase balance currents are produced. At $t = 0.3s$, the proposed control strategy is

TABLE 4.1 System parameters for simulations.

	Symbol	Value
DC link voltage	v_{dc}	$800V$
IFCs' power ratings	S_i	$S_1 = 9kVA; S_2 = 4kVA;$ $S_3 = 10kVA$
IFCs' current ratings	I_i^{rate}	$I_1^{rate} = 30A; I_2^{rate} = 13A$ $I_3^{rate} = 34A$
Grid voltage (rms) and frequency	$v_g - f_g$	$240V - 60Hz$
Grid coupling impedance	Z_{Grid}	$R_{Grid}: 0.2\Omega; X_{Grid}: 1.88\Omega$

applied to cancel out active power oscillations, which results in oscillation-free DC link voltage.

4.5.1 IFCs under unity power factor operation mode

In this simulation, during $0 < t < 0.75$, the average active powers of IFCs are $P_1 = 6kW$, $P_2 = 2.7kW$, and $P_3 = 3kW$. At $t = 0.75$, average active powers of IFCs are modified into $P_1 = 7kW$, $P_2 = 3kW$, and $P_3 = 2.5kW$. The simulation results are shown in Figure 4.9 to Figure 4.17.

As mentioned, the proposed control strategy is applied at $t = 0.3s$. During $0.3 < t < 0.5$, the proposed control strategy initially sets k_{p1}, k_{p2} and k_{p3} on -1 (see Figure 4.9). Although the initial set point provides zero active power oscillations for IFCs (see Figure 4.11 to Figure 4.13), the first and second IFCs' peak currents exceed their rating limits (see Figure 4.10). Therefore, at $t = 0.5s$, the proposed control strategy sets the first and second IFCs' peak currents on their rating limits (see Figure 4.10) by moving k_{p1} and k_{p2} toward zero (see Figure 4.9), and cancels out active power oscillations produced by the IFCs' peak currents control using redundant IFC (see Figure 4.11 to Figure 4.14).

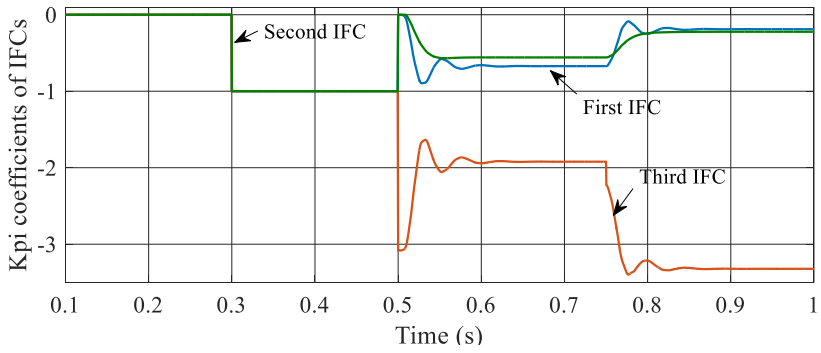

Figure 4.9 k_{pi} coefficient factors of the first, second, and third IFCs.

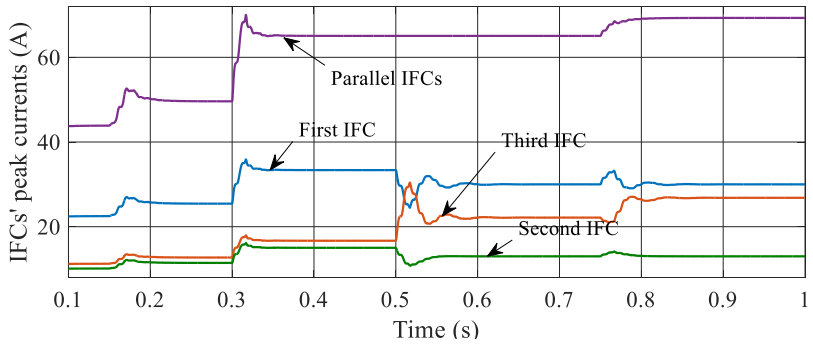

Figure 4.10 Peak currents' of IFCs.

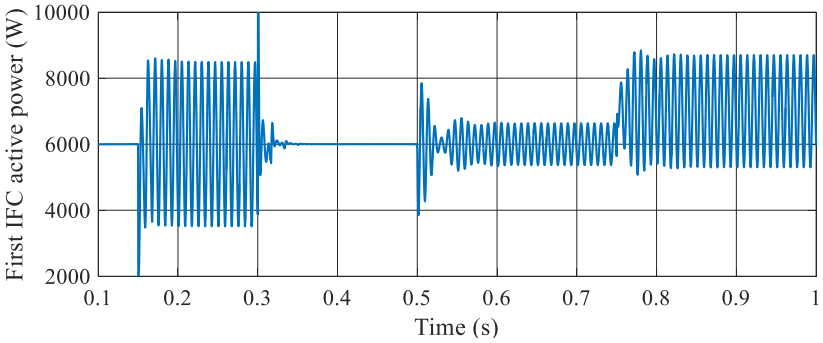

Figure 4.11 First IFC's output active power.

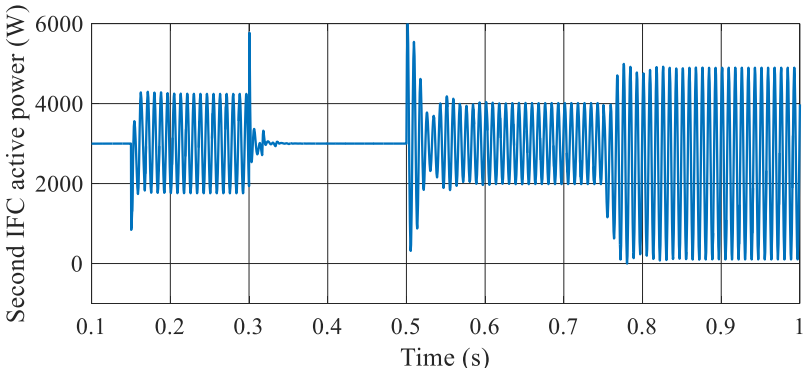

Figure 4.12 Second IFC's output active power.

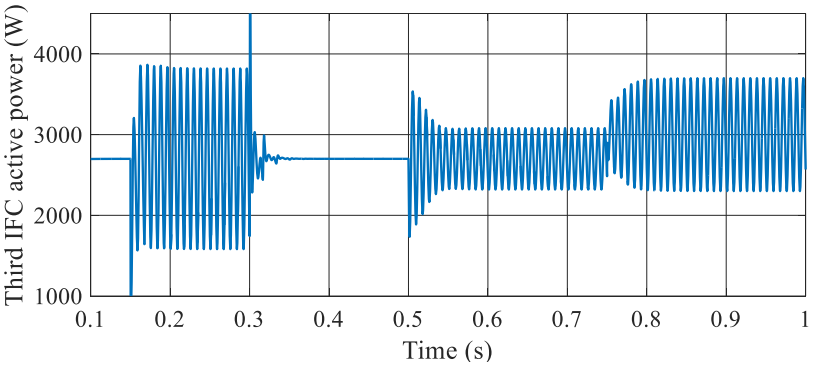

Figure 4.13 Third IFC's output active power.

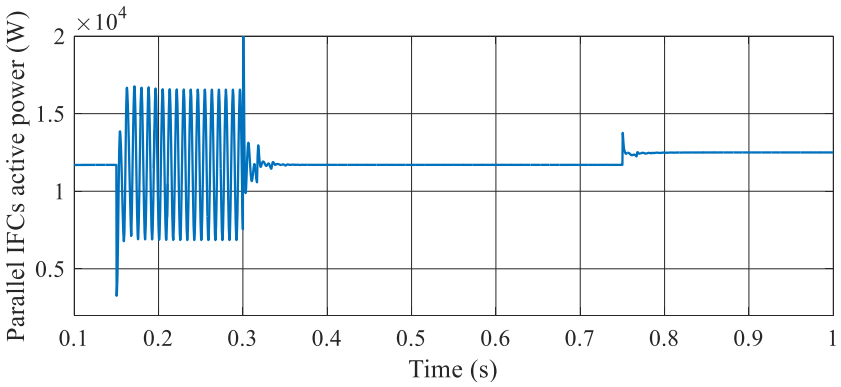

Figure 4.14 Parallel IFCs' collective active power.

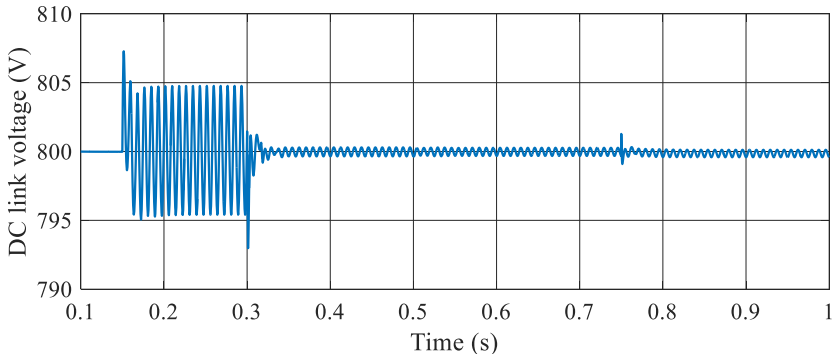

Figure 4.15 DC link voltage.

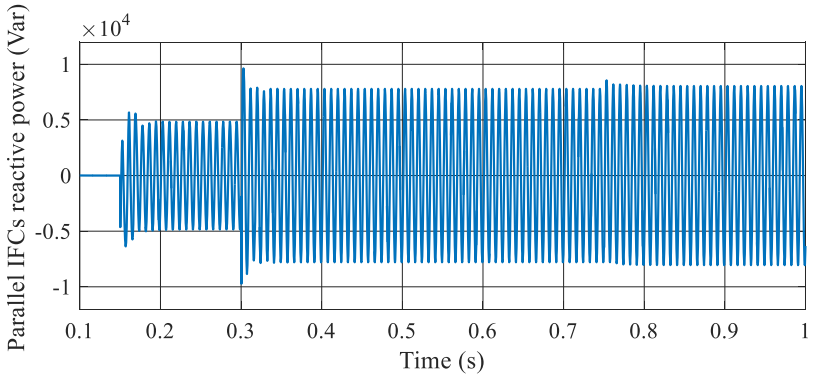

Figure 4.16 Parallel IFCs' collective reactive power.

The cancellation of parallel IFCs' active power oscillations provides oscillation-free DC link voltage which is shown in Figure 4.15 ($t > 0.3s$, $\Delta V_{peak-peak}\big|_{max} = 0.4V$). After average powers variations at $t = 0.75$, the proposed control again sets the first and second IFCs' peak currents on their rating limits since they hit limits, and provides zero collective active power.

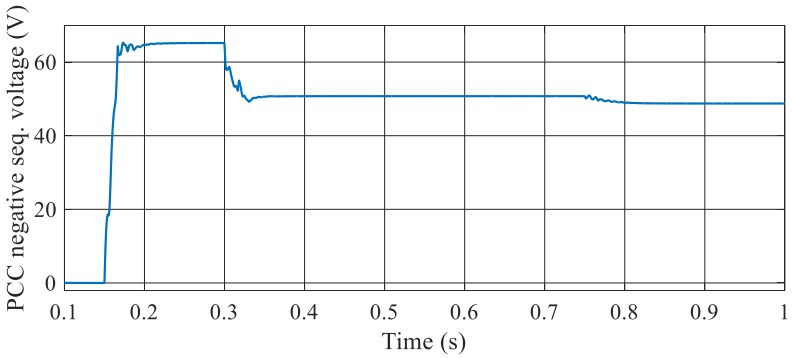

Figure 4.17 Negative sequence of PCC voltage.

According to the results, the collective peak current of parallel IFCs is independent from k_{pi} variations under $\Delta P = 0$, and it is just affected by average active powers' variations. In this simulation, under $0.5 < t < 0.75s$, $\rho = 45.26°$ and $\beta_1 = \beta_2 = \beta_3 = 0°$, and under $0.75 < t < 1s$, $\rho = 46.25°$ and $\beta_1 = \beta_2 = \beta_3 = 0°$, so all IFCs' peak currents and the collective peak current of parallel IFCs are in phase b, as expected fromFigure 4.3. As a result, the redundant IFC's peak current is reduced. The collective reactive power of parallel IFCs is shown in Figure 4.16 which is constant under $\Delta P = 0$ and just affected by average active powers' variations. The PCC negative sequence of voltage is shown in Figure 4.17. As seen from this figure, the proposed control strategy improves the unbalanced condition due to negative sequence current injection.

4.5.2 IFCs under non-unity power factor operation mode

In this operation mode, average active and reactive powers of IFCs are set to $P_1 = 7.5kW$, $Q_1 = 3.17kVar$, $P_2 = 1.5kW$, $Q_2 = 634.6Var$, $P_3 = 4kW$, and $Q_3 = 1.69kVar$ during $t < 0.75$. At $t = 0.75$, the average active and reactive powers of IFCs are changed into $P_1 = 8kW$, $Q_1 = 2.66kVar$, $P_2 = 2kW$, $Q_2 = 666.6kVar$, $P_3 = 3.5kW$, and $Q_3 = 1.16kVar$. The simulation results are shown in Figure 4.18 to Figure 4.27. The proposed control strategy is applied at $t = 0.3s$, and it initially sets k_{p1}, k_{p2} and k_{p3} on -1 during $0.3 < t < 0.5$ (see Figure 4.18), which results in $k_{q1} = k_{q2} = k_{q3} = 1$ (see Figure 4.19). This initial set point provides zero active power oscillations of IFCs (see Figure 4.21 to Figure 4.23), but first IFC's peak current exceeds its limit (see Figure 4.20).

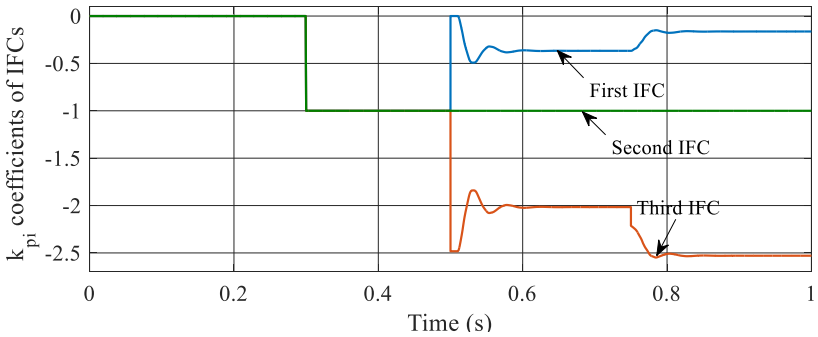

Figure 4.18 k_{pi} coefficient factors of the first, second, and third IFCs.

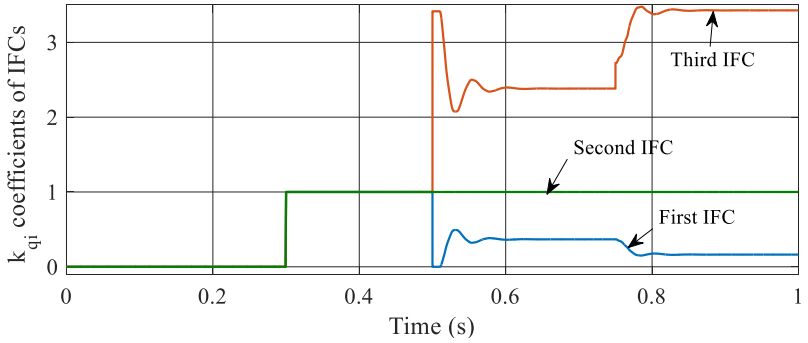

Figure 4.19 k_{qi} coefficient factors of the first, second, and third IFCs.

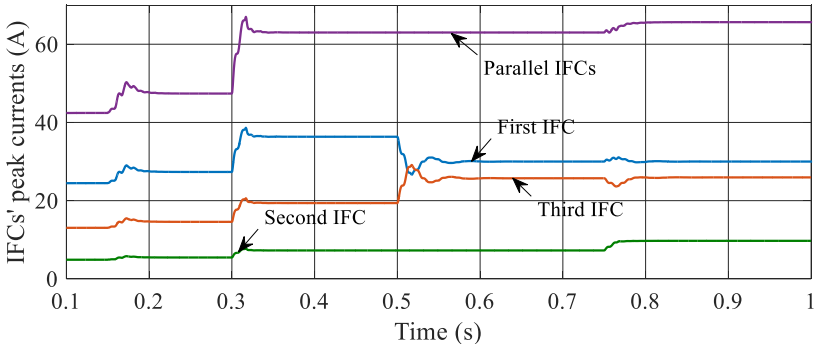

Figure 4.20 Peak currents' of IFCs.

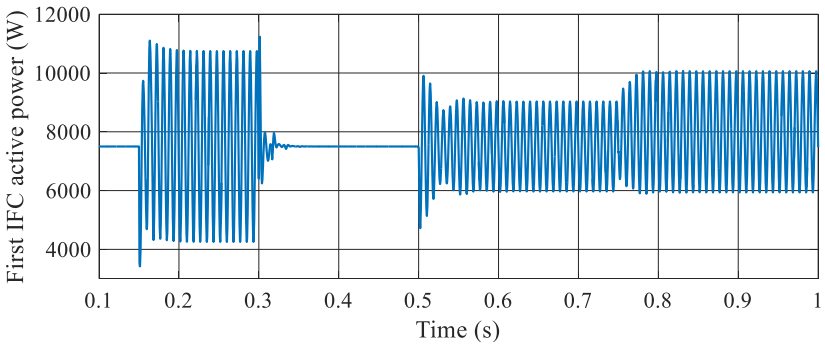

Figure 4.21 First IFC's output active power.

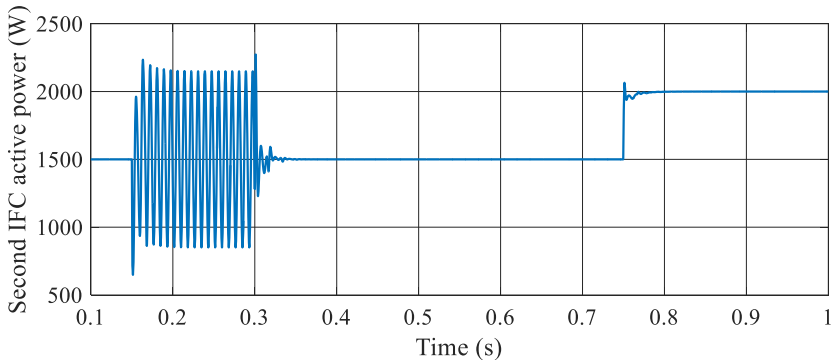

Figure 4.22 Second IFC's output active power.

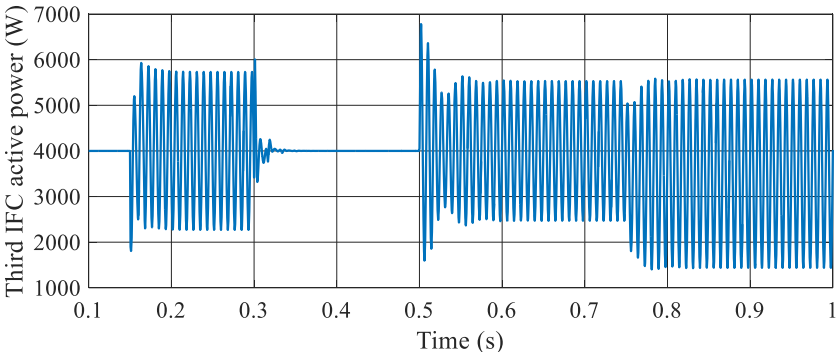

Figure 4.23 Third IFC's output active power.

At $t = 0.5s$, control system moves k_{p1} toward zero (consequently k_{q1} moves toward zero, too) to reduce the first IFC's peak current and set it on rating value (see Figure 4.18 to Figure 4.20). The produced active power oscillation by the first IFC's current control (see Figure 4.21) is cancelled out by redundant IFC (see Figure 4.23 and Figure 4.24). Since the second IFC's peak current does not hit the rating limit, it operates under $k_{p2} = -1$ and $k_{q2} = 1$ with oscillation-free output active power (see Figure 4.22). After average powers variations at $t = 0.75s$, the control system has similar performance since the first IFC's peak current exceeds the rating limit, and the second IFC peak current does not hit the rating limit. In this simulation, cancellation of collective active power oscillations by redundant IFC provides oscillation-free DC link voltage as shown in Figure 4.25 ($t > 0.3s$, $\Delta V_{peak-peak}\big|_{max} = 0.6V$).

In this simulation, during $0.5 < t < 0.75s$, $\rho = 39.85°$, and $\beta_1 = 0°$, $\beta_2 = 0°$, $\beta_3 = 357.23°$ and under $0.75 < t < 1s$, $\rho = 41.1°$, and $\beta_1 = 0°$, $\beta_2 = 0°$,

$\beta_3 = 356.09°$. Therefore, as expected, the shaded areas in Figure 4.3 are very narrow. Thus, all IFCs' peak currents and collective peak current of parallel IFCs are in phase b, which provides reduced peak current of redundant IFC.

In this operation mode, the collective peak current of parallel IFCs under $\Delta P = 0$ is independent from k_{pi} and k_{qi}. However, each IFC average active and reactive powers variation will affect its value. Moreover, the collective reactive power oscillation is constant under $\Delta P = 0$ and depends on average active-reactive powers (see Figure 4.26). In Figure 4.27, the negative sequence of PCC voltage is shown, which clarifies the improvement of unbalanced condition after proposed strategy's application.

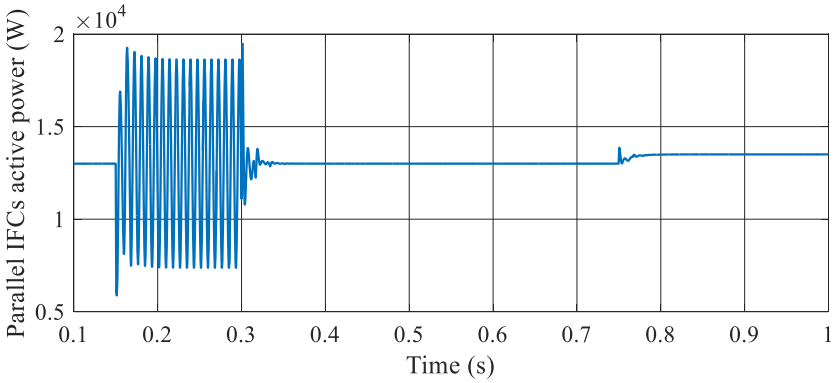

Figure 4.24 Parallel IFCs' collective active power.

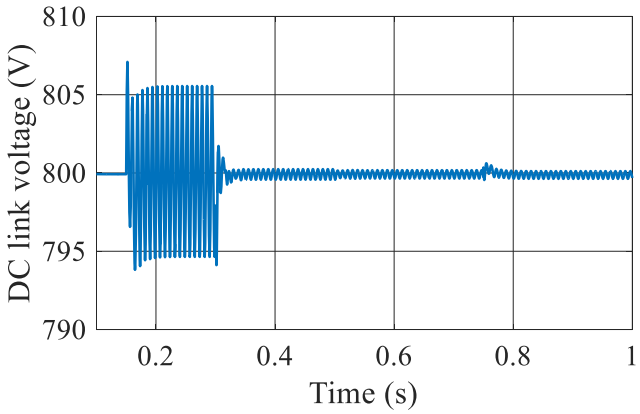

Figure 4.25 DC link voltage.

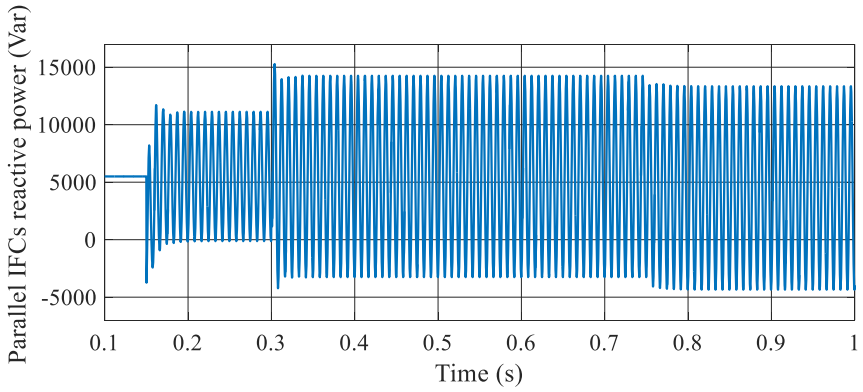

Figure 4.26 Parallel IFCs' collective reactive power.

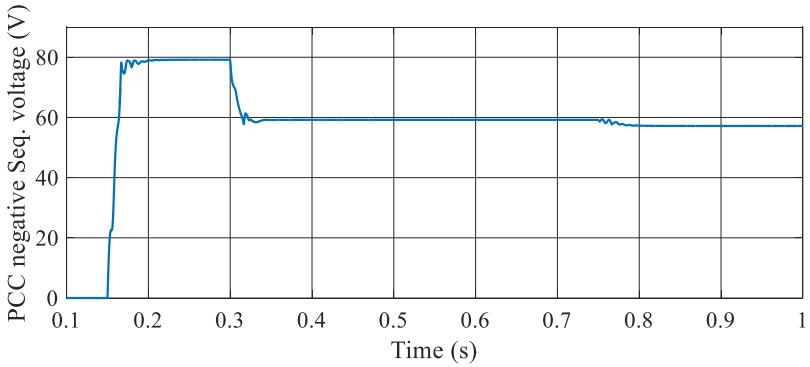

Figure 4.27 Negative sequence of PCC voltage.

4.6 Experimental Verification

The proposed control strategy is applied into two-parallel IFCs' experimental setup to verify its performance under different operating conditions. The experimental setup specifications are listed in TABLE 4.2. Here, the results of

TABLE 4.2 System parameters for experiments.

	Symbol	Value
DC link voltage	v_{dc}	$400V$
IFCs' current ratings	I_i^{rate}	$I_1^{rate} = 4A; I_2^{rate} = 5A$
Unbalance grid voltage	v_g	$v_A = 55\angle 0°;$ $v_B = 83.8\angle 250.9°;$ $v_C = 83.8\angle 109.1°$
IFCs' output filters	L_f-C_f	$3.6mH$-$4\mu F$
Switching frequency	f_s	$10kHz$

IFCs under non-unity PF operation mode are shown and discussed, which can be extended to unity PF operation mode.

In the experiments, the second IFC is considered as the redundant converter. Moreover, two-phase to ground fault is applied as a source of unbalance condition. In this experiment, the output currents of IFCs and grid voltage waveforms are achieved by scopecorder (YOKOGAWA DL850E), and their saved data is used in MATLAB/Simulink to achieve powers waveforms.

At the beginning, the average active and reactive powers of IFCs are set to $P_1 = 600W$, $P_2 = 600W$, $Q_1 = 300Var$, $Q_2 = 300Var$, and power coefficients are adjusted on $k_{p1} = k_{p2} = -1$ and $k_{q1} = k_{q2} = 1$ (power oscillation of IFCs are zero). Since the first IFC's peak current exceeds its rating limit, the proposed control strategy adjusts the power coefficients on $k_{p1} = -0.6$, $k_{p2} = -1.4$, $k_{q1} = 0.6$, and $k_{q2} = 1.4$ to set the first IFC's peak current on its rating and provide zero active power oscillation. The first and second IFCs three-phase currents are shown in Figure 4.28. In Figure 4.29, the first and second IFCs' output active powers and parallel IFCs collective active power are shown. As seen from this figure, the active power oscillation of first IFC is cancelled out by redundant IFC. In this figure, small errors in active power oscillation cancellation are due to errors in voltage and current measurements.

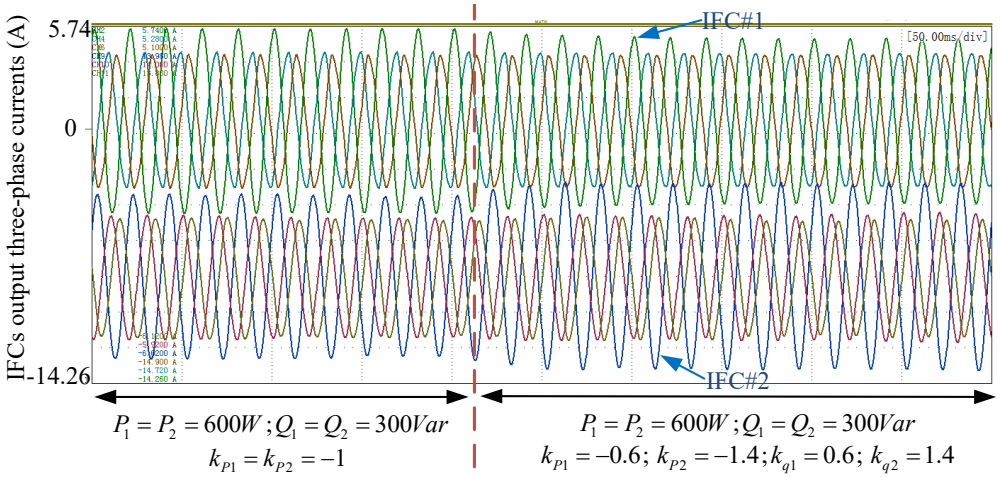

Figure 4.28 First and second IFCs' output three-phase currents under non-unity PF, 2A/div; (50ms/div).

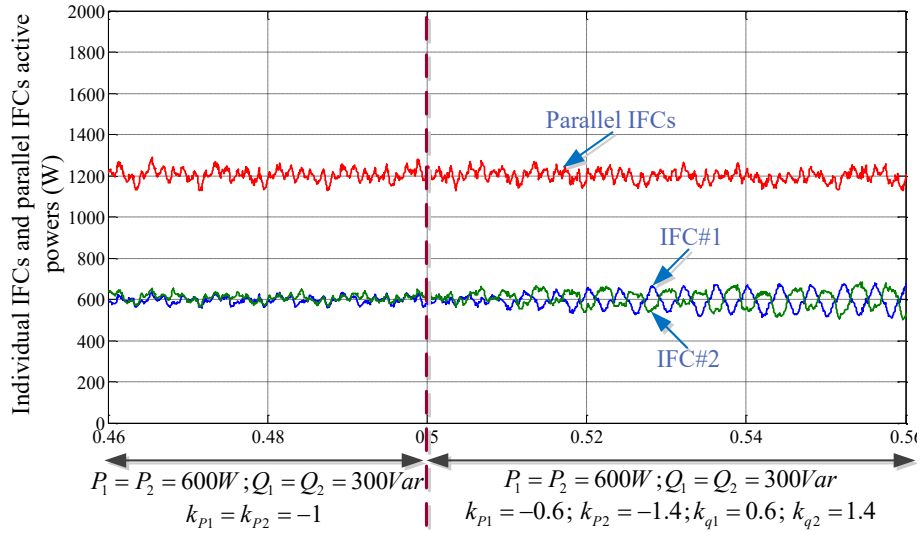

Figure 4.29 First and second IFCs' output active powers and collective active power of parallel IFCs under non-unity PF.

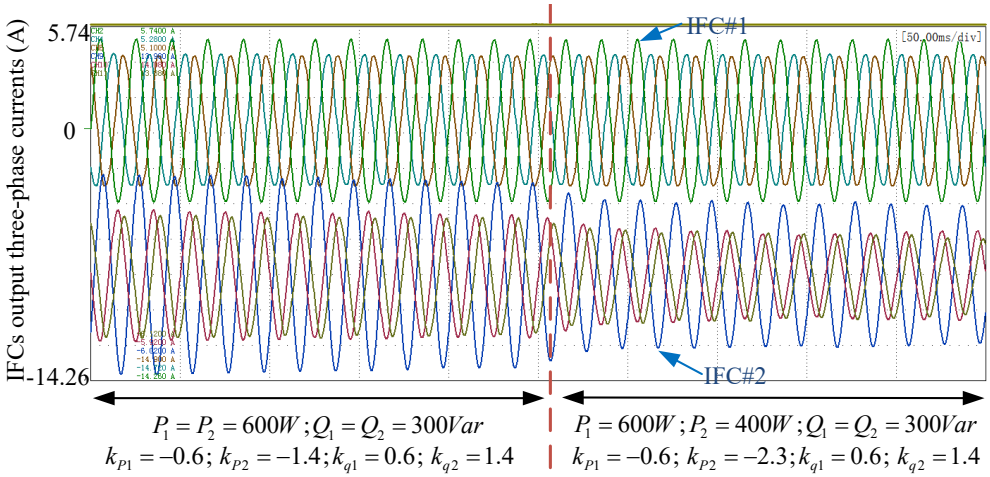

Figure 4.30 First and second IFCs' output three-phase currents under non-unity PF, 2A/div; (50ms/div).

In order to evaluate the performance of proposed control strategy under the variation of average active-reactive powers, these powers are modified into $P_1 = 600W$, $P_2 = 400W$, $Q_1 = 300Var$, $Q_2 = 300Var$. The proposed control achieves the control targets by adjusting the power coefficients on $k_{p1} = -0.6$, $k_{p2} = -2.3$, $k_{q1} = 0.6$, $k_{q2} = 1.4$, shown in Figure 4.30 and Figure 4.31.

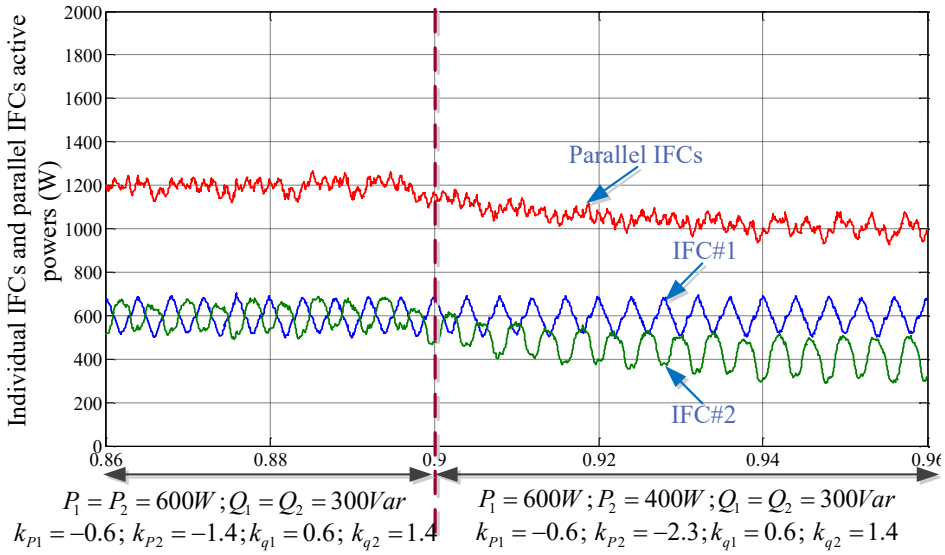

Figure 4.31 First and second IFCs' output active powers and collective active power of parallel IFCs under non-unity PF.

4.7 Conclusion

In this Chapter, a control strategy for parallel IFCs operation under unbalanced voltage in hybrid AC/DC microgrids was proposed. The proposed control strategy cancels out the collective active power oscillations of parallel IFCs by using the IFC with the largest power rating among the parallel IFCs as the redundant IFC. The proposed control strategy has the capability to be applied to parallel IFCs with various PFs and different average active-reactive powers in terms of flow directions and values, and could improve unbalanced condition. In this chapter, based on a thorough analysis of the peak currents of IFCs, it was found that, under zero active power oscillations, (1) the collective peak current of parallel IFCs was constant in the fixed average active and reactive powers, and (2) individual IFCs' peak currents could be either in the same phase or in different phases as that of the collective peak current. The proposed control strategy kept all IFCs' peak currents in the same phase as that of the collective peak current, providing a reduced peak current for the redundant IFC.

Chapter 5

Parallel Three-Phase Interfacing Converters Control under Unbalanced Voltage in Hybrid AC/DC Microgrids: Active Power Oscillation Cancellation with Peak Current Sharing[1]

In Chapter 4, a novel control strategy for parallel three-phase IFCs operation under unbalanced voltage in hybrid AC/DC microgrids was proposed. In the proposed control strategy, one dedicated IFC (called the redundant IFC) cancelled out the active power oscillation of the parallel IFCs. Since only the redundant IFC was used to reject the power oscillations of the parallel IFCs under unbalanced voltage, this IFC's power rating should be large enough for this work. On the other hand, the collective peak current of the parallel IFCs (which was a constant under the fixed average active and reactive powers, as proved in Chapter 4) was not shared among the IFCs based on their power ratings. Therefore, some IFCs worked at their rating limits while the others operated far from their rating limits. To address the above current-sharing concern, this chapter aims at sharing the active power oscillations cancellation and collective peak current among parallel IFCs.

In this chapter, two new control strategies for parallel three-phase IFCs with unity power factor (PF) operation under unbalanced voltage in hybrid AC/DC microgrids are proposed. Such parallel IFCs can be AC and DC-subsystems IFCs or can be used to connect DGs/SEs to an AC subsystem in hybrid microgrids. The

[1] Publication out of this chapter:

- F. Nejabatkhah, Y. W. Li., K. Sun, and S. Qiong "Operation of Parallel Interfacing Converters under Unbalanced Voltage: Active Power Oscillation Cancellation with Peak Current Sharing", *IEEE Transactions Power Electronics, Conditional Accepted, Under Final Review*.

proposed control strategies focus on cancelling the active power oscillations, sharing the collective peak current of the parallel IFCs among them based on their power ratings, and maximizing the power/current transferring capability of parallel IFCs. Moreover, the proposed control strategies provide non-adjustable unbalanced voltage compensation. In the first proposed control strategy, the IFCs' power coefficients are controlled by solving a set of nonlinear equations, and this method is called the coefficient-based strategy. In the second proposed control strategy, the peak currents of IFCs are controlled directly through the derived relationship of the IFCs' peak currents under zero power oscillation, and this method is called the peak current-based strategy. This strategy features much simplified calculations and could be easily applied online.

In this chapter, maximizing the power/current transferring capability of n-parallel IFCs under an unbalanced condition is investigated. Based on the study, it is proven the collective peak current of IFCs is a constant under zero total active power oscillation, and therefore keeping all IFCs' peak currents in the same phase and in-phase with the collective peak current optimizes the utilization range of parallel IFCs (maximize the power/current transferring capability). Both simulation and experimental results are provided.

5.1 Parallel Three-Phase IFCs Instantaneous Power Analysis under Unity PF Operation

In Figure 5.1, n-parallel three-phase IFCs operating under unity power factor with common DC and AC links is shown. In this figure, "p" refers to unity PF operation of IFCs. Similar to Chapter 4, in this Chapter the calculated reference current in Section 2.2.2 of Chapter 2 is used to control adverse effects of unbalanced voltage on IFC operation. From (2.21), the calculated reference current for individual three-phase IFC under unity PF operation is provided in following again:

$$i_{pi}^{*} = i_{pi}^{+} + i_{pi}^{-} = \frac{P_i}{|v^{+}|^2 + k_{pi}|v^{-}|^2} v^{+} + \frac{P_i k_{pi}}{|v^{+}|^2 + k_{pi}|v^{-}|^2}\, v^{-} \tag{5.1}$$

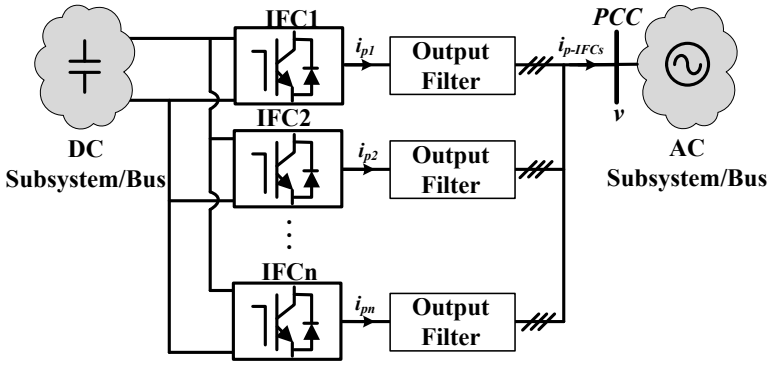

Figure 5.1 Parallel three-phase interfacing converters with common DC and AC links under unity power factor operation.

Considering (5.1), individual i^{th}-IFC's instantaneous active and reactive powers under unity PF operation can be achieved using (2.3) and (2.4) as:

$$p_i = P_i + \Delta P_i = P_i + \frac{P_i\left(1 + k_{pi}\right)(v^+.v^-)}{|v^+|^2 + k_{pi}|v^-|^2} \tag{5.2}$$

$$q_i = \Delta Q_i = \frac{P_i\left(1 - k_{pi}\right)(v^+.v_\perp^-)}{|v^+|^2 + k_{pi}|v^-|^2} \tag{5.3}$$

These relations can also be derived from (4.1) to (4.3) under $Q_i = 0$. From (5.1) to (5.3), it can be concluded that under unbalanced condition (1) individual IFC's output active and reactive powers will oscillate, (2) IFC's output current will increase in the fixed average active power output, (3) $k_{pi} = -1$ results in zero active power oscillation of i^{th}-IFC, and (4) $k_{pi} = 0$ provides balanced output current of i^{th}-IFC. All these discussions can be verified by the provided example in Figure 4.2(a) of Chapter 4.

From (5.1) to (5.3), for n-parallel IFCs with common DC and AC links under unity PF operation (see Figure 5.1), the reference current vector and instantaneous active and reactive powers can be achieved as follows:

$$i_{p-IFCs}^* = \sum_{i=1}^{n} i_{pi}^* = \sum_{i=1}^{n} \frac{P_i}{|v^+|^2 + k_{p_i}|v^-|^2} v^+ + \sum_{i=1}^{n} \frac{P_i k_{p_i}}{|v^+|^2 + k_{p_i}|v^-|^2} v^- \tag{5.4}$$

$$p = \sum_{i=1}^{n} P_i + \sum_{i=1}^{n} \Delta P_i = \sum_{i=1}^{n} P_i + \sum_{i=1}^{n} \frac{P_i\left(1 + k_{p_i}\right)(v^+.v^-)}{|v^+|^2 + k_{p_i}|v^-|^2} \tag{5.5}$$

$$q = \sum_{i=1}^{n} \Delta Q_i = \sum_{i=1}^{n} \frac{P_i \left(1 - k_{p_i}\right)(v^+ . v_\perp^-)}{|v^+|^2 + k_{p_i}|v^-|^2} \tag{5.6}$$

From (5.5), to cancel out n-parallel IFCs' active power oscillations under unity PF, following constraint should be satisfied:

$$\sum_{i=1}^{n} \frac{P_i\left(1 + k_{pi}\right)(v^+ . v^-)}{|v^+|^2 + k_{pi}|v^-|^2} = 0 \Rightarrow \sum_{i=1}^{n} \frac{P_i}{|v^+|^2 + k_{pi}|v^-|^2} = \frac{\sum_{i=1}^{n} P_i}{|v^+|^2 - |v^-|^2} \tag{5.7}$$

By applying (5.7) into (5.4)-(5.6), the reference current vector and instantaneous active and reactive powers of n-parallel IFCs with unity PF operation under zero active power oscillations are obtained as:

$$i^*_{p-IFCs}\big|_{\Delta P=0} = \left(\sum_{i=1}^{n} i^*_{pi}\right)\Bigg|_{\Delta P=0} = \frac{\sum_{i=1}^{n} P_i}{|v^+|^2 - |v^-|^2} v^+ + \frac{-\sum_{i=1}^{n} P_i}{|v^+|^2 - |v^-|^2} v^- \tag{5.8}$$

$$p = \sum_{i=1}^{n} P_i \tag{5.9}$$

$$q = \frac{2(v^+ . v_\perp^-)}{|v^+|^2 - |v^-|^2} \sum_{i=1}^{n} P_i \tag{5.10}$$

Considering (5.8) to (5.10), the positive and negative sequences current as well as reactive power oscillation of parallel IFCs under unity PFs are independent from k_{pi} under zero active power oscillations, and they are just affected by $\sum_{i=1}^{n} P_i$ variations.

5.2 Parallel Three-Phase IFCs' Current/Power Transferring Capability

Here, current/power transferring capability of parallel IFCs is studied in detail. For that, a thorough study on individual and parallel IFCs' peak currents under unbalanced voltage is conducted. From the study, it is proven that if all individual IFCs' peak currents are kept in the same phase and in-phase as that of the collective peak current of parallel IFCs, their power/current transferring capability will be maximized. It is worth mentioning that as mentioned in Chapter

4, Section 4.2, parallel IFCs' collective peak current with fixed average active powers is a constant value under zero active power oscillations.

5.2.1 Peak current analysis of parallel IFCs under unity PF

For individual i^{th}-IFC under unity PF operation, considering reference current vector in (5.1) and assuming $v^+ = |v^+|e^{j(\omega t+\theta^+)}$, $v^- = |v^-|e^{j(-\omega t-\theta^-)}$, and $\rho = (\theta^+ - \theta^-)/2$, the locus of PCC positive and negative sequence voltage vectors and the output reference current vector are shown in Figure 5.2. In this figure, the big and small dashed circles are the locus of positive and negative sequence current vectors, and total reference current vector is shown by an ellipse.

Considering reference current ellipse in Figure 5.2, the maximum current at each phase of the individual i^{th}-IFC is the maximum projection of that ellipse on the abc axis [45]. Considering (5.1) and Figure 5.2, the projection of reference current ellipse on the abc axis can be derived as:

$$i_{xpi}^{*\prime} = \underbrace{\left(\frac{P_i|v^+|}{|v^+|^2 + k_{pi}|v^-|^2} + \frac{P_i k_{pi}|v^-|}{|v^+|^2 + k_{pi}|v^-|^2}\right)}_{I_{pLi}} cos\,\gamma\, cos(\omega t)$$
$$- \underbrace{\left(\frac{P_i|v^+|}{|v^+|^2 + k_{pi}|v^-|^2} - \frac{P_i k_{pi}|v^-|}{|v^+|^2 + k_{pi}|v^-|^2}\right)}_{I_{pSi}} sin\,\gamma\, sin(\omega t) \qquad x = a, b, c \tag{5.11}$$

where I_{pLi} and I_{pSi} are semi major and semi minor axis' lengths of ellipse. From (5.11), for individual i^{th}-IFC, maximum current at each phase, the peak current, and the phase angle of peak current under unity PF can be derived:

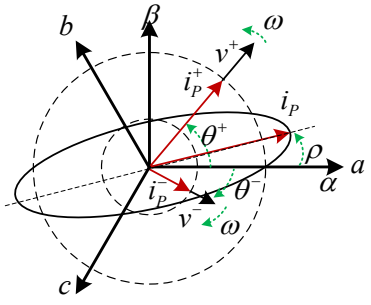

Figure 5.2 Locus of the PCC voltage and the i^{th}-IFC reference current vectors under unity power factor operation mode.

$$I_{xpi}^{max} = \sqrt{\left(\frac{P_i}{|v^+|^2 + k_{pi}|v^-|^2}\right)^2 \times \left(|v^+|^2 + |v^-|^2 k_{pi}^2 + 2|v^+||v^-|k_{pi}\cos(2\gamma)\right)} \quad (5.12)$$

$x = a, b, c$

$$I_{pi}^{max} = max\left(I_{api}^{max}, I_{bpi}^{max}, I_{cpi}^{max}\right) \quad (5.13)$$

$$\delta_i|_{I_{pi}^{max}} = \tan^{-1}\left(\cot\gamma\left(-1 - \frac{2k_{pi}|v^-|}{|v^+| - k_{pi}|v^-|}\right)\right) \quad (5.14)$$

where γ is rotation angle which is equal to ρ, $\rho + \pi/3$ and $\rho - \pi/3$ for abc axis, respectively. It should be mentioned that the aforementioned equations about individual IFC's peak current under unity PF operation can also be achieved from (4.19) to (4.21) when $Q_i = 0$. From (5.12) to (5.14), the individual IFC's maximum current at each phase and its peak current amplitude and phase angle depend on power coefficient and the PCC voltage components.

In a simulated case study in Figure 5.3, it is shown that how different values of k_{pi} affect maximum current at each phase and the peak current of individual IFC under different phase angles ρ and average active powers output. As seen from this figure, different values of k_{pi} and ρ lead peak current to different phases, which will be discussed in more details.

For n-parallel IFCs with unity PF operation under zero active power oscillations, the projection of collective reference currents ellipse on abc axis can be achieved using (5.8) and (5.11) as follows:

$$\begin{aligned} i_{xp-IFCs}^{*\prime}\big|_{\Delta P=0} = & \underbrace{\left(\frac{|v^+|\sum_{i=1}^n P_i}{|v^+|^2 - |v^-|^2} - \frac{|v^-|\sum_{i=1}^n P_i}{|v^+|^2 - |v^-|^2}\right)}_{I_{pL-IFCs}|_{\Delta P=0}} \cos\gamma\cos(\omega t) \\ & - \underbrace{\left(\frac{|v^+|\sum_{i=1}^n P_i}{|v^+|^2 - |v^-|^2} + \frac{|v^-|\sum_{i=1}^n P_i}{|v^+|^2 - |v^-|^2}\right)}_{I_{pS-IFCs}|_{\Delta P=0}} \sin\gamma\sin(\omega t) \quad x = a, b, c \end{aligned} \quad (5.15)$$

From (5.15), the collective maximum current in each phase, and the collective peak current and its phase angle can be obtained as follows:

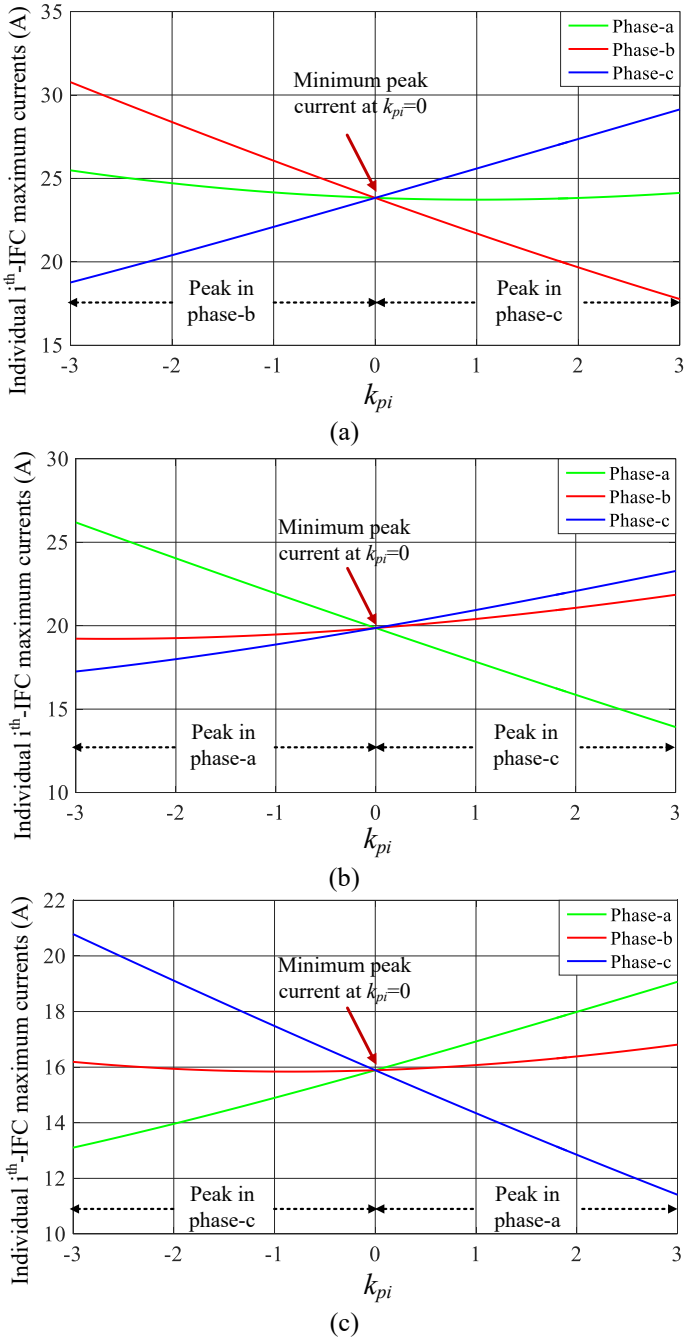

Figure 5.3 Individual i^{th}-IFC's maximum currents in *abc* phases under different k_{pi}, phase angle (ρ), and average active powers ($|v^+|$=168V, $|v^+|$=16V); (a) $\rho = 45$, P_i=6kW, (b) $\rho = 85$, P_i=5kW, and (c) $\rho = 160$, P_i=4kW.

$$I_{xp-IFCs}^{max}\big|_{\Delta P=0} = \sqrt{\left(\frac{\sum_{i=1}^{n} P_i}{|v^+|^2 - |v^-|^2}\right)^2 \times (|v^+|^2 + |v^-|^2 - 2|v^+||v^-|\,cos(2\gamma))} \quad x = a, b, c \tag{5.16}$$

$$I_{p-IFCs}^{max}\big|_{\Delta P=0} = max\left(I_{ap-IFCs}^{max}\big|_{\Delta P=0}, I_{bp-IFCs}^{max}\big|_{\Delta P=0}, I_{cp-IFCs}^{max}\big|_{\Delta P=0}\right) \tag{5.17}$$

$$\delta|_{I_{p-IFCs}^{max}|_{\Delta P=0}} = tan^{-1}\left(cot\,\gamma\left(-1 + \frac{2|v^-|}{|v^+| + |v^-|}\right)\right) \tag{5.18}$$

From (5.16) to (5.18), the parallel IFCs' collective peak current amplitude and phase angle under $\Delta P = 0$ are independent from k_{Pi}, and they are constant values with fixed active powers output.

5.2.2 Maximizing power/current transferring capability of parallel IFCs

As mentioned, under the unbalance condition, IFCs' output peak currents increase, and active power oscillation cancellation may worsen this situation. As a result, power/current transferring capability of IFCs is reduced. Here, it is proven that to maximize the power/current transferring capability of parallel IFCs under a given voltage condition (in other words to optimize the utilization range of parallel IFCs), peak currents of all individual IFCs should be kept in the same phase and in-phase with collective peak current of parallel IFCs.

In general, for n-parallel IFCs under various PFs, three phases current phasors based on maximum currents can be represented as follows:

$$\begin{aligned}
&I_{a1}^{max}\angle\delta_{a1}|_{I_{a1}^{max}} + I_{a2}^{max}\angle\delta_{a2}|_{I_{a2}^{max}} + \cdots + I_{an}^{max}\angle\delta_{an}|_{I_{an}^{max}} = I_{a-IFCs}^{max}|_{\Delta P=0}\angle\delta_a|_{I_{a-IFCs}^{max}|_{\Delta P=0}} \\
&I_{b1}^{max}\angle\delta_{b1}|_{I_{b1}^{max}} + I_{b2}^{max}\angle\delta_{b2}|_{I_{b2}^{max}} + \cdots + I_{bn}^{max}\angle\delta_{bn}|_{I_{bn}^{max}} = I_{b-IFCs}^{max}|_{\Delta P=0}\angle\delta_b|_{I_{b-IFCs}^{max}|_{\Delta P=0}} \\
&I_{c1}^{max}\angle\delta_{c1}|_{I_{c1}^{max}} + I_{c2}^{max}\angle\delta_{c2}|_{I_{c2}^{max}} + \cdots + I_{cn}^{max}\angle\delta_{cn}|_{I_{cn}^{max}} = I_{c-IFCs}^{max}|_{\Delta P=0}\angle\delta_c|_{I_{c-IFCs}^{max}|_{\Delta P=0}}
\end{aligned} \tag{5.19}$$

In (5.19), subscript "p" is not used since IFCs under different PFs are considered. It is worth mentioning again that $I_{x-IFCs}^{max}|_{\Delta P=0}$ (amplitude of collective maximum current of parallel IFCs in phase-x under $\Delta P = 0$) and $\delta_x|_{I_{x-IFCs}^{max}|_{\Delta P=0}}$ (phase angle of collective maximum current of parallel IFCs in phase-x under

$\Delta P = 0$) are constant values. Assuming that the phase angles of individual IFCs' maximum currents in each phase are equalized with the phase angle of collective maximum current of parallel IFCs in that phase $\left(\angle\delta_{x1}|_{I_{x1}^{max}} = \angle\delta_{x2}|_{I_{x2}^{max}} = \cdots = \delta_{xn}|_{I_{xn}^{max}} = \angle\delta_{x}|_{I_{x-IFCs}^{max}|_{\Delta P=0}}; x = a, b, c\right)$, (5.19) can be rewritten as follows:

$$\begin{aligned} I_{a1}^{max'} + I_{a2}^{max'} + \cdots + I_{an}^{max'} &= \sum_{i=1}^{n} I_{ai}^{max'} = I_{a-IFCs}^{max}|_{\Delta P=0} \\ I_{b1}^{max'} + I_{b2}^{max'} + \cdots + I_{bn}^{max'} &= \sum_{i=1}^{n} I_{bi}^{max'} = I_{b-IFCs}^{max}|_{\Delta P=0} \\ I_{c1}^{max'} + I_{c2}^{max'} + \cdots + I_{cn}^{max'} &= \sum_{i=1}^{n} I_{ci}^{max'} = I_{c-IFCs}^{max}|_{\Delta P=0} \end{aligned} \tag{5.20}$$

where superscript "′" refers to maximum currents values after phase angles' equalization. From (5.20), although phase angles equalization can reduce the summation of individual IFCs maximum currents in each phase ($\sum_{i=1}^{n} I_{xi}^{max'} \leq \sum_{i=1}^{n} I_{xi}^{max}; x = a, b, c$), it cannot guarantee the minimization of individual IFCs peak currents summation. In other words, it cannot guarantee to maximize power/current transferring capability of parallel IFCs without considering the phases that the peak currents are in. In more details, if it is assumed that m numbers of IFCs' peak currents are in the phase-*a*, u numbers are in the phase-*b*, and $n - m - u$ numbers are in the phase-*c* $(n \geq m + u)$, the following expression will be obtained:

$$\begin{aligned} \sum_{i=1}^{m} I_{ai}^{max'} + \sum_{i=m+1}^{m+u} I_{bi}^{max'} + \sum_{i=m+u+1}^{n} I_{ci}^{max'} &> I_{a-IFCs}^{max}|_{\Delta P=0} \\ \sum_{i=1}^{m} I_{ai}^{max'} + \sum_{i=m+1}^{m+u} I_{bi}^{max'} + \sum_{i=m+u+1}^{n} I_{ci}^{max'} &> I_{b-IFCs}^{max}|_{\Delta P=0} \\ \sum_{i=1}^{m} I_{ai}^{max'} + \sum_{i=m+1}^{m+u} I_{bi}^{max'} + \sum_{i=m+u+1}^{n} I_{ci}^{max'} &> I_{c-IFCs}^{max}|_{\Delta P=0} \end{aligned} \tag{5.21}$$

Therefore, considering (5.21), it is concluded that to minimize the summation of individual IFCs peak currents (which is equal to collective peak current of parallel IFCs; $min(\sum_{i=1}^{n} I_i^{max}) = I_{IFCs}^{max}|_{\Delta P=0}$) or in other words to maximize the

parallel IFCs power/current transferring capability, all individual IFCs' peak currents should be kept in the same phase and in-phase with parallel IFCs' collective peak current.

It is worth mentioning that this strategy can be used for parallel IFCs operating under different PFs. It should be also highlighted that, here, summation of n-parallel IFCs peak currents are minimized to maximize parallel IFCs power/current transferring capability, and the individual IFCs peak current values are not addressed directly. Although in most cases individual IFCs peak currents are reduced by this strategy, the distribution of peak current among parallel IFCs are not controlled. Considering this issue, in both proposed control strategies, individual IFCs peak currents will be adjusted based on their power ratings. As a result, not only parallel IFCs power/current transferring capability is maximized, but also individual IFCs operation is optimized.

Under unity PF operation, from (5.14) and (5.18), the phase angles of individual IFCs maximum currents in each phase depend on k_{pi} while in parallel IFCs under $\Delta P = 0$, the phase angles of collective maximum currents in each phase are independent from k_{pi}. However, since in parallel IFCs with common DC and AC links, $|v^+|$, $|v^-|$ and γ are common values in individual and parallel IFCs, and the variations of $\delta_{xi}|_{I_{xpi}^{max}}$ (when k_{pi} deviates from $k_{pi} = -1$) is small enough (under $k_{pi} = -1$, $\delta_{xi}|_{I_{xpi}^{max}} = \delta_x|_{I_{xp-IFCs}^{max}|_{\Delta P=0}}; x = a, b, c$), the $\delta_{xi}|_{I_{xpi}^{max}}$ in each phase can be assumed constant under k_{pi} variations and equal to $\delta_x|_{I_{xp-IFCs}^{max}|_{\Delta P=0}}$ with a good approximation. For more investigation, the variation of $\delta_{xi}|_{I_{xpi}^{max}}$ respect to k_{pi} deviation is derived as in (5.22) using (5.14).

$$\Delta\delta_{xi}|_{I_{xpi}^{max}} = \frac{-2|v^+||v^-|\cot\gamma}{\left(|v^+| - k_{pio}|v^-|\right)^2 + (\cot\gamma)^2 \times \left(|v^+| + k_{pio}|v^-|\right)^2}\Delta k_{pi} \qquad (5.22)$$

$x = a, b, c$

where k_{pio} is the initial operation point which is -1 in our case. From (5.22), it can be understood that $\Delta\delta_{xi}|_{I_{xpi}^{max}}$ over Δk_{Pi} is small value in each phase. As a numerical example, in 3-parallel IFCs with $P_1 = 6kW$, $P_2 = 2kW$, $P_3 = 3.6kW$,

$k_{pio} = -1$, $p = 55°$, $|v^+| = 168V$ and $|v^-| = 16V$, the deviation of $\delta_{xi}|_{I_{xpi}^{max}}$ in three abc phases from its initial point (where $k_{pi} = -1$ and $\delta_{xi}|_{I_{xpi}^{max}} = \delta_x|_{I_{xp-IFCs}^{max}|_{\Delta P=0}}; x = a, b, c$) under $\Delta k_{pi} = 2$ are $\Delta\delta_{ai}|_{I_{xpi}^{max}} \approx 8°$, $\Delta\delta_{bi}|_{I_{xpi}^{max}} \approx 6°$, and $\Delta\delta_{ci}|_{I_{xpi}^{max}} \approx 2°$. Therefore, it can be concluded that $\delta_{xi}|_{I_{xpi}^{max}} \approx \delta_x|_{I_{xp-IFCs}^{max}|_{\Delta P=0}}; x = a, b, c$ in the range of k_{pi} operation with a good approximation. However, as mentioned before, to guarantee maximum power/current transferring capability of parallel IFCs, all IFCs peak currents should also be in the same phase with collective peak current of parallel IFCs.

From (5.16), among three phases, the collective peak current of parallel IFCs is in the phase in which $\cos(2\gamma)$ has its minimum value. For individual i^{th}-IFC, the phase with minimum value of $\cos(2\gamma)$ will have the peak current if $k_{pi} < 0$ (see (5.14)). Since keeping all IFCs peak currents in the same phase with collective peak current of parallel IFCs is desired, all IFCs power coefficients are controlled to be less than zero ($k_{pi} < 0$). As a result, regardless of ρ and active power flow direction, all IFCs peak currents will be in the same phase with collective peak current of parallel IFCs. These discussions have been provided in Section 4.3.1 as well.

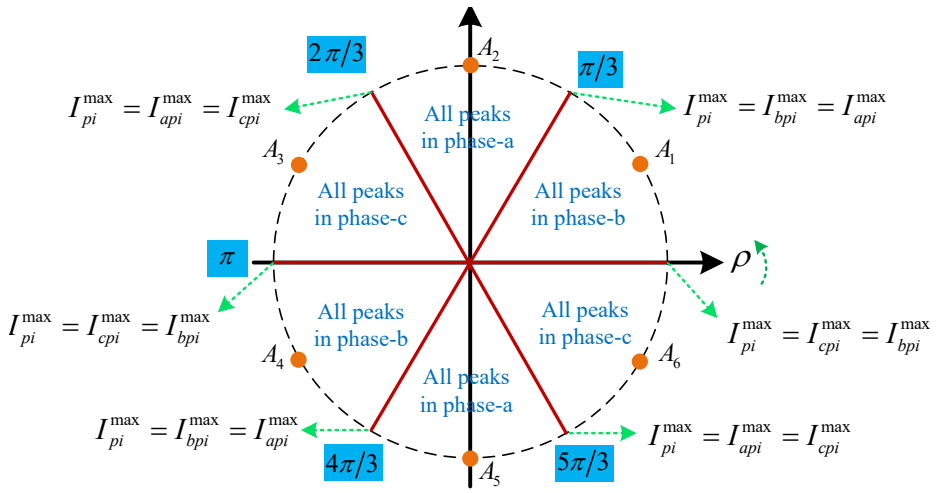

Figure 5.4 The phase of IFCs' peak currents in different values of ρ when $k_{pi}<0$ for all IFCs.

In Figure 5.4, the phase in which all IFCs peak currents and collective peak current of parallel IFCs are in that phase is shown under different values of ρ while $k_{pi} < 0$. From this figure and Figure 5.3, it is clear that the grid conditions in terms of different values of ρ affect which phase the peak currents are in. In following, more details are provided.

Considering (5.12) and Figure 5.4, in the grid condition that $\rho = i\pi/6\,;\ i = 1,3,5,7,9,11$, ($A_i; i = 1, \dots, 6$ operation points), individual IFCs' peak currents have their maximum possible values ($\cos(2\gamma)|_{I_{pi}^{max}} = -1$). It is worth mentioning that the range of $\cos(2\gamma)$ variations in the phase that all peak currents are in that phase is $-1 < \cos(2\gamma)|_{I_{pi}^{max}} < -0.5$ (see (5.12), Figure 5.3, and Figure 5.4). When ρ moves toward boundaries in $\rho = i\pi/3\,;\ i = 1, \dots, 6$, the peak currents of individual IFCs will reduce. At $\rho = i\pi/3\,;\ i = 1, \dots, 6$, the peak current of individual IFC will be equal to one of other phases' maximum current (see these points in Figure 5.4), and increasing ρ will lead the peak current to the other phase. For example, under $\rho = \pi/3$, the peak current, which is in phase-*b*, and the maximum current of phase-*a* are equal, and increasing ρ will lead the peak currents to phase-*a*. It should be mentioned that the results of Figure 5.4 verify the results of Figure 5.3.

With the aforementioned discussions, under $k_{pi} < 0; i = 1, \dots, n$, following relation among peak currents of individual IFCs and collective peak current of parallel IFCs with unity PF operation could be derived:

$$I_{p-IFCs}^{max} \cong \sum_{i=1}^{n} I_{pi}^{max} \tag{5.23}$$

From (5.23), two conclusions can be obtained; first, when $k_{pi} < 0; i = 1, \dots, n$, maximum power/current transferring capability of n-parallel IFCs under unity PF operation can be achieved, and second, the collective peak current of n-parallel IFCs, which is a constant value under fixed output active powers, can be shared linearly among individual IFCs.

5.3 Proposed Control Strategies for Parallel Three-Phase IFCs' Operation under Unbalanced Voltage: Active Power Oscillations Cancellation with Peak Current Sharing

Two control strategies are proposed for parallel IFCs operation with unity PF under unbalanced voltage, which reduce the adverse effects of unbalanced voltage on IFCs' operation. The proposed control strategies ensure zero collective active power oscillations, share the collective peak current among parallel IFCs based on their power/current ratings, and maximize the power/current transferring capability of n-parallel IFCs.

5.3.1 Coefficient-based control strategy

In this control strategy, in order to cancel out active power oscillations, to keep all IFCs peak currents in the same phase with collective peak current of parallel IFCs for maximizing power/current transferring capability, and to share collective peak current among n-parallel IFCs based on their ratings, the following expressions are considered:

$$\sum_{i=1}^{n} \frac{P_i}{|v^+|^2 + k_{p_i}|v^-|^2} = \frac{\sum_{i=1}^{n} P_i}{|v^+|^2 - |v^-|^2} \tag{5.24}$$

$$U_1 I_{p1}^{max} = U_2 I_{p2}^{max} = \cdots = U_n I_{pn}^{max} \tag{5.25}$$

$$U_i = \frac{S_1}{S_i} \qquad i = 1, 2, \dots, n \tag{5.26}$$

$$k_{pi} \leq 0 \qquad i = 1, 2, \dots, n \tag{5.27}$$

where I_{pi}^{max} is obtained using (5.13). Solving the set of non-linear equations in (5.24)-(5.26) considering (5.27), k_{pi} of all IFCs are determined. The determined k_{pi} of IFCs provide zero collective active power oscillation of parallel IFCs by (5.24), share collective peak current of parallel IFCs among them based on their power ratings using (5.25) and (5.26), and assure maximum power/current transferring capability of parallel IFCs by (5.27). If determined k_{pi} from (5.24)-

(5.26) are greater than zero, which lead IFCs peak currents to different phases, they will be set to zero and the calculation will be repeated for rest of IFCs' k_{pi} determinations. It is worth mentioning that the sharing factors in (5.26) are independent from the converters' operating points, and these factors provide the same available room for IFCs' operation. In this control strategy, since the control objectives are achieved by power coefficients control, this control strategy is named as coefficient-based control strategy.

The proposed control strategy is discussed in more details using example in Figure 5.5. In Figure 5.5, the relation between 2-parallel IFCs' peak currents and k_{pi} under the same average output active powers ($P_1 = P_2$) and different rating powers ($S_1 < S_2$) is shown. In this example, $I_{pi}^{max} - k_{pi}$ relations are assumed linear in the operation range (see Figure 5.3). The proposed control strategy initially sets k_{p1} and k_{p2} on -1 (point-1), where the active powers oscillation of both IFCs are zero.

In order to share the constant collective peak current of parallel IFCs (I_{p-IFCs}^{max}) between 2-parallel IFCs based on their power ratings (in other words, to satisfy (5.25)), the first IFC's peak current should be decreased and the second IFC's peak current should be increased toward point-2 (since $S_1 < S_2$). At point-2, although part of first IFC's peak current is shifted to the second IFC with larger

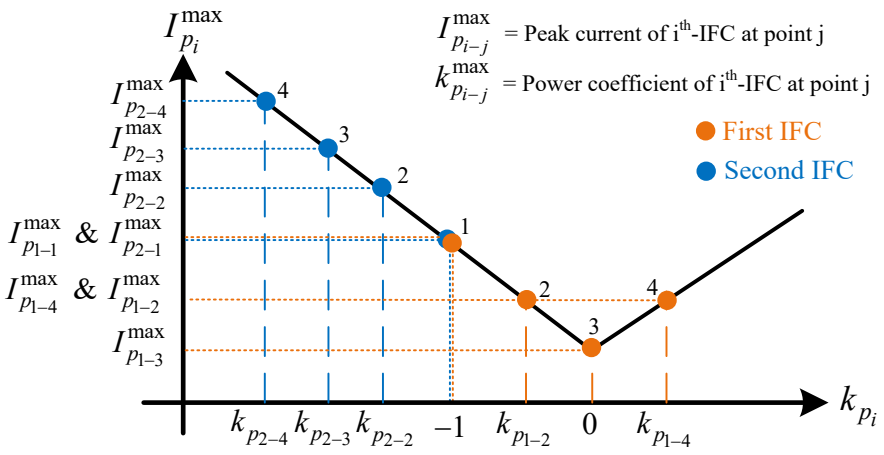

Figure 5.5 Example for explanation of the proposed control strategy; 2-parallel IFCs peak currents relation with k_{pi} under P_1=P_2 and S_1<S_2.

power rating (consider that I_{p-IFCs}^{max} is constant) and collective active power oscillation is zero, it is assumed that (5.25) is not satisfied, and the collective peak current has not been shared among IFCs based on their power ratings. As a result, the first IFC's peak current is reduced more which result in second IFC's peak current enhancement toward point-3. If (5.25) cannot be satisfied up to point-3 where $k_{p1} = 0$, k_{p1} will be set to zero and k_{p2} will be controlled to cancel out active power oscillation. Although sharing of collective peak current among 2-parallel IFCs may not be satisfied in point-3, all peak currents are in the same phase to provide minimum summation of peak currents of parallel IFCs and maximize the power/current transferring capability. For better explanation, assuming that (5.25) is satisfied at point-4 (where $\Delta P = 0$ and the first IFC peak current is not in the same phase with collective peak current). Comparing this operating point with point-2 clarifies that the summation of parallel IFCs peak currents at point-4 is greater that point-2 ($I_{p1-4}^{max} + I_{p2-4}^{max} > I_{p1-2}^{max} + I_{p2-2}^{max}$). Therefore, power/current transferring capability of parallel IFCs at point-4 is less than point-2 although the collective peak current is shared based on power ratings at point-4. In addition, at point-4, the higher active power oscillations of individual IFCs lead to greater circulating current than point-2. Therefore, in this control strategy, keeping IFCs peak currents in the same phase with collective peak current of parallel IFCs has the higher priority. Then, control strategy tries to share collective peak current among parallel IFCs based on their power/current ratings.

In general in this proposed control strategy, the operating point information of all IFCs and the PCC voltage are sent to the central controller for all IFCs' k_{P_i} determination. Due to computational complexity in solving the set of non-linear equations, the control strategy may not run online, and small delay may be imposed. The proposed control strategy will not have any errors in active power oscillation cancellation. However, under variation of IFCs' average active powers flow directions and values, the power coefficients of IFCs should be recalculated and updated.

5.3.2 Peak current-based control strategy

In order to reduce the computational burden of the first proposed control strategy, the peak current-based control strategy is proposed here. This control strategy is based on the conclusion that has been achieved from (5.23). In more details, the collective peak current of parallel IFCs under $\Delta P = 0$ is a constant value with fixed average active powers. Moreover, individual IFCs peak currents can be controlled to be in the same phase and in-phase with the collective peak current of parallel IFCs under unity PF operation. Thus, in order to cancel out active power oscillations, to keep individual IFCs peak currents in the same phase with collective peak current of parallel IFCs (which maximizes the power/current transferring capability), and to share constant collective peak current among parallel IFCs, following expressions are considered in the second proposed control:

$$I_{p1}^{max} + I_{p2}^{max} + \cdots + I_{pn}^{max} \cong I_{p-IFCs}^{max}\Big|_{\Delta P=0} \tag{5.28}$$

$$U_1 I_{p1}^{max} = U_2 I_{p2}^{max} = \cdots = U_n I_{pn}^{max} \tag{5.29}$$

where $I_{p-IFCs}^{max}\Big|_{\Delta P=0}$ and U_i are obtained using (5.17) and (5.26), respectively. In this control strategy, active power oscillation cancellation constraint is embedded in (5.28), and collective peak current sharing target is achieved using (5.29). From (5.28) and (5.29), the I_{pi}^{max} for individual i^{th}-IFC under $\Delta P = 0$ can be calculated as:

$$I_{pi}^{max} \cong \left(\frac{S_i}{S_1 + S_2 + \cdots + S_n}\right) \times I_{p-IFCs}^{max}\Big|_{\Delta P=0} \quad i = 1, \dots, n \tag{5.30}$$

After each IFC's reference peak current's calculation, k_{pi} can be determined using (5.12). Similarly, k_{pi} of all IFCs should be less than zero to keep all IFCs' peak currents in the same phase with collective peak current of parallel IFCs to minimize IFCs peak currents' summation and maximize power/current transferring capability of parallel IFCs. It is worth mention that the minimum possible value of I_{pi}^{max} is $P_i/|v^+|$ ($k_{pi} = 0$ in (5.12) and see Figure 5.3), and if

any calculated I_{pi}^{max} is less than $P_i/|v^+|$, it will be set to the limited value and the calculation will be repeated for rest of IFCs. In this control strategy, since IFCs' peak currents are directly controlled, this control strategy is named peak current-based control strategy.

Considering (5.12), it can be concluded that if $P_i/|v^+| \leq I_{pi}^{max} \leq P_i/|v^-|$, the $I_{pi}^{max} - k_{pi}$ quadratic equation will have two different real roots for k_{pi} under each determined I_{pi}^{max} and different values of γ. These two roots have different signs. As mentioned in this proposed method, all IFCs peak currents are controlled to be $I_{pi}^{max} \geq P_i/|v^+|$. In addition, $I_{pi}^{max} \leq P_i/|v^-|$ is always satisfied since $|v^-|$ is small percentage of $|v^+|$ [76], and $P_i/|v^-|$ exceeds the current rating limit of IFC. As a result, $P_i/|v^+| \leq I_{pi}^{max} \leq P_i/|v^-|$ is always satisfied, which leads to two districts real roots for k_{pi} with different signs.

As a numerical example, the $I_{pi}^{max} - k_{pi}$ quadratic equation variations $\left(f\left(k_{pi}, I_{pi}^{max}\right)\right)$ under fixed value of I_{pi}^{max} and different values of k_{pi} and γ are shown in Figure 5.6. As seen from the figure, for determined I_{pi}^{max}, the $f\left(k_{pi}, I_{pi}^{max}\right)$ quadratic equation has two real roots for k_{pi} with different signs (I_{pi}^{max} is in the aforementioned boundary). In this figure, the roots with positive

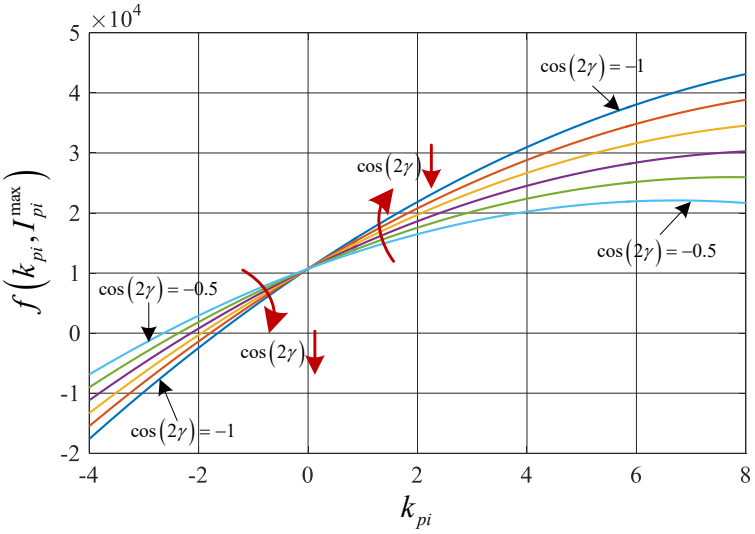

Figure 5.6 Numerical example for I_{pi}^{max}-k_{pi} quadratic equation variations under fixed value of $I_{pi}^{max} = 35A$ and different values of k_{pi} (k_{pi}: $-4 \longrightarrow 8$) and γ ($\cos 2\gamma$: $-1 : 0.1 : -0.5$); (*$|v^+|$=168V, $|v^+|$=16V, P_i=5kW*).

signs are not shown. From these discussions, it can be concluded that there is always a $k_{pi} < 0$ to satisfy calculated I_{pi}^{max} from (5.29), which keeps the i^{th}-IFC's peak current in the same phase with collective peak current of parallel IFCs.

In general, peak current-based control strategy reduces the computational burden of active power oscillation cancellation and collective peak current sharing of parallel IFCs, and can be run online in distributed control structure of parallel IFCs. Due to approximate calculations, the proposed control strategy may have small errors in active power oscillation cancellation. Similarly, individual IFCs' peak currents should be recalculated under variations of average active powers flow directions and values.

As mentioned before, in the first coefficient-based control strategy, all IFCs' k_{Pi} are generated in the central controller and sent to individual IFCs' local controllers while in the second peak current-based control strategy, the k_{Pi} of IFCs are generated individually in the outer control layer of IFCs' local controllers. These parameters are used to generate individual IFCs' reference currents using (5.1). In these control strategies, all parallel IFCs operate on power/current control mode in which the output currents of individual IFCs are controlled in the inner control loops to regulate output average powers on their reference values (see Figure 2.2).

5.4 Simulations and Experiments

Here, the effectiveness and performances of the two proposed control strategies under different operating conditions are verified by simulation and experimental results.

5.4.1 Simulation verification

The two proposed control strategies are applied into three parallel three-phase IFCs with unity PF operation, and simulated in MATLAB/Simulink. The simulated system parameters are shown in TABLE 5.1, which is the same as TABLE 4.1. In the simulation, at $t = 0.15s$ unbalance condition is applied to the system. As a result, individual and parallel IFCs' output active powers will

TABLE 5.1 System parameters for simulations.

	Symbol	Value
DC link voltage	v_{dc}	$800V$
IFCs' power ratings	S_i	$S_1 = 9kVA$ $S_2 = 4kVA$ $S_3 = 10kVA$
IFCs' current ratings	I_i^{rate}	$I_1^{rate} = 30A$ $I_2^{rate} = 13A$ $I_3^{rate} = 34A$
Grid voltage (rms) and frequency	$v_g - f_g$	$240V - 60Hz$
Grid coupling impedance	Z_{Grid}	$R_{Grid}: 0.2\Omega; X_{Grid}: 1.88\Omega$

oscillate and their peak currents will increase. Since during $0 < t < 0.3$, power coefficients are set to $k_{p1} = k_{p2} = k_{p3} = 0$, balance three-phase current is produced by IFCs. During $0.3 < t < 0.5$, parallel IFCs' power coefficients are initially set to $k_{p1} = k_{p2} = k_{p3} = -1$. Although the initial point provides zero active power oscillations of IFCs, the first IFC's current exceeds its rating limit. Moreover, the collective peak current is not shared among parallel IFCs based on their power ratings. Therefore, at $t = 0.5s$, the proposed control strategies are applied to control IFCs' peak currents not to exceed their rating limits, share collective peak current among three parallel IFCs, and cancel out total active power oscillation.

In these simulations, IFCs peak currents are kept in the same phase with collective peak current of parallel IFCs to maximize power/current transferring capability of parallel IFCs. In both simulations, during $t < 0.75$, average active powers of IFCs are set to $P_1 = 6kW$, $P_2 = 2kW$, and $P_3 = 3.6kW$, and at $t = 0.75s$, they are modified into $P_1 = 6.5kW$, $P_2 = 1.5kW$, and $P_3 = 4.5kW$.

5.4.1.1 Coefficient-based control strategy

The simulation results are shown in Figure 5.7 to Figure 5.12. As mentioned, in the initial operating point since the first IFC's peak current exceeds its rating limit and collective peak current is not shared among parallel IFCs based on their power ratings, the proposed control strategy is applied at $t = 0.5s$. Since the third

IFC's room for operation is greater than other two IFCs, the first IFC's peak current is shifted to third IFC, and the third IFC provides higher portion of collective peak current (see Figure 5.7 and Figure 5.8).

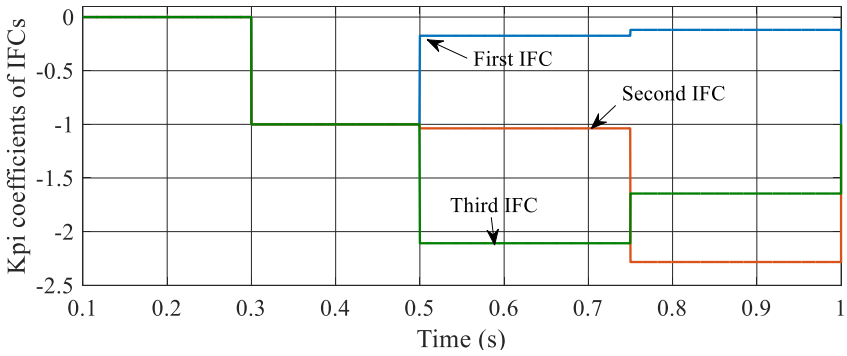

Figure 5.7 k_{pi} coefficient factors of the first, second, and third IFCs.

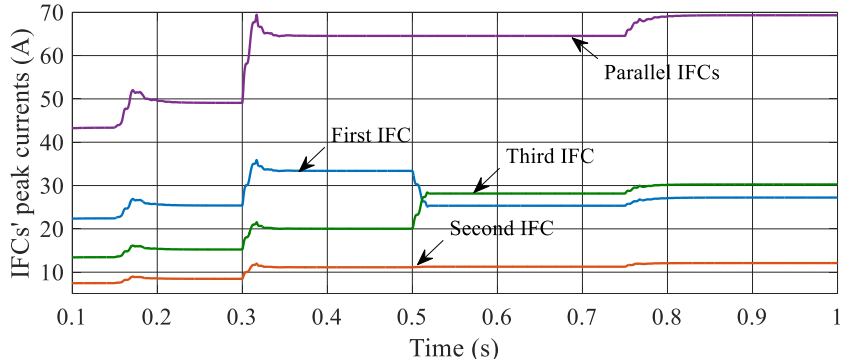

Figure 5.8 Peak currents' of IFCs.

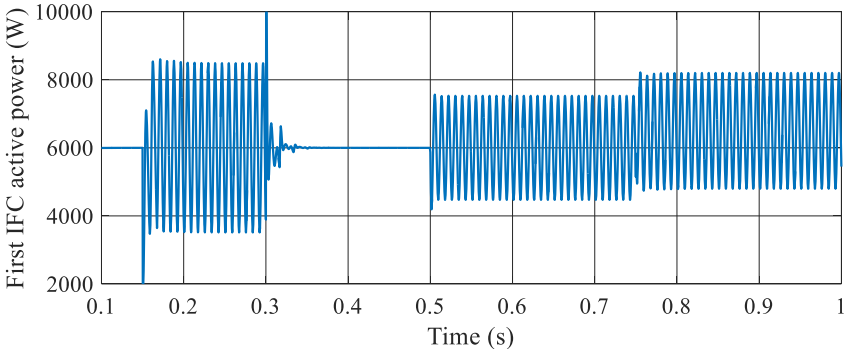

Figure 5.9 First IFC's output active power.

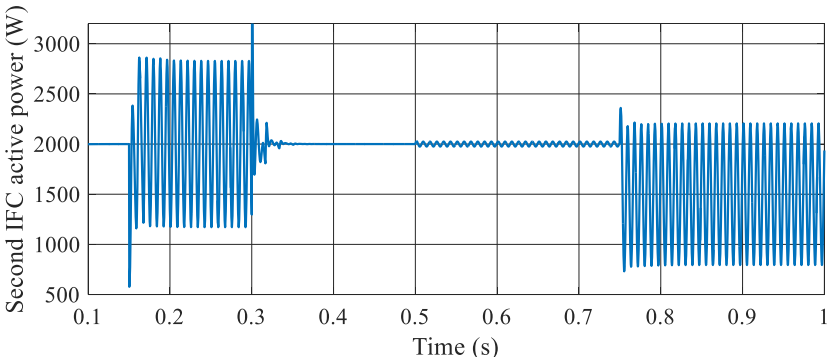

Figure 5.10 Second IFC's output active power.

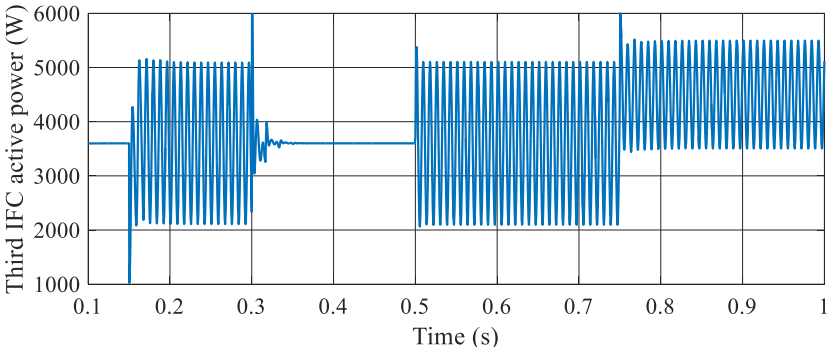

Figure 5.11 Third IFC's output active power.

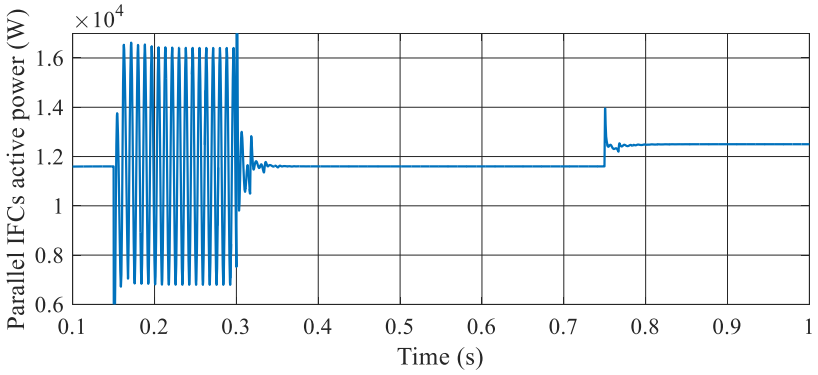

Figure 5.12 Parallel IFCs' collective active power.

Since collective peak current is independent from k_{pi} variations under zero active power oscillations, its value does not change at $t = 0.5s$. At $t = 0.75s$, as a result of $\sum_{i=1}^{3} P_i$ enhancement, collective peak current of parallel IFCs increases (see (5.16) and Figure 5.8). Also, the increased value is shared among three parallel IFCs based on their power ratings (see TABLE 5.1 and Figure 5.7 and Figure 5.8). In all operating points, the proposed control strategy provides zero collective active power oscillations, which is shown in Figure 5.12.

In this control strategy, since all k_{pi} are controlled to be less than zero (see Figure 5.7), all IFCs peak currents are in the same phase with collective peak current, which provides maximum power/current transferring capability for parallel IFCs. Moreover, total active power oscillation cancellation and collective peak current sharing among parallel IFCs are done without any error (see Figure 5.8 and Figure 5.12). This control strategy is running off-line; however, the calculation delays (at $t = 0.5s$ and $t = 0.75s$) have not been shown in simulation results.

5.4.1.2 Peak current-based control strategy

The similar test is repeated for the peak current-based proposed control strategy, and the results are provided in Figure 5.13 to Figure 5.19.

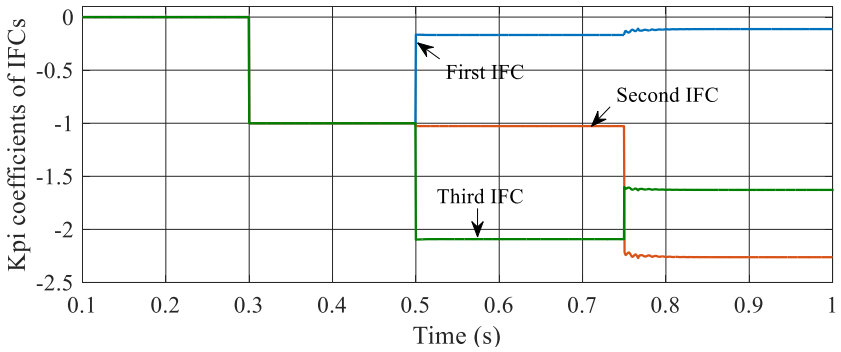

Figure 5.13 k_{pi} coefficient factors of the first, second, and third IFCs.

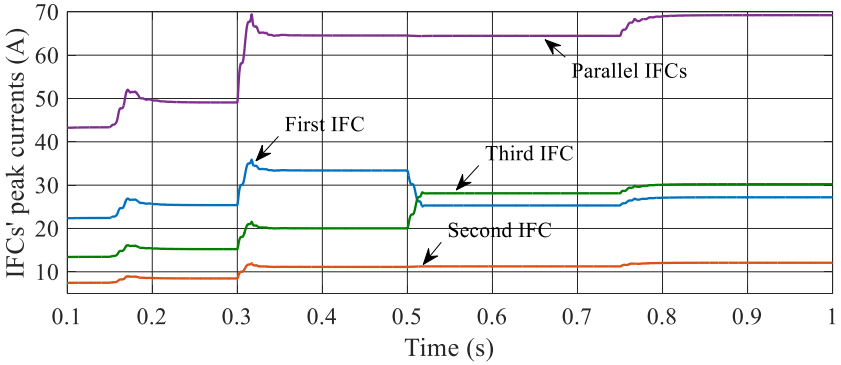

Figure 5.14 Peak currents' of IFCs.

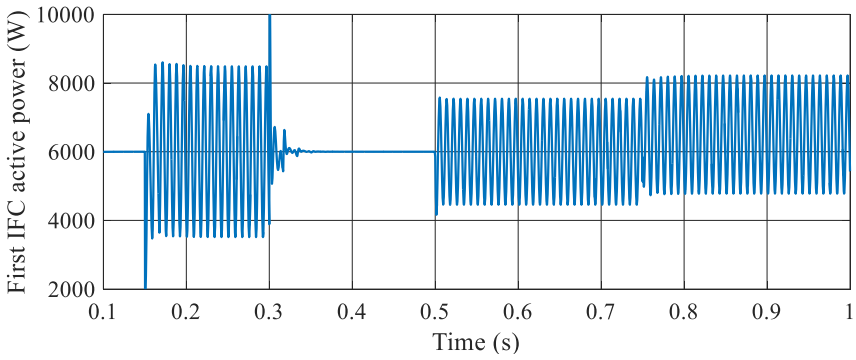

Figure 5.15 First IFC's output active power.

As seen from the results, the performances of the two proposed control strategies are approximately the same; (1) all IFCs peak currents are kept in the same phase with collective peak current of parallel IFCs (see Figure 5.13 where $k_{pi} < 0$), (2) collective peak current is shared among parallel IFCs, and third IFC's peak current's portion is higher than other two IFCs due to higher power rating and room for operation (see Figure 5.16), and (3) active power oscillations are collectively cancelled out (see Figure 5.18). This control strategy is running online. Also, due to use of approximation in peak currents' calculation, this control strategy induces small errors, which can be seen in Figure 5.18 ($\Delta P_{peak} = 38W$ during $0.5 < t < 0.75$ and $\Delta P_{peak} = 41W$ during $0.75 < t < 1$). The PCC negative sequence of voltage is shown in Figure 5.19, which confirms the improvement of the unbalanced conditions after proposed control strategy application.

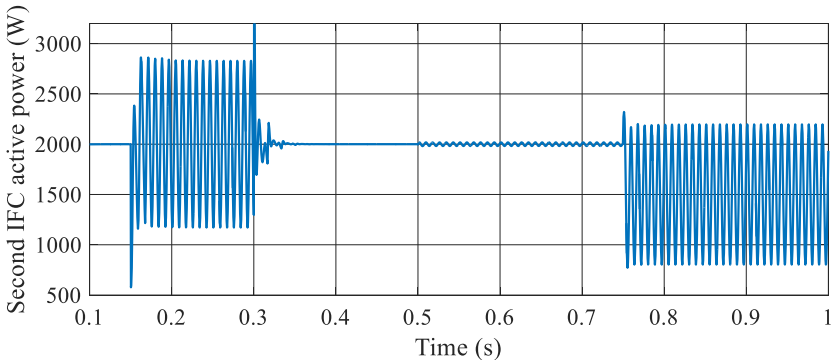

Figure 5.16 Second IFC's output active power.

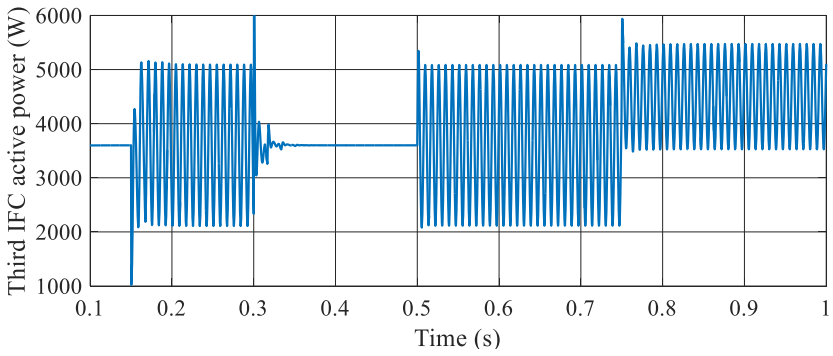

Figure 5.17 Third IFC's output active power.

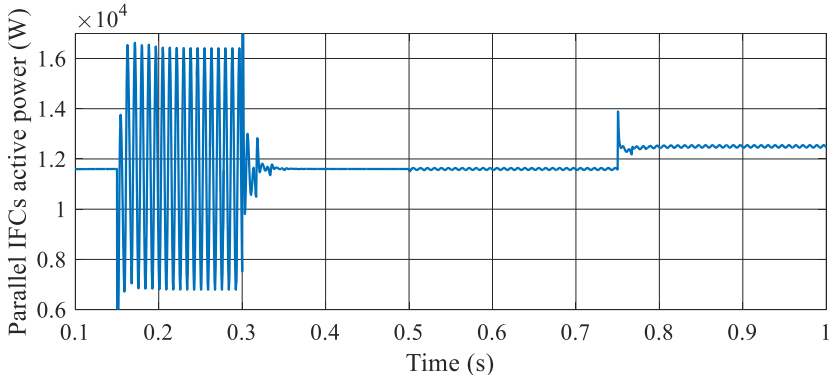

Figure 5.18 Parallel IFCs' collective active power.

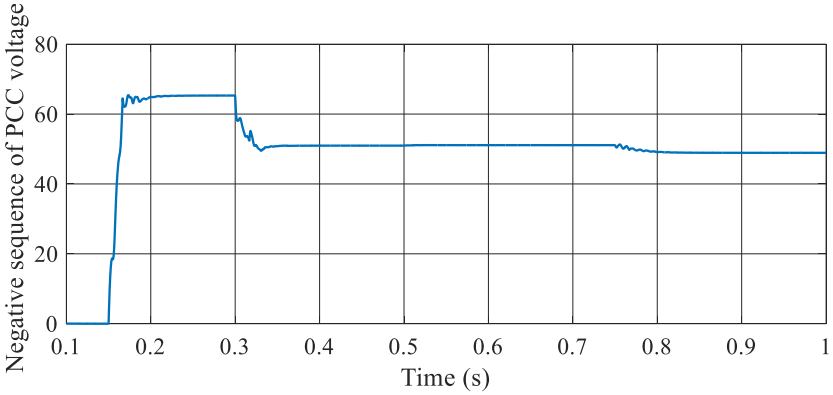

Figure 5.19 Negative sequence of PCC voltage.

5.4.2 Experimental verification

The online peak current-based control strategy is applied into two parallel three-phase IFCs' experimental setup to verify its performance under different operating conditions. In TABLE 5.2, the experimental setup specifications are listed. In the experiment, two-phase to ground fault is applied as a source of

unbalance condition. Moreover, the output currents of IFCs and grid voltage waveforms are measured by scopecorder (YOKOGAWA DL850E), and their saved data is used in MATLAB/Simulink to get powers waveforms.

Here, the average active powers of the first and second IFCs are set to $P_1 = 600W$ and $P_2 = 600W$. At the beginning, the power coefficient factors are set to $k_{p1} = k_{p2} = -1$, which leads to zero collective active power oscillations of parallel IFCs. Since the collective peak current of parallel IFCs is not shared among them based on their power ratings, the proposed control strategy is applied. The coefficient factor results are shown in Figure 5.20. From the results, it is clear that the proposed control strategy provides maximum power/current transferring capability for parallel IFCs since $k_{pi} < 0$. The collective peak current of parallel IFCs and the first and second IFCs' peak currents are shown in Figure 5.21. As clear from the figure, the parallel IFCs collective peak current is constant under fixed average active powers of IFCs. Moreover, this current is shared between IFCs based on their power ratings after proposed control strategy's application (since $S_1/S_2 \approx 4/3$, the first IFC provides higher portion of collective IFCs peak current; $I_{p1}^{max} \approx 4/3 \times I_{p2}^{max}$). It should be mentioned that before applying the proposed control strategy, since average active powers of IFCs are equal, and k_{p1} and k_{p2} are equal to -1, the individual IFCs peak currents values are the same. In Figure 5.22, the collective active power of parallel IFCs and active powers of the first and second IFCs are shown. As seen from the figure, after applying the proposed control strategy, the collective active power

TABLE 5.2 System parameters for experiments.

	Symbol	Value
DC link voltage	v_{dc}	$400V$
IFCs' power ratings	S_i	$S_1 = 1.4kVA; S_2 = 1kVA$
Unbalance grid voltage	v_g	$v_A = 55\angle 0°;$ $v_B = 83.8\angle 250.9°;$ $v_C = 83.8\angle 109.1°$
IFCs' output filters	L_f-C_f	$3.6mH$-$4\mu F$
Switching frequency	f_s	$10kHz$

oscillation remains zero. It is worth mentioning that small errors in active power oscillation cancellation are due to errors in voltage and current measurements.

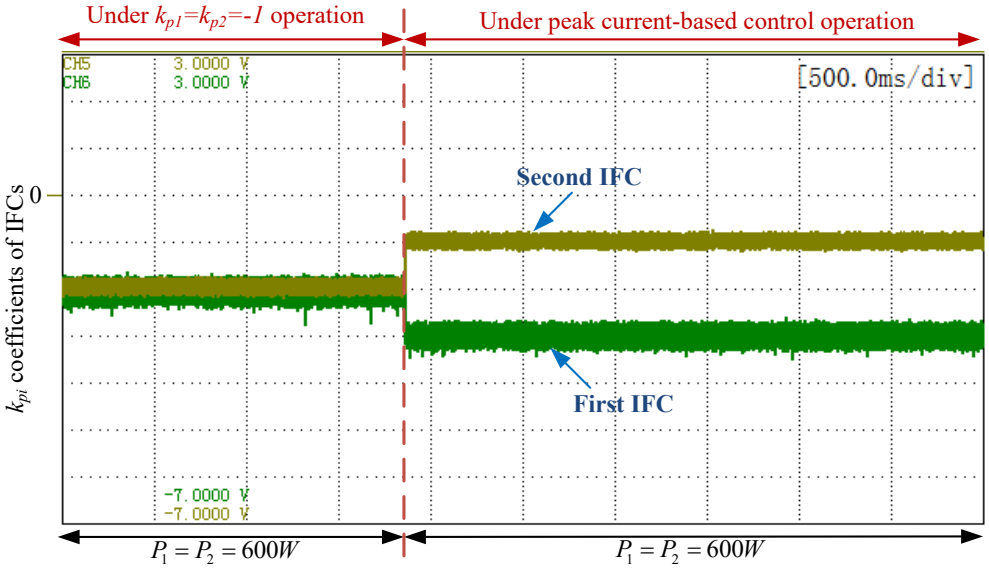

Figure 5.20 k_{p1} and k_{p2} coefficient factors, k_{p1} *(0.5/div)* and k_{p2} *(0.5/div)*; *(500ms/div)*.

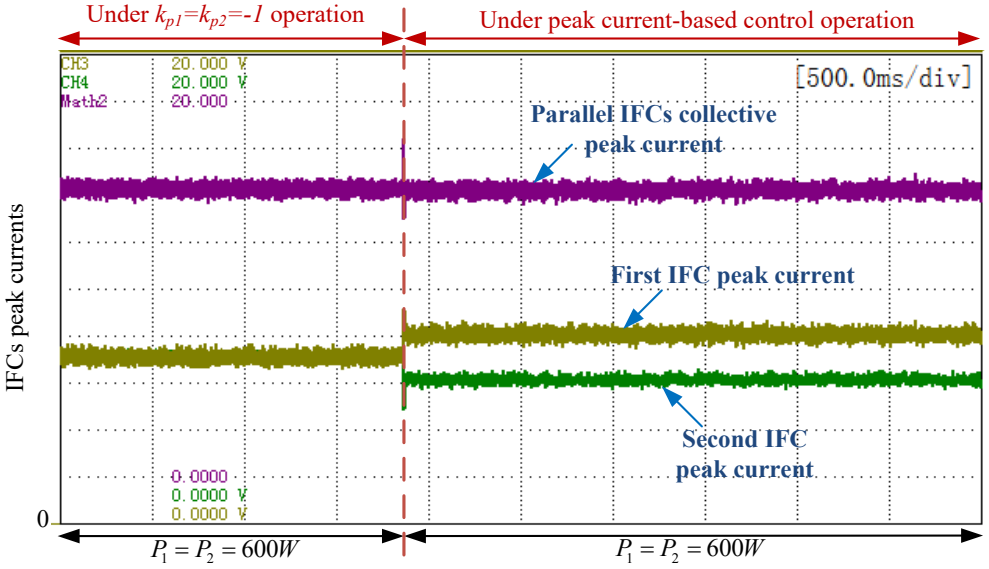

Figure 5.21 Peak currents' of individual IFCs and collective peak current of parallel IFCs; I_{p-IFCs}^{max}*(1A/div)*, I_{p1}^{max}*(1A/div)*, and I_{p2}^{max}*(1A/div)*; *(500ms/div)*.

5.5 Conclusion

In this chapter, two control strategies for parallel three-phase power electronics interfacing converters under unbalanced voltage in hybrid AC/DC microgrids were proposed to reduce the adverse effects of the unbalanced

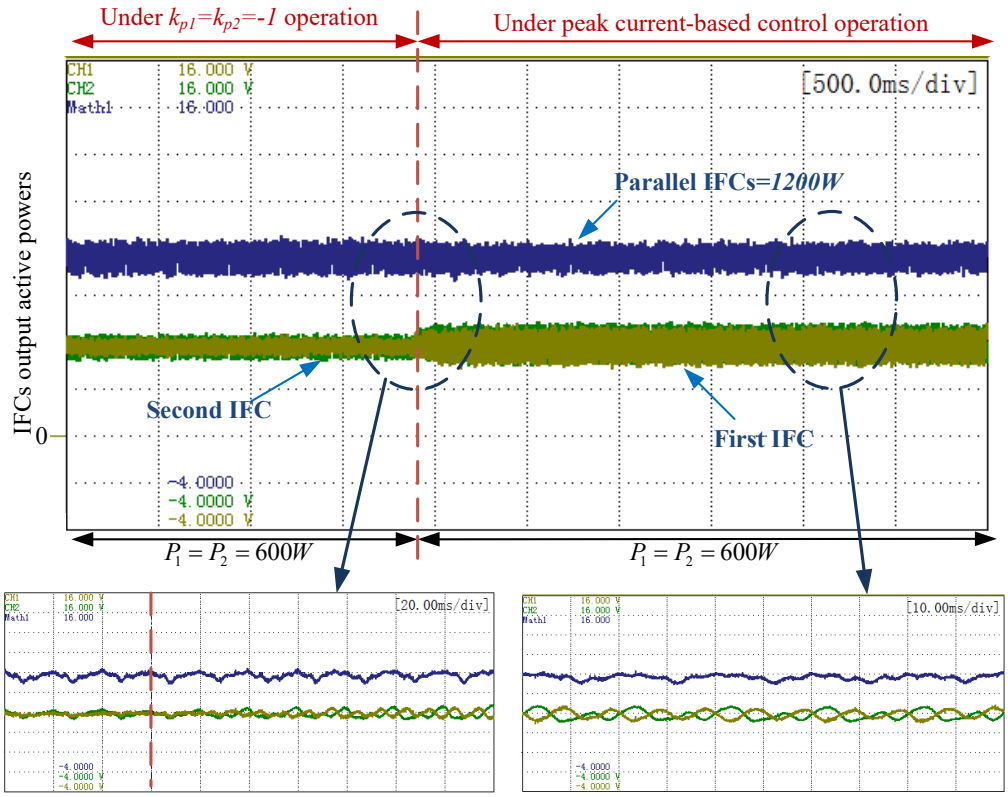

Figure 5.22 Parallel IFCs collective active power, and first and second IFCs output active powers.

condition on their operation. The proposed control strategies cancelled out the active power oscillation, shared the collective peak current among the IFCs based on their power ratings, and maximized the power/current transferring capability of the parallel IFCs. Both proposed control strategies are applicable for parallel IFCs under unity PF operation.

In the first proposed control strategy, the power coefficients of IFCs are controlled in a central control structure to achieve the objectives. Due to computational complexity and calculation delay, this control strategy may not be able to be run in real-time online. In the second proposed control strategy, the peak currents of IFCs are directly controlled. This control strategy, which can be implemented in a distributed control structure, can be easily run online due to the reduction of the computations' complexity. In this chapter, a thorough study of parallel IFCs' power/current transferring capability was conducted. After a detailed analysis of individual and parallel IFCs' peak currents, a strategy for

maximizing the power/current transferring capability of parallel IFCs was provided. The results showed that the power/current transferring capability of parallel IFCs was maximized when peak currents of all the individual IFCs and the collective peak current of parallel IFCs were in the same phase and in-phase. Both simulation and experimental results were obtained to verify the analysis and the two control strategies proposed in this chapter.

Chapter 6

Multiple Single-Phase Interfacing Converters Control for Flexible Compensation of Unbalanced Condition in Hybrid AC/DC Microgrids[1]

Due to the high penetration level of single-phase interfacing converters in hybrid AC/DC microgrids, there is a great opportunity for unbalanced voltage compensation. Such single-phase IFCs can be either DGs/SEs interfacing converters connected to the AC subsystem in AC-coupled or AC-DC-coupled hybrid microgrids, or AC and DC-subsystems interfacing converters in DC-coupled or AC-DC-coupled hybrid microgrids (it should be considered that DC subsystem can be connected to one of the phases of three-phase AC subsystem with a single-phase IFC). In this chapter, a new control strategy is proposed for single-phase IFCs to compensate for the unbalanced condition in hybrid AC/DC microgrids. The proposed control strategy focuses on flexible compensation of negative and zero sequences current in three-phase power systems. With the IFCs operating at given active power productions, the reactive powers of the single-phase IFCs are controlled in the proposed control strategy. The instantaneous power analysis from a single-phase perspective, which is developed in Section 2.3 of Chapter 2, is used to achieve the objective function for flexible compensation of the negative and zero sequences current. In the compensation strategy, the

[1] Publication out of this chapter:

F. Nejabatkhah and Y. W. Li "Flexible Unbalanced Compensation of Three-Phase Distribution System Using Single-Phase Distributed Generation Inverters", *IEEE Transactions on Smart Grid, Conditional Accepted, Under Final Review*.

voltage regulation of the three phases and also the available power ratings of IFCs are considered as constraints. The optimization problem is solved by using Karush–Kuhn–Tucker (KKT) method online due to its simplicity. The calculated reference reactive power of each phase from the optimization method is shared among the single-phase IFCs in that phase by considering their available power ratings. In this chapter, the influences of voltages regulation, IFCs available power ratings, and active power equalization among the phases of the proposed control strategy are studied. Finally, the proposed control strategy is evaluated under the IEEE 13-node test system.

6.1 Single-Phase IFCs Instantaneous Power Analysis and Active and Reactive Currents

Figure 6.1 shows a typical three-phase AC-coupled hybrid AC/DC microgrid including single-phase IFCs of PV systems. In general, the single-phase IFCs of hybrid microgrids can be AC and DC-subsystems interfacing converters or IFCs of DGs/SEs connected to the AC subsystem. Here, the hybrid system is connected to the grid at the point of common coupling (PCC). Also, it is assumed that the

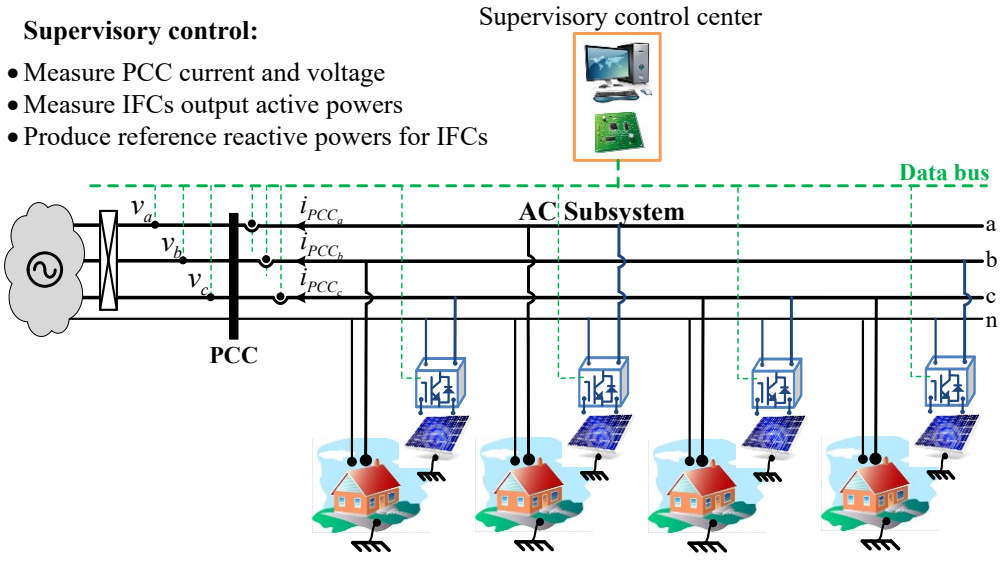

Figure 6.1 Three-phase AC-coupled hybrid AC/DC microgrid with single-phase IFCs.

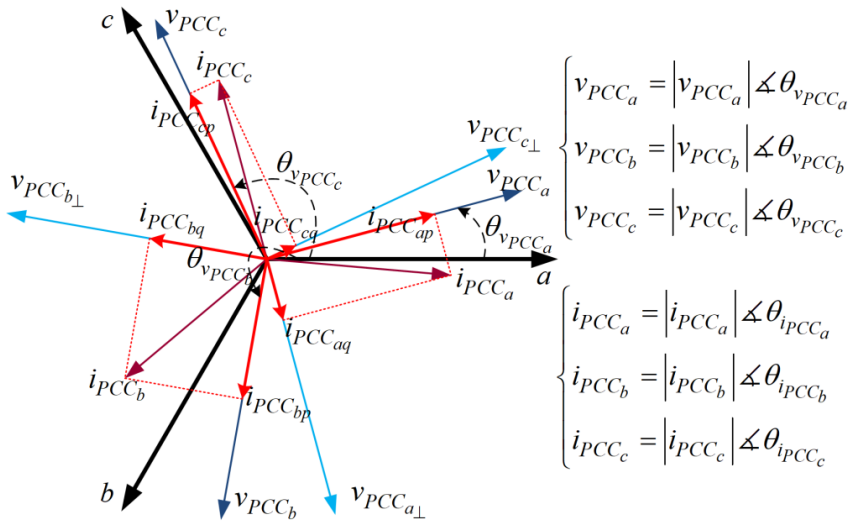

Figure 6.2 PCC voltage and current.

PCC three-phase voltages and currents are unbalanced due to single-phase loads and generators, shown in Figure 6.2.

In this chapter, the developed reference current of single-phase IFCs from the instantaneous power analysis from a single-phase perspective in Section 2.3 of Chapter 2 is used. As mentioned in Section 2.3, the reference current of single-phase IFCs can be controlled to exchange a certain amount of active and reactive powers with the grid in each phase under given voltage conditions. This reference current, which has been presented in (2.28), is provided in (6.1) again, in which $\left((P_{PCC,a}, Q_{PCC,a}), (P_{PCC,b}, Q_{PCC,b}), (P_{PCC,c}, Q_{PCC,c})\right)$ are exchanged with the grid.

$$i_{PCC} = \begin{bmatrix} i_{PCC_a} \\ i_{PCC_b} \\ i_{PCC_c} \end{bmatrix} = \begin{bmatrix} i_{PCC_{ap}} + i_{PCC_{aq}} \\ i_{PCC_{bp}} + i_{PCC_{bq}} \\ i_{PCC_{cp}} + i_{PCC_{cq}} \end{bmatrix} = \begin{bmatrix} \dfrac{P_{PCC,a}}{|v_{PCC_a}|^2} v_{PCC_a} + \dfrac{Q_{PCC,a}}{|v_{PCC_a}|^2} v_{PCC_{a\perp}} \\ \dfrac{P_{PCC,b}}{|v_{PCC_b}|^2} v_{PCC_b} + \dfrac{Q_{PCC,b}}{|v_{PCC_b}|^2} v_{PCC_{b\perp}} \\ \dfrac{P_{PCC,c}}{|v_{PCC_c}|^2} v_{PCC_c} + \dfrac{Q_{PCC,c}}{|v_{PCC_c}|^2} v_{PCC_{c\perp}} \end{bmatrix} \tag{6.1}$$

As mentioned, the three-phase unbalanced power system quantities can be replaced by positive, negative and zero sequences. Since negative and zero

sequences of active and reactive currents are addressed in this chapter, they will explain in more detail.

6.1.1 Negative sequence of active and reactive currents

From developed reference current in from (6.1), negative sequence component of PCC current vector can be derived as follows:

$$\begin{aligned} &\bar{i}_{PCC} = \bar{i}_{PCC_p} + \bar{i}_{PCC_q} = \\ &\frac{1}{3}\left(\frac{P_{PCC,a}}{\left|v_{PCC_a}\right|^2} v_{PCC_a} + \frac{P_{PCC,b}}{\left|v_{PCC_b}\right|^2} e^{j\frac{4\pi}{3}} v_{PCC_b} + \frac{P_{PCC,c}}{\left|v_{PCC_c}\right|^2} e^{j\frac{2\pi}{3}} v_{PCC_c} \right) + \\ &\frac{1}{3}\left(\frac{Q_{PCC,a}}{\left|v_{PCC_a}\right|^2} v_{PCC_{a_\perp}} + \frac{Q_{PCC,b}}{\left|v_{PCC_b}\right|^2} e^{j\frac{4\pi}{3}} v_{PCC_{b_\perp}} + \frac{Q_{PCC,c}}{\left|v_{PCC_c}\right|^2} e^{j\frac{2\pi}{3}} v_{PCC_{c_\perp}} \right) \end{aligned} \tag{6.2}$$

In (6.2), it is seen that the negative sequence of PCC current vector ($\bar{i}_{PCC}$) encompasses negative sequence components of active and reactive current vectors ($\bar{i}_{PCC_p}$ and $\bar{i}_{PCC_q}$). Also, it is concluded that unequal values of not only three-phase average active powers but also reactive powers cause negative sequence current. Assuming that the active current negative sequence $\left(\bar{i}_{PCC_p}\right)$ is constant, the reactive current negative sequence $\left(\bar{i}_{PCC_q}\right)$ can be controlled to reduce the value of $\bar{i}_{PCC}$. In other words, assuming constant average active powers, the reactive powers can be controlled to reduce/minimize the negative sequence current.

Considering (6.2), it is also concluded that equalizing average active powers in three phases could reduce negative sequence current. For example, when three phases average active powers are equalized $P_{PCC,a} \approx P_{PCC,b} \approx P_{PCC,c}$, the active current negative sequence value $\left(\bar{i}_{PCC_p}\right)$ goes down obviously. However, for minimizing the $\bar{i}_{PCC}$, the value of $\bar{i}_{PCC_q}$ should be considered at the same time.

For better illustration, the negative sequence model of hybrid system seen from the PCC is shown in Figure 6.3. As clear form the figure, $\bar{i}_{PCC_q}$ can be controlled to absorb $\bar{i}_{PCC_p}$ in order to reduce/minimize the value of $\bar{i}_{PCC}$. In the

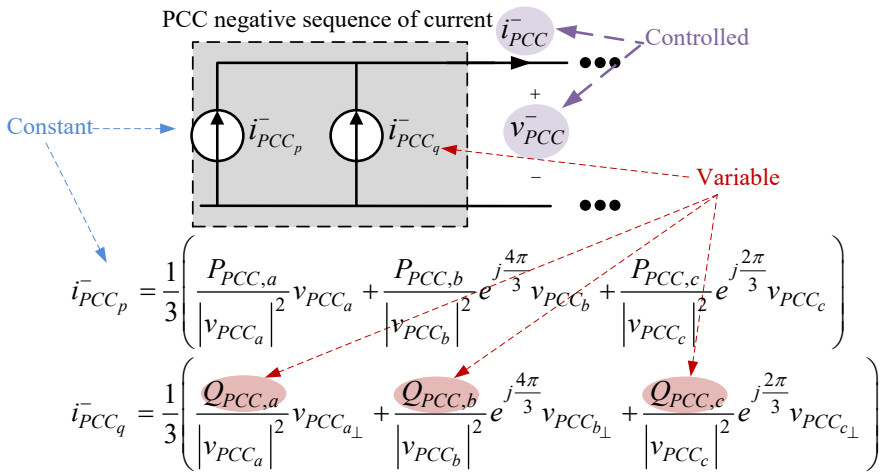

Figure 6.3 Negative sequence model of the system seen from the PCC.

proposed control strategy, reactive powers of single-phase IFCs will be controlled to absorb $i^{-}_{PCC_p}$, which will be discussed later. In case that $i^{-}_{PCC_q} = -i^{-}_{PCC_p}$, the negative sequence current is zero.

6.1.2 Zero sequence of active and reactive currents

The zero sequence component of PCC current vector can be achieved from the developed reference current in (6.1):

$$i^{0}_{PCC} = i^{0}_{PCC_p} + i^{0}_{PCC_q} = \frac{1}{3}\left(\frac{P_{PCC,a}}{\left|v_{PCC_a}\right|^2}v_{PCC_a} + \frac{P_{PCC,b}}{\left|v_{PCC_b}\right|^2}v_{PCC_b} + \frac{P_{PCC,c}}{\left|v_{PCC_c}\right|^2}v_{PCC_c}\right) + \frac{1}{3}\left(\frac{Q_{PCC,a}}{\left|v_{PCC_a}\right|^2}v_{PCC_{a\perp}} + \frac{Q_{PCC,b}}{\left|v_{PCC_b}\right|^2}v_{PCC_{b\perp}} + \frac{Q_{PCC,c}}{\left|v_{PCC_c}\right|^2}v_{PCC_{c\perp}}\right) \tag{6.3}$$

From (6.3), unequal values of three-phase average active powers and/or reactive powers produce zero sequence current. Assuming constant active current zero sequence $\left(i^{0}_{PCC_p}\right)$, the reactive current zero sequence $\left(i^{0}_{PCC_q}\right)$ can be controlled by three-phase reactive powers to reduce/minimize the value of i^{0}_{PCC}. Similarly, equalizing average active powers in three phases can reduce the zero

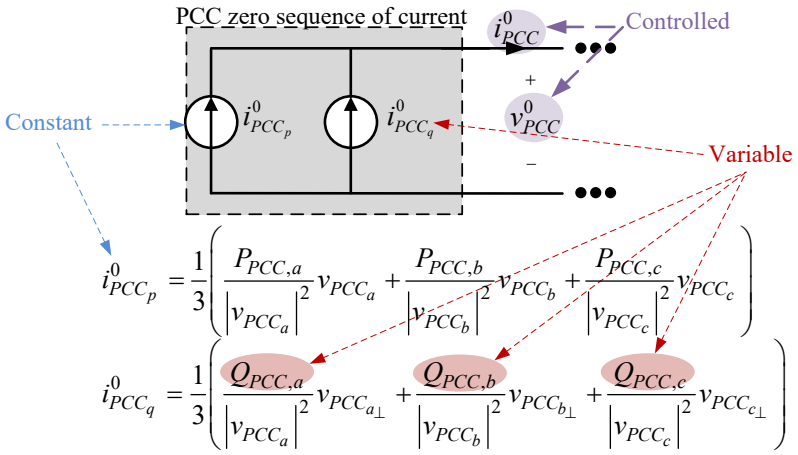

Figure 6.4 Zero sequence model of the system seen from the PCC.

sequence current (i^0_{PCC}), but it cannot realize the complete removal of zero sequence current.

In Figure 6.4, the zero sequence model of hybrid system seen from the PCC is shown. As seen from this figure, zero sequence of active current can be absorbed by $i^0_{PCC_q}$ (single-phase IFCs will be used) for compensation purposes, and the desired value of $i^0_{PCC_q}$ is $-i^0_{PCC_p}$ where i^0_{PCC} is zero.

6.2 Proposed Flexible Compensation of Negative and Zero Sequences Current in Hybrid AC/DC Microgrids using Multiple Single-Phase IFCs

In this Chapter, flexible compensation of negative and zero sequences current in hybrid AC/DC microgrids using single-phase IFCs is proposed. In the proposed method, single-phase IFCs are controlled under constant active power for unbalanced compensation. In this section, the objective function for flexible compensation is achieved from the developed instantaneous power analysis from the single-phase perspective and the resultant reference current. In the compensation strategy, voltage regulation of three phases and available reactive powers of IFCs are considered. The required reactive power of each phase for compensation purpose is shared among its IFCs based on their available power ratings.

6.2.1 Objective function

6.2.1.1 Negative sequence current compensation

In other to minimize the negative sequence component of PCC current vector ($\bar{i_{PCC}}$) in (6.2), the square of its amplitude is defined as an objective function for minimization as follows:

$$F_1\left(Q_{PCC,a}, Q_{PCC,b}, Q_{PCC,c}\right) = C_1 Q_{PCC,a}^2 + C_2 Q_{PCC,b}^2 + C_3 Q_{PCC,c}^2 + C_4 Q_{PCC,a} Q_{PCC,b} + C_5 Q_{PCC,a} Q_{PCC,c} + C_6 Q_{PCC,b} Q_{PCC,c} + C_7 Q_{PCC,a} + C_8 Q_{PCC,b} + C_9 Q_{PCC,c} + C_{10} \quad (6.4)$$

where C_1 to C_{10} are constant values at each operating points, which are provided in Appendix A, and $Q_{PCC,a}$, $Q_{PCC,b}$, and $Q_{PCC,c}$ are three control variables for minimization purposes.

6.2.1.2 Zero sequence current compensation

To minimize the zero sequence component of the PCC current (i_{PCC}^0), the objective function in (6.5) is defined, which is the square of zero sequence current amplitude in (6.3). Similar to (6.4), three control variables $Q_{PCC,a}$, $Q_{PCC,b}$, and $Q_{PCC,c}$ are adjusted for minimization purposes. Also, D_1 to D_{10} are constant values at each operating points, provided in Appendix A.

$$F_2\left(Q_{PCC,a}, Q_{PCC,b}, Q_{PCC,c}\right) = D_1 Q_{PCC,a}^2 + D_2 Q_{PCC,b}^2 + D_3 Q_{PCC,c}^2 + D_4 Q_{PCC,a} Q_{PCC,b} + D_5 Q_{PCC,a} Q_{PCC,c} + D_6 Q_{PCC,b} Q_{PCC,c} + D_7 Q_{PCC,a} + D_8 Q_{PCC,b} + D_9 Q_{PCC,c} + D_{10} \quad (6.5)$$

6.2.1.3 Flexible negative and zero sequences current compensation

From (6.4) and (6.5), to flexibly compensate the negative and zero sequence components of the PCC current, the objective function in (6.6) is defined to be minimized. In (6.6), k^- and k^0 are two controllable weighting factors that are related as (6.7).

$$F\left(Q_{PCC,a},Q_{PCC,b},Q_{PCC,c}\right)=k^{-}F_1\left(Q_{PCC,a},Q_{PCC,b},Q_{PCC,c}\right)+ k^{0}F_2\left(Q_{PCC,a},Q_{PCC,b},Q_{PCC,c}\right) \quad (6.6)$$

$$k^{-}+k^{0}=1 \quad (6.7)$$

From (6.6) and (6.7), k^{-} and k^{0} can be controlled to flexibly compensate the negative and zero sequences current to keep them in their desired level. For example, when $k^{-}=1(k^{0}=0)$, three variables $Q_{PCC,a}$, $Q_{PCC,b}$, and $Q_{PCC,c}$ are controlled to minimize the negative sequence current; otherwise $k^{-}=0(k^{0}=1)$ leads to minimization of zero sequence current. In case that $k^{-}\neq 1$ and $k^{0}\neq 1$, both negative and zero sequences current are compensated in which their compensation levels are determined by k^{-} and k^{0}.

For better clarification of weighting factors effect on the compensation scheme, a numerical example is provided in Figure 6.5. In this example, the reactive powers of three phases in IEEE standard 13-node test system [77] are controlled by integrated single-phase DGs interfacing converters (one single-phase DG per phase) under different values of k^{-} and k^{0} (the optimization problem is solved in each point, which will be discussed later). As seen in Figure 6.5, when $k^{-}=1(k^{0}=0)$, the negative sequence current is minimized ($|i_{PCC}^{-}|$ reduced from $102A$ to $9A$), and when $k^{-}=0(k^{0}=1)$, the current zero sequence is minimized ($|i_{PCC}^{0}|$ reduced from $75A$ into $6A$). In cases that $k^{-}\neq 1$ and $k^{0}\neq 1$, the objective function minimization provides minimum possible values for negative and zero sequences current based on defined weighting factors. Therefore, the weighting factors can be controlled to keep the negative and zero sequences current on their desired limits.

In Figure 6.6, the phasor diagrams of negative and zero sequences current are shown when (a) negative sequence current is minimized and (b) zero sequence current is minimized (the same results of Figure 6.5 in $k^{-}=1(k^{0}=0)$ and $k^{-}=0(k^{0}=1)$ points). From the figure, it is concluded that (1) under negative sequence minimization, the controlled $i_{PCC_q}^{-}$ cancels out $i_{PCC_p}^{-}$, which leads to i_{PCC}^{-}

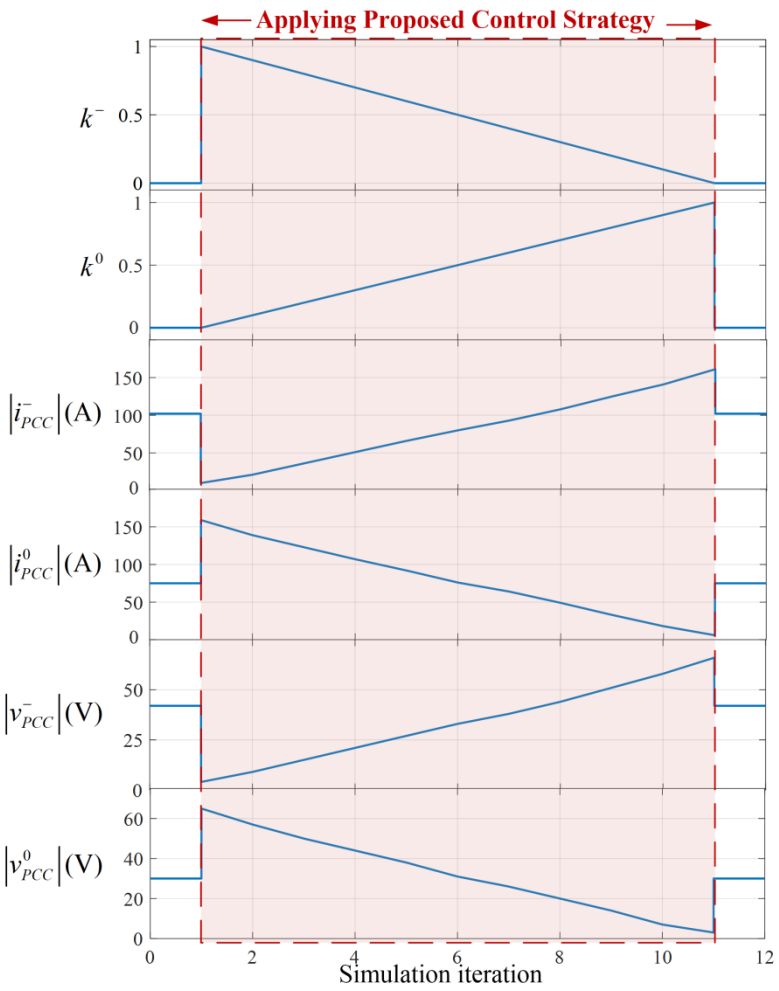

Figure 6.5 Example of k^- and k^0 variations effect on the proposed control strategy in IEEE standard 13-node test system.

minimization, but the resultant $i^0_{PCC_q}$ increases the i^0_{PCC}, (2) under zero sequence minimization, although controlled $i^0_{PCC_q}$ could compensate $i^0_{PCC_p}$ and minimize the i^0_{PCC}, the resultant $i^-_{PCC_q}$ increases i^-_{PCC}.

6.2.2 Constraints

In the proposed strategy, three control variables ($Q_{PCC,a}$, $Q_{PCC,b}$, and $Q_{PCC,c}$) are restricted considering phase voltages regulation and IFCs available reactive power ratings.

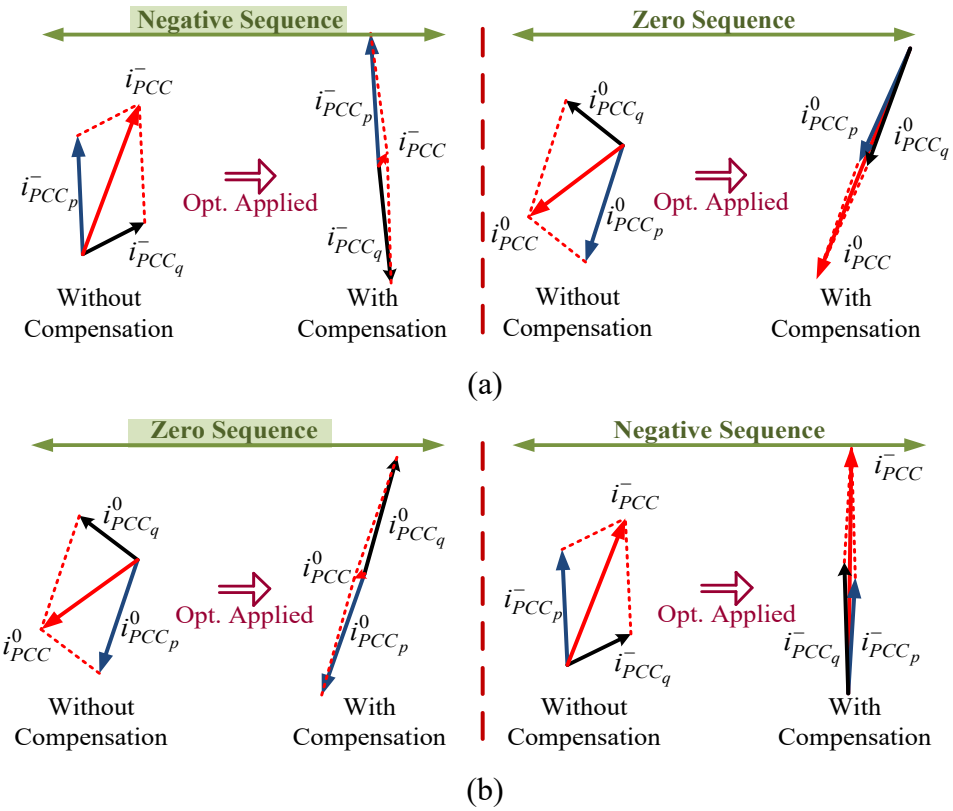

Figure 6.6 Phasor diagram of negative and zero sequences of the PCC current under a) negative sequence current minimization $k^{-}=1(k^{0}=0)$ and b) zero sequence current minimization $k^{-}=0(k^{0}=1)$.

6.2.2.1 Voltage regulation

In general, three phases voltage regulation cannot guarantee the unbalanced voltage compensation, and also unbalanced voltage compensation cannot guarantee all three phases voltage regulation [78]-[79] (more discussion will be provided in the Simulation section). As a result, in the proposed control strategy, voltage regulation of three phases is also considered in addition to flexible unbalanced compensation. To do that, the reactive power of each phase at the PCC is restricted between upper and lower limits to keep its voltage amplitude in the acceptable range. Considering Figure 6.1 and assuming that the PCC voltage phasor of phase-x is $|v_{PCC_x}|\angle\theta_{v_{PCC_x}}$, the grid voltage phasor of phase-x is $|v_{Grid_x}|\angle\theta_{v_{Grid_x}}$, and the grid coupling impedance of phase-x is $|Z_x|\angle\delta_x$, upper

and lower limits of phase-x reactive power for regulating its voltage between $\left|v_{PCC_x}^{min}\right| \le \left|v_{PCC_x}\right| \le \left|v_{PCC_x}^{max}\right|$ is achieved as [80]:

$$Q_{PCC,\mathrm{x}\ V-reg}^{\max} = \frac{\left(\left|v_{PCC_x}^{\max}\right|\right)^2}{\left|Z_x\right|}\sin\left(\delta_x\right) - \frac{\left|v_{PCC_x}^{\max}\right|\left|v_{Grid_x}\right|}{\left|Z_x\right|}\sin\left(\delta_x + \theta_{v_{PCC_x}} - \theta_{v_{Grid_x}}\right) \quad x = a,b,c \tag{6.8}$$

$$Q_{PCC,\mathrm{x}\ V-reg}^{\min} = \frac{\left(\left|v_{PCC_x}^{\min}\right|\right)^2}{\left|Z_x\right|}\sin\left(\delta_x\right) - \frac{\left|v_{PCC_x}^{\min}\right|\left|v_{Grid_x}\right|}{\left|Z_x\right|}\sin\left(\delta_x + \theta_{v_{PCC_x}} - \theta_{v_{Grid_x}}\right) \quad x = a,b,c \tag{6.9}$$

where $\left|v_{PCC_x}^{max}\right|$ and $\left|v_{PCC_x}^{min}\right|$ are maximum and minimum acceptable rms voltages of PCC in phase-x. Therefore, constraints in (6.10) should be considered for the PCC three phases voltage regulation.

$$Q_{PCC,\mathrm{x}\ V-reg}^{\min} \le Q_{PCC,\mathrm{x}} \le Q_{PCC,\mathrm{x}\ V-reg}^{\max} \qquad x = a,b,c \tag{6.10}$$

Considering (6.8) and (6.9), just the grid impedance in fundamental frequency is needed, which can be easily obtained using different methods [69]-[71]. Here, the impedance is considered as a known value in control system.

6.2.2.2 Maximum available reactive power of single-phase IFCs

In the proposed control strategy, since existing single-phase IFCs are used for unbalance compensation purposes, their maximum available reactive powers should be considered. Among different methods [78]-[79], in the proposed control strategy the nominal power rating of single-phase IFCs $\left(S_{DG_i}\right)$ and their operating active powers $\left(P_{DG_i}\right)$ are used for maximum available reactive power determination:

$$Q_{IFC_i}^{\max} = \pm\sqrt{S_{IFC_i}^2 - P_{IFC_i}^2} \tag{6.11}$$

After determining maximum available reactive powers of DGs at each phase, they are used to restrict the PCC reactive power injection/absorption capability in that phase:

$$Q^{\min}_{PCC,\mathrm{x}\ IFCs} \le Q_{PCC,\mathrm{x}} \le Q^{\max}_{PCC,\mathrm{x}\ IFCs} \qquad x = a,b,c \tag{6.12}$$

With reactive powers limitations considering voltages regulation (see (6.10)) and IFCs maximum available reactive powers (see (6.12)), their intersections are used to determine each phase reactive power constraint at the PCC:

$$\begin{aligned} &\max\left(Q^{\min}_{PCC,\mathrm{x}\ V-reg}, Q^{\min}_{PCC,\mathrm{x}\ IFCs}\right) \le Q_{PCC,\mathrm{x}} \le \min\left(Q^{\max}_{PCC,\mathrm{x}\ V-reg}, Q^{\max}_{PCC,\mathrm{x}\ IFCs}\right) \\ \Rightarrow \quad & Q^{\min}_{PCC,\mathrm{x}} \le Q_{PCC,\mathrm{x}} \le Q^{\max}_{PCC,\mathrm{x}} \qquad x = a,b,c \end{aligned} \tag{6.13}$$

6.2.3 Optimization problem solution

The developed objective function in (6.6) is a quadratic function that can be represented in the general form of $(1/2)x^T Px + q^T x + r$. This function is convex since P is positive semidefinite. The convex objective function subjected to convex linear constraints in (6.13) can be minimized using Karush–Kuhn–Tucker (KKT) method [68]. Using this method, following equation is achieved:

$$-\nabla F\left(Q_{PCC,x}\right) = \sum_{j=1}^{m} \mu_j \nabla g_j\left(Q_{PCC,x}\right) \qquad x = a,b,c \tag{6.14}$$

where m is number of inequality constraints (which is 6 from (6.13)), μ_j are KKT multipliers, and $g_j\left(Q_{PCC,x}\right)$ are inequality constraint functions, which are obtained using (6.13) as follows.

$$\begin{cases} g_j\left(Q_{PCC,x}\right) = Q_{PCC,x} - Q^{\max}_{PCC,x} \le 0 & (j,x) = (1,\mathrm{a}),(3,\mathrm{b}),(5,c) \\ g_j\left(Q_{PCC,x}\right) = -Q_{PCC,x} + Q^{\min}_{PCC,x} \le 0 & (j,x) = (2,\mathrm{a}),(4,\mathrm{b}),(6,c) \end{cases} \tag{6.15}$$

In this optimization method, the KKT multipliers $\left(\mu_j\right)$ should satisfy following equality and inequality functions:

$$\mu_j \ge 0 \qquad j = 1,\ldots,6 \tag{6.16}$$

$$\mu_j g_j\left(Q_{PCC,x}\right)=0 \qquad j=1,...,6 \tag{6.17}$$

Solving (6.14) considering (6.16) and (6.17), systems of three linear equations with three variables are obtained, which can be solved online easily due to their simplicity. Then, the determined reference reactive powers from optimization are shared among single-phase IFCs as follows.

6.2.4 Reactive power sharing among single-phase IFCs

Considering maximum available reactive powers of single-phase IFCs, the reference reactive power in each phase is shared among the single-phase IFCs in that phase as follows:

$$Q_{IFCs_x}=Q_{IFC1_x}+Q_{IFC2_x}+...+Q_{IFCr_x} \qquad x=a,b,c \tag{6.18}$$

$$T_{1_x}Q_{IFC1_x}=T_{2_x}Q_{IFC2_x}=...=T_{r_x}Q_{IFCr_x} \qquad x=a,b,c \tag{6.19}$$

$$T_{i_x}=\frac{Q_{IFC_{1_x}}^{\max}}{Q_{IFC_{i_x}}^{\max}} \qquad x=a,b,c \;\&\; i=1,...,r \tag{6.20}$$

where Q_{IFCs_x} is the total reference reactive powers of single-phase IFCs in phase-x, which is calculated from optimization problem results. Moreover, r_x is the number of single-phase IFCs in phase-x (they can be different in each phase), and T_{i_x} is the sharing factor of i^{th}-IFC in phase-x. Since T_{i_x} is based on maximum available reactive powers of IFCs, it provides the same available room for IFCs' operation.

In general, the proposed control strategy is a secondary controller that compensates the unbalanced condition of hybrid AC/DC microgrids in the steady-state operation mode. The three-phase currents and voltages at the PCC as well as operating active powers of single-phase IFCs are measured and sent to a supervisory control center (see Figure 6.1). In the supervisory control center, the optimization problem is solved online to determine the reference reactive powers of each single-phase IFC. The reference reactive powers are transferred into local

controllers of IFCs, which track reference active and reactive powers. It is worth mentioning that data communication is crucial in this control strategy. Moreover, the active powers of IFCs are not used for unbalanced compensation.

6.3 Simulation Verification

6.3.1 Test system

The proposed control strategy is applied into IEEE 13-node test system [77], which is shown in Figure 6.7. The configuration data of the test system is provided in Appendix B. In the test system, bus#632 is considered as PCC, which is connected to the main grid in bus#650 with over-head line and a transformer. Here, for simplicity, transformer between buses 632 and 650 is not considered, and the voltage of bus#650 is assumed balance with $1P.U.(v_{LL-rms} = 4.16kV)$. It is worth mentioning that the coupling impedance between buses 632 and 650 is the over-head line impedance (see Appendix B). In the original IEEE 13-node test system, the PCC current and voltage vectors positive, negative and zero sequence components are as follows:

$$\left|v_{PCC}^{+}\right| = 3487V;\ \left|v_{PCC}^{-}\right| = 22V\left(\%0.63\left|v_{PCC}^{+}\right|\right);\ \left|v_{PCC}^{0}\right| = 35V\left(\%1.01\left|v_{PCC}^{+}\right|\right) \tag{6.21}$$

$$\left|i_{PCC}^{+}\right| = 735\,A;\ \left|i_{PCC}^{-}\right| = 91\,A\left(\%12.3\left|i_{PCC}^{+}\right|\right);\ \left|i_{PCC}^{0}\right| = 67\,A\left(\%9.1\left|i_{PCC}^{+}\right|\right) \tag{6.22}$$

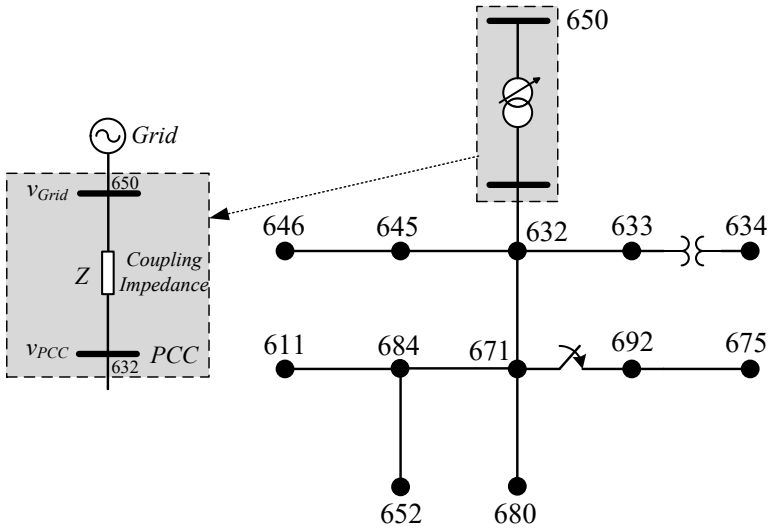

Figure 6.7 Configuration of IEEE 13-node test system.

TABLE 6.1 Distributed load modifications connected to Bus#671 (Model: Y-PQ).

	Phase-a	Phase-b	Phase-c
Old values	17kW-10kVAr	66kW-38kVAr	117kW-68kVAr
New values	400kW-0kVAr	300kW-0kVAr	1040kW-0kVAr

To worsen the unbalanced condition in the PCC in order to clearly illustrate the control strategy performance, distributed load connected to bus#671 is modified as shown in TABLE 6.1. Applying this modification, the PCC current and voltage vectors positive, negative and zero sequence components vary as follows:

$$\left|v_{PCC}^{+}\right| = 3181V;\ \left|v_{PCC}^{-}\right| = 64V\left(\%2.1\left|v_{PCC}^{+}\right|\right);\ \left|v_{PCC}^{0}\right| = 43V\left(\%1.35\left|v_{PCC}^{+}\right|\right) \tag{6.23}$$

$$\left|i_{PCC}^{+}\right| = 736A;\ \left|i_{PCC}^{-}\right| = 156A\left(\%21.2\left|i_{PCC}^{+}\right|\right);\ \left|i_{PCC}^{0}\right| = 104A\left(\%14.13\left|i_{PCC}^{+}\right|\right) \tag{6.24}$$

As another modification, single-phase DGs interfacing converters are connected to different buses, provided in more details in TABLE 6.2. As mentioned, in the proposed control strategy, only reactive powers of single-phase IFCs are controlled. Therefore, in the simulations, the IFCs active powers are assumed constant. From TABLE 6.2, constraints on the PCC reactive powers considering maximum available reactive powers of single-phase IFCs are achieved as follows (see (6.12)):

TABLE 6.2 Single-phase IFCs of DGs connected to IEEE 13-bus test system.

		Bus Number	Power rating of DGs inverters	Operating active power	Max available reactive power
Phase-a	IFC1	#633	1 MVA	120 kW	±992.7 kVAr
	IFC2	#684	1 MVA	80 kW	±996.7 kVAr
Phase-b	IFC1	#692	500 kVA	50 kW	±497.4 KVAr
	IFC2	#680	300 kVA	40 kW	±297.3 kVAr
	IFC3	#632	700 kVA	60 kW	±697.4 kVAr
Phase-c	IFC1	#611	800 kVA	150 kW	±785.8 kVAr
	IFC2	#645	1 MVA	120 kW	±992.7 kVAr

$$-2.49\,MVAr = Q^{\min}_{PCC,a\ IFCs} \le Q_{PCC,a} \le Q^{\max}_{PCC,a\ IFCs} = 1.488\,MVAr \tag{6.25}$$

$$-1.77\,MVAr = Q^{\min}_{PCC,\mathrm{b}\ IFCs} \le Q_{PCC,b} \le Q^{\max}_{PCC,\mathrm{b}\ IFCs} = 1.206\,MVAr \tag{6.26}$$

$$-2.28MVAr = Q^{\min}_{PCC,c\ IFCs} \le Q_{PCC,c} \le Q^{\max}_{PCC,c\ IFCs} = 1.277\,MVAr \tag{6.27}$$

For determining reactive power constraints at the PCC considering three phases voltage regulation, the maximum and minimum acceptable rms voltages of the PCC are considered as follows:

$$\left|v^{\max}_{PCC_x}\right| = 1.05 \times \left|v_{Grid_x}\right| = 1.05 \times \frac{4.16kV}{\sqrt{3}} = 2.521^{kV}_{ph-rms} \quad x = a,b,c \tag{6.28}$$

$$\left|v^{\min}_{PCC_x}\right| = 0.95 \times \left|v_{Grid_x}\right| = 0.95 \times \frac{4.16kV}{\sqrt{3}} = 2.281^{kV}_{ph-rms} \quad x = a,b,c \tag{6.29}$$

These values are used in (6.8) and (6.9) to calculate the upper and lower limits of three phases' reactive powers to address the voltage regulation.

In all simulations, initial total reference reactive powers of IFCs in phase-a, -b and $-c$ are $Q_{DGs_a} = Q_{DGs_b} = Q_{DGs_c} = 1kVar$, which are shared among IFCs based on (6.18) to (6.20). In simulations, the proposed control strategy is applied at $t = 0.2\,s$.

6.3.2 Flexible negative/zero sequence current compensation

6.3.2.1 Negative sequence current compensation

In this simulation, minimization of negative sequence of PCC current is studied. Therefore, in (6.6), $k^{-} = 1$ and $k^{0} = 0$. The PCC reference reactive powers of three phases ($Q_{PCC,x}$), resulted from optimization problem, and their constraints due to three phases voltage regulation ($Q^{\min}_{PCC,\mathrm{x}\ V-reg}$ and $Q^{\max}_{PCC,\mathrm{x}\ V-reg}$) and IFCs available reactive powers ($Q^{\min}_{PCC,\mathrm{x}\ DGs}$ and $Q^{\max}_{PCC,\mathrm{x}\ DGs}$) are shown in Figure 6.8 to Figure 6.10. As seen, the results are in the determined boundaries.

In Figure 6.11 to Figure 6.13, total reference reactive powers of IFCs in three phases $\left(Q_{IFCs_x}\right)$ and each IFC share in different phases ($Q_{IFC_{i_x}}$) are shown. It is clear from the results that the reference reactive powers of IFCs are less than their maximum available reactive powers (see TABLE 6.2). Moreover, reactive powers sharing among IFCs are based on their available rating. For example, from Figure 6.12, the reference reactive power of IFC3 is 1.4 times of IFC1, and IFC2 is 0.59 times of IFC1, similar to their available reactive powers ratios in TABLE 6.2. Controlling the single-phase IFCs reactive powers, the negative sequence of PCC current is minimized, which leads to reduction of negative sequence of PCC voltages. These results are seen in Figure 6.14 and Figure 6.15. The zero sequence of current and voltage at the PCC are shown in Figure 6.16 and Figure 6.17. In Figure 6.18, the amplitudes of PCC three-phase voltages are shown. As seen from this figure, all three phases are in their defined boundaries by voltage regulation, between $3226\,{}^{V}_{ph-peak} \le \left|v^{peak}_{PCC_x}\right| \le 3566\,{}^{V}_{ph-peak}$ (see (6.28) and (6.29)).

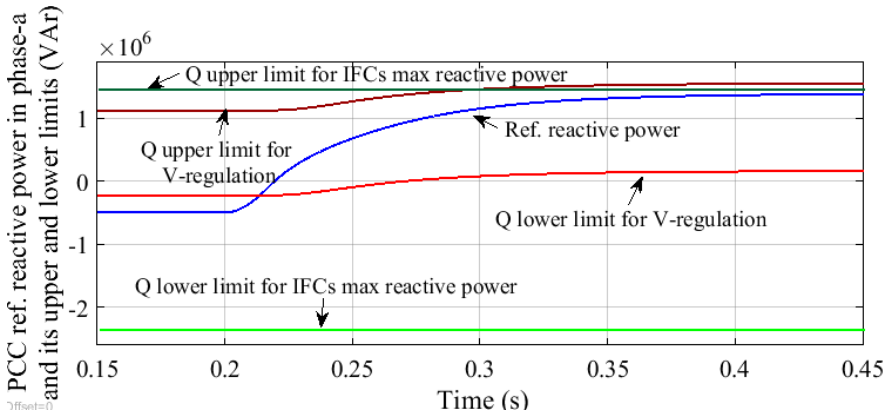

Figure 6.8 PCC reference reactive power in phase-a and its boundary limits *(k^{-}=1; k^{0}=0).*

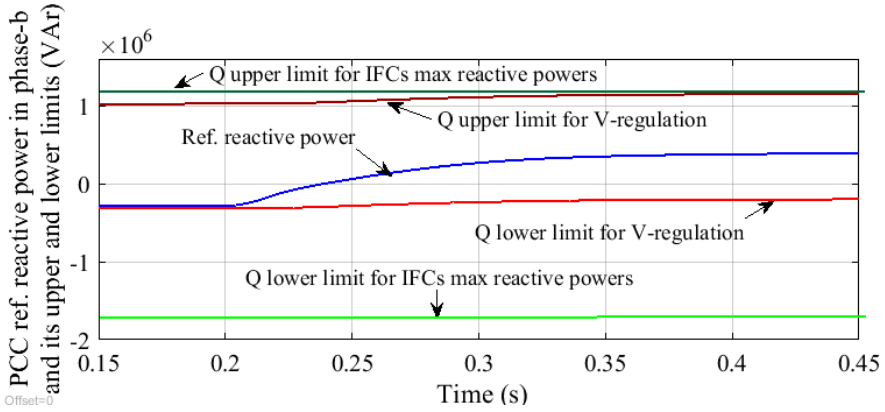

Figure 6.9 PCC reference reactive power in phase-b and its boundary limits *(k^-=1; k^0=0)*.

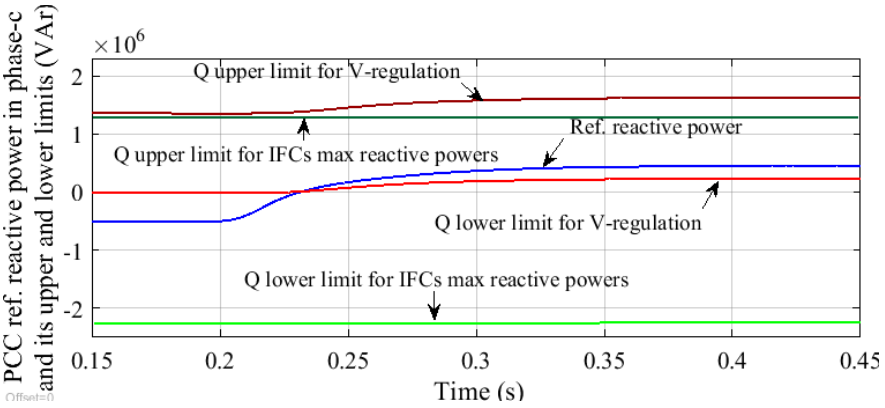

Figure 6.10 PCC reference reactive power in phase-c and its boundary limits *(k^-=1; k^0=0)*.

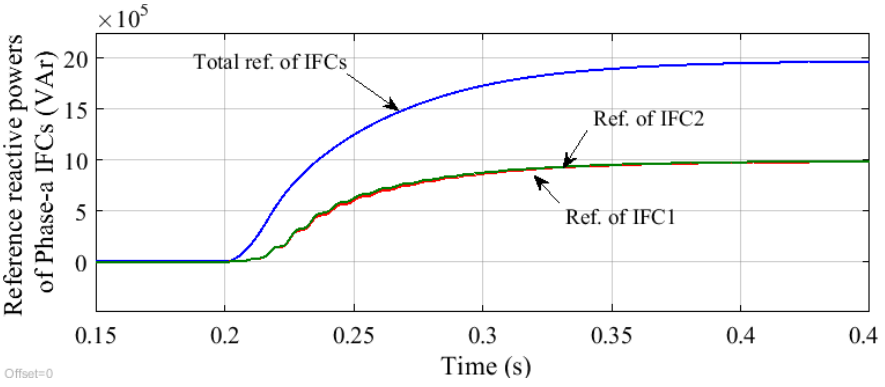

Figure 6.11 Total reference reactive power of phase-a IFCs, and IFC1 and IFC2 shares *(k^-=1; k^0=0)*.

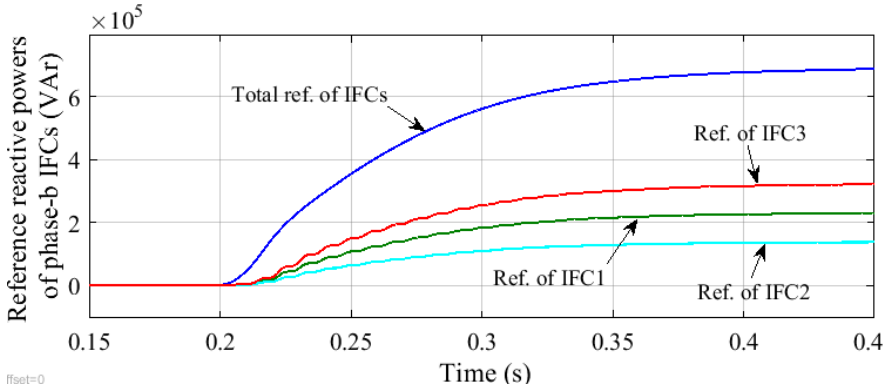

Figure 6.12 Total reference reactive power of phase-b IFCs, and IFC1, IFC2, and IFC3 shares *(k^{-}=1; k^{0}=0)*.

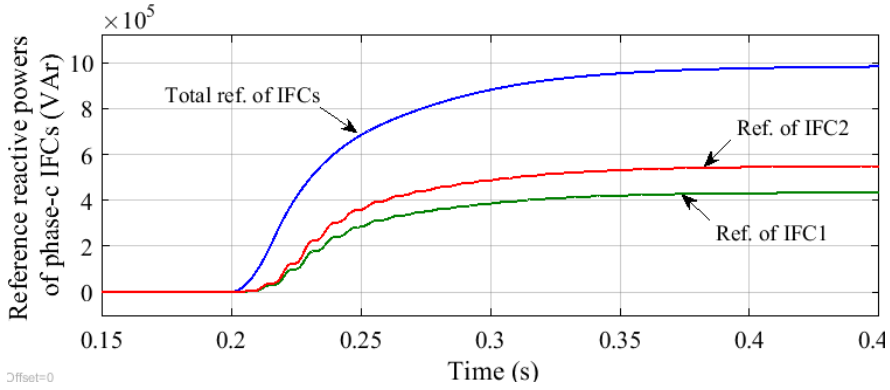

Figure 6.13 Total reference reactive power of phase-c IFCs, and IFC1 and IFC2 shares *(k^{-}=1; k^{0}=0)*.

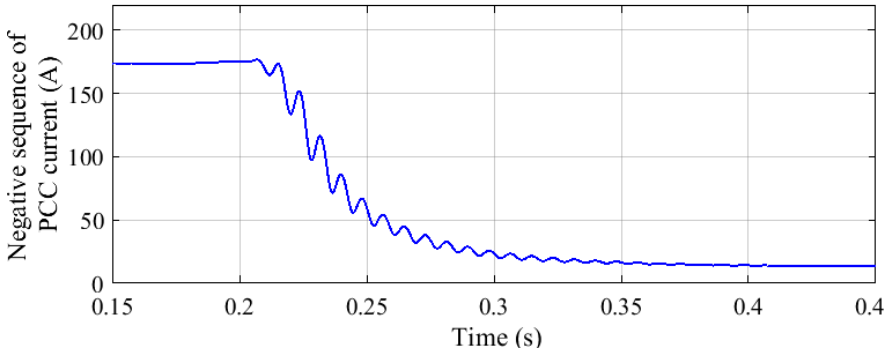

Figure 6.14 Negative sequence of the PCC current *(k^{-}=1; k^{0}=0)*.

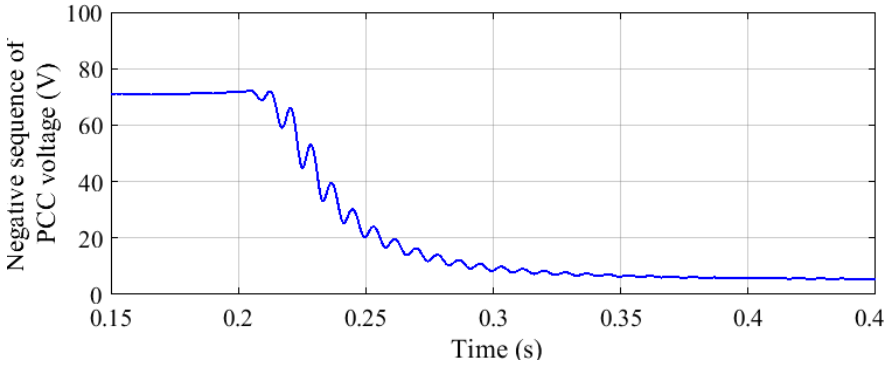

Figure 6.15 Negative sequence of the PCC voltage *(k^{-}=1; k^{0}=0)*.

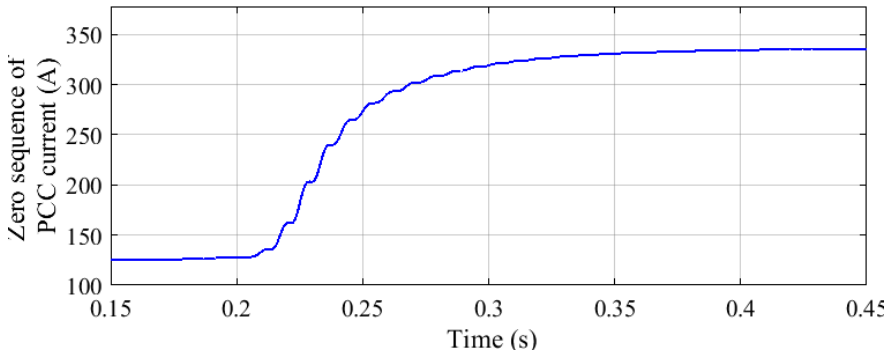

Figure 6.16 Zero sequence of the PCC current *(k^{-}=1; k^{0}=0)*.

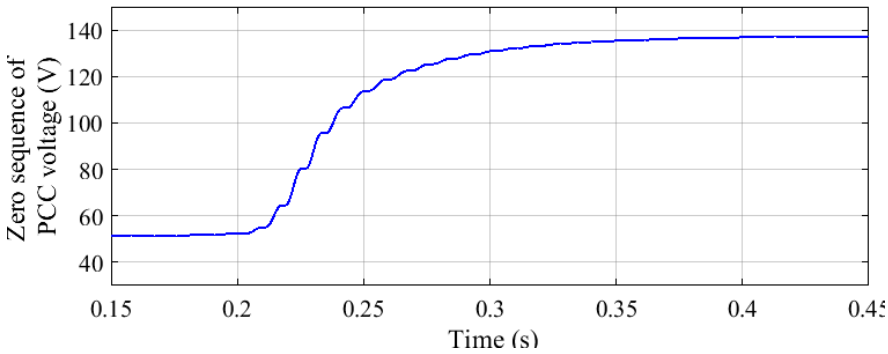

Figure 6.17 Zero sequence of the PCC voltage *(k^{-}=1; k^{0}=0)*.

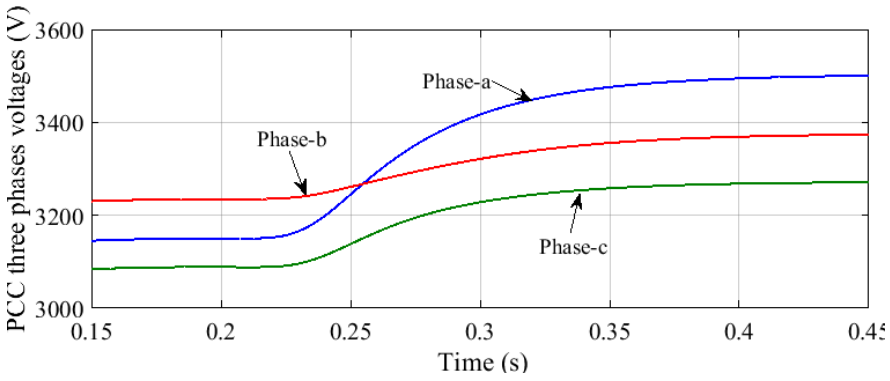

Figure 6.18 Amplitudes of PCC three-phase voltages *(k^-=1; k^0=0)*.

6.3.2.2 Zero sequence current compensation

Here, since minimization of zero sequence of PCC current is implemented, k^- and k^0 are chosen as $k^- = 0$ and $k^0 = 1$. The optimization problem results (the PCC three phases reactive power references) and their boundaries are shown in Figure 6.19 to Figure 6.21. The total reference reactive power of IFCs in three phases and each IFC share in different phases are shown in Figure 6.22 to Figure 6.24. Due to generation of these reactive powers by single-phase IFCs in each phase, the PCC zero sequence current is minimized, which is shown in Figure 6.25. The minimization of zero sequence of PCC current leads to the PCC zero sequence voltage reduction, which is shown in Figure 6.26. The negative sequences of the PCC voltage and current are shown in Figure 6.27 and Figure 6.28. The PCC three-phase voltages amplitudes are shown in Figure 6.29, where all of them are in their boundary limits based on voltage regulation constraints.

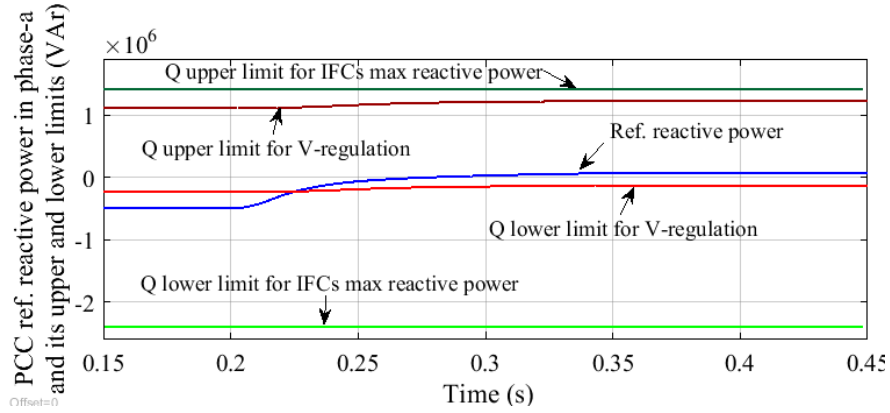

Figure 6.19 PCC reference reactive power in phase-a and its boundary limits *(k^-=0; k^0=1)*.

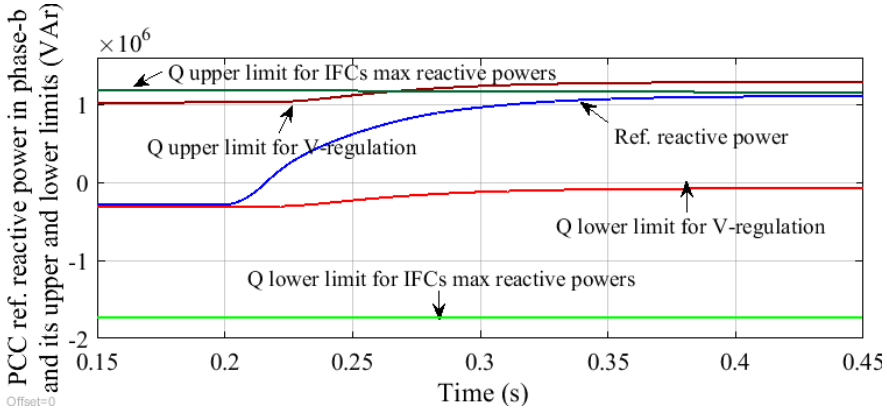

Figure 6.20 PCC reference reactive power in phase-b and its boundary limits *(k^-=0; k^0=1)*.

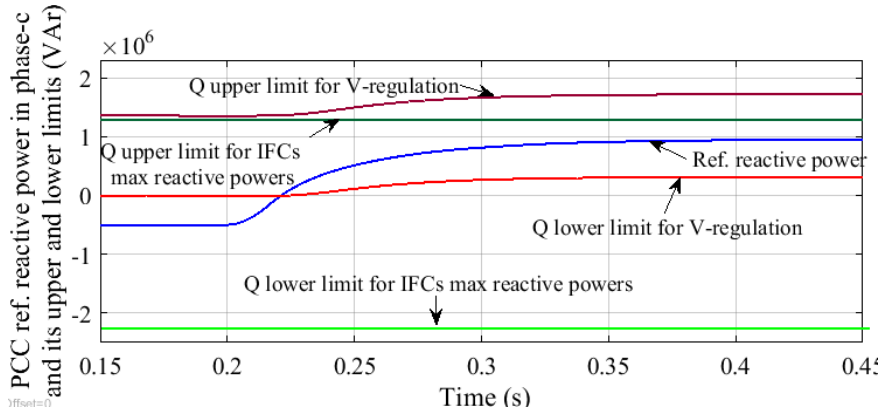

Figure 6.21 PCC reference reactive power in phase-c and its boundary limits *(k^-=0; k^0=1)*.

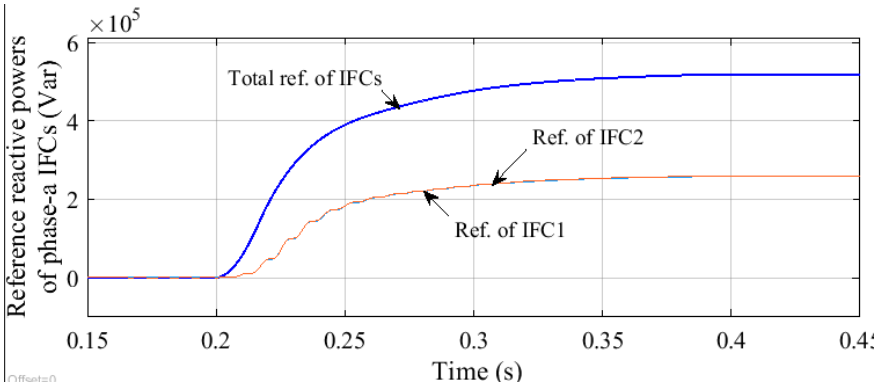

Figure 6.22 Total reference reactive power of phase-a IFCs, and IFC1 and IFC2 shares *(k^-=0; k^0=1)*.

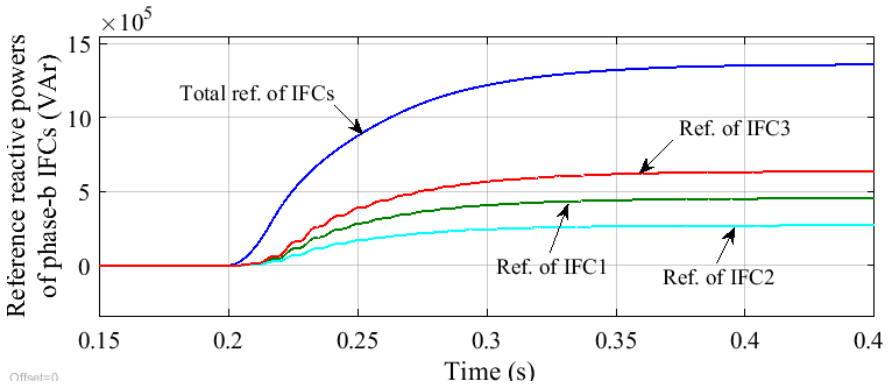

Figure 6.23 Total reference reactive power of phase-b IFCs, and IFC1, IFC2, and IFC3 shares *($k^{-}=0$; $k^{0}=1$)*.

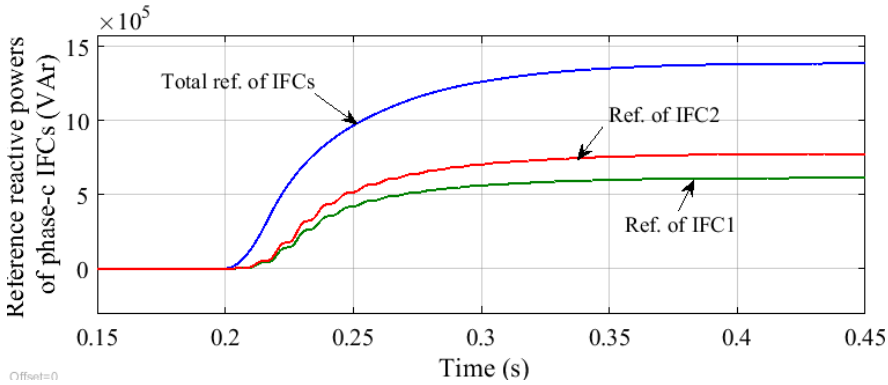

Figure 6.24 Total reference reactive power of phase-c IFCs, and IFC1 and IFC2 shares *($k^{-}=0$; $k^{0}=1$)*.

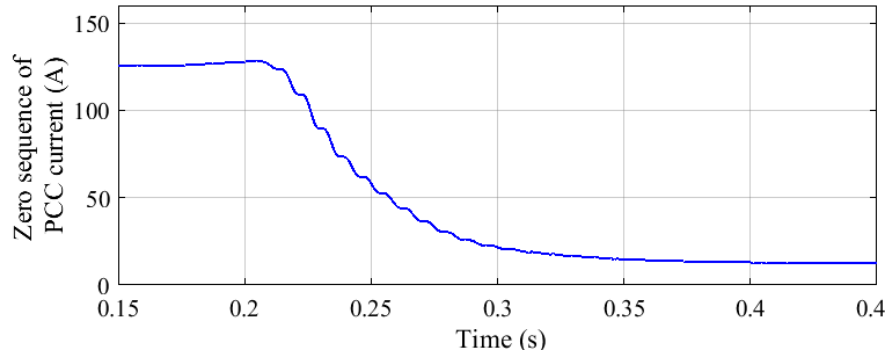

Figure 6.25 Zero sequence of the PCC current *($k^{-}=0$; $k^{0}=1$)*.

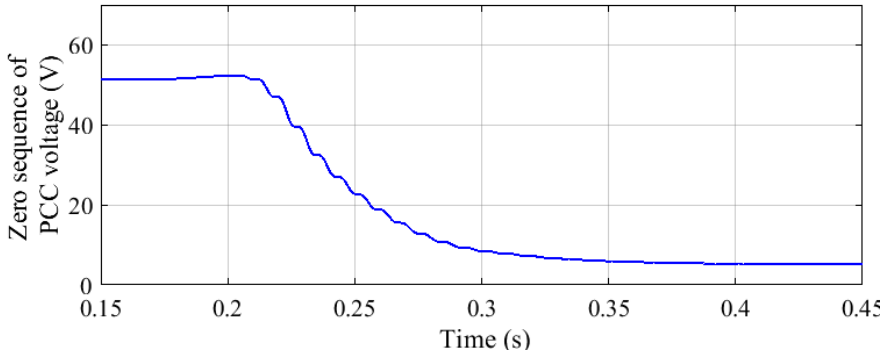

Figure 6.26 Zero sequence of the PCC voltage *(k^{-}=0; k^{0}=1)*.

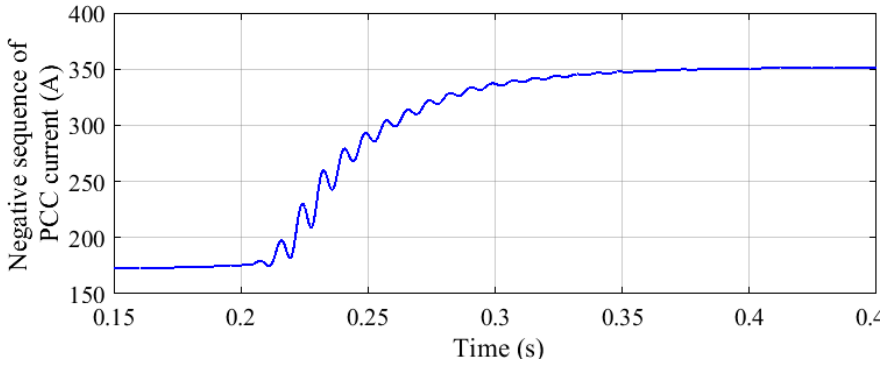

Figure 6.27 Negative sequence of the PCC current *(k^{-}=0; k^{0}=1)*.

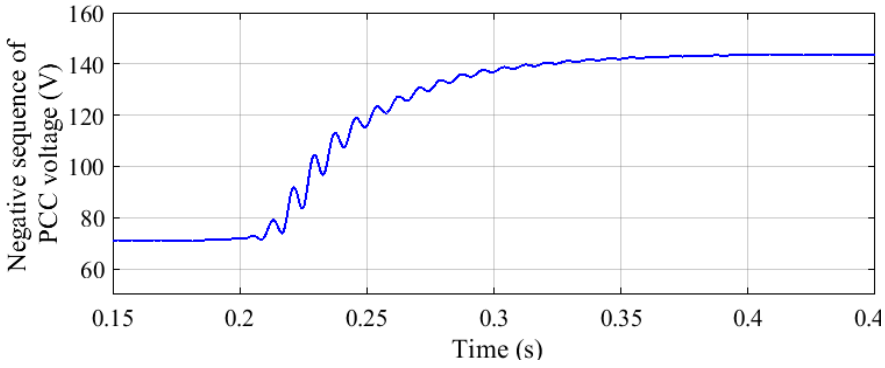

Figure 6.28 Negative sequence of the PCC voltage *(k^{-}=0; k^{0}=1)*.

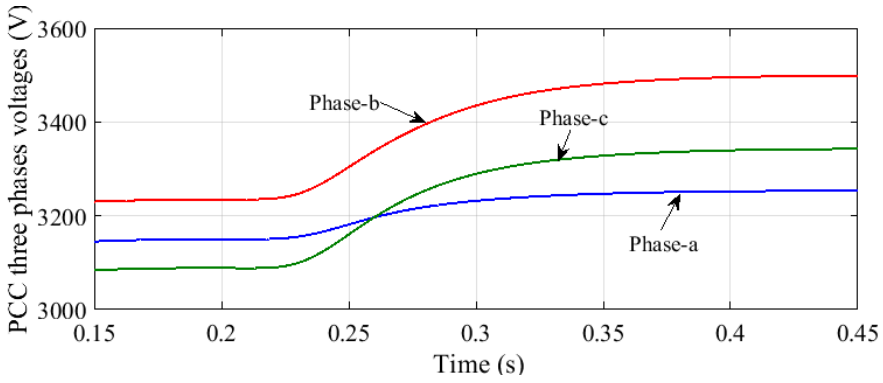

Figure 6.29 Amplitudes of PCC three-phase voltages *($k^-=0$; $k^0=1$).*

6.3.2.3 Both negative and zero sequences current compensation

Compensation of both negative and zero sequences of the PCC current are investigated here. Since negative sequence of current is larger than zero sequence before compensation (see (6.24)), more reduction of negative sequence current is desired. As a result, the weighting factors are considered as $k^- = 0.65$ and $k^0 = 0.35$. Considering these weighting factors, the reduction level of negative sequence current will be less than the case that $k^- = 1\left(k^0 = 0\right)$ (see Figure 6.14). However, this will provide the opportunity to reduce the zero sequence of current compare to $k^- = 1\left(k^0 = 0\right)$ (see Figure 6.16). In Figure 6.30, Figure 6.31, and Figure 6.32, reference reactive powers of the PCC three phases and their boundary limits are shown. As seen from Figure 6.32, the reference reactive power in phase-c reaches its minimum limit corresponding to voltage regulation in phase-c. This result means that the unbalanced compensation is restricted by voltage regulation of the PCC, and more compensation can be done if voltage regulation is not considered. The influences of reactive power restriction due to voltage regulation will be discussed later. The PCC three-phase voltages amplitudes are shown in Figure 6.33. As seen from this figure, phase-*a* and phase-*b* voltages are in their boundary limits. However, the voltage of phase-*c* is slightly smaller than minimum limit $\left(3226^{V}_{ph-peak}\right)$, which is due to power loss in the system.

Each IFCs reference reactive powers in three phases are shown in Figure 6.34, Figure 6.35, and Figure 6.36. In Figure 6.37 and Figure 6.38, the negative sequence of the PCC current and voltage are shown. As expected, the negative sequence current and as a result the negative sequence voltage are reduced. But, their reduction level is less than Figure 6.14 and Figure 6.15. The zero sequences of PCC current and voltage are shown in Figure 6.39 and Figure 6.40. Compare to Figure 6.16, the zero sequence current is reduced from $335A$ into $203A$ by choosing k^0 as $k^0 = 0.35$. From the negative and zero sequences current results, the optimization program provides their minimum possible values under defined k^- and k^0 values.

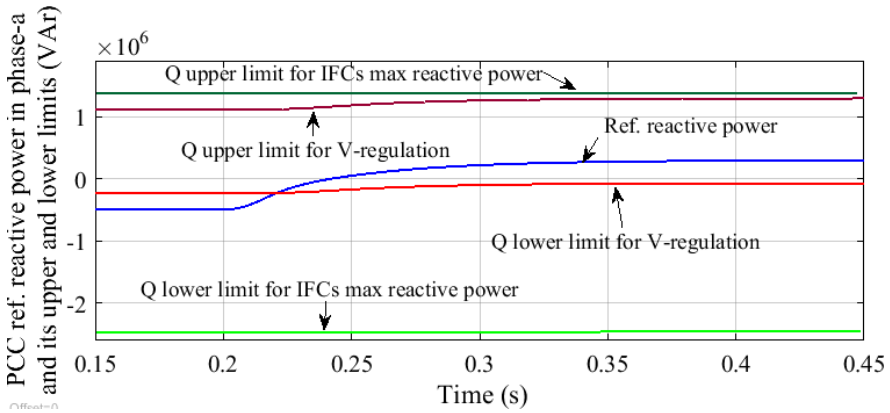

Figure 6.30 PCC reference reactive power in phase-a and its boundary limits *(k^-=0.65; k^0=0.35)*.

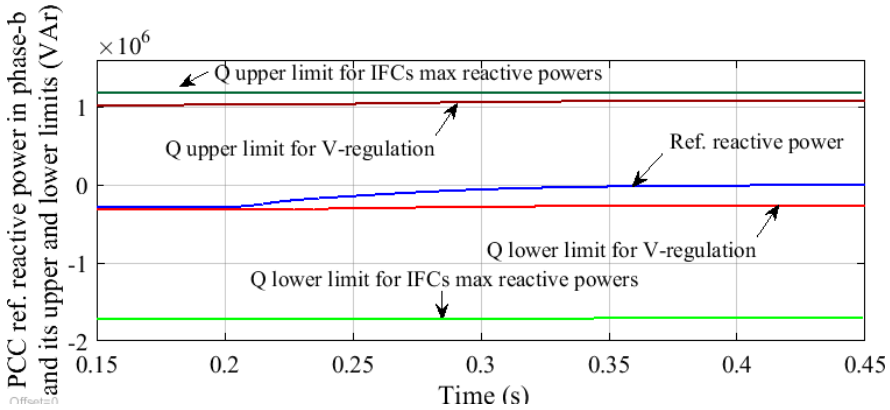

Figure 6.31 PCC reference reactive power in phase-b and its boundary limits *(k^-=0.65; k^0=0.35)*.

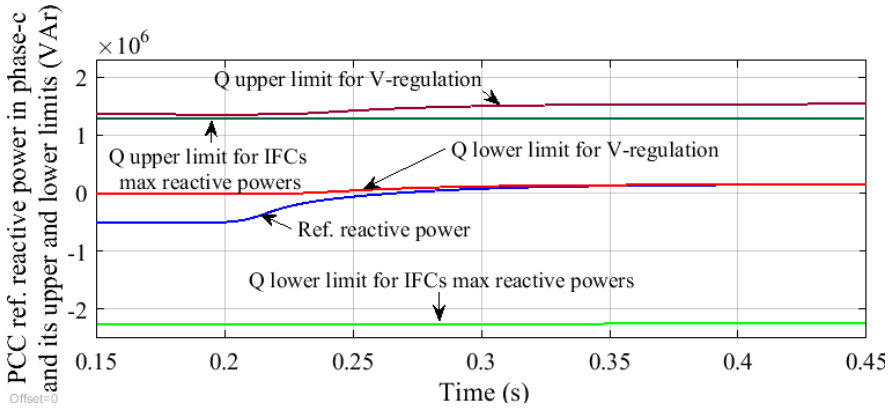

Figure 6.32 PCC reference reactive power in phase-c and its boundary limits *(k^{-}=0.65; k^{0}=0.35)*.

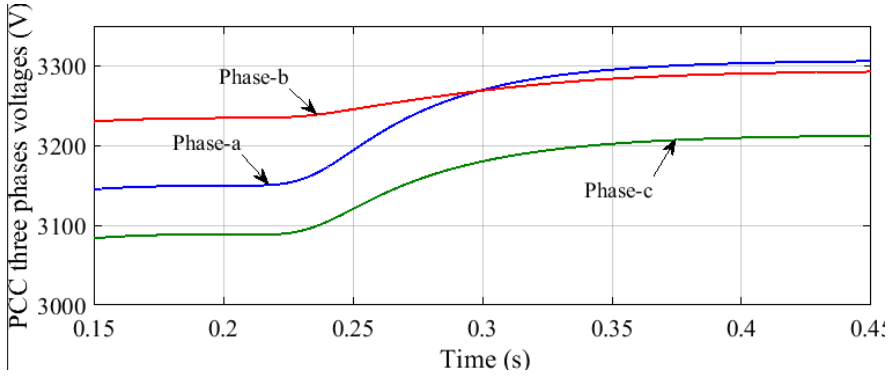

Figure 6.33 Amplitudes of PCC three-phase voltages *(k^{-}=0.65; k^{0}=0.35)*.

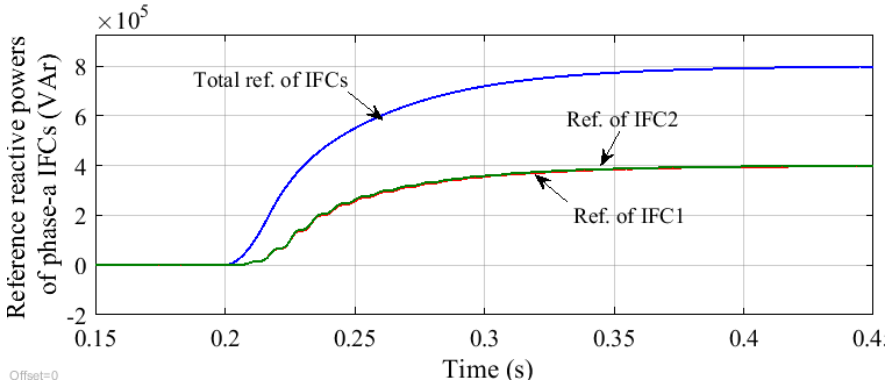

Figure 6.34 Total reference reactive power of phase-a IFCs, and IFC1 and IFC2 shares *(k^{-}=0.65; k^{0}=0.35)*.

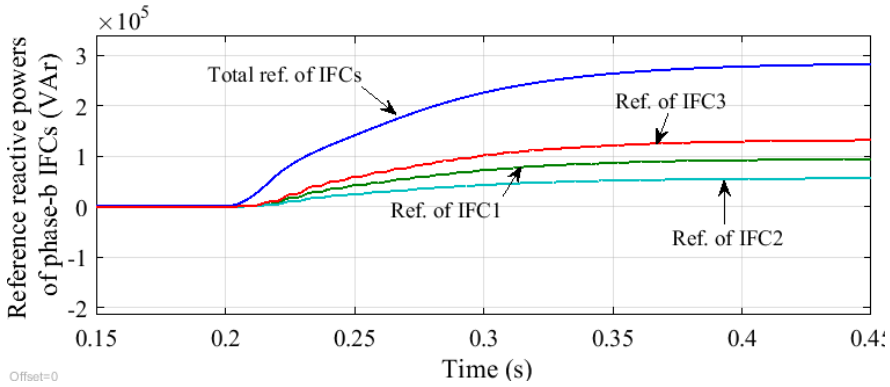

Figure 6.35 Total reference reactive power of phase-b IFCs, and IFC1, IFC2, and IFC3 shares *(k^{-}=0.65; k^{0}=0.35)*.

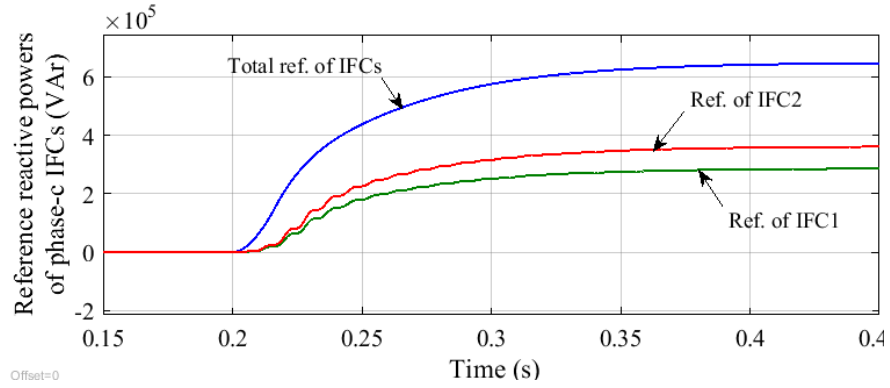

Figure 6.36 Total reference reactive power of phase-c IFCs, and IFC1 and IFC2 shares *(k^{-}=0.65; k^{0}=0.35)*.

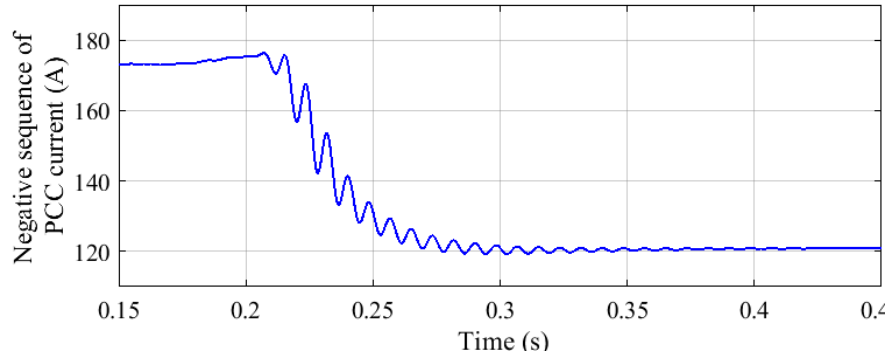

Figure 6.37 Negative sequence of the PCC current *(k^{-}=0.65; k^{0}=0.35)*.

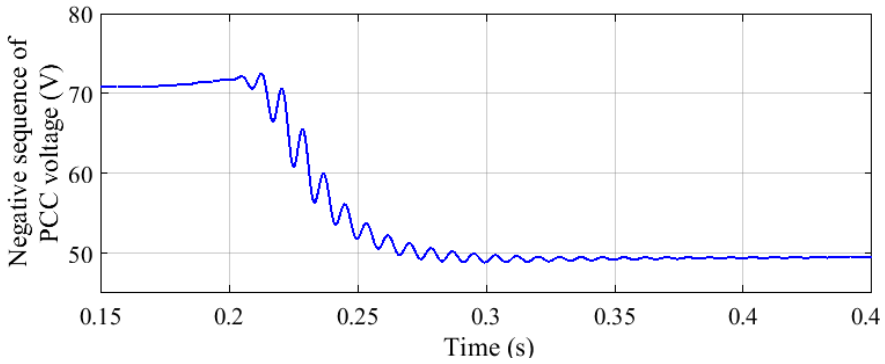

Figure 6.38 Negative sequence of the PCC voltage *(k^{-}=0.65; k^{0}=0.35)*.

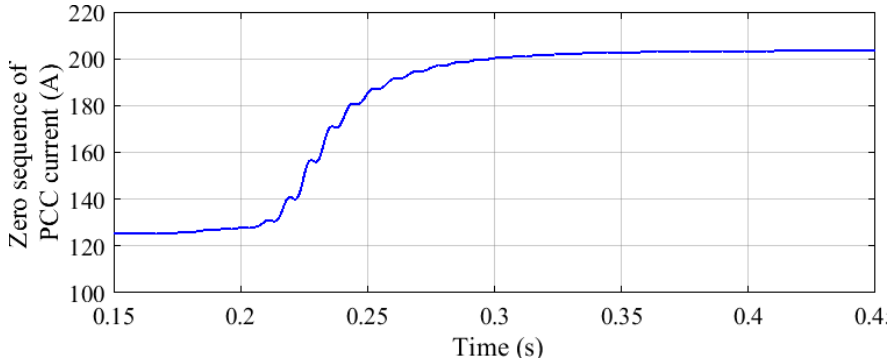

Figure 6.39 Zero sequence of the PCC current *(k^{-}=0.65; k^{0}=0.35)*.

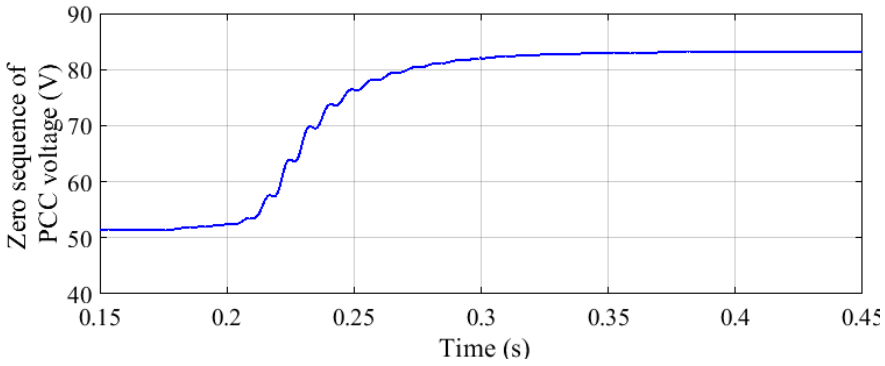

Figure 6.40 Zero sequence of the PCC voltage *(k^{-}=0.65; k^{0}=0.35)*.

From all aforementioned results, it is concluded that weighting factors can be flexibly controlled to restrain both the negative and zero sequence components in their desired limits. For better illustration, the simulation results are summarized in TABLE 6.3. To study the effects of three phases active powers equalization on the proposed method, the simulation of zero sequence current minimization is repeated under equalized active powers [81]-[82], and the results are provided in TABLE 6.3 and Figure 6.41. From the results, it is concluded that by applying three phases' average active powers equalization with the proposed control strategy, both negative and zero sequence currents could be reduced obviously compared to non-compensated method. The reason is that active powers equalization could reduce the unbalance level and significantly remove the trade-off of negative and zero sequence current compensation.

6.3.3 Influence of voltage regulation constraints

This part studies how voltage regulation constraints affect the proposed control strategy performance. It also shows that whether solitary voltage regulation control strategy (without compensation considerations) can guarantee unbalanced compensation.

To study the influence of voltages regulation on flexible unbalanced compensation, the simulation in Section 6.3.2.3 is repeated (k^- =0.65 and $k^0 =$ 0.35) under new voltage regulation constraints, where the maximum and minimum possible rms voltages of PCC are considered as follows:

TABLE 6.3 Simulation Results Summary.

	Without Compensation	Negative Seq. Comp.	Both Negative and Zero Seq. Comp.	Zero Seq. Comp.	Zero Seq. Comp. with Active Power Equalization
k^-	0	1	0.65	0	0
k^0	0	0	0.35	1	1
$\lvert i_{PCC}^{-}\rvert\ (A)$	$173.5A$	$13A$	$121A$	$351A$	$50.3A$
$\lvert v_{PCC}^{-}\rvert\ (V)$	$71.5V$	$5.4V$	$49.5V$	$143V$	$20.5V$
$\lvert i_{PCC}^{0}\rvert\ (A)$	$127.9A$	$335A$	$203A$	$12.3A$	$7.5A$
$\lvert v_{PCC}^{0}\rvert\ (V)$	$52.3V$	$137.5V$	$83V$	$5V$	$3V$

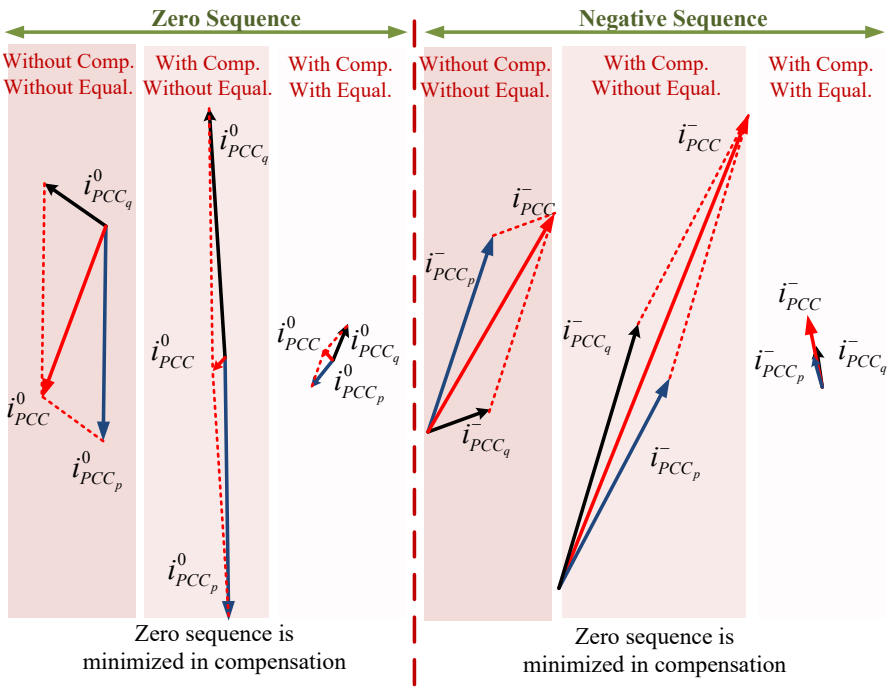

Figure 6.41 Negative and zero sequence current phasor diagrams with and without active powers equalizations under zero sequence current minimization.

$$\left|v_{PCC_x}^{\max}\right| = 1.02 \times \left|v_{Grid_x}\right| = 1.02 \times \frac{4.16kV}{\sqrt{3}} = 2.449^{kV}_{ph-rms} \qquad x = a,b,c \tag{6.30}$$

$$\left|v_{PCC_x}^{\min}\right| = 0.98 \times \left|v_{Grid_x}\right| = 0.98 \times \frac{4.16kV}{\sqrt{3}} = 2.353^{kV}_{ph-rms} \qquad x = a,b,c \tag{6.31}$$

So, the boundary of PCC voltage amplitude in each phase has been changed from $3226^{V}_{ph-peak} \le \left|v_{PCC_x}^{peak}\right| \le 3566^{V}_{ph-peak}$ to $3328^{V}_{ph-peak} \le \left|v_{PCC_x}^{peak}\right| \le 3463^{V}_{ph-peak}$. Since the boundary has become smaller, the unbalance compensation is expected to be lower (since in Figure 6.32, the PCC reference reactive power in phase-*c* was restricted to its minimum voltage regulation boundary limit for objective function minimization, decreasing that boundary limit will increase the objective function minimum value). In Figure 6.42, the PCC reference reactive power in phase-c is restricted to its minimum voltage regulation limit as expected.

In Figure 6.43, negative sequence of PCC current is shown. Comparing this figure with Figure 6.37 clarifies that the negative sequence current reduction level

has increased from $121A$ into $137A$. The PCC zero sequence of current is shown in Figure 6.44. Similarly, the zero sequence current has increased from $203A$ in Figure 6.39 into $219A$ in Figure 6.44. Therefore, when boundaries of reactive powers in PCC become smaller, the compensation capability is reduced. The PCC three-phase voltage amplitudes are shown in Figure 6.45. From this figure, it is clear that all voltages except phase-c are restricted between $3328\,^{V}_{ph-peak} \le \left|v^{peak}_{PCC_x}\right| \le 3463\,^{V}_{ph-peak}$. The phase-$c$ voltage is slightly smaller than lower limit ($3328\,^{V}_{ph-peak}$) due to power loss in the system.

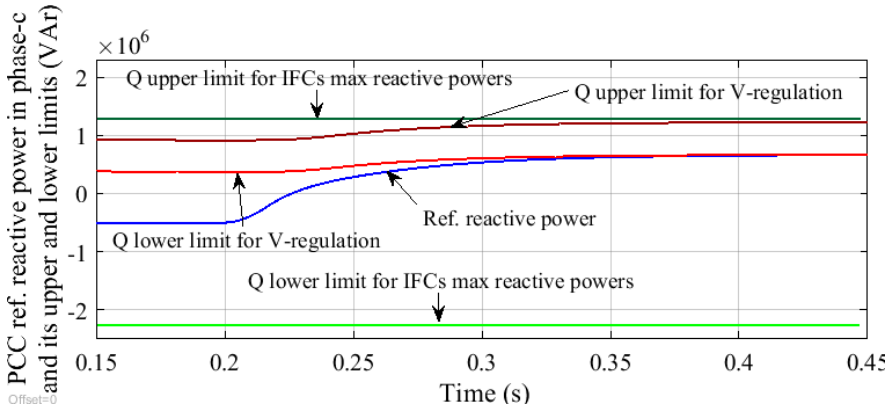

Figure 6.42 PCC reference reactive power in phase-c; study the voltage regulation effects on compensation *(k^{-}=0.65; k^{0}=0.35)*.

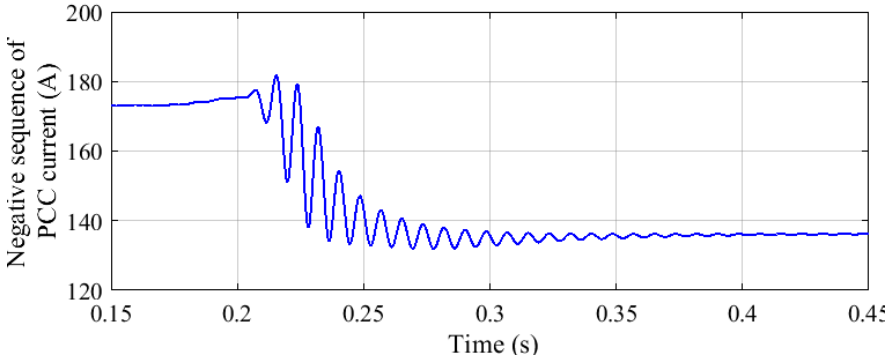

Figure 6.43 Negative sequence of the PCC current; study the voltage regulation effects on compensation *(k^{-}=0.65; k^{0}=0.35)*.

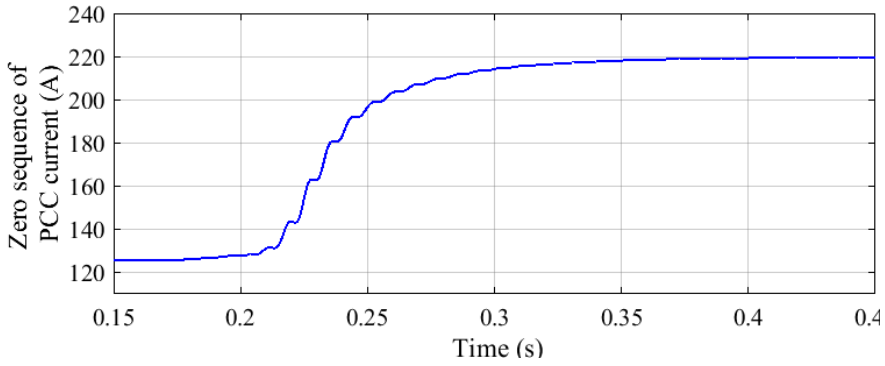

Figure 6.44 Zero sequence of the PCC current; study the voltage regulation effects on compensation *(k^{-}=0.65; k^{0}=0.35)*.

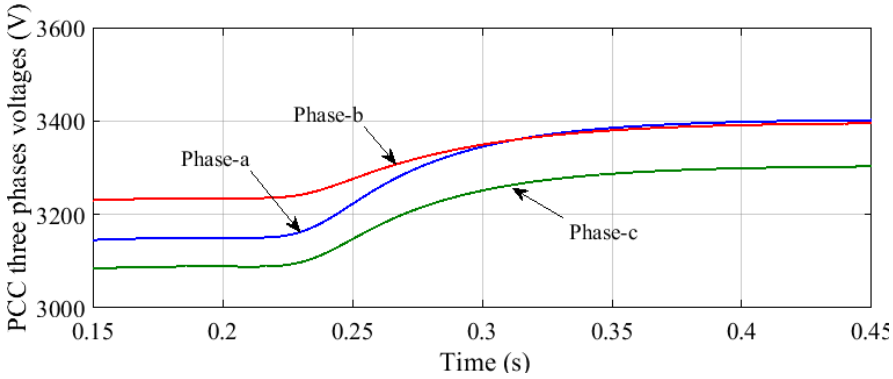

Figure 6.45 Amplitudes of PCC three-phase voltages; study the voltage regulation effects on compensation *(k^{-}=0.65; k^{0}=0.35)*.

In the second study of this section, it is shown that solitary voltages regulation control strategy cannot guarantee unbalanced compensation. For that, the PCC voltages in three phases are regulated on $0.98 \times \left|v_{Grid_x}\right| = 2.353^{kV}_{ph-rms}$ without any unbalanced compensation strategy. In Figure 6.46, the PCC three-phase voltage amplitudes are shown. It can be seen all three-phase voltages are regulated on their reference values (2.353^{kV}_{ph-rms}). The negative and zero sequences of the PCC current and voltage are shown in Figure 6.47 to Figure 6.50. From the figures, it is clear that negative and zero sequences current are increased after voltage regulation applied at $t = 0.2s$. Thus, voltage regulation cannot guarantee unbalanced condition compensation.

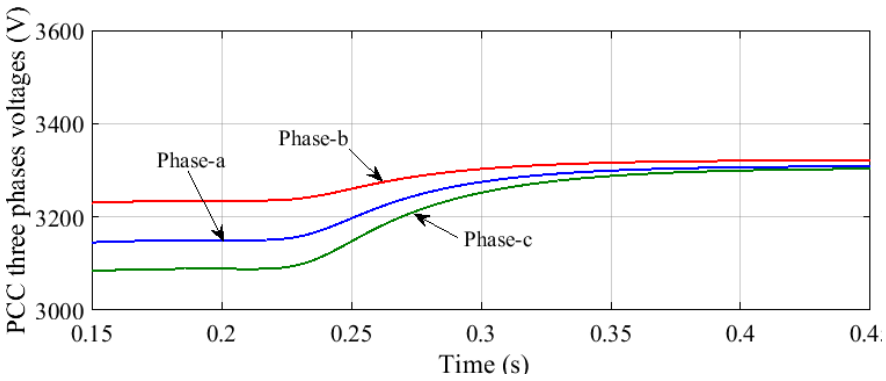

Figure 6.46 Amplitudes of PCC three-phase voltages; only voltage regulation strategy.

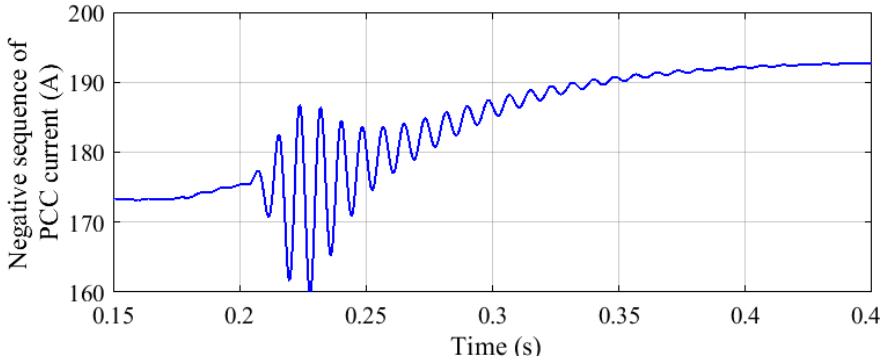

Figure 6.47 Negative sequence of the PCC current; only voltage regulation strategy.

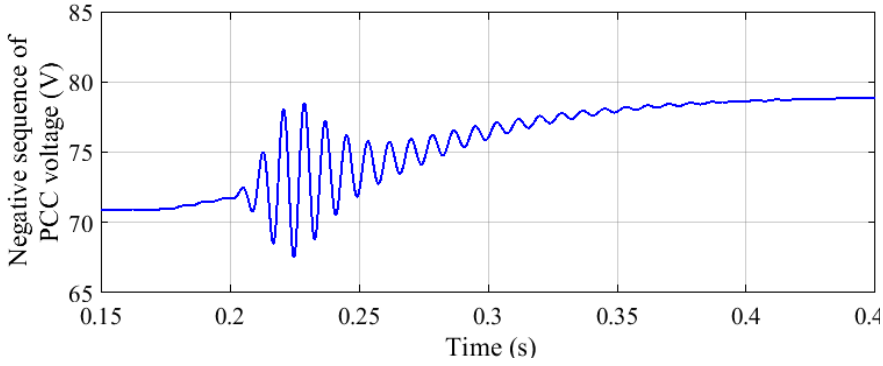

Figure 6.48 Negative sequence of the PCC voltage; only voltage regulation strategy.

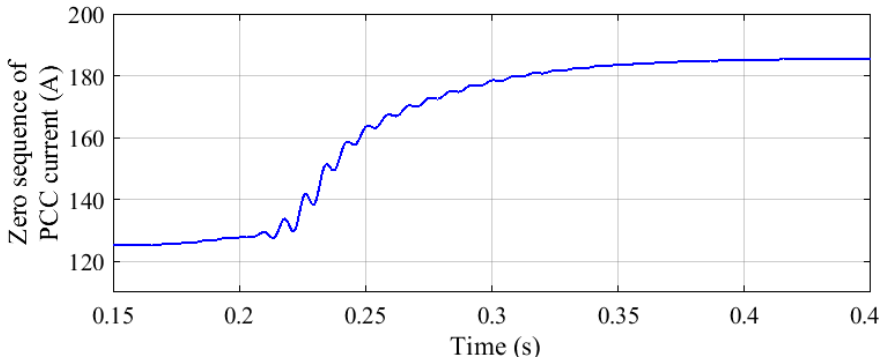

Figure 6.49 Zero sequence of the PCC current; only voltage regulation strategy.

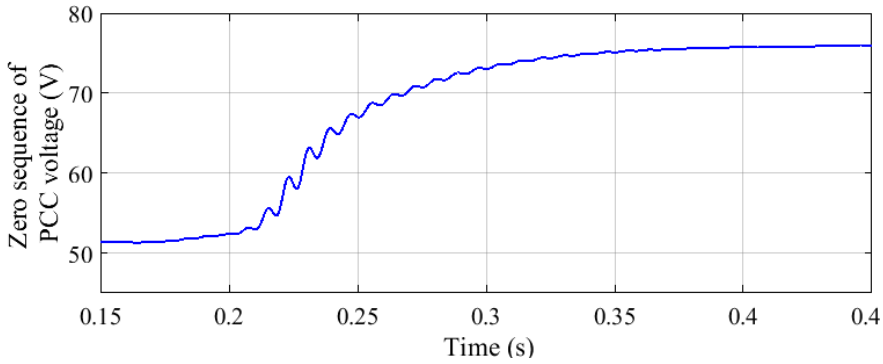

Figure 6.50 Zero sequence of the PCC voltage; only voltage regulation strategy.

6.3.4 Influence of single-phase IFCs available reactive powers

To study how maximum available reactive powers of single-phase IFCs affect the proposed strategy performance, the simulation in Section 6.3.2.2 is repeated under k^{-} =0 and $k^{0} = 1$; however, the total maximum available reactive power of phase-b IFCs is modified from $Q_{PCC,b_{IFCs}}^{max} = 1.206MVAr$ to $Q_{PCC,b_{IFCs}}^{max} = 0.7MVAr$ (see (6.26)). The PCC reference reactive power in phase-b and its upper and lower constraints are shown in Figure 6.51. As clear, the PCC reference reactive power in phase-b is restricted to IFCs maximum available reactive power (see Figure 6.20). In Figure 6.52, zero sequence of PCC current is shown. Due to IFCs rating limitations, the minimum value of zero sequence of PCC current is

increased from $12.37A$ in Figure 6.25 into $24.33A$ in Figure 6.52. In Figure 6.53, the zero sequence of PCC voltage is shown. Compare to Figure 6.26, the zero sequence voltage is increased from $5.05V$ into $9.95V$ value as a result of IFCs available reactive power limit in phase-*b*.

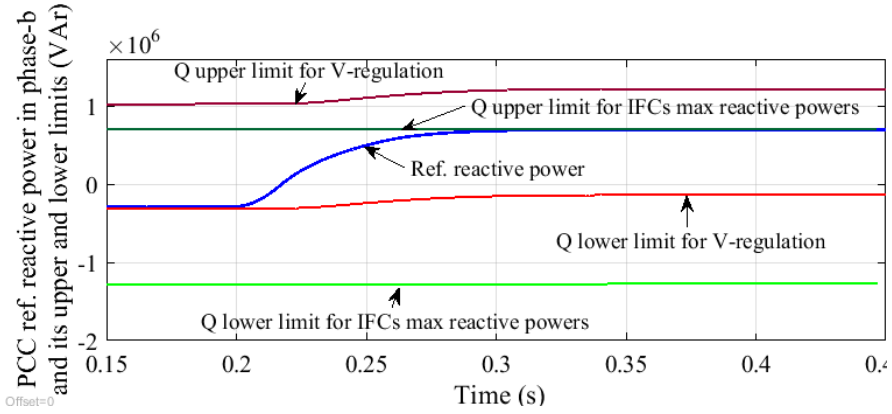

Figure 6.51 PCC reference reactive power in phase-b; study the effects of max available reactive powers of IFCs on compensation *(k^-=0; k^0=1)*.

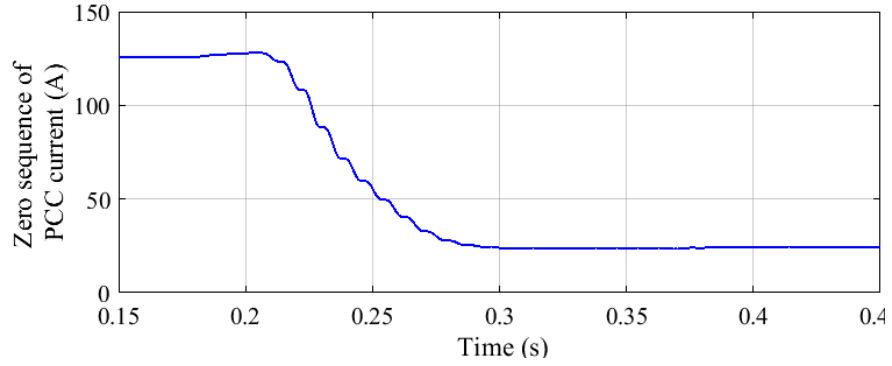

Figure 6.52 Zero sequence of the PCC current; study the effects of max available reactive powers of IFCs on compensation *(k^-=0; k^0=1)*.

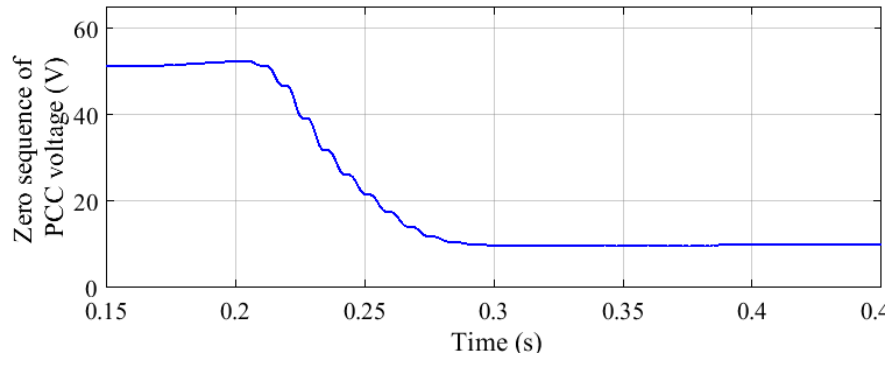

Figure 6.53 Zero sequence of the PCC voltage; study the effects of max available reactive powers of IFCs on compensation *(k^-=0; k^0=1)*.

6.4 Conclusion

In this chapter, the negative and zero sequences current in hybrid AC/DC microgrids were flexibly compensated by using smart single-phase interfacing converters (IFCs) with communications, in which their power factors are controlled without active powers production modifications. In the proposed control strategy, the objective function for negative and zero sequences current compensation was achieved from the developed single-phase perspective of the instantaneous power analysis. Moreover, three phases' voltage regulations and IFCs available reactive power ratings were considered as constraints. The proposed objective function was minimized subjected to constraints by using the Karush–Kuhn–Tucker (KKT) method. Due to the simplicity of the optimization problem, this method can be run online in a supervisory controller. The calculated reference reactive power in each phase is shared among the IFCs in that phase based on their available power rating, providing the same available room for IFCs' operation. In this chapter, comprehensive studies of the voltage regulation and the IFCs' available powers ratings effects on the proposed control strategy were conducted. Moreover, it was shown that the phases' active powers equalization could improve the effectiveness of the proposed strategy in both negative and zero sequences current minimization.

Chapter 7

Conclusions and Future Work

7.1 Thesis Conclusions and Contributions

The main objective of this thesis was to deal with unbalanced voltage in hybrid AC/DC microgrids. Thus, different novel control strategies were proposed for three-phase and single-phase interfacing converters (IFCs) to compensate for the unbalanced condition in such hybrid microgrids. The conclusions and contributions are as follows:

- In order to facilitate the design of three-phase and single-phase IFCs control strategies, a thorough review and a derivation of the instantaneous power analysis from three-phase and single-phase perspectives were conducted in Chapter 2. The analysis provided three methods to generate the reference currents of IFCs to achieve specific goals. These methods were used in the proposed control strategies in the rest of this thesis. The first reference current was used to adjustably compensate for the unbalanced voltage by the three-phase IFC in Chapter 3, in which positive and negative sequences' active and reactive currents were directly controlled by the two coefficients k_1 and k_2. To easily reduce/minimize the adverse effects of the unbalanced voltage on IFCs' operation, the second reference current was used in Chapter 4 and Chapter 5 to cancel out the parallel three-phase IFCs' active power oscillation and DC link voltage ripple by using the two coefficients k_p and k_q. The third reference current, which was developed for single-phase IFCs, was used to adjustably compensate for the unbalanced condition in Chapter 6. In this

reference current, the three-phase active and reactive powers were controlled to adjust the positive, negative and zero sequences currents.

- Two new control strategies were proposed for single three-phase IFC to adjustably compensate for the unbalanced voltage of hybrid AC/DC microgrids, together with adverse effects consideration, in Chapter 3. Also, the effectiveness of unbalanced voltage compensation was considered. The three-phase IFC could be either AC and DC-subsystems interfacing converter in DC-coupled or AC-DC-coupled hybrid microgrids or IFC of DG/SE connected to the AC subsystem in AC-coupled or AC-DC-coupled hybrid microgrids. In the first proposed strategy, the IFC's active power oscillation was minimized, and the unbalanced voltage was compensated with adjustable level. In the second proposed strategy, the IFC's negative sequence current was set to be in-phase with the grid negative sequence current to effectively reduce the negative sequence voltage of the grid. The results showed that the performance of the two proposed control strategies in terms of power oscillations and the AC subsystem negative sequence voltage reduction differed under the normal inductive grid with large X_{Grid}/R_{Grid} ratios and the IFC was controlled by the high power factor, or the weak grid with small X_{Grid}/R_{Grid} ratios and the IFC worked as a reactive power compensator. In other grid conditions and IFC operating conditions, the two strategies had similar performances. The validity of both proposed strategies was verified by simulations and experiments.

- In parallel three-phase IFCs, because of interactions, the adverse effects of the unbalanced voltage on IFCs' operation can be multiplied by the number of IFCs. In AC/DC hybrid microgrids, the parallel IFCs can be an interlinking path between the AC and DC-subsystems in DC-coupled or AC-DC-coupled hybrid microgrids, or DGs/SEs interfacing converters connected to the AC subsystem in AC-coupled or AC-DC-coupled hybrid microgrids. Two scenarios were proposed to deal with the adverse effects amplification issue in parallel IFCs' operation in hybrid microgrids: first, the use of one dedicated

redundant converter for adverse effects minimization, and second, the use of all IFCs to share the adverse effects minimization. More specifically, a new control strategy was proposed for parallel three-phase IFCs' operation under unbalanced voltage in Chapter 4, where the redundant IFC was used to cancel out the collective active power oscillations. The proposed control strategy can be applied to parallel IFCs with various PFs and different average active-reactive powers. In this chapter, a thorough study of single and parallel IFCs' peak currents was conducted. It was found that under zero active power oscillations, the collective peak current of parallel IFCs was a constant in the fixed average active and reactive powers. Moreover, the peak currents of IFCs can be kept in the same phase as the collective peak current, and provide a reduced peak current for the redundant IFC in the proposed control strategy. Finally, the proposed control strategy was verified by simulations and experiments under different operations of IFCs.

- For the second scenario of parallel IFCs operation under unbalanced condition, two new control strategies were proposed in Chapter 5, in which adverse effect minimization was shared among parallel IFCs. Both proposed control strategies were applicable for IFCs operating under unity PF, and they focused on the collective active power oscillations cancellation, sharing the collective peak current of parallel IFCs among them based on their power ratings, and maximizing the power/current transferring capability of parallel IFCs. In the first proposed control strategy, which may not be able to be run in real-time online due to its complexity, the IFCs' power coefficients were controlled by solving a set of nonlinear equations. In the second proposed control strategy, the peak currents of IFCs were controlled directly through the derived relationship of the IFCs' peak currents under zero power oscillation. Since this method featured more simplified calculations, it could be easily applied online. However, this control strategy may induce small errors into the active power oscillation cancellation. In this chapter, a detailed analysis of individual and parallel IFCs' peak currents was conducted to maximize the power/current transferring capability of parallel IFCs. In both proposed

control strategies, the maximum power/current transferring capability of parallel IFCs was achieved by controlling the IFCs' peak currents phases. Both simulation and experimental results were obtained to verify the analysis and the two proposed control strategies.

- In Chapter 6, a new control strategy was proposed for multiple single-phase IFCs to compensate for the unbalanced condition in three-phase hybrid microgrids. The single-phase IFCs can be DGs/SEs interfacing converters connected to the AC subsystem in AC-coupled or AC-DC-coupled hybrid microgrids. Also, the DC subsystem can be connected by a single-phase IFC to one of the phases of the three-phase AC subsystem in DC-coupled or AC-DC-coupled hybrid microgrids. The proposed control strategy flexibly compensated for the negative and zero sequences current, resulting in unbalanced voltage compensation. In the proposed control strategy, the power factors of the IFCs were controlled while their active power productions remained unchanged. The objective function derived from the developed instantaneous power analysis from the single-phase perspective was minimized online due to its simplicity by using the Karush–Kuhn–Tucker (KKT) optimization method in a supervisory control center. Three-phase voltages regulation and IFCs' available power ratings were considered as practical constraints in the optimization problem. The outcomes of the optimization problem, which were the reference reactive powers in each phase, were shared among the IFCs in that phase based on their power ratings. This chapter also studied the influences of voltage regulations, IFCs available power ratings, and three-phase active powers equalization on the proposed control strategy. Finally, the IEEE 13-node test system with seven embedded single-phase IFCs was adopted for case studies.
- The proposed control strategies for single-phase and three-phase interfacing converters in Chapter 3 to Chapter 6 focus on dealing with unbalanced voltage in hybrid AC/DC microgrids. In case when multiple individual three-phase and single-phase IFCs participate in the unbalanced voltage compensation, in-

phase current compensation strategy would be a good choice for three-phase IFCs' control since all three-phase IFCs behave as negative sequence impedances with the same phase angle as the grid, resulting in zero negative sequence circulation current among them. Moreover, single-phase IFCs would mainly focus on zero sequence voltage compensation since negative sequence voltage is already compensated by three-phase IFCs. It should be mentioned that all the proposed control strategies for three-phase and single-phase IFCs can also be used for conventional AC power systems to compensate the unbalanced condition by using power electronic converters of distributed generations or energy storage devices.

7.2 Suggestions for Future Work

The suggestions for extending this research are as follows:

- Coordinate control of both single-phase and three-phase IFCs to compensate for the unbalanced condition.
- Provide power quality control in the DC subsystems of hybrid AC/DC microgrids by using DC-DC and DC-AC interfacing converters.
- Develop parallel three-phase IFCs control to adjustably compensate for the unbalanced voltage and to reduce the adverse effects of unbalanced voltage on the IFCs' operation.
- Study the stability of future hybrid AC/DC microgrids with high penetration of interfacing converters.

References

[1] M. H. Nehrir, C. Wang, K. Strunz, H. Aki, R. Ramakumar, J. Bing, Z. Miao, and Z. Salameh, "A review of hybrid renewable/alternative energy systems for electric power generation: configurations, control, and applications", *IEEE Trans. Sustain. Energy*, vol. 2, no. 4, pp. 392–403, Oct. 2011.

[2] D. Rastler, "Electricity energy storage technology options, a white paper primer on applications, costs, and benefits", *EPRI Publication* 1020676, Dec. 2010.

[3] K. Strunz and H. Louie, "Cache energy control for storage: power system integration and education based on analogies derived from computer engineering", *IEEE Trans. Power System*, vol. 24, no. 1, pp. 12-20, Feb. 2009.

[4] A. Mohamed, V. Salehi, and O. Mohammed, "Real-Time energy management algorithm for mitigation of pulse loads in hybrid microgrids", *IEEE Trans. Smart Grid*, vol. 3, no. 4, pp. 1911-1922, Dec. 2012.

[5] B. Kroposki, R. Lasseter, T. Ise, S. Morozumi, S. Papathanassiou, and N. Hatziargyriou, "A look at microgrid technologies and testing projects from around the world", *IEEE Power Energy Mag.*, vol. 6, no. 3, pp. 40–53, May/Jun. 2008.

[6] N. W. A. Lidula and A. D. Rajapakse, "Microgrids research: a review of experimental microgrids and test systems", *Renewable and Sustainable Energy Reviews*, vol. 15, no. 1, pp. 186–202, 2011.

[7] I. Mitra, T. Degner, and M. Braun, "Distributed generation and microgrids for small island electrification in developing countries: a review", *SESI Journal*, vol. 18, no. 1, pp. 6-20, Jan. 2008.

[8] I. Araki, M. Tatsunokuchi, H. Nakahara, and T. Tomita, "Bifacial PV system in Aichi Airport-site demonstrative research plant for new energy power

generation", *Elsevier Journal, Solar Energy Materials and Solar Cells,* vol. 93, no. 6, pp. 911-916, Jun. 2009.

[9] Cesi Ricerca DER Test Facility (DER-TF), Italy, [Online]. Available: http://www.der-ri.net/index.php?id=10.

[10] Hawaii Natural Energy Institute, Hawaii Hydrogen Power Park, [Online]. Available: http://www.hnei.hawaii.edu/research/hawaii-hydrogen-power-park

[11] J. F. Chen and C. L. Chu, "Combination voltage-controlled and current controlled PWM inverters for UPS parallel operation", *IEEE Trans. Power Electron.*, vol. 10, no. 5, pp. 547–558, Sep. 1995.

[12] X. Sun, Y. S. Lee, and D. H. Xu, "Modeling, analysis, and implementation of parallel multi-inverter systems with instantaneous average current- sharing scheme", *IEEE Trans. Power Electron.*, vol. 18, no. 3, pp. 844–856, May 2003.

[13] T. F. Wu, Y. K. Chen, and Y. H. Huang, "3C strategy for inverters in parallel operation achieving an equal current distribution", *IEEE Trans. Ind. Electron.*, vol. 47, no. 2, pp. 273–281, Apr. 2000.

[14] P. Ch. Loh, D. Li, Y. K. Chai, and F. Blaabjerg, "Autonomous operation of hybrid microgrid with ac and dc subgrids", *IEEE Trans. Power Electron.* vol. 28, no. 5, pp. 2214–2223, May. 2013.

[15] Y. W. Li, D. M. Vilathgamuwa, and P. C. Loh, "Design, analysis and real-time testing of controllers for multi-bus microgrid system," *IEEE Trans. Power Electron.*, vol. 19, pp. 1195-1204, Sep. 2004.

[16] J. He, and Y. W. Li, "An enhanced microgrid load demand sharing strategy," *IEEE Trans. Power Electron.*, vol. 27, no. 9, pp. 3984–3995, Sep. 2012.

[17] D. Van Hertem, M. Ghandhari, M. Delimar, "Technical limitations towards a SuperGrid-A European perspective", in *Proc. 2010 IEEE Energy Conference and Exhibition (Energy Con),* pp. 302-309.

[18] P. Fairley, "Germany jump-starts the supergrid", *Spectrum, IEEE*, vol.50, no.5, pp. 36-41, May 2013.

[19] Q. Sun, J. Zhou, J. M. Guerrero, and H. Zhang, "Hybrid three-phase/single-phase microgrid architecture with power management capabilities", *IEEE Trans. Power Electron.*, vol. 30, no. 10, pp. 5964-5977, Oct. 2015.

[20] F. Shahnia, P. J. Wolfs and A. Ghosh, "Voltage unbalance reduction in low voltage feeders by dynamic switching of residential customers among three phases", *IEEE Trans. Smart Grid*, vol. 5, no. 3, pp. 1318-1327, May 2014.

[21] S. Deilami, A. S. Masoum, P. S. Moses and M. A. S. Masoum, "Real-Time coordination of plug-in electric vehicle charging in smart grids to minimize power losses and improve voltage profile", *IEEE Trans. Smart Grid*, vol. 2, no. 3, pp. 456-467, Sept. 2011.

[22] T. Klayklueng and S. Dechanupaprittha, "Performance analysis of future PEA distribution network under high penetration of PEVs home charging", in *Proc. 2015 IEEE Innovative Smart Grid Technologies - Asia (ISGT ASIA)*, Bangkok, 2015, pp. 1-5.

[23] K. Elyasibakhtiari, M. A. Azzouz, E. A. Rezai and E. F. El-Saadany, "Real-time analysis of voltage and current in low-voltage grid due to electric vehicles' charging", in *Proc. 2015 IEEE International Conference on Smart Energy Grid Engineering (SEGE)*, Oshawa, ON, 2015, pp. 1-5.

[24] F. Shahnia, A. Ghosh, G. Ledwich and F. Zare, "Voltage unbalance sensitivity analysis of plug-in electric vehicles in distribution networks", in *Proc. 2011 AUPEC 2011*, Brisbane, QLD, 2011, pp. 1-6.

[25] L. Degroote, B. Renders, B. Meersman and L. Vandevelde, "Neutral-point shifting and voltage unbalance due to single-phase DG units in low voltage distribution networks", in *Proc. 2009 IEEE Bucharest PowerTech*, Bucharest, 2009, pp. 1-8.

[26] R. Majumder, A. Ghosh, G. Ledwich and F. Zare, "Operation and control of single phase micro-sources in a utility connected grid", in *Proc. 2009 IEEE Power & Energy Society General Meeting*, Calgary, AB, 2009, pp. 1-7.

[27] A. Von Jouanne, and B. Banerjee, "Assessment of voltage unbalance", *IEEE Trans. Power Del.,* vol. 16, no. 4, pp. 782-790, Oct 2001.

[28] L. Tzung-Lin, H. Shang-Hung, and C. Yu-Hung, "D-STATCOM with positive-sequence admittance and negative-sequence conductance to mitigate voltage fluctuations in high-level penetration of distributed-generation systems", *IEEE Trans. Ind. Electron.,* vol. 60, no. 4, pp. 1417-1428, Apr. 2013.

[29] M. Savaghebi, A. Jalilian, J. C. Vasquez, and J. M. Guerrero, "Autonomous voltage unbalance compensation in an islanded droop-controlled microgrid", *IEEE Trans. Ind. Electron.,* vol.60, no.4, pp.1390,1402, Apr. 2013.

[30] A. Camacho, M. Castilla, J. Miret, R. Guzman, and A. Borrell, "Reactive power control for distributed generation power plants to comply with voltage limits during grid faults", *IEEE Trans. Power Electron.*, vol. 29, no. 11, pp. 6224–6234, Nov. 2014.

[31] D. Graovac, V. A. Kati, and A. Rufer, "Power quality problems compensation with universal power quality conditioning system," *IEEE Trans. Power Del.*, vol. 22, no. 2, pp. 968–976, Apr. 2007.

[32] F. Barrero, S. Martínez, F. Yeves, F. Mur, and P. Martínez, "Universal and reconfigurable to UPS active power filter for line conditioning," *IEEE Trans. Power Del.,* vol. 18, no. 1, pp. 283–290, Jan. 2003.

[33] S. George and V. Agarwal, "A DSP-based optimal algorithm for shunt active filter under nonsinusoidal supply and unbalanced load conditions", *IEEE Trans. Power Electron.*, vol. 22, no. 2, pp. 593–601, Mar. 2007.

[34] B. Singh and J. Solanki, "An implementation of an adaptive control algorithm for a three-phase shunt active filter", *IEEE Trans. Ind. Electron.*, vol. 56, no. 8, pp. 2811–2820, Aug. 2009.

[35] F. Wang, J. L. Duarte, and M. A. M. Hendrix, "Grid-Interfacing converter systems with enhanced voltage quality for microgrid application—concept and implementation", *IEEE Trans. Power Electron.*, vol. 26, no. 12, pp. 3501–3513, Dec. 2011.

[36] J. M. Guerrero, P. Ch. Loh, T. L. Lee, and M. Chandorkar, “Advanced control architectures for intelligent microgrids—Part II: power quality, energy storage, and ac/dc microgrids”, *IEEE Trans. Ind. Electron.*, vol. 60, no. 4, pp. 1263–1270, Apr. 2013.

[37] J. Miret, A. Camacho, M. Castilla, L. G. Vicuna, and J. Matas, “Voltage support control strategies for static synchronous compensators under unbalanced voltage sags”, *IEEE Trans. Ind. Electron.*, vol. 61, no. 2, pp. 808–820, Apr. 2013.

[38] K. Yunus and H.Z. De La Parra, "Distribution grid impact of plug-in electric vehicles charging at fast charging stations using stochastic charging model," in *Proc. 2011-14th European Conference on Power Electronics and Applications (EPE 2011)*, pp.1-11.

[39] P. Juanuwattanakul, M. A. S. Masoum and S. Hajforoosh, "Application of SVC and single-phase shunt capacitor to improve voltage profiles and reduce losses of unbalanced multiphase smart grid with PEV charging stations," in *Proc. 2012 22nd Australasian Universities Power Engineering Conference (AUPEC)*, Bali, 2012, pp. 1-6.

[40] J. Lu, F. Nejabatkhah, Y. Li, and B. Wu, "DG control strategies for grid voltage unbalance compensation," in *Proc. 2014 IEEE Energy Conversion Congress and Exposition (ECCE),* 2014, pp.2932-2939.

[41] S. Chaudhary, R. Teodorescu, P. Rodriguez, P. Kjaer, and A. Gole, “Negative sequence current control in wind power plants with VSCHVDC connection,” *IEEE Trans. Sustain. Energy*, vol. 3, no. 3, pp. 535–544, Jul. 2012.

[42] I. E. Otadui, U. Viscarret, M. Caballero, A. Rufer, and S. Bacha, “New optimized PWM VSC control structures and strategies under unbalanced voltage transients,” *IEEE Trans. Ind. Electron.*, vol. 54, no. 5, pp. 2902–2914, Oct. 2007.

[43] A. Camacho, M. Castilla, J. Miret, A. Borrell, and L. de Vicuna, “Active and reactive power strategies with peak current limitation for distributed

generation inverters during unbalanced grid faults," *IEEE Trans. Ind. Electron.*, vol. 62, no. 3, pp. 1515-1525, Mar. 2015.

[44] F. Wang, J. L. Duarte, and M. A. M. Hendrix, "Pliant active and reactive power control for grid-interactive converters under unbalanced voltage dips," *IEEE Trans. Power Electron.*, vol. 26, no. 5, pp. 1511–1521, May 2011.

[45] R. Teodorescu, M. Liserre, and P. Rodrıguez, *Grid Converters for Photovoltaic and Wind Power Systems*. New York, NY, USA: Wiley, 2011.

[46] J. Miret, M. Castilla, A. Camacho, L. Garcıa de Vicua, and J. Matas, "Control scheme for photovoltaic three-phase inverters to minimize peak currents during unbalanced grid-voltage sags," *IEEE Trans. Power Electron*., vol. 27, no. 10, pp. 4262–4271, 2012.

[47] A. Camacho, M. Castilla, J. Miret, J. Vasquez, and E. Alarcon-Gallo, "Flexible voltage support control for three phase distributed generation inverters under grid fault," *IEEE Trans. Ind. Electron.*, vol. 60, no. 4, pp. 1429–1441, 2013.

[48] J. Miret, A. Camacho, M. Castilla, L. G. de Vicuna, and J. Matas, "Control scheme with voltage support capability for distributed generation inverters under voltage sags," *IEEE Trans. Power Electron.*, vol. 28, no. 11, pp. 5252–5263, Nov. 2013.

[49] C. T. Lee, C. W. Hsu, and P. T. Cheng, "A low-voltage ride-through technique for grid-connected converters of distributed energy resources," *IEEE Trans. Ind. Appl.*, vol. 47, no. 4, pp. 1821–1832, Jul. 2011.

[50] P. Rodriguez, A. Luna, J. Hermoso, I. E. Otadui, R. Teodorescu, and F. Blaabjerg, "Current control method for distributed generation power generation plants under grid fault conditions," in *Proc. 37th Ann. Conf. on IEEE Ind. Electron. Society (IECON)*, Nov. 2011, pp. 1262–1269.

[51] S. Alepuz, S. B. Monge, J. Bordonau, J. M. Velasco, C. Silva, J. Pont, and J. Rodriguez, "Control strategies based on symmetrical components for grid-connected converters under voltage dips," *IEEE Trans. Ind. Electron.*, vol. 56, no. 6, pp. 2162–2173, Jun. 2009.

[52] P. T. Cheng, C. Chen, T. L. Lee, and S. Y. Kuo, “A cooperative imbalance compensation method for distributed-generation interface converters,” *IEEE Trans. Ind. Appl.*, vol. 45, no. 2, pp. 805–815, Mar./Apr. 2009.

[53] Fei Wang; Hualong Mao; Dezhi Xu; Yi Ruan, "Negative-sequence admittance control scheme for distributed compensation of grid voltage unbalance," in *Proc. 2012 IEEE Control and Modeling for Power Electronics (COMPEL),* 2012, pp.1-8.

[54] M. Hamzeh, H. Karimi, and H. Mokhtari, “A new control strategy for a multi-bus MV microgrid under unbalanced conditions,” *IEEE Trans. Power Sys.*, vol. 27, no. 4, pp. 2225–2233, Nov. 2012.

[55] D. De and V. Ramanarayanan, “Decentralized parallel operation of inverters sharing unbalanced and non-linear loads,” *IEEE Trans. Power Electron.*, vol. 25, pp. 3015–3025, Aug. 2010.

[56] M. Savaghebi, A. Jalilian, J. C. Vasquez, and J. M. Guerrero, “Secondary control scheme for voltage unbalance compensation in an islanded droop-controlled microgrid,” *IEEE Trans. Smart Grid*, vol. 3, no. 2, pp. 797–808, Jun. 2012.

[57] L. Meng, F. Tang, M. Savaghebi, J. C. Vasquez, and J. M. Guerrero, “Tertiary control of voltage unbalance compensation for optimal power quality in islanded microgrids,” *IEEE Trans. Energy Conv.*, vol. 29, no. 4, pp. 802–816, Dec. 2014.

[58] J. Fernandez, S. Bacha, D. Riu, H. Turker and M. Paupert, "Current unbalance reduction in three-phase systems using single phase PHEV chargers," in *Proc. 2013 IEEE International Conference on Industrial Technology (ICIT)*, Cape Town, 2013, pp. 1940-1945.

[59] M. Coppo, A. Raciti, R. Caldon and R. Turri, "Exploiting inverter-interfaced DG for Voltage unbalance mitigation and ancillary services in distribution systems," in *Proc. 2015 IEEE 1st International Forum on Research and Technologies for Society and Industry Leveraging a better tomorrow (RTSI)*, Turin, 2015, pp. 371-376.

[60] R. Caldon, M. Coppo and R. Turri, "Coordinated voltage control in MV and LV distribution networks with inverter-interfaced users," in *Proc. 2013 IEEE Grenoble Conference*, Grenoble, 2013, pp. 1-5.

[61] R. Caldon, M. Coppo and R. Turri, "A network voltage control strategy for LV inverter interfaced users," in *Proc. 2012 8th Mediterranean Conference on Power Generation, Transmission, Distribution and Energy Conversion (MEDPOWER 2012)*, Cagliari, 2012, pp. 1-5.

[62] Akagi, H.,Watanabe, E. and Aredes, M., *Instantaneous Power Theory and Applications to Power Conditioning*, Wiley–IEEE Press, April 2007. ISBN 978-0-470-10761-4.

[63] F. Nejabatkhah, Y. W. Li and B. Wu, "Control strategies of three-phase distributed generation inverters for grid unbalanced voltage compensation," *IEEE Trans. Power Electron.*, vol. 31, no. 7, pp. 5228-5241, July 2016.

[64] F. Nejabatkhah; Y. Li; K. Sun, "Parallel three-phase interfacing converters operation under unbalanced voltage in hybrid ac/dc microgrid," *IEEE Trans. Smart Grid* , Early Access.

[65] K. Sun, X. Wang, Y. W. Li, F. Nejabatkhah, Y. Mei and X. Lu, "Parallel operation of bi-directional interfacing converters in a hybrid ac/dc microgrid under unbalanced grid voltage conditions," *IEEE Trans. Power Electron.*, vol. 32, no. 3, pp. 1872-1884, March 2017.

[66] F. Wang, J, Duarte, and M. Hendrix, “Design and analysis of active power control strategies for distributed generation converters under unbalanced grid faults,” *IET Gener. Transmiss. Distrib.*, vol. 4, no. 8, pp. 905-916, 2010.

[67] P. M. Andersson, *Analysis of Faulted Power Systems*. New York, NY, USA: IEEE Press, 1995.

[68] S. Boyd and L.Vandenberghe, *Convex Optimization*.NewYork,NY, USA: Cambridge Univ. Press, 2004.

[69] N. Hoffmann and F. W. Fuchs, “Minimal invasive equivalent grid impedance estimation in inductive–resistive power networks using extended Kalman filter,” *IEEE Trans. Power Electron.*, vol. 29, no. 2, pp. 631–641, Feb. 2014.

[70] M. Liserre, F. Blaabjerg, and R. Teodorescu, “Grid impedance estimation via excitation of LCL-filter resonance,” *IEEE Trans. Ind. App.*, vol. 43, no. 5, pp. 1401–1407, Sep./Oct. 2007.

[71] J. Huang, K. A. Corzine, and M. Belkhayat, “Small-signal impedance measurement of power-electronics-based AC power systems using lineto-line current injection,” *IEEE Trans. Power Electron*., vol. 24, no. 2, pp. 445–455, Sep. 2009.

[72] P. Rodriguez, J. Pou, J. Bergas, J. I. Candela, R. P. Burgos, and D. Boroyevich, “Decoupled double synchronous reference frame PLL for power converters controls,” *IEEE Trans. Power Electron.*, vol. 22, no. 2, pp. 584–592, Mar. 2007.

[73] P. Roncero-Sanchez, X. del Toro Garcia, A. Parreno Torres, and V. Feliu, “Fundamental positive- and negative-sequence estimator for grid synchronization under highly disturbed operating conditions,” *IEEE Trans. Power Electron.*, vol. 28, no. 8, pp. 3733–3746, Aug. 2013.

[74] P. Rodriguez, A. Luna, I. Candela, R. Mujal, R. Teodorescu, and F. Blaabjerg, “Multiresonant Frequency-Locked Loop for Grid Synchronization of Power Converters Under Distorted Grid Conditions”, *IEEE Trans. Ind. Electron.*, vol. 58, no. 1, pp. 127–138, Jan. 2011.

[75] A. Vidal, F. Freijedo, A. Yepes, P. Fernandez-Comesana, J. Malvar, O. Lopez, and J. Doval-Gandoy, “Assessment and optimization of the transient response of proportional-resonant current controllers for distributed power generation systems,” *IEEE Trans. Ind. Electron.*, vol. 60, no. 4, pp. 1367–1383, 2013.

[76] IEEE Standard 1159™, *IEEE Recommended Practice for Monitoring Electric Power Quality*, New York, NY, USA, Jun. 2009.

[77] Distribution Test Feeders, IEEE Power and Energy Society (PES), [Online]. Available: https://ewh.ieee.org/soc/pes/dsacom/testfeeders/.

[78] R. Caldon, M. Coppo and R. Turri, "Voltage unbalance compensation in LV networks with inverter interfaced distributed energy resources, "*2012*

IEEE International Energy Conference and Exhibition (ENERGYCON), Florence, 2012, pp. 527-532.

[79] R. Caldon, M. Coppo, M. Tessari and R. Turri, "Use of single-phase inverter-interfaced DGs for power quality improvement in LV networks," in *Proc. 2012 47th International Universities Power Engineering Conference (UPEC)*, London, 2012, pp. 1-5.

[80] Saadat, Hadi. *Power system analysis*. WCB/McGraw-Hill, 1999.

[81] R. P. S. Chandrasena, F. Shahnia, S. Rajakaruna and A. Ghosh, "Operation and control of three phase microgrids consisting of single-phase DERs," in *Proc. 2013 IEEE 8th International Conference on Industrial and Information Systems*, Peradeniya, 2013, pp. 599-604.

[82] F. Shahnia, R. P. S. Chandrasena, A. Ghosh and S. Rajakaruna, "Application of DSTATCOM for surplus power circulation in MV and LV distribution networks with single-phase distributed energy resources," in *Proc. 2014 IEEE PES General Meeting-Conference & Exposition*, National Harbor, MD, 2014, pp. 1-5.

Appendix A

Coefficients of Objective Function for Negative and Zero Sequences Current Minimization Using Single-Phase IFCs

The values of C_1 to C_{10} in (6.4) are presented here:

$$C_1 = \frac{1}{9\left|v_{PCC_a}\right|^2}$$

$$C_2 = \frac{1}{9\left|v_{PCC_b}\right|^2}$$

$$C_3 = \frac{1}{9\left|v_{PCC_c}\right|^2}$$

$$C_4 = \frac{2}{9\left|v_{PCC_a}\right|\left|v_{PCC_b}\right|}\cos\left(\theta_{v_{PCC_a}} - \theta_{v_{PCC_b}} - \frac{4\pi}{3}\right)$$

$$C_5 = \frac{2}{9\left|v_{PCC_a}\right|\left|v_{PCC_c}\right|}\cos\left(\theta_{v_{PCC_a}} - \theta_{v_{PCC_c}} - \frac{2\pi}{3}\right)$$

$$C_6 = \frac{2}{9\left|v_{PCC_b}\right|\left|v_{PCC_c}\right|}\cos\left(\theta_{v_{PCC_b}} - \theta_{v_{PCC_c}} + \frac{2\pi}{3}\right)$$

$$C_7 = \frac{2P_{PCC,b}}{9\left|v_{PCC_a}\right|\left|v_{PCC_b}\right|}\sin\left(\theta_{v_{PCC_a}} - \theta_{v_{PCC_b}} - \frac{4\pi}{3}\right) + \frac{2P_{PCC,c}}{9\left|v_{PCC_a}\right|\left|v_{PCC_c}\right|}\sin\left(\theta_{v_{PCC_a}} - \theta_{v_{PCC_c}} - \frac{2\pi}{3}\right)$$

Appendix A: Coefficients of Objective Function for Negative/Zero Sequence Current Minimization

$$C_8 = \frac{2P_{PCC,a}}{9\left|v_{PCC_a}\right|\left|v_{PCC_b}\right|}\sin\left(\theta_{v_{PCC_b}} - \theta_{v_{PCC_a}} + \frac{4\pi}{3}\right) + \frac{2P_{PCC,c}}{9\left|v_{PCC_b}\right|\left|v_{PCC_c}\right|}\sin\left(\theta_{v_{PCC_b}} - \theta_{v_{PCC_c}} + \frac{2\pi}{3}\right)$$

$$C_9 = \frac{2P_{PCC,a}}{9\left|v_{PCC_a}\right|\left|v_{PCC_c}\right|}\sin\left(\theta_{v_{PCC_c}} - \theta_{v_{PCC_a}} + \frac{2\pi}{3}\right) + \frac{2P_{PCC,b}}{9\left|v_{PCC_b}\right|\left|v_{PCC_c}\right|}\sin\left(\theta_{v_{PCC_c}} - \theta_{v_{PCC_b}} - \frac{2\pi}{3}\right)$$

$$C_{10} = \left(\frac{P_{PCC,a}\cos\left(\theta_{v_{PCC_a}}\right)}{3\left|v_{PCC_a}\right|} + \frac{P_{PCC,b}\cos\left(\theta_{v_{PCC_b}} + \frac{4\pi}{3}\right)}{3\left|v_{PCC_b}\right|} + \frac{P_{PCC,c}\cos\left(\theta_{v_{PCC_c}} + \frac{2\pi}{3}\right)}{3\left|v_{PCC_c}\right|}\right)^2 + \left(\frac{P_{PCC,a}\sin\left(\theta_{v_{PCC_a}}\right)}{3\left|v_{PCC_a}\right|} + \frac{P_{PCC,b}\sin\left(\theta_{v_{PCC_b}} + \frac{4\pi}{3}\right)}{3\left|v_{PCC_b}\right|} + \frac{P_{PCC,c}\sin\left(\theta_{v_{PCC_c}} + \frac{2\pi}{3}\right)}{3\left|v_{PCC_c}\right|}\right)^2$$

Moreover, the values of D_1 to D_{10} in (6.5) are presented here:

$$D_1 = \frac{1}{9\left|v_{PCC_a}\right|^2}$$

$$D_2 = \frac{1}{9\left|v_{PCC_b}\right|^2}$$

$$D_3 = \frac{1}{9\left|v_{PCC_c}\right|^2}$$

$$D_4 = \frac{2}{9\left|v_{PCC_a}\right|\left|v_{PCC_b}\right|}\cos\left(\theta_{v_{PCC_a}} - \theta_{v_{PCC_b}}\right)$$

$$D_5 = \frac{2}{9\left|v_{PCC_a}\right|\left|v_{PCC_c}\right|}\cos\left(\theta_{v_{PCC_a}} - \theta_{v_{PCC_c}}\right)$$

Appendix A: Coefficients of Objective Function for Negative/Zero Sequence Current Minimization

$$D_6 = \frac{2}{9\left|v_{PCC_b}\right|\left|v_{PCC_c}\right|}\cos\left(\theta_{v_{PCC_b}} - \theta_{v_{PCC_c}}\right)$$

$$D_7 = \frac{2P_{PCC,b}}{9\left|v_{PCC_a}\right|\left|v_{PCC_b}\right|}\sin\left(\theta_{v_{PCC_a}} - \theta_{v_{PCC_b}}\right) + \frac{2P_{PCC,c}}{9\left|v_{PCC_a}\right|\left|v_{PCC_c}\right|}\sin\left(\theta_{v_{PCC_a}} - \theta_{v_{PCC_c}}\right)$$

$$D_8 = \frac{2P_{PCC,a}}{9\left|v_{PCC_a}\right|\left|v_{PCC_b}\right|}\sin\left(\theta_{v_{PCC_b}} - \theta_{v_{PCC_a}}\right) + \frac{2P_{PCC,c}}{9\left|v_{PCC_b}\right|\left|v_{PCC_c}\right|}\sin\left(\theta_{v_{PCC_b}} - \theta_{v_{PCC_c}}\right)$$

$$D_9 = \frac{2P_{PCC,a}}{9\left|v_{PCC_a}\right|\left|v_{PCC_c}\right|}\sin\left(\theta_{v_{PCC_c}} - \theta_{v_{PCC_a}}\right) + \frac{2P_{PCC,b}}{9\left|v_{PCC_b}\right|\left|v_{PCC_c}\right|}\sin\left(\theta_{v_{PCC_c}} - \theta_{v_{PCC_b}}\right)$$

$$D_{10} = \left(\frac{P_{PCC,a}\cos\left(\theta_{v_{PCC_a}}\right)}{3\left|v_{PCC_a}\right|} + \frac{P_{PCC,b}\cos\left(\theta_{v_{PCC_b}}\right)}{3\left|v_{PCC_b}\right|} + \frac{P_{PCC,c}\cos\left(\theta_{v_{PCC_c}}\right)}{3\left|v_{PCC_c}\right|}\right)^2 + \left(\frac{P_{PCC,a}\sin\left(\theta_{v_{PCC_a}}\right)}{3\left|v_{PCC_a}\right|} + \frac{P_{PCC,b}\sin\left(\theta_{v_{PCC_b}}\right)}{3\left|v_{PCC_b}\right|} + \frac{P_{PCC,c}\sin\left(\theta_{v_{PCC_c}}\right)}{3\left|v_{PCC_c}\right|}\right)^2$$

Appendix B

IEEE 13-Node Test Feeder: Configuration Data

TABLE B.1 Overhead Line Configuration Data

Configuration	Phasing	Phase	Neutral	Spacing
		ACSR	ACSR	ID
601	B A C N	556,500 26/7	4/0 6/1	500
602	C A B N	4/0 6/1	4/0 6/1	500
603	C B N	1/0	1/0	505
604	A C N	1/0	1/0	505
605	C N	1/0	1/0	510

TABLE B.2 Underground Line Configuration Data

Configuration	Phasing	Cable	Neutral	Space ID
606	A B C N	250,000 AA, CN	None	515
607	A N	1/0 AA, TS	1/0 Cu	520

TABLE B.3 Line Segment Data

Node A	Node B	Length (ft.)	Configuration
632	645	500	603
632	633	500	602
633	634	0	XFM-1
645	646	300	603
650	632	2000	601
684	652	800	607
632	671	2000	601
671	684	300	604
671	680	1000	601
671	692	0	Switch
684	611	300	605
692	675	500	606

TABLE B.4 Transformer Data

	kVA	kV-high	kV-low	R - %	X - %
Substation:	5,000	115 - D	4.16 Gr. Y	1	8
XFM -1	500	4.16 – Gr.W	0.48 – Gr.W	1.1	2

TABLE B.5 Capacitor Data

Node	Ph-A	Ph-B	Ph-C
	kVAr	kVAr	kVAr
675	200	200	200
611			100
Total	200	200	300

TABLE B.6 Regulator Data

Regulator ID:	1		
Line Segment:	650 - 632		
Location:	50		
Phases:	A - B -C		
Connection:	3-Ph,LG		
Monitoring Phase:	A-B-C		
Bandwidth:	2.0 volts		
PT Ratio:	20		
Primary CT Rating:	700		
Compensator Settings:	Ph-A	Ph-B	Ph-C
R - Setting:	3	3	3
X - Setting:	9	9	9
Voltage Level:	122	122	122

TABLE B.7 Spot Load Data

Node	Load	Ph-1	Ph-1	Ph-2	Ph-2	Ph-3	Ph-3
	Model	kW	kVAr	kW	kVAr	kW	kVAr
634	Y-PQ	160	110	120	90	120	90
645	Y-PQ	0	0	170	125	0	0
646	D-Z	0	0	230	132	0	0
652	Y-Z	128	86	0	0	0	0
671	D-PQ	385	220	385	220	385	220
675	Y-PQ	485	190	68	60	290	212
692	D-I	0	0	0	0	170	151
611	Y-I	0	0	0	0	170	80
	TOTAL	1158	606	973	627	1135	753

TABLE B.8 Distributed Load Data

Node A	Node B	Load	Ph-1	Ph-1	Ph-2	Ph-2	Ph-3	Ph-3
		Model	kW	kVAr	kW	kVAr	kW	kVAr
632	671	Y-PQ	17	10	66	38	117	68